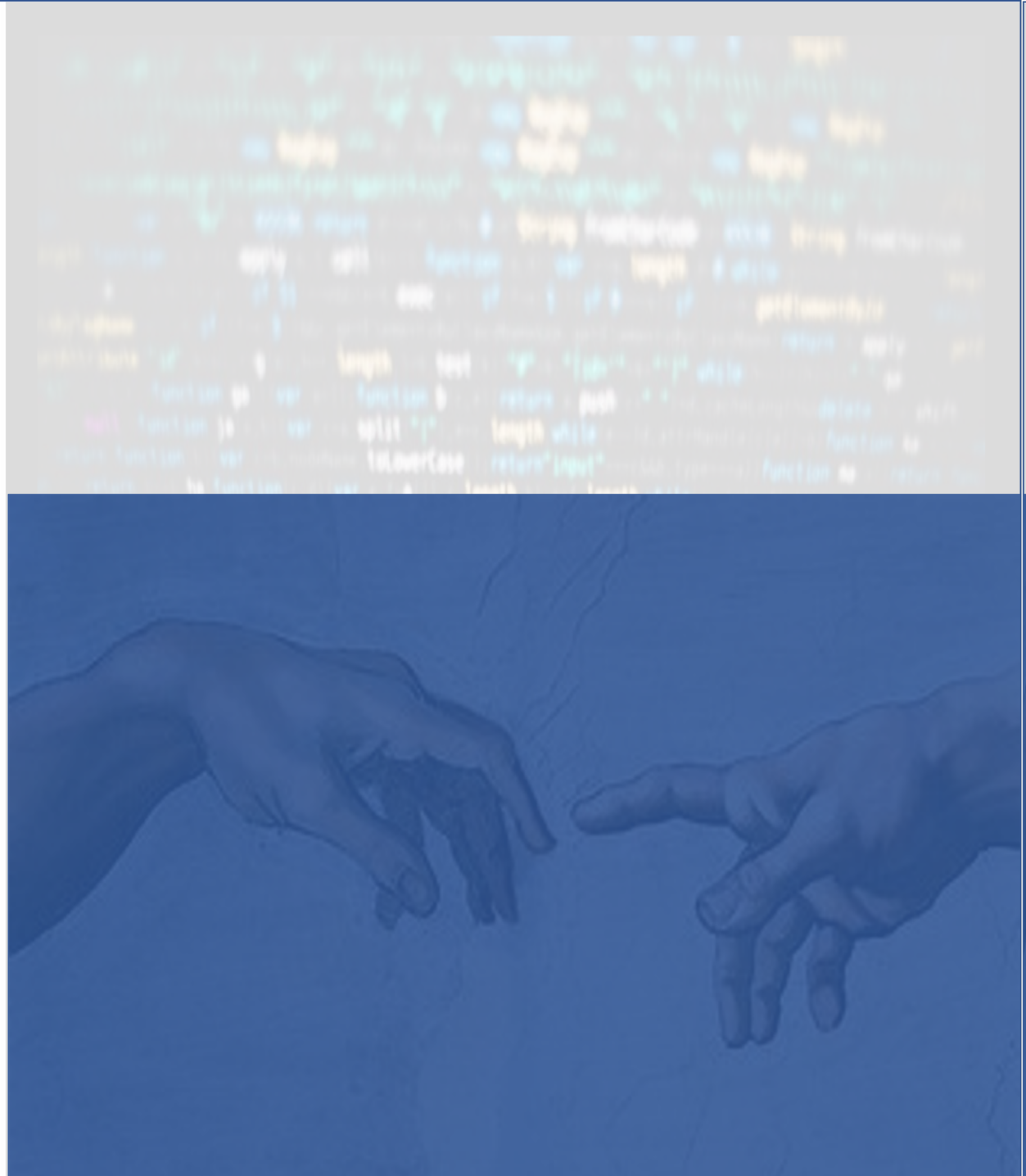

UNIVERSITAT JAUME I

Doping and phase transitions processes on semiconductors and vibrational properties in complex glasses: A theoretical and experimental investigation

Doctoral Thesis

2021

Eduardo de Oliveira Gomes

Doping and phase transitions processes on semiconductors and vibrational properties in complex glasses: A theoretical and experimental investigation

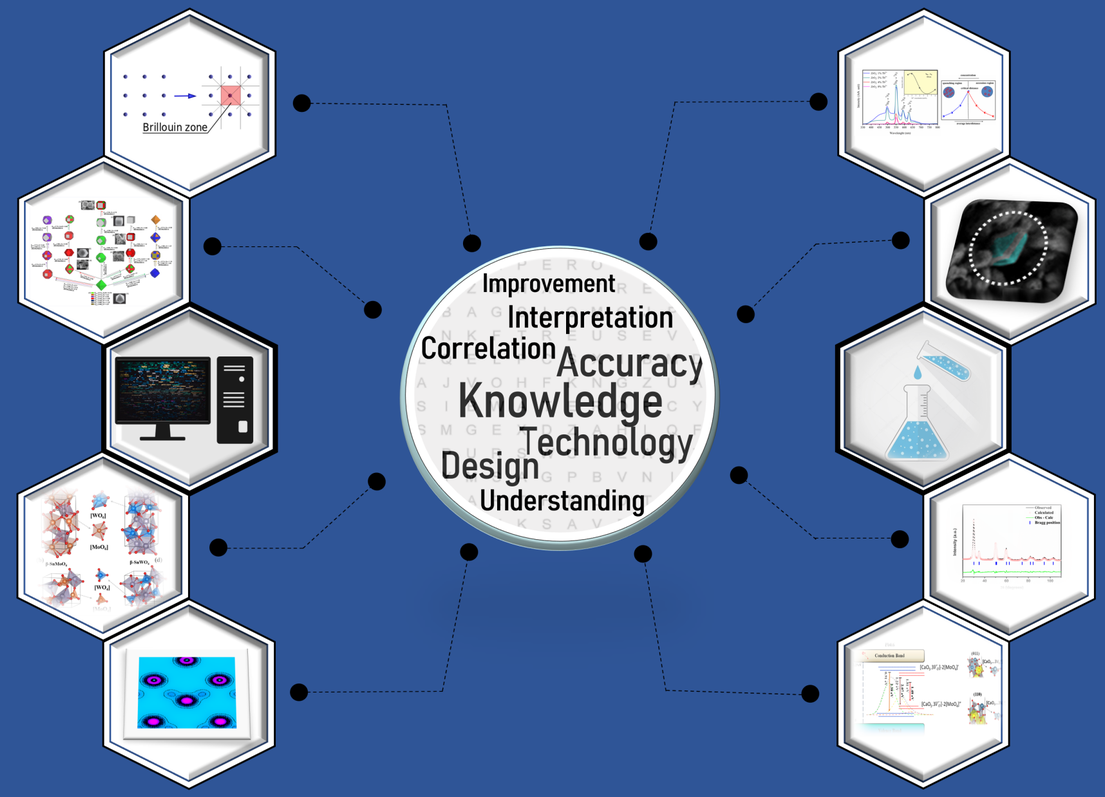

Ph.D. Candidate:

Eduardo de Oliveira Gomes
December/2021

Supervisors:

Prof. Juan Andrés Bort
Prof. Lourdes Gracia Edo

Doctoral Program in Theoretical Chemistry and Computational Modelling

Universitat Jaume I Doctoral School

Doping and phase transitions processes on semiconductors and vibrational properties in complex glasses: A theoretical and experimental investigation

Report submitted by Eduardo de Oliveira Gomes in order to be eligible for a doctoral degree awarded by the Universitat Jaume I

Eduardo de Oliveira Gomes (Ph.D. candidate)

Prof. Juan Andrés Bort (Supervisor)

Prof. Lourdes Gracia Edo (Supervisor)

EDUARDO\| DE OLIVEIRA GOMES Firmado digitalmente por EDUARDO\|DE OLIVEIRA GOMES Fecha: 2021.12.09 16:30:19 +01'00'

JUAN MANUEL\| ANDRES\| BORT Firmado digitalmente por JUAN MANUEL\| ANDRES\|BORT Fecha: 2021.12.09 15:37:05 +01'00'

LOURDES \|GRACIA\| EDO Firmado digitalmente por LOURDES\|GRACIA\|EDO Nombre de reconocimiento (DN): CN = LOURDES\|GRACIA\| EDO, SN = GRACIA EDO, G = LOURDES, C = ES, O = ACCV, OU = CIUDADANOS Fecha: 2021.12.09 14:47:15 +01'00'

Castelló de la Plana (Spain), December 2021

Funding:

- Generalitat Valenciana through the grant **Santiago Grisolia program** (2018/064) and **BEFPI**/2021.

- Universitat Jaume I through the project **UJI-B2019-30.**

Thesis by compendium of publications:

I- Title: Identifying and explaining vibrational modes of sanbornite (low-$BaSi_2O_5$) and $Ba_5Si_8O_{21}$: A joint experimental and theoretical study
Authors: Eduardo de Oliveira Gomes, Benjamin J.A. Moulton, Thiago R. Cunha, Lourdes Gracia, Paulo S. Pizani, Juan Andrés.
Journal: Spectrochimica Acta Part A: Molecular and Biomolecular Spectroscopy **2021**, 248, 119130. *doi.org/10.1016/j.saa.2020.119130* (IF: 4.098 - Q1)

II- Title: A theoretical and experimental investigation of hetero-versus homo connectivity in barium silicates
Authors: Benjamin J. A. Moulton, Eduardo de Oliveira Gomes, Thiago R. Cunha, Carsten Doerenkamp, Lourdes Gracia, Hellmut Eckert, Juan Andrés, Paulo S. Pizani.
Journal: American Mineralogist **2022** (*in press*). *doi.org/10.2138/am-2021-7910* (IF: 3.003 - Q1)

III- Title: Joint theoretical and experimental study on the La doping process in In_2O_3: Phase transition and electrocatalytic activity
Authors: Samantha C. S. Lemos, Edson Nossol, John. L. Ferrari, Eduardo de Oliveira Gomes, Juan Andrés, Lourdes Gracia, Iván Sorribes, Renata C. Lima.
Journal: Inorganic Chemistry **2019**, 58, 17, 11738–11750.
doi.org/10.1021/acs.inorgchem.9b01728 (IF: 5.165 - Q1)

IV- Title: Structure, electronic properties, morphology evolution, and photocatalytic activity in $PbMoO_4$ and $Pb_{1-2x}Ca_xSr_xMoO_4$ (x= 0.1, 0.2, 0.3, 0.4 and 0.5) solid solutions
Authors: Eduardo de Oliveira Gomes, Lourdes Gracia, Anderson A. G. Santiago, Ricardo L. Tranquilin, Fabiana V. Motta, Rafael A. C. Amoresi, Elson Longo, Mauricio R. D. Bomio, Juan Andrés.
Journal: Physical Chemistry Chemical Physics **2020,** 22, 25876-25891.
doi.org/10.1039/D0CP04596A (IF: 3.676 - Q1)

V- Title: Integrated experimental and theoretical study on the phase transition and photoluminescent properties of ZrO_2: xTb^{3+} (x= 1, 2, 4 and 8 mol%)
Authors: Laura X. Lovisa, Eduardo de Oliveira Gomes, Lourdes Gracia, Anderson A. G. Santiago, M. Siu Li, Juan Andrés, Elson Longo, Mauricio R. D. Bomio, Fabiana V. Motta
Journal: Materials Research Bulletin **2022**, 145, 111532.
doi.org/10.1016/j.materresbull.2021.111532 (IF: 4.641- Q1)

VI- Title: Photoluminescence emissions of $Ca_{1-x}WO_4$: xEu^{3+}: Bridging between experiment and DFT calculations
Authors: Amanda Fernandes Gouveia, Marcelo Assis, Lara Kelly Ribeiro, Aline Estefany Brandão Lima, Eduardo de Oliveira Gomes, Daniele Souza, Yara Gobato Galvão, Ieda Lucia Viana Rosa, Geraldo Eduardo da Luz Jr., Eva Guillamón, Elson Longo, Juan Andrés, Miguel Angel San-Miguel
Journal: Journal of Rare Earths **2021** (*in press*). *doi.org/10.1016/j.jre.2021.08.023* (IF: 3.712 - Q2)

VII- Book chapter Title: Morphology-dependent properties in inorganic semiconductors: An experimental and theoretical approach
Authors: Amanda Fernandes Gouveia, Luis Henrique da Silveira Lacerda, Eduardo de Oliveira Gomes, Lourdes Gracia, Marcelo Assis, Camila Cristina de Foggi, Elson Longo, Juan Andrés, Miguel Angel San-Miguel
Book title: Advances in Material Research and Technology Series, (*pre-proof*)
Editorial: Springer (Series Ed.: Ikhmayies, Shadia Jamil)
https://www.springer.com/series/16426 ISSN: 2662-4761.

VIII- Title: Unveiling the relationship between the phase transition induced by pressure and the substitution processes along α- and β-$SnMo_{1-x}W_xO_4$ (x=0, 0.25. 05, 0.75 and 1) solid solutions (*drafting*).
Authors: Eduardo de Oliveira Gomes, Amanda F. Gouveia, Lourdes Gracia, Juan Andrés

"This thesis has been accepted by the co-authors of the publications listed above that have waved the right to present them as a part of another PhD thesis"

" Nunca vou deixar de Te agradecer porque cada dia da minha vida é um motivo para reconhecer tudo o que sempre fazes por mim e pelos meus ".

João 3.16

Acknowledgements

"*La gratitud no se trata de las bendiciones que tenemos, sino de qué hacemos con ellas*". W.T. Purkiser

Quero finalizar esta etapa da minha vida dedicando e agradecendo a todos que estiveram e me apoiaram em todo o caminho até aqui, inúmeras são as pessoas que contribuíram na trajetória, na construçao e conclusão. Desejo expresar a gratidão a cada um de vocês, talvez possa esquecer alguma ou outra pessoa, mas sei da importancia de cada um em toda a caminhada.

Agradezco a la Generalitat Valenciana por la financiación recibida a través del Programa Santiago Grisolía (2018/064) y BEFPI/2021, a la Universitat Jaume I por la oportunidad que me ha dado para realizar y defender la presente Tesis Doctoral y al proyecto UJI-B2019-30 que me ha cubierto los gastos ocasionados en la participación en congresos y cursos relacionados con mi formación como investigador, y también al Servei d'Informatica en cuyos ordenadores de cálculo científico he realizado la mayor parte de los cálculos que constituyen los trabajos de esta Tesis.

Quiero dar las gracias a mis directores de Tesis, Prof. Dr. Juan Andrés y Dr. Lourdes Gracia, por su cooperación, dedicación, confianza y los conocimientos transmitidos, haciendo así posible la realización de este trabajo.

A los profesores de la Universitat Jaume I, en el departamento de Química Física i Analítica: Sixte Safont, Rosa Llusar, Armando Beltrán, Mónica Oliva y Amanda Gouveia del laboratorio de Quimica Teórica y Computacional y a Sergio Martí, Vicente Moliner, Raquel Castillo, Maite Roca y Eva Guillamón por la recepción y cooperación durante estos años.

A los compañeros de laboratorio y todas las personas que he tenido la suerte de conocer, a los doctorandos Miquel, Natalia, Daria, Ezequiel y Santiago, con vosotros he pasado la mayor parte del tiempo durante estos años, y por eso os quiero agradecer por los buenos momentos, conversaciones, comidas y cervezas. Bem como a Samantha, Marcelo, Leonélio e Emerson que no inicio foram primordiais na minha chegada e adpataçao a Espanha, me permitindo ainda que fora, estar no Brasil. A los doctores, Kemel, Rafael, Ivo y Camila por toda experiencia passada. A Los compañeros del grupo de Materiales Moleculares; Maria Gutiérrez y Juan José por las conversaciones y buenos momentos.

Agradezco también a la querida Merche, por toda paciencia y la ayuda que me ha ofrecido en los trámites burocráticos y administrativos.

Como parte da menção internacional Ik wil Prof. Dr. Frederik Tielens bedanken voor het project en voor zijn gastvrijheid tijdens mijn verblijf, alsook voor de steun, de leerrijke lessen en de aangename momenten en etentjes bij hem thuis. Vorrei ringraziare il Dr. Flavio a nome dei colleghi dell'ALGC Bruxelles, per il suo supporto, i suoi insegnamenti e le discussioni sulle idee del progetto.

Al profesor José Manuel Recio (Michi) y todos los compañeros del (QTCMAT) por la recepción durante mi estancia en la universidad de Oviedo.

Ao Prof. Elson longo e ao CDMF pelas colaborações e parcerias nos projetos e trabalhos desenvolvidos, assim como os demais grupos participantes.

Tambem quero agradecer àqueles que fazem parte de onde tudo começou, ao Prof. Mauricio Bomio e a Prof. Fabiana Villela, bem como a todos pesquisadores/colegas e professores do LSQM, na UFRN Brasil.

E, não por último, mas como base e suporte a isso tudo, quero agradecer a minha familia, em especial a senhora Edneide Olivira, minha mãe, aos meus irmãos e sobrinhos, ao Pr. Ângelo Filho e toda sua família, em nome da IECZS, bem como a todos amigos, de perto e de longe.

Esses são os meus mais sinceros agradecimentos a todos.

Muito obrigado, Muchas gracias, Grazie molte, Heel erg bedankt!

Abstract

Technological advances have always accompanied the human progress and are largely driven by the design and discovery of new materials. Its impact on modern society plays a fundamental role in the strategies for the establishment of sustainable chemical technologies that are efficient from the energy point of view and respect the environment.

Due to the rapid advancements in computing processors, computing hardware, and software, and in particular, the trade-off between accuracy and computational cost provided by the Density Functional Theory (DFT), the methods and techniques of the Theoretical and Computational Chemistry (TCC) not only play a central role in explaining, rationalizing, and predicting experimental results, but it has also increasingly become a valuable tool aimed at discovering and simulating new materials and catalysts. Modeling, at the atomic level, and the use of TCC calculations are a central aspect of modern chemistry and physics, providing a deeper insight into how advanced materials work. The design and synthesis processes for obtaining new materials can be accelerated using first principles calculations and it has rapidly evolved from an explanatory tool to support experimental characterization, allowing theory-driven design and optimization of materials to address some of the most pressing technological challenges of our time.

Bridging the gap between experimental and computational researchers by fostering close collaborations is mandatory for making a breakthrough in the investigation of materials. The combined forces of these two pillars, experiment and in-depth computational analyses are more powerful than ever and capable of quantitative predictions, though care must still be taken in comparing results from theory and experiment. It is the main strength of the present Ph. D, which cover a multidisciplinary field combining physics, chemistry, theoretical and computational chemistry, and materials science pushing the boundaries for find and understand the structure and properties, at atomic level, of two types of materials: glasses (Ba_2SiO_4, high-$BaSiO_3$, $Ba_4Si_6O_{16}$, $Ba_5Si_8O_{21}$, $Ba_6Si_{10}O_{26}$, high-$BaSi_2O_5$ and low-$BaSi_2O_5$) and semiconductors ($PbMoO_4$, In_2O_3, ZrO_2, $CaWO_4$ and $SnMoO_4$/$SnWO_4$). We discuss and present recent advances for understanding, by the use of first-principles quantum-mechanical calculations, at DFT level, their structural, electronic, and optical properties. We also studied the doping processes, the formation of solid solution, and phase transitions induced by pressure, that play key roles in the further development of these materials for optoelectronic and photocatalytic applications. We hope that present results guide the synthesis for the most promising candidates of a particular application.

Index

1. Introduction

Joseph MacDouall writes: ‘‘Chemistry is a game that electrons play’’ (*J. J. W. MacDouall, Computational Quantum Chemistry: Molecular Structure and Properties in Silico. RSC Theoretical and Computational Chemistry Series, Royal Society of Chemistry, 2013)*, cited by Ali and Allam [1]. If we are capable to known and understand the nature of their interactions, then we could control the *“game”* and unveiling the behavior and applications of materials, which are the backbone of our modern civilization. This comment can be employed in the investigation of materials, *i.e.*, the understanding, at atomic level, control and prediction of functional materials behavior is not only of immense fundamental significance, but also represents a crucial step toward important wide-ranging applications [2].

Understanding the structure−property relationship of inorganic solids has emerged as a prevailing strategy to provide guidelines for predicting and designing desired functional materials. Experimental discoveries followed by theoretical interpretations that pave the way of further advances by experimentalists is a developing pattern in modern chemistry and materials science. The revolution of these sciences started with the development of experimental techniques such as *X-ray* diffraction, infrared and Raman spectroscopy, electron microscopy, in which the close collaboration between experimentalists and theorists led to the quantitative determination of structure and composition. For example, the experimental discovery of the chemical activity of surface defects and the trends in the reactivity of transitional metals followed by the explanations from the theoretical studies led to the molecular level understanding of active sites in catalysis [3]. The molecular level knowledge, in turn, provided a guide for experiments to search for new generation of catalysts. These and many other examples of successes in experiment-and-theory-combined studies demonstrate the importance of the collaboration between experimentalists and theorists in the development of modern science, Figure 1.

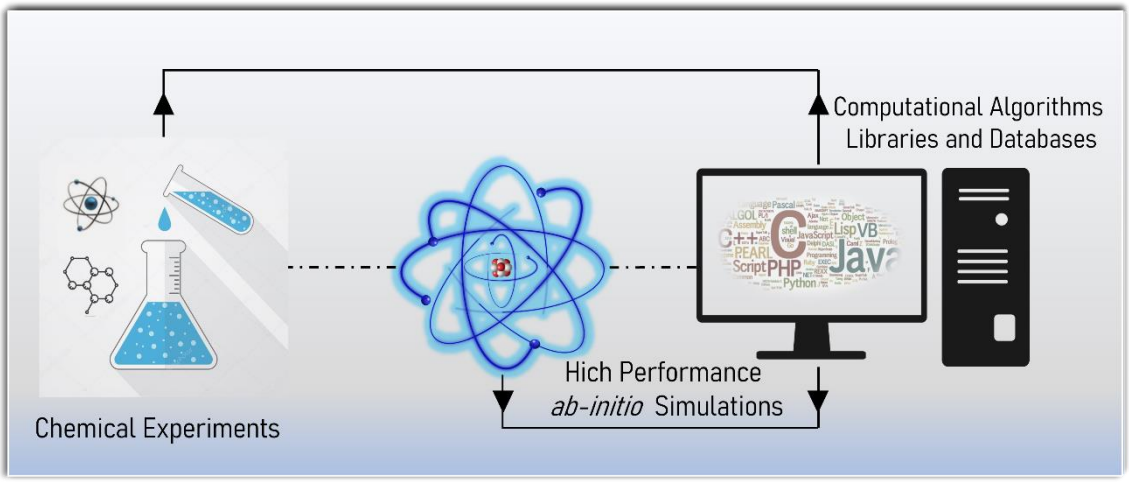

Figure 1: A schematic presentation of experiment-and-theory combination.

1.1. Quantum mechanics: calculations and simulations

Materials are real-world developments of quantum mechanics, embodying what is described as interactions in a Hamiltonian. Novel states of matter emerge, depending on relative coupling strengths of these interactions as well as external excitations. An intricate interplay involving different degrees of freedom and excitations of charge, spin, and lattice determines underlying time scales and, hence, real-time dynamics. These interactions are at the heart of how the materials display their properties and then the corresponding functions. Intriguing and rich information about electrons, atoms and ions of a material is encoded in these interactions that are dominated by quantum-mechanical effects.

The emergence of new phenomena challenges the limits of our fundamental understanding of nature at microscopic length and ultrafast time scales. In other words, the atomic and molecular world, unlike the macroscopic world, can only be accurately described by quantum mechanics, and is dominated by quantum mechanical effects. The natural properties and behavior of molecules and materials are difficult to understand and rationalize, as well as they are impossible to predict without resorting to approximations. In this context, quantum mechanical calculations and simulations play a central role in understanding the properties of materials and, increasingly, predicting the properties of new materials.

Computational materials science is a robust research field with has significant advances over the last decades. In the early stages of the field, pre-total-energy methods that used parametrizations for many-body integrals were the most popular tools used for evaluating the properties of molecules and solids. The emphasis was mainly on understanding the energy, atom positions, and band structure and results were mostly qualitative. The advent of density functional theory (*DFT*) [4-7] led to better simulation capabilities, which delivered a deeper understanding of the properties of multi-atomic systems.

Actual sophisticated methods and the ever-increasing speed of computers over the last decades, have allowed quantum mechanical calculations to achieve a status at the same level as the experiments. It is a key component of science research and established a place for itself in the chemistry, physics, and materials science toolbox next to such common laboratory techniques as *X-ray* diffraction, infrared and Raman spectroscopy, electron microscopy, and so on. Computational modeling and molecular simulations have

substantially contributed to the progress in the fundamental understanding of many fields of research, such as chemical reactivity [8,9].

Over the past decade computational materials science has undergone a tremendous growth thanks to the availability, power, and relatively limited cost of high-performance computational equipment. Computations have become indispensable in providing an atomistic framework for the interpretation of spectroscopic data and elucidation of reaction mechanisms. State-of-the-art quantum chemical methodologies and, particularly, the methods are well-suited for studying chemical reactivity, analyzing complex reaction paths, and modeling kinetics of complex chemical reactions. The widespread application of computational chemistry is facilitated by the availability of convenient quantum chemistry and molecular modeling software that enables the practice of quantum chemistry in the absence of advanced programming skills and dedicated theoretical training. Computational chemistry is currently routinely employed not only by theoreticians, but by a wide range of experimental catalysis groups who often use results of atomistic *DFT* modeling to support mechanistic proposals derived from the experiments. The direct correlation between the results of molecular modeling and experimental data has become a common practice supported by the great success of near-chemical accuracy that can potentially be achieved with the modern computational approaches.

Conventionally, the accuracy in theoretical computational chemistry refers to the performance of a particular methodology in computing specific fundamental chemical properties with respect to experimental or highly accurate theoretical results. In practical calculations, the overall accuracy also strongly depends on the quality of the model, that is, how well it accounts for the important chemical details of the specific material or property in question. There is a natural trade-off between the method (level of theoretical approximation) and model accuracies (level of chemical details included in the model). The maturity of the field arose with the development, within the last 30 years, of different *DFT* computational packages [10-16].

In this context, the methods and techniques of theoretical and computational chemistry have permanently reshaped the landscape of chemical and materials science by providing tools to support and guide experimental efforts and for the prediction, understanding, and rationalization of structure and electronic properties at the atomic level. In this regard, electronic structure packages have played a special role by using first principle-driven methodologies to model complex chemical and materials processes.

Over the past few decades, the rapid development of computing technologies and the tremendous increase in computational power have offered a unique chance to study complex systems and transformations in and condensed phase systems at different levels of theory.

In this Doctoral Thesis we will investigate two types of materials: semiconductors composed of binary and ternary metal oxides and boron silicates as representative family of glasses. We are in front of complex systems, in which their variety and the different constituents of these systems are prone for the appearance of new properties. For understanding their functions, it is mandatory to consider local properties and/or events, and this concept is contrary to the philosophy of reductionism, the traditional physics hallmark. Then, we can move to local analysis, in which structural and electronic disorder prevails.

First, a brief introduction on semiconductors (metal oxides) and glasses (barium silicates) are shown in Section 1.2. and 1.3., respectively. In particular, the doping process, formation of solid solutions, pressure effects, Raman vibrational spectra and photoluminescence emissions and morphology have been highlighted. Section 2 introduces the aims of present Doctoral Thesis. Section 3 shows the main computational methods used. Section 4 describes the results and discussion derived from the different articles. Section 5 a brief conclusion and an outlook based on the results special wettability are shown. In the final section 6, the list of published and submitted papers are shown.

1.2. Semiconductors: metal oxides

Over the last decades, tremendous efforts have been made in science pushed by the need for high-efficiency and technologically useful systems for the development of functional materials. Nowadays, environmental sustainability, renewable energy, and health issues are the focus of global concern. To solve these problems, semiconductor-based materials has attracted considerable attention for its promising potential by finding solutions in these subjects. Semiconductors are currently considered as an important class of materials both for fundamental studies and technological applications because of their unique combination of remarkable properties and nature of ease of fabrication and processing. These materials display excellent properties when applied in solar energy

conversion, optoelectronic devices, molecular and cellular imaging, photocatalysis and catalysis, and ultrasensitive detection. The rapid progress in semiconductor technology, thus, relies on the control of materials themselves and on the success in understanding and controlling their structure and properties. Some semiconductors are low in cost, rich in material choices, and broadly tunable these advantages are attractive for a plethora de technological applications.

The network structure of semiconductors can be modified by doping processes, and such a modification has been used to control the physical and chemical properties. They also show high versatility, since it is possible to tune the band gap by modifying the structure by doping processes. Doping or alloying process, *i.e.*, the intentional incorporation of atoms or ions of specific elements into host lattices, provides a fundamental approach to modify the properties of semiconductor crystals by means of tailoring the crystal's compositions. It is a widely applied technological process to control and manipulate the properties of semiconductors to generate materials with desirable functions. Doping is essential for modern semiconductor industry. Doping is also expected to play a key role in the future nanoscience and nanotechnology by means of creating doped nanocrystals and nanostructures with unprecedented properties. As recently remarked by Stevanovic: "To be practical, semiconductors need to be doped. Sometimes, they need to be doped to nearly degenerate levels, *e.g.*, in applications such as thermoelectric, transparent electronics, or power electronics" [17].

At the same time, various strategies, including doping processes has been largely pursued to extend the spectral breadth and efficiency of photo response. The charged carrier recombination and the interfacial electron transfer rates can be significantly altered by semiconductor doping. For instance, the photo reactivity of doped TiO_2 is influenced by several parameters such as the dopant concentration, the energy levels of dopants differently located within the TiO_2 lattice, their electronic configuration, as well as by the irradiation intensity [18]. Therefore, the specific preparation method is expected to have significant impact on the overall photoactivity of doped TiO_2. In addition, crystal phase tailoring and textural modification [19-25], surface sensitization and modification of semiconductor photocatalysts [25,26] have been developed in the attempt to modify and possibly tune the photocatalytic processes involving light harvesting and semiconductor excitation, in relation to bulk diffusion, surface trapping and interfacial transfer of the electrons and holes photoproduced on the semiconductor surface upon irradiation [26-32].

Over the past few years great effort has been dedicated to the study of inorganic metal oxides as semiconductors. The preparation of these novel semiconductors has always been the goal of chemistry and material scientists because almost all contemporary electronic technologies involve the use of semiconductors [33-36]. The study of these materials constitutes an active research topic due to their excellent performance, and they are often encountered in science and engineering disciplines. Therefore, metal oxides semiconductors figure prominently in many current technologies, and they will play an important role in enabling a host of future applications.

The semiconductor photocatalyst are used for several decades in the past, which is called as green technology having received great attention and shows an excellent ability for degrading contaminant by utilizing sunlight without causing any pollution. They also show high versatility, since it is possible to tune the band gap by modifying the structure and/or the nature of metals. The achievable rapid fabrication of these materials with tunable physical and chemical properties facilitates tailoring the macroscopic properties of particle assemblies through contacts at the nanoscale. An ideal semiconductor needs to fulfill the following: should be chemically and biologically inert, stable, photochemically active and cheap. Nowadays, semiconductors play a central role in acing new global environment- and energy-related issues [37]. In fact, this research field is widely, not only for promoting the solar into chemical energy conversion through thermodynamically up-hill reactions producing fuels, such as H_2 evolution from H_2O [38-41], but also the obtention of CH_4 and CH_3OH from CO_2 [42-44].

The typical mechanism of a semiconductor involves three key processes, namely harvesting light to generate charge, charge separation and transfer to surface active sites, as well as specific interfacial catalytic reactions [45-47]. In other words, the activity of a semiconductor begins with the generation of charge carriers. Following rapid hot carrier thermalization, the energy of the charge carriers is determined by the band alignment and occupancy in the semiconductor. In the excited state (conduction band), there is a competition between recombination and spatial charge separation, and this kinetics are strongly influenced by the presence of surface defects and mid gap states in the material. If the carriers avoid recombination long enough, the possibility for interfacial charge injection provides a pathway for chemical rearrangement (redox) taking place at the surface. The competition between charge generation, separation, recombination, and injection determines the efficiency of the material. Many of these processes occur on the

ultrafast time scale. Additionally, they are strongly influenced by complex surface chemistry, a result of various structural defects and associated electronic/magnetic states.

Characterization techniques of surfaces and/or bulk are used to find a correlation among the semiconductor surface properties and the resultant activity performance of semiconductor materials [48-49]. This research field is very active and different procedures have been reported for the modification, tailoring and engineering of structure and electronic/magnetic properties at the morphology to modulate the bulk diffusion, surface trapping and interfacial transfer of the electrons and holes photoproduced on the semiconductor surface [19-24][26-28][50-52].

1.3. Glasses: barium silicates

Crystals and crystalline materials have a three-dimensional periodic structure with translational and point symmetries, therefore, their physical and chemical properties are anisotropic. On the other hand, glasses, as amorphous materials, have a random structure with no translational symmetry and no point symmetry, therefore their macroscopic properties are isotropic. A glass is formed through a liquid-glass transition by rapid cooling from a supercooled liquid state into a nonequilibrium glassy state. Various kinds of organic and inorganic glasses are known among polymers, drugs, minerals, metals, semiconductors, etc. [53-55].

Barium silicates are a subclass of inorganic glasses with significance in chemical, physical and materials sciences for their excellent material properties and device performance in a range of important technological applications. They present a rich structural diversities and potential applications in diverse technological fields. For example, barium silicate-based ceramics are used as solid-oxide sealant materials [56], erasable-writable optical storage devices [55], and, when doped with rare-earth elements, as light emitting diode materials [57-58]. Despite the potential importance, the structural origin of the properties of these non-crystalline oxides has remained a challenging problem in physical chemistry and materials research.

Barium silicates are built of SiO_4^{n-} tetrahedra, the fundamental building blocks of almost all silicate minerals and liquids [59-60]. Its remarkable stability through the transition from the solid into the liquid state is central to understanding and predicting the properties of silicate crystals, glasses, and melts. The modified random network model of silicate liquids describes them as having two entangled subnetworks: one constructed

from interconnected silica tetrahedra and one comprised of ill-defined modifier-oxygen polyhedra (MO_x, where M = *K*, *Ba*, etc.) [61]. The silica subnetwork contains tetrahedra that may be connected by up to four additional tetrahedra units. Connectivity is defined by the number of *Si-O-Si* bonds found around a central tetrahedron and described using the Q^n species notation, where *n* is the number of *bridging oxygen* (*BO*) atoms shared between tetrahedra and 4^{-n} is the number of *non-bridging oxygen* (*NBO*) atoms bound to *M* cations [62]. Most crystalline silicates are built from a single Q^n species, whereas in silicate liquids and glasses have two or more Q^n species that are assumed to be randomly linked. They are stabilized in a wide range of structures from neso- (Q^0), ino- (Q^2), and phyllo-(Q^3) silicates, which are built from a single Q^n species [63-65]. When bonding is between Q^n of equal *n*, *e.g.* Q^3-Q^3, refer to this as *homo-connectivity*. In this mineralogically rare situation, where Q^n are bound to $Q^{n\pm1}$, *e.g.* Q^2-Q^3 linkages, refer to this as *hetero-connectivity*, figure 2. By far the most common hetero-connective mineral phases are found within the amphibole group (*e.g.* tremolite, $Ca_2Mg_5Si_8O_{22}(OH)_2$), which have complex chemistry including hydroxyl groups. Beyond their structures and thermal expansion behavior [66], little is known about these hetero-connected phases.

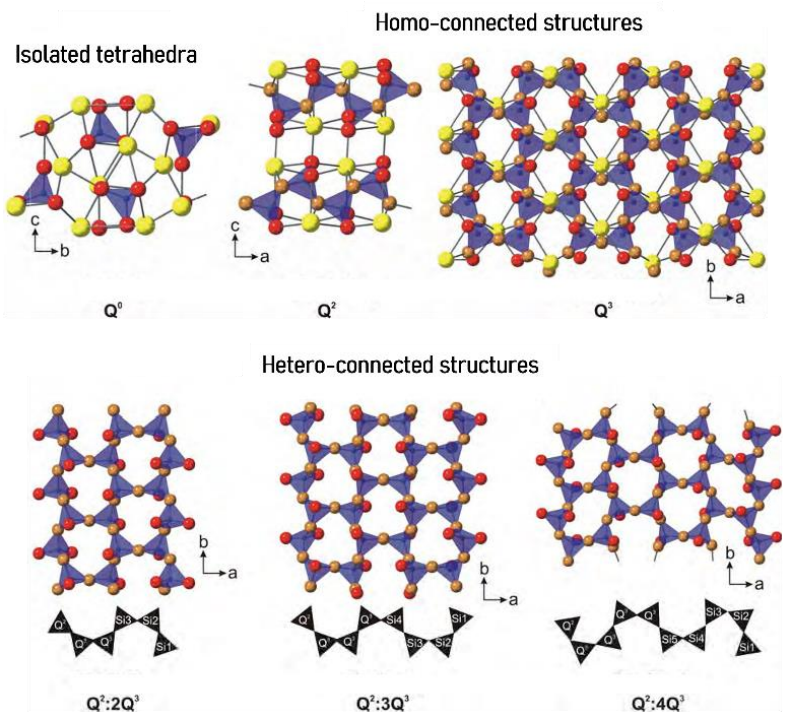

Figure 2: A schematic representation of Barium silicates. *Ba* are large yellow spheres. Blue *Si*-centered tetrahedra show dark red *BO* and lighter pink *NBO*.

1.4. Doping

Environmental-friendly synthesis and development of new photoluminescent materials with high efficiency for optical devices is a global demand. Light-emitting diodes (*LEDs*) present the new generation lighting resources owing to their outstanding merits such as energy saving, high efficiency and long device lifetime over conventional lighting resources[67-69]. According to the chromatics, red, green, and blue (*RGB*) lights are the three primary colors, and any color can be decomposed into these three primary colors. The principle of *RGB* is widely used in many fields such as lighting, displaying, painting, and photography. As one of the *RGB* phosphors and the core materials for preparing ultraviolet (*UV*) white light *LEDs* (*WLEDs*), blue light-emitting materials have always been the active research topics in the *LED* fields. Blue light emitting materials are commonly obtained by doping rare-earth (*RE*) metal cations in inorganic compounds as host materials, playing a crucial role in *LED* illumination sources, activator and sensitizer [70-71]. The advantage of this approach relies on the high absorption of the matrix and energy transfer to the *RE* elements, their long luminescence lifetime, deep tissue penetration depth, and high photostability. These materials have attracted considerable attention for applications in different fields such as optical amplifiers, biomedical diagnostics, and optical bio probes [72-75]. Then, the doping processes in semiconductors and optical materials with *RE* elements offer the opportunity of introducing the dopant species in a controlled manner (concentration, depth distribution, lateral distribution), thus allowing the tailoring of electrical and optical devices. For a successful manufacturing of such devices the depth distribution of the rare earth dopant must be known.

Their photoluminescence spectra are associated to the abundant *4f* orbitals electron configurations, displaying mainly three kinds of transitions: *4f–4f* transitions, *4f–5d* transitions and charge transfer transitions, which results in narrow emission lines, high photostability, and an intense luminescence from ultraviolet (*UV*) to near-infrared. On one hand, the local environments around luminescence centers invariably depend on crystal structures and chemical compositions of hosts. On the other hand, most of the luminescence centers in a phosphor are sensitive to the chemical environment of the host lattice, especially the centers with *f−d* or *d−d* transitions (*e.g.*, Eu^{3+}, Pr^{3+}, Yb^{2+}, Ce^{3+}, Mn^{2+}, Mn^{4+}, Cr^{3+}, Tb^{3+}) and lattice defects. These activators are generally coordinated by ligands in a solid host lattice. The positively charged activator ion and the negatively

charged nonbonding electrons of the ligands can generate crystal field interaction which affects the splitting of *d*-orbitals and then affects luminescence [76-77]. Admittedly, learning the relationship between structure and property in the existing mineral hosts provides the necessary basis to identify experimental trends for researchers to predict desired phosphors material.

Among *RE* elements, terbium (Tb^{3+}) is the most promising for this purpose and it exhibits intense green emission due to ${}^5D_4 \rightarrow {}^7F_5$ transition around 550 *nm*. Examples of Tb^{3+} doping different kinds of materials like glasses, organic compounds, polymers, inorganic matrix, among others are extensively published [78-80].

1.5. Solid solutions

A solid solution is a multi-component system formed by a mixture of two or more crystalline solids where the crystal structure remains unchanged within a single homogeneous phase. This strategy provides interesting ways to modify materials properties. For that reason, obtaining solid solutions is found to be a very effective strategy to tailor the crystal structure, continuous tenability of band gap values, and optical properties [81,82]. The synthesis and formation mechanisms of the solid solutions of metal molybdate and tungstate, their stability and corresponding properties, as well as the potential technological applications, are important topics of research [83,85]. Formation of solid solutions, is a widely used strategy to fine-tune the colligative properties, crystal structure, band gap values, and optical properties, and this has many positive impacts on material functionalities [86], as well as representing an opportunity to understand structure-property relationships.

When a semiconductor is grown under conditions of thermodynamic equilibrium, impurity atoms can be incorporated up to their solubility limit. This thermodynamic limit is determined by the Gibbs free energy controlled by the value of the impurity formation energy and the growth temperature. A wide variety of experimental results and theoretical investigations in recent years have convincingly demonstrated that semiconductors based on transition metal oxides have dominant states that are not spatially homogeneous. They are composed by quantum particles on a lattice with competing long-range interactions [87]. This occurs in cases in which several physical interactions, involving the electron, spin, charge, and lattice are simultaneously active. This phenomenon causes the different

interesting effects, and it also appears crucial to understand their properties and applications. The emergence of electronic nanometer-scale structures in these materials, and the existence of many competing structures and electronic states, are properties often associated with complex matter where nonlinearities dominate, such as soft materials and biological systems. The understanding of these materials has dramatically challenged our view of solids. Important experimental results gathered in recent years have revealed an unexpected property of semiconductors: Many of them are inhomogeneous at the nanoscale (and sometimes at even longer length scales); in particular at the exposed surfaces of the morphology. This explains why the theories based on homogeneous and ordered systems were not successful and raises hopes that a novel avenue for progress has opened.

In particular, the uniqueness of the metallic molybdates and wolframates lies in their extreme chemical complexity enveloped in a single crystallographic structure, which in many cases results in novel functionalities. They have aroused interest in several sectors of the industry due to their potential applications in different areas, such as photoluminescence, photocatalysis, and gas sensors [88-90].

1.6. High-Pressure

The response of materials to high-pressure (HP) is a growing scientific domain, especially in condensed matter physics, crystal chemistry, geophysics, biology, and materials science, for the analysis of new phenomena, and it is an attractive area for fundamental theory and simulations. By applying pressure, the physical and chemical properties of condensed matter can be significantly altered since the atoms approach each other by modifying the interatomic distances with concomitant changes in the local environment and bonding patterns, which may lead to the formation of new structures (polymorphs) through phase transitions [91-96]. Therefore, high pressure effects have substantial significance in continuously tuning the crystalline and electronic structures, revealing the underlying transformation mechanism and giving rise to new materials with unexpected physical and chemical properties that are not accessible under ambient conditions. Knowledge of how these basic interactions within the system evolve under extreme conditions is fundamental to help understand their technological applications.

In the last decade, the behavior under HP of several oxides have been studied. For example, the MTO_4 compounds was highly studied by Errandonea [97]. The occurrence of pressure-induced phase transitions, as well as the influence of compression in the vibrational, optical, and transport properties was analyzed. To understand all the evidence on the HP behavior of MTO_4 monazites, was used the diagram proposed by Bastide [98], which has been successfully used to understand and predict HP phase transitions in many compounds. In the diagram, Figure 3, the compounds are organized according to the ionic radii of the M and T cations (r_M and r_T, respectively). It is also possible to find in the literature several studies presenting scheelite-type structures at high-pressures. After the pioneer work of Hazen et al., [99] in the last two decades several (HP) studies in scheelite form can be highlighted [100-104]. They showed that compression is an efficient tool to improve the understanding of their main physical properties and predict new structures.

High-pressure experiments on materials, such as static pressure using a diamond anvil cell [105] and dynamic pressure using shock waves [106], are of considerable interest from both a basic and an applied point of view. However, high pressure is not easy to achieve/access and control in X-ray diffraction experiments using these techniques. In this context, using and applying reliable theoretical methods which simulate such properties would help significantly. Atomic-level information is the key to the exploration of the properties of materials. The utilization and application of reliable theoretical methods and computational models which simulate such properties would be a valuable aid, by performing first-principles calculations, mainly within the framework of density functional theory (DFT) [107-108]. In this context, our group is engaged in a large research project devoted to finding crystal structures under pressure on different complex metal oxides [109-111].

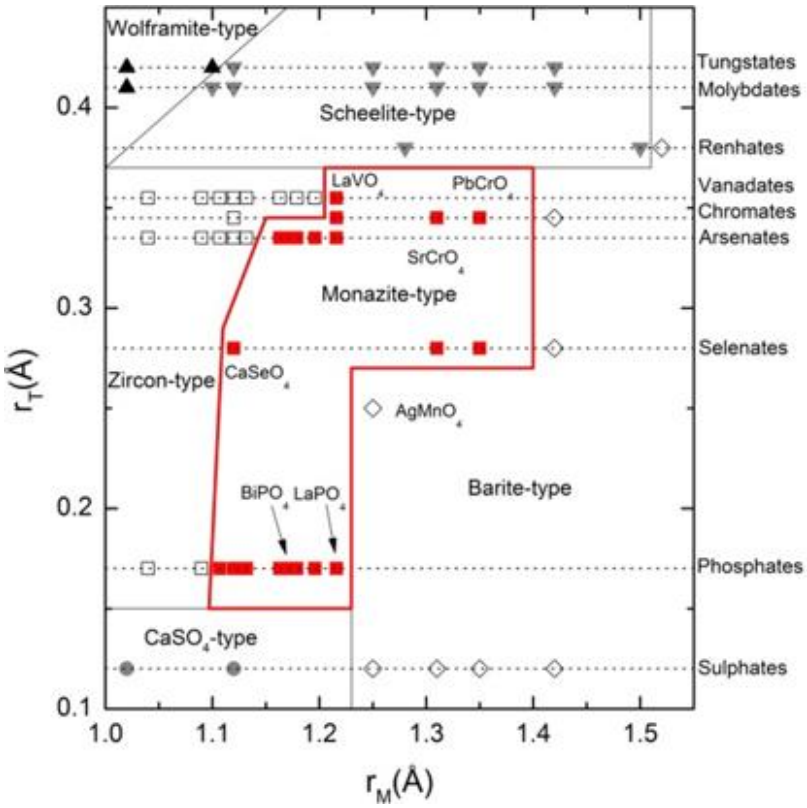

Figure 3: High-pressure phase transitions of MTO_4 compounds [97].

1.7. Surfaces and Morphology

In general, the function and application of a crystal are determined by its structure, size and morphology. In order to broaden the application prospects, it is very significant to synthesize crystals with diverse morphologies and high purity. Understanding the surface structure, properties and processes, such as adsorption, bonding, thermal stability, and reaction pathways, on metal oxides at the atomic level is of importance in refining or controlling heterogeneous reactions, surface functionalization, sensor application, etc.

By using the calculated values for surface energy of the exposed surfaces at the morphology and the Wulff construction, our research group has developed a method to obtain the available morphologies of a given materials by tuning the ratio of the surface energy values of the different surfaces. As reported in several works in the literature [112-117], we can match the experimental (observed by electronic microscopy)and

theoretical morphologies and find the reaction path associated to the different morphology transformations.

Our study is useful in understanding the origin of the exposed surfaces that are formed as a result of surface energy anisotropy. It can also serve as a guide for choosing parameters for obtaining specific morphologies consistent with symmetry of the material. In fact, specific surface and/or bulk characterization techniques, typical of materials' surface science, can be employed in order to get better insight into the potential specific correlation existing between the semiconductor surface properties and the resultant photoactivity performance of photoactive semiconductor materials, to be considered in the design of efficient and easily applicable photocatalysts [49,48][118]. A surface of a crystalline structure consists in sectioning the bulk perpendicularly to the vector of the desired direction, forming a periodic structure in two dimensions (x,y), but with finite thickness in the direction (z). In this way the surfaces are defined by two vectors orthogonal to the chosen direction [hkl].

The control of crystal morphology is one of the current challenges in the field of nanotechnology and materials science. Small changes in the growth environment can directly affect the morphology of the materials and their exposed surfaces, which are important factors influencing their application [119-122], as can be seen in Figure 4. That is, different crystal planes exhibit different anisotropic responses to various mechanical, physical and chemical activities[123,124]. Therefore, the combination of theoretical studies and experimental techniques has become a fundamental tool for the compression of the morphology of crystals and their production mechanisms at the atomic level.

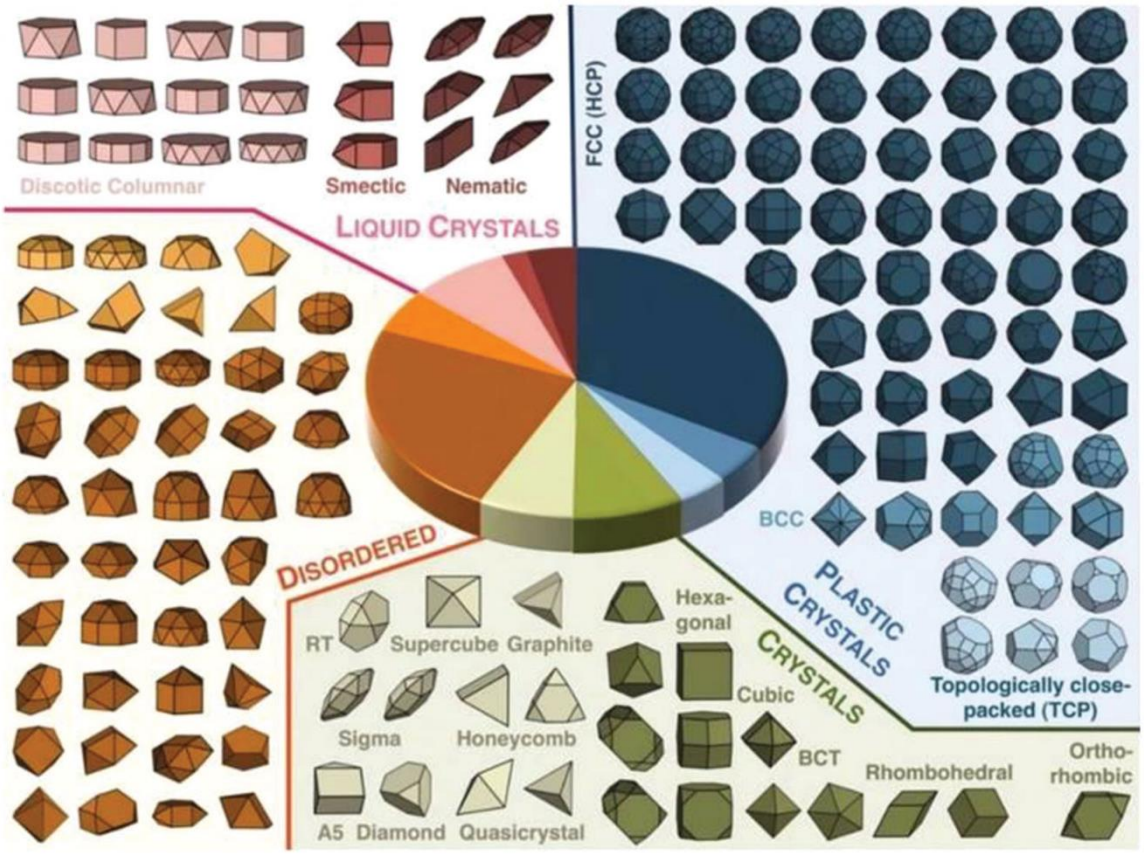

Figure 4: Possible polyhedral morphologies separated and indicated by different colors: liquid crystals, plastic crystals, crystals, and disordered (glassy) phases [125].

In a solid, the surface energy depends on the orientation of the crystallographic planes due to the intrinsic anisotropy associated with the different atomic arrangements of the planes. Thus, G. Wulff [126] proposed that the morphology of a (nano)crystal can be represented by a group of planes with different Miller indices [*hkl*], their respective energies ($Y[hkl]$) being proportional to the distance of that plane ($d[hkl]$) relative to the origin to the center of the surface (c), according to the equation:

$$c = \frac{Y[hkl]}{d[hkl]} \qquad (1)$$

Thus, the Wulff construction combines different values of the surface energy as a function of the orientation, where the size of the vector ($d[hkl]$) connecting the origin to the center of the surface is proportional to Y. The combination of all the vectors represented in the two-dimensional plane allows to obtain a polyhedron containing the different crystallographic planes, as can be seen in Figure 5.

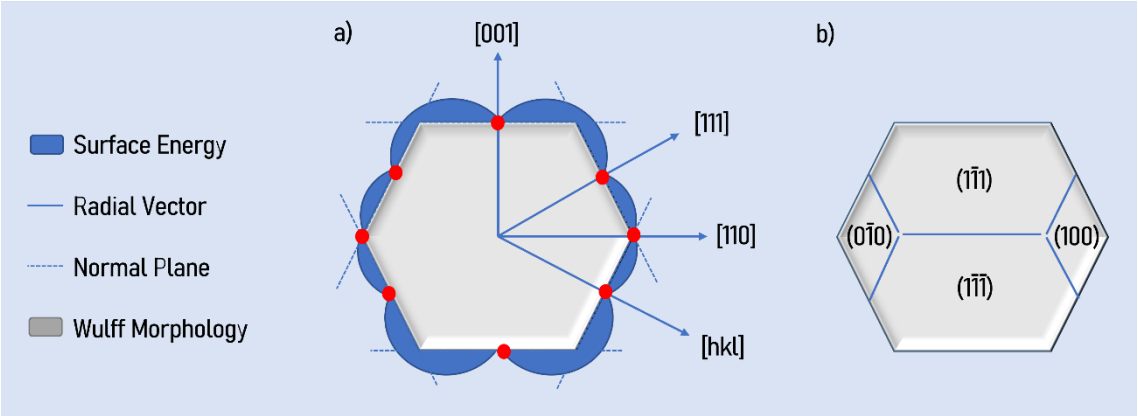

Figure 5: Squematic representation of different crystallographic planes (a); polyhedron representing the equilibrium morphology for a (nano)crystal (b).

To obtain the morphology using the Wulff construction it is necessary to calculate the surface energies (*Y*) of a given material. *Y* can be represented as E_{surf}, and also referred to as surface energy. It can be calculated from the shear in a crystallographic plane of the crystal, and corresponds to the cleavage energy [127]. These crystallographic planes depend on the point symmetry group of the material and the surfaces are obtained by cutting the crystal through a perpendicular section of the bulk in relation to the vectors of the desired direction, thus obtaining a periodic structure in two dimensions ("*slab*"), but with finite thickness (*z-axis*) [128]. Thus, the surface or cleavage energy (E_{surf}) is defined as the energy per unit area required to form the *2-D* surface relative to the bulk and is calculated by the following expression at T=0^{o} K:

$$E_{surf} = \frac{1}{2A}(E_{slab} - N.E_{bulk}) \qquad (2)$$

where E_{slab} is the total energy of the *2D slab*, E_{bulk} is the total energy of the bulk, respectively, while *N* and *A* represent the number of minimum formula units and the area of the, respectively. The factor *2* in the denominator comes from the existence of the top and bottom surfaces of the slab, which has a symmetric composition. After the corresponding optimization process and after checking that the value of *Y* has converged, i.e., that it has reached a constant value and does not depend on the thickness of the slab, the value of E_{surf} is obtained.

In our research group the combination of experimental and theoretical work is a specific feature in the field of materials research, as can be seen in Figure 6. These two research procedures, when applied together, cause a favorable synergy, being a powerful

tool to study and explain the structural and electronic properties of materials, responsible for subsequent technological applications. Therefore, there are two research fronts: (1) the experimental front in which the objective is the development of new synthesis methodology to find a material with desirable properties and (2) the theoretical front in which first principles calculations complement the experimental results, being a fundamental guide for a rational design of innovative materials.

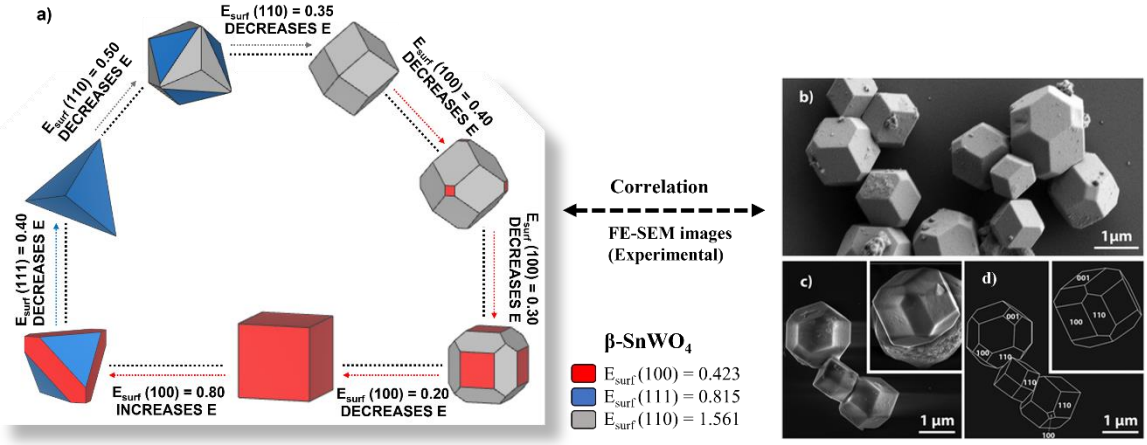

Figure 6: a) Map of morphologies from theoretical calculations for β-$SnMoO_4$. (E_{surf} are given in J m^{-2}). b) The experimental FE-SEM images [129].

After the optimization process and convergence tests on thickness, slab models are obtained and the relaxation process, with the relaxed energy (E_{relax}) being calculated as the difference between the total energies for relaxed and unrelaxed slabs:

$$E_{relax} = \frac{(E_{slab}^{unrlx} - E_{slab}^{relax})}{2A} \quad (3)$$

being E_{slab}^{unrlx} and E_{slab}^{relax} correspond to the total energies for the unrelaxed and relaxed slab models, respectively. In addition, the broken bonding density (D_b), defined as the number of broken bonds per unit cell area when a surface is created, are calculate by using Equation 4,

$$D_b = \frac{N_b}{A} \quad (4)$$

References

[1] B. A. Ali and N. K. Allam, “A first-principles roadmap and limits to design efficient supercapacitor electrode materials,” Phys. Chem. Chem. Phys., vol. 21, no. 32, pp. 17494–17511, 2019, doi: 10.1039/c9cp02614b.

[2] “Complex Systems: Science for the 21st Century,” Science (80).

[3] P. Reviewed, L. Berkeley, and B. Cancer, “Lawrence Berkeley National Laboratory Lawrence Berkeley National Laboratory,” no. July, pp. 35–43, 2010.

[4] P. Hohenberg; W. Kohn, “Inhomogeneous Electron Gas,” Phys. Rev. B, vol. 136, 1964.

[5] W. KOHN; and L. J. SHAM, “Self-Consistent Equations Including Exchange and Correlation Effects,” Phys. Rev., vol. 140, 1965.

[6] K. Capelle, “A Bird’s-Eye View of Density-Functional Theory,” vol. 36, no. 4, pp. 1318–1343, 2006.

[7] G. R. Schleder, A. C. M. Padilha, C. M. Acosta, M. Costa, and A. Fazzio, “From DFT to machine learning: recent approaches to materials science–a review,” J. Phys. Mater., vol. 2, no. 3, p. 032001, 2019, doi: 10.1088/2515-7639/ab084b.

[8] G. J. Cheng, X. Zhang, L. W. Chung, L. Xu, and Y. D. Wu, “Computational organic chemistry: Bridging theory and experiment in establishing the mechanisms of chemical reactions,” J. Am. Chem. Soc., vol. 137, no. 5, pp. 1706–1725, 2015, doi: 10.1021/ja5112749.

[9] J. J. Spivey et al., “Synthesis, characterization, and computation of catalysts at the center for atomic-level catalyst design,” J. Phys. Chem. C, vol. 118, no. 35, pp. 20043–20069, 2014, doi: 10.1021/jp502556u.

[10] G. Kresse and J. Furthmüller, “Efficiency of ab-initio total energy calculations for metals and semiconductors using a plane-wave basis set,” Comput. Mater. Sci., vol. 6, no. 1, pp. 15–50, 1996, doi: 10.1016/0927-0256(96)00008-0.

[11] S. Goedecker and M. Teter, “Separable dual-space Gaussian pseudopotentials,” Phys. Rev. B - Condens. Matter Mater. Phys., vol. 54, no. 3, pp. 1703–1710, 1996, doi: 10.1103/PhysRevB.54.1703.

[12] J. M. Soler et al., “The SIESTA method for ab initio order-N materials simulation,” J. Phys. Condens. Matter, vol. 14, no. 11, pp. 2745–2779, 2002, doi: 10.1088/0953-8984/14/11/302.

[13] P. Giannozzi et al., “QUANTUM ESPRESSO: A modular and open-source software project for quantum simulations of materials,” J. Phys. Condens. Matter, vol. 21, no. 39, 2009, doi: 10.1088/0953-8984/21/39/395502.

[14] V. Blum et al., “Ab initio molecular simulations with numeric atom-centered orbitals,” Comput. Phys. Commun., vol. 180, no. 11, pp. 2175–2196, 2009, doi: 10.1016/j.cpc.2009.06.022.

[15] R. Dovesi et al., “Quantum-mechanical condensed matter simulations with CRYSTAL,” Wiley Interdiscip. Rev. Comput. Mol. Sci., vol. 8, no. 4, pp. 1–36, 2018, doi: 10.1002/wcms.1360.

[16] G. Kresse and J. Hafner, “Ab initio molecular dynamics for liquid metals,” Phys. Rev. B, vol. 47, no. 1, pp. 558–561, 1993, doi: 10.1103/PhysRevB.47.558.

[17] A. Goyal, P. Gorai, S. Anand, E. S. Toberer, G. J. Snyder, and V. Stevanović, “On the Dopability of Semiconductors and Governing Material Properties,” Chem. Mater., vol. 32, no. 11, pp. 4467–4480, 2020, doi: 10.1021/acs.chemmater.9b05126.

[18] V. Kumaravel, S. Mathew, J. Bartlett, and S. C. Pillai, “Photocatalytic hydrogen production using metal doped TiO_2: A review of recent advances,” Appl. Catal. B Environ., vol. 244, no. September 2018, pp. 1021–1064, 2019, doi: 10.1016/j.apcatb.2018.11.080.

[19] S. Bai, L. Wang, Z. Li, and Y. Xiong, “Facet-Engineered Surface and Interface Design of Photocatalytic Materials,” Adv. Sci., vol. 4, no. 1, 2017, doi: 10.1002/advs.201600216.

[20] K. Wang et al., “Morphology-and crystalline composition-governed activity of titania-based photocatalysts: Overview and perspective,” Catalysts, vol. 9, no. 12, 2019, doi: 10.3390/catal9121054.

[21] S. J. A. Moniz, S. A. Shevlin, D. J. Martin, Z. X. Guo, and J. Tang, “Visible-light driven heterojunction photocatalysts for water splitting-a critical review,” Energy Environ. Sci., vol. 8, no. 3, pp. 731–759, 2015, doi:10.1039/c4ee03271c.

[22] K. Afroz, M. Moniruddin, N. Bakranov, S. Kudaibergenov, and N. Nuraje, “A heterojunction strategy to improve the visible light sensitive water splitting performance of photocatalytic materials,” J. Mater. Chem. A, vol. 6, no. 44, pp. 21696–21718, 2018, doi: 10.1039/c8ta04165b.

[23] L. Zhang and M. Jaroniec, “Toward designing semiconductor-semiconductor heterojunctions for photocatalytic applications,” Appl. Surf. Sci., vol. 430, pp. 2–17, 2018, doi: 10.1016/j.apsusc.2017.07.192.

[24] L. Wei, C. Yu, Q. Zhang, H. Liu, and Y. Wang, “TiO_2-based heterojunction photocatalysts for photocatalytic reduction of CO2 into solar fuels,” J. Mater. Chem. A, vol. 6, no. 45, pp. 22411–22436, 2018, doi: 10.1039/c8ta08879a.

[25] S. Bera, D. Il Won, S. B. Rawal, H. J. Kang, and W. I. Lee, “Design of visible-light photocatalysts by coupling of inorganic semiconductors,” Catal. Today, vol. 335, no. November 2018, pp. 3–19, 2019, doi:10.1016/j.cattod.2018.11.001.

[26] W. Yang, R. R. Prabhakar, J. Tan, S. D. Tilley, and J. Moon, “Strategies for enhancing the photocurrent, photovoltage, and stability of photoelectrodes for photoelectrochemical water splitting,” Chem. Soc. Rev., vol. 48, no. 19, pp. 4979–5015, 2019, doi: 10.1039/c8cs00997j.

[27] C. Jiang, S. J. A. Moniz, A. Wang, T. Zhang, and J. Tang, "Photoelectrochemical devices for solar water splitting-materials and challenges," Chem. Soc. Rev., vol. 46, no. 15, pp. 4645–4660, 2017, doi: 10.1039/c6cs00306k.

[28] M. Xiao, B. Luo, Z. Wang, S. Wang, and L. Wang, "Recent Advances of Metal-Oxide Photoanodes: Engineering of Charge Separation and Transportation toward Efficient Solar Water Splitting," Sol. RRL, vol. 4, no. 8, pp. 1–24, 2020, doi: 10.1002/solr.201900509.

[29] A. V. Vorontsov, H. Valdés, P. G. Smirniotis, and Y. Paz, "Recent Advancements in the Understanding of the Surface Chemistry in TiO_2 Photocatalysis," Surfaces, vol. 3, no. 1, pp. 72–92, 2020, doi: 10.3390/surfaces3010008.

[30] M. V. Dozzi and E. Selli, "Specific facets-dominated anatase TiO_2: Fluorine-mediated synthesis and photoactivity," Catalysts, vol. 3, no. 2, pp. 455–485, 2013, doi: 10.3390/catal3020455.

[31] M. Maisano, M. V. Dozzi, and E. Selli, "Searching for facet-dependent photoactivity of shape-controlled anatase TiO_2," J. Photochem. Photobiol. C Photochem. Rev., vol. 28, pp. 29–43, 2016, doi: 10.1016/j.jphotochemrev.2016.07.002.

[32] S. Wang, G. Liu, and L. Wang, "Crystal Facet Engineering of Photoelectrodes for Photoelectrochemical Water Splitting," Chem. Rev., vol. 119, no. 8, pp. 5192–5247, 2019, doi: 10.1021/acs.chemrev.8b00584.

[33] Y. Wang, T. Wu, B. Julien, K. Weiyu, C. Danyu, C. Han, Y. Xudong., "Stabilizing heterostructures of soft perovskite semiconductors," Science (80)., vol. 365, no. 6454, pp. 687–691, 2019, doi: 10.1126/science. aax8018.

[34] Ubirajara Coleto Jr., Rafael A. C. Amoresi, Vinícius Teodoro, Isabela M. Iani, Elson Longo, Maria A. Zaghete, Leinig A. Perazolli., "An approach for photodegradation mechanism at $TiO_2/SrTiO_3$ interface," J. Mater. Sci. Mater. Electron., vol. 29, no. 23, pp. 20329–20338, 2018, doi: 10.1007/s10854-018-0167-x.

[35] Marisa C. Oliveira, Lourdes Gracia, Marcelo Assis, Ieda L. V. Rosa, Maria F. Carmo, Elson Longo Juan Andrés., "Mechanism of photoluminescence in intrinsically disordered $CaZrO_3$ crystals: First principles modeling of the excited electronic states," J. Alloys Compd., vol. 722, pp. 981–995, Oct. 2017, doi: 10.1016/J.JALLCOM.2017.06.052.

[36] T. Thongtem, S. Kungwankunakorn, B. Kuntalue, A. Phuruangrat, and S. Thongtem, "Luminescence and absorbance of highly crystalline $CaMoO_4$, $SrMoO_4$, $CaWO_4$ and $SrWO_4$ nanoparticles synthesized by co-precipitation method at room temperature," J. Alloys Compd., vol. 506, no. 1, pp. 475–481, 2010, doi: 10.1016/j.jallcom.2010.07.033.

[37] F. E. Osterloh, “Photocatalysis versus Photosynthesis: A Sensitivity Analysis of Devices for Solar Energy Conversion and Chemical Transformations,” ACS Energy Lett., vol. 2, no. 2, pp. 445–453, 2017, doi: 10.1021/acsenergylett.6b00665.

[38] Z. Wang, C. Li, and K. Domen, “Recent developments in heterogeneous photocatalysts for solar-driven overall water splitting,” Chem. Soc. Rev., vol. 48, no. 7, pp. 2109–2125, 2019, doi: 10.1039/c8cs00542g.

[39] J. Cai et al., “Light-Driven Sustainable Hydrogen Production Utilizing TiO_2 Nanostructures: A Review,” Small Methods, vol. 3, no. 1, pp. 1–24, 2019, doi: 10.1002/smtd.201800184.

[40] F. Pellegrino, F. Sordello, M. Minella, C. Minero, and V. Maurino, “The role of surface texture on the photocatalytic H_2 production on TiO_2,” Catalysts, vol. 9, no. 1, 2019, doi: 10.3390/catal9010032.

[41] Yiou Wang, Hajime Suzuki, Jijia Xie, Osamu Tomita, David James Martin, Masanobu Higashi, Dan Kong, Ryu Abe, Junwang Tang., “Mimicking Natural Photosynthesis: Solar to Renewable H_2 Fuel Synthesis by Z-Scheme Water Splitting Systems,” Chem. Rev., vol. 118, no. 10, pp. 5201–5241, 2018, doi: 10.1021/acs.chemrev.7b00286.

[42] X. Chang, T. Wang, and J. Gong, “CO_2 photo-reduction: Insights into CO_2 activation and reaction on surfaces of photocatalysts,” Energy Environ. Sci., vol. 9, no. 7, pp. 2177–2196, 2016, doi: 10.1039/c6ee00383d.

[43] P. Prabhu, V. Jose, and J. M. Lee, “Heterostructured Catalysts for Electrocatalytic and Photocatalytic Carbon Dioxide Reduction,” Adv. Funct. Mater., vol. 30, no. 24, pp. 1–32, 2020, doi: 10.1002/adfm.201910768.

[44] S. Xu and E. A. Carter, “Theoretical Insights into Heterogeneous (Photo)electrochemical CO_2 Reduction,” Chem. Rev., vol. 119, no. 11, pp. 6631–6669, 2019, doi: 10.1021/acs.chemrev.8b00481.

[45] W. Yichen, Z. Xi, X. Yetong, H. Zhicheng, T. Haoran, L. Wei, H. Fei, C. Yong., “Substituent Regulation Improves Photocatalytic Hydrogen Evolution of Conjugated Polyelectrolytes,” ACS Mater. Lett., vol. 1, no. 6, pp. 620–627, 2019, doi: 10.1021/acsmaterialslett.9b00325.

[46] S. Wang, Y. Wang, S. L. Zhang, S. Q. Zang, and X. W. Lou, “Supporting Ultrathin $ZnIn_2S_4$ Nanosheets on Co/N-Doped Graphitic Carbon Nanocages for Efficient Photocatalytic H_2 Generation,” Adv. Mater., vol. 31, no. 41, pp. 1–7, 2019, doi: 10.1002/adma.201903404.

[47] Y. Zhou, L. Zhang, and W. Wang, “Direct functionalization of methane into ethanol over copper modified polymeric carbon nitride via photocatalysis,” Nat. Commun., vol. 10, no. 1, 2019, doi: 10.1038/s41467-019-08454-0.

[48] L. Zhang, J. Ran, S. Z. Qiao, and M. Jaroniec, “Characterization of semiconductor photocatalysts,” Chem. Soc. Rev., vol. 48, no. 20, pp. 5184–5206, 2019, doi: 10.1039/c9cs00172g.

[49] C. Luo, X. Ren, Z. Dai, Y. Zhang, X. Qi, and C. Pan, “Present Perspectives of Advanced Characterization Techniques in TiO_2-Based Photocatalysts,” ACS Appl. Mater. Interfaces, vol. 9, no. 28, pp. 23265–23286, 2017, doi: 10.1021/acsami.7b00496.

[50] S. Bera, D. Il Won, S. B. Rawal, H. J. Kang, and W. I. Lee, “Design of visible-light photocatalysts by coupling of inorganic semiconductors,” Catal. Today, vol. 335, no. August 2018, pp. 3–19, 2019, doi: 10.1016/j.cattod.2018.11.001.

[51] N. Guijarro, M. S. Prévot, and K. Sivula, “Surface modification of semiconductor photoelectrodes,” Phys. Chem. Chem. Phys., vol. 17, no. 24, pp. 15655–15674, 2015, doi: 10.1039/c5cp01992c.

[52] S. G. Kumar and K. S. R. K. Rao, “Comparison of modification strategies towards enhanced charge carrier separation and photocatalytic degradation activity of metal oxide semiconductors (TiO_2, WO_3 and ZnO),” Appl. Surf. Sci., vol. 391, pp. 124–148, 2017, doi: 10.1016/j.apsusc.2016.07.081.

[53] J. H. Park, J. S. Kim, and J. T. Kim, “Luminescent properties of $BASi_2O_5:Eu^{2+}$ phosphor film fabricated by spin-coating of Ba-Eu precursor on SiO_2 glass,” J. Opt. Soc. Korea, vol. 18, no. 1, pp. 45–49, 2014, doi: 10.3807/JOSK.2014.18.1.045.

[54] R. Trejo, E. Lara-Curzio, A. Shyam, M. J. Kirkham, V. Garcia-Negron, and Y. Wang, “Physical and Mechanical Properties of Barium Alkali Silicate Glasses for SOFC Sealing Applications,” Int. J. Appl. Glas. Sci., vol. 3, no. 4, pp. 369–379, 2012, doi: 10.1111/ijag.12004.

[55] Shisheng Lin, Hang Lin, Qingming Huang, Yao Cheng, Ju Xu, Jiaomei Wang, Xiaoqiang Xiang, Congyong Wang, Liqiang Zhang,Yuansheng Wang., “A Photostimulated $BaSi_2O_5:Eu^{2+}$, Nd^{3+} Phosphor-in-Glass for Erasable-Rewritable Optical Storage Medium,” Laser Photonics Rev., vol. 13, no. 4, pp. 1–11, 2019, doi: 10.1002/lpor.201900006.

[56] P. Namwong, N. Laorodphan, W. Thiemsorn, M. Jaimasith, A. Wannakon, and T. Chairuangsri, “A barium-calcium silicate glass for use as seals in planar SOFCs,” Chiang Mai J. Sci., vol. 37, no. 2, pp. 231–242, 2010.

[57] P. Wang, X. Xu, D. Zhou, X. Yu, and J. Qiu, “Sunlight activated long-lasting luminescence from $Ba_5Si_8O_{21}$: Eu^{2+},Dy^{3+} phosphor,” Inorg. Chem., vol. 54, no. 4, pp. 1690–1697, 2015, doi: 10.1021/ic5026312.

[58] A. Herrmann, A. Simon, and C. Rüssel, “Preparation and luminescence properties of Eu^{2+}-doped $BaSi_2O_5$ glass-ceramics,” J. Lumin., vol. 132, no. 1, pp. 215–219, 2012, doi: 10.1016/j.jlumin.2011.08.024.

[59] Z. Kristallographie, R. O. Verlag, M. Institut, U. Kiel, and D.- Kiel, “synthetic a-eucryptite,” vol. 1985, pp. 147–151, 1985.

[60] Z. Keilany, “Book Reviews: Book Reviews,” Rev. Soc. Econ., vol. 36, no. 2, pp. 228–229, 1978, doi: 10.1080/00346767800000037.

[61] G. N. Greaves, “Exafs and the structure of glass g.n. greaves,” J. Non. Cryst. Solids, vol. 71, pp. 203–217, 1985.

[62] G. Calas, G. S. Henderson, and J. F. Stebbins, “Glasses and Melts: and Materials Science,” Elements, vol. 2, pp. 265–268, 2006.

[63] R. S. Roth and E. M. Levin, “" Phase Equilibria in the Subsystem Barium Disilicate Dibarium Trisilicate,” vol. 62, no. 5, pp. 193–200, 1959.

[64] G. Oehlschlegel, “Crystallization of Glasses in the System $BaO{\cdot}2SiO_2$-$2BaO{\cdot}3SiO_2$,” J. Am. Ceram. Soc., vol. 58, no. 3–4, pp. 148–148, 1975, doi: 10.1111/j.1151-2916. 1975.tb19584.x.

[65] A. Shukla, I. H. Jung, S. A. Decterov, and A. D. Pelton, “Thermodynamic evaluation and optimization of the BaO-SiO_2 and BaO-CaO-SiO_2 systems,” Calphad Comput. Coupling Phase Diagrams Thermochem., vol. 61, no. March, pp. 140–147, 2018, doi: 10.1016/j.calphad.2018.03.001.

[66] L. A. Gorelova, R. S. Bubnova, S. V. Krivovichev, M. G. Krzhizhanovskaya, and S. K. Filatov, “Thermal expansion and structural complexity of Ba silicates with tetrahedrally coordinated Si atoms,” J. Solid State Chem., vol. 235, pp. 76–84, 2016, doi: 10.1016/j.jssc.2015.12.012.

[67] Thomas Jüstel, Hans Nikol, Cees Ronda*., “periodic table of the " lighting " elements New Developments in the Field of Luminescent Materials for Lighting and Displays,” Angew. ChemieInternational Ed., vol. 37, no. 22, pp. 3084–3103, 1998, [Online]. Available: http://www3.interscience.wiley.com/journal/10005128/abstract.

[68] B. Shao, J. Huo, and H. You, “Prevailing Strategies to Tune Emission Color of Lanthanide-Activated Phosphors for WLED Applications,” Adv. Opt. Mater., vol. 7, no. 13, pp. 1–23, 2019, doi: 10.1002/adom.201900319.

[69] M. Shang, C. Li, and J. Lin, “How to produce white light in a single-phase host?” Chem. Soc. Rev., vol. 43, no. 5, pp. 1372–1386, 2014, doi: 10.1039/c3cs60314h.

[70] Neha Jain, Ruchi Paroha, Rajan K. Singh, Siddhartha K. Mishra, Shivendra K. Chaurasiya, R. A. Singh, Jai Singh., “Synthesis and Rational design of Europium and Lithium Doped Sodium Zinc Molybdate with Red Emission for Optical Imaging,” Sci. Rep., vol. 9, no. 1, pp. 1–14, 2019, doi: 10.1038/s41598-019-38787-1.

[71] I. M. Pinatti, P. F. S. Pereira, M. de Assis, E. Longo, and I. L. V. Rosa, “Rare earth doped silver tungstate for photoluminescent applications,” J. Alloys Compd., vol. 771, pp. 433–447, 2019, doi: 10.1016/j.jallcom.2018.08.302.

[72] Yu Wang, Langping Tu, Junwei Zhao, Yajuan Sun, Xianggui Kong, and Hong Zhang., “Upconversion Luminescence Properties of β-$NaYF4{:}Yb^{3+}$/Er3+@β-$NaYF4{:}Yb^{3+}$,” Faguang Xuebao/Chinese J. Lumin., vol. 41, no. 6, pp. 679–683, 2020, doi: 10.3788/fgxb20204106.0679.

[73] D. Li, W. Wang, X. Liu, C. Jiang, and J. Qiu, “Discovery of non-reversible thermally enhanced upconversion luminescence behavior in rare-earth doped nanoparticles,” J. Mater. Chem. C, vol. 7, no. 15, pp. 4336–4343, 2019, doi: 10.1039/c9tc01009b.

[74] Feng Wang, Yu Han, Chin Seong Lim, Yunhao Lu, Juan Wang, Jun Xu, Hongyu Chen, Chun Zhang, Minghui Hong, Xiaogang Liu., “Simultaneous phase and size control of upconversion nanocrystals through lanthanide doping,” Nature, vol. 463, no. 7284, pp. 1061–1065, 2010, doi: 10.1038/nature08777.

[75] H. Dong, L. D. Sun, and C. H. Yan, “Energy transfer in lanthanide upconversion studies for extended optical applications,” Chem. Soc. Rev., vol. 44, no. 6, pp. 1608–1634, 2015, doi: 10.1039/c4cs00188e.

[76] G. B. Nair, H. C. Swart, and S. J. Dhoble, “A review on the advancements in phosphor-converted light emitting diodes (pc-LEDs): Phosphor synthesis, device fabrication and characterization,” Prog. Mater. Sci., vol. 109, no. November 2019, p. 100622, 2020, doi: 10.1016/j.pmatsci.2019.100622.

[77] X. Zhou, J. Qiao, and Z. Xia, “Learning from Mineral Structures toward New Luminescence Materials for Light-Emitting Diode Applications,” Chem. Mater., vol. 33, no. 4, pp. 1083–1098, 2021, doi: 10.1021/acs.chemmater.1c00032.

[78] Vu X. Quang, Phan V. Do, Nguyen X. Ca, Luong D. Thanh, Vu P. Tuyen, Pham M. Tan, Vu X. Hoa, Nguyen T. Hien., “Role of modifier ion radius in luminescence enhancement from 5D4 level of Tb^{3+} ion doped alkali-alumino-telluroborate glasses,” J. Lumin., vol. 221, no. November 2019, p. 117039, 2020, doi: 10.1016/j.jlumin.2020.117039.

[79] W. T. Carnall, P. R. Fields, and K. Rajnak, “Electronic Energy Levels of the Trivalent Lanthanide Aquo Ions. III. Tb^{3+},” J. Chem. Phys., vol. 49, no. 10, pp. 4447–4449, 1968, doi: 10.1063/1.1669895.

[80] Hongxia Guan, Ye Sheng, Yanhua Song, Keyan Zheng, Chengyi Xu, Xiaoming Xie, Yunzhi Dai, Haifeng Zou., “White light-emitting, tunable color luminescence, energy transfer and paramagnetic properties of terbium and samarium doped $BaGdF_5$ multifunctional nanomaterials,” RSC Adv., vol. 6, no. 77, pp. 73160–73169, 2016, doi: 10.1039/c6ra14296f.

[81] S. Vidya, S. Solomon, and J. K. Thomas, “Structral, Optical and Dielectric Characterization of Nanocrystalline $AMo_{0.5}W_{0.5}O_4$ (where A=Ba,Sr and Ca) Prepared by Single Step Modified Combustion Technique,” Mater. Today Proc., vol. 2, no. 3, pp. 904–908, 2015, doi: 10.1016/j.matpr.2015.06.006.

[82] Marisa C. Oliveira, Juan Andrés, Lourdes Gracia, Michelle S. M. P. Oliveira, Jose M. R. Mercury, Elson Longo, Içamira C. Nogueira., “Geometry, electronic structure, morphology, and photoluminescence emissions of $BaW_{1-}MoxO_4$($x = 0$, 0.25, 0.50, 0.75, and 1) solid solutions: Theory and experiment in concert,” Appl. Surf. Sci., vol. 463, no. May 2018, pp. 907–917, 2019, doi: 10.1016/j.apsusc.2018.08.146.

[83] V. D. Zhuravlev, O. G. Reznitskikh, Y. A. Velikodnyi, T. A. Patrusheva, and O. V. Sivtsova, “Analysis of solid solutions stability in scheelite-type molybdates and tungstates,” J. Solid State Chem., vol. 184, no. 10, pp. 2785–2789, Oct. 2011, doi: 10.1016/J.JSSC.2011.08.003.

[84] S. P. Culver, M. J. Greaney, A. Tinoco, and R. L. Brutchey, “Lowerature synthesis of homogeneous solid solutions of scheelite-structured $Ca_{1-x}Sr_xWO_4$ and $Sr_{1-x}Ba_xWO_4$ nanocrystals,” Dalt. Trans., vol. 44, no. 33, pp. 15042–15048, 2015, doi: 10.1039/c5dt01722j.

[85] Y. Wang, C. Wu, L. Geng, and S. Chen, “Unexpected formation of scheelite-structured $Ca_{1-x}Cd_xWO_4$ ($0 \leq x \leq 1$) continuous solid solutions with tunable photoluminescent and electronic properties,” Phys. Chem. Chem. Phys., vol. 19, no. 34, pp. 23204–23212, 2017, doi: 10.1039/c7cp04521b.

[86] M. Lusi, “Engineering Crystal Properties through Solid Solutions,” Cryst. Growth Des., vol. 18, no. 6, pp. 3704–3712, 2018, doi: 10.1021/acs.cgd.7b01643.

[87] E. Dagotto, “Complexity in strongly correlated electronic systems,” Science (80)., vol. 309, no. 5732, pp. 257–262, 2005, doi: 10.1126/science.1107559.

[88] N. F. A. Neto, T. B. O. Nunes, M. Li, E. Longo, M. R. D. Bomio, and F. V. Motta, “Influence of microwave-assisted hydrothermal treatment time on the crystallinity, morphology and optical properties of $ZnWO_4$ nanoparticles: Photocatalytic activity,” Ceram. Int., vol. 46, no. 2, pp. 1766–1774, 2020, doi: 10.1016/j.ceramint.2019.09.151.

[89] S. Zou, J. Luo, Z. Lin, P. Fu, and Z. Chen, “Acetone gas sensor based on iron molybdate nanoparticles prepared by hydrothermal method with PVP as surfactant,” Mater. Res. Express, vol. 5, no. 12, 2018, doi: 10.1088/2053-1591/aae170.

[90] G. Kianpour, F. Soofivand, M. Badiei, M. Salavati-Niasari, and M. Hamadanian, “Facile synthesis and characterization of nickel molybdate nanorods as an effective photocatalyst by co-precipitation method,” J. Mater. Sci. Mater. Electron., vol. 27, no. 10, pp. 10244–10251, 2016, doi: 10.1007/s10854-016-5103-3.

[91] T. B. Ballaran, A. Kurnosov, and D. Trots, “Single-crystal X-ray diffraction at extreme conditions: A review,” High Press. Res., vol. 33, no. 3, pp. 453–465, 2013, doi: 10.1080/08957959.2013.834052.

[92] R. Lee, J. A. K. Howard, M. R. Probert, and J. W. Steed, “Structure of organic solids at low temperature and high pressure,” Chem. Soc. Rev., vol. 43, no. 13, pp. 4300–4311, 2014, doi: 10.1039/c4cs00046c.

[93] P. Bhardwaj and S. Singh, “Pressure induced structural phase transitions - A review,” Cent. Eur. J. Chem., vol. 10, no. 5, pp. 1391–1422, 2012, doi: 10.2478/s11532-012-0090-6.

[94] A. F. Goncharov, R. T. Howie, and E. Gregoryanz, “Hydrogen at extreme pressures,” Low Temp. Phys., vol. 39, no. 5, pp. 402–408, 2013, doi: 10.1063/1.4807051.

[95] D. D. Klug and Y. Yao, “Metallization of solid hydrogen: The challenge and possible solutions,” Phys. Chem. Chem. Phys., vol. 13, no. 38, pp. 16999–17006, 2011, doi: 10.1039/c1cp21791g.

[96] E. Zurek and W. Grochala, “Predicting crystal structures and properties of matter under extreme conditions via quantum mechanics: The pressure is on,” Phys. Chem. Chem. Phys., vol. 17, no. 5, pp. 2917–2934, 2015, doi: 10.1039/c4cp04445b.

[97] D. Errandonea, “High-pressure phase transitions and properties of MTO_4 compounds with the monazite-type structure,” Phys. Status Solidi Basic Res., vol. 254, no. 5, 2017, doi: 10.1002/pssb.201700016.

[98] J. P. Bastide, “Systématique simplifiée des composés ABX4 ($X = O^{2-}$, F^-) et evolution possible de leurs structures cristallines sous pression,” J. Solid State Chem., vol. 71, no. 1, pp. 115–120, 1987, doi: 10.1016/0022-4596(87)90149-6.

[99] R. M. Hazen, L. W. Finger, and J. W. E. Mariathasan, “High-pressure crystal chemistry of scheelite-type tungstates and molybdates,” J. Phys. Chem. Solids, vol. 46, no. 2, pp. 253–263, 1985, doi: 10.1016/0022-3697(85)90039-3.

[100] A. Jayaraman, S. Y. Wang, S. K. Sharma, and L. C. Ming, “High-pressure Raman Study of $SrMo0_4$,” vol. 26, no. March, pp. 451–455, 1995.

[101] D. Christofilos, G. A. Kourouklis, and S. Ves, “A high pressure Raman study of calcium molybdate,” J. Phys. Chem. Solids, vol. 56, no. 8, pp. 1125–1129, 1995, doi: 10.1016/0022-3697(95)00034-8.

[102] S. R. Shieh, L. C. Ming, and A. Jayaraman, “Pressure-induced phase transitions in $CdMoO_4$: An in-situ high pressure X-ray diffraction study up to 52GPa,” J. Phys. Chem. Solids, vol. 57, no. 2, pp. 205–209, 1996, doi: 10.1016/0022-3697(95)00196-4.

[103] D. Christofilos, J. Arvanitidis, E. Kampasakali, K. Papagelis, S. Ves, and G. A. Kourouklis, “High pressure Raman study of $BaMoO_4$,” Phys. Status Solidi Basic Res., vol. 241, no. 14, pp. 3155–3160, 2004, doi: 10.1002/pssb.200405234.

[104] R. Vilaplana, O. Gomis, F. J. Manjón, P. Rodríguez-Hernández, A. Muñoz, D. Errandonea, S. N. Achary, A. K. Tyagi., “Raman scattering study of bulk and nanocrystalline $PbMoO_4$ at high pressures,” J. Appl. Phys., vol. 112, no. 10, 2012, doi: 10.1063/1.4765717.

[105] A. Jayaraman, “Diamond anvil cell and high-pressure physical investigations,” Rev. Mod. Phys., vol. 55, no. 1, pp. 65–108, 1983, doi: 10.1103/RevModPhys.55.65.

[106] J. Wackerle, “Shock-wave compression of quartz,” J. Appl. Phys., vol. 33, no. 3, pp. 922–937, 1962, doi: 10.1063/1.1777192.

[107] L. Zhang, Y. Wang, J. Lv, and Y. Ma, “Materials discovery at high pressures,” Nat. Rev. Mater., vol. 2, no. 4, pp. 1–16, 2017, doi: 10.1038/natrevmats.2017.5.

[108] Elena Boldyreva; Przemyslaw Dera, High-Pressure Crystallography. 2010.

[109] L. Gracia, J. Andre, and A. Beltra, “Polymorphs of ZnV_2O_6 under Pressure: A First-Principle Investigation,” 2019, doi: 10.1021/acs.jpcc.8b12515.

[110] A. Beltrán, L. Gracia, and J. Andrés, “Density functional theory study of the brookite surfaces and phase transitions between natural titania polymorphs,” J. Phys. Chem. B, vol. 110, no. 46, pp. 23417–23423, 2006, doi: 10.1021/jp0643000.

[111] L. Gracia, A. Beltrán, and J. Andrés, “Characterization of the high-pressure structures and phase transformations in SnO_2. A density functional theory study,” J. Phys. Chem. B, vol. 111, no. 23, pp. 6479–6485, 2007, doi: 10.1021/jp067443v.

[112] M. R. D. Bomio, R. L. Tranquilin, F. V. Motta, C. A. Paskocimas, R. M. Nascimento, L. Gracia, J. Andres, E. Longo., “Toward understanding the photocatalytic activity of $PbMoO_4$ powders with predominant (111), (100), (011), and (110) facets. A combined experimental and theoretical study,” J. Phys. Chem. C, vol. 117, no. 41, pp. 21382–21395, 2013, doi: 10.1021/jp407416h.

[113] Valeria M. Longo, Laécio S. Cavalcante, Elaine C. Paris, Júlio C. Sczancoski, Paulo S. Pizani, Maximo Siu Li, Juan Andrés, Elson Longo, and José A. Varela., “Hierarchical Assembly of $CaMoO_4$ Nano-Octahedrons and Their Photoluminescence Properties,” J. Phys. Chem. C, vol. 115, no. 13, pp. 5207–5219, Apr. 2011, doi: 10.1021/jp1082328.

[114] G. Botelho, J. Andres, L. Gracia, L. S. Matos, and E. Longo, “Photoluminescence and Photocatalytic Properties of Ag_3PO_4 Microcrystals: An Experimental and Theoretical Investigation,” Chempluschem, vol. 81, no. 2, pp. 202–212, 2016, doi: 10.1002/cplu.201500485.

[115] Maria T. Fabbro, Carla Saliby, Larissa R. Rios, Felipe A. La Porta, Lourdes Gracia, Máximo S. Li, Juan Andrés, Luís P. S. Santos, Elson Longo., “Identifying and rationalizing the morphological, structural, and optical properties of β-Ag_2MoO_4 microcrystals, and the formation process of Ag nanoparticles on their surfaces: Combining experimental data and first-principles calculations,” Sci. Technol. Adv. Mater., vol. 16, no. 6, p. 65002, 2015, doi: 10.1088/1468-6996/16/6/065002.

[116] Marisa C. Oliveira, Lourdes Gracia, Içamira C. Nogueira, Maria F. Carmo G., Jose M. R. Mercury, Elson Longo, JuanAndrés., “Synthesis and morphological transformation of $BaWO_4$ crystals: Experimental and theoretical insights,” Ceram. Int., vol. 42, no. 9, pp. 10913–10921, 2016, doi: 10.1016/j.ceramint.2016.03.225.

[117] Gabriela S. Silva, Lourdes Gracia, Maria T. Fabbro, Luis P. Serejo dos Santos, Hector Beltrán-Mir, Eloisa Cordoncillo, Elson Longo, Juan Andrés., "Theoretical and Experimental Insight on Ag_2CrO_4 Microcrystals: Synthesis, Characterization, and Photoluminescence Properties," Inorg. Chem., vol. 55, no. 17, pp. 8961–8970, 2016, doi: 10.1021/acs.inorgchem.6b01452.

[118] Q. Guo, C. Zhou, Z. Ma, and X. Yang, "Fundamentals of TiO_2 Photocatalysis: Concepts, Mechanisms, and Challenges," Adv. Mater., vol. 31, no. 50, pp. 1–26, 2019, doi: 10.1002/adma.201901997.

[119] Maria Alfredsson, Furio Corà, David P. Dobson, James Davya, John P. Brodholta, Steve C.Parkerd, G. David Price., "Dopant control over the crystal morphology of ceramic materials," Surf. Sci., vol. 601, no. 21, pp. 4793–4800, 2007, doi: 10.1016/j.susc.2007.07.025.

[120] A. S. Barnard, C. A. Feigl, and S. P. Russo, "Morphological and phase stability of zinc blende, amorphous and mixed core-shell ZnS nanoparticles," Nanoscale, vol. 2, no. 10, pp. 2294–2301, 2010, doi: 10.1039/c0nr00417k.

[121] C. S. Tan, S. C. Hsu, W. H. Ke, L. J. Chen, and M. H. Huang, "Facet-dependent electrical conductivity properties of Cu2O crystals," Nano Lett., vol. 15, no. 3, pp. 2155–2160, 2015, doi: 10.1021/acs.nanolett.5b00150.

[122] K. D. Gilroy, H. C. Peng, X. Yang, A. Ruditskiy, and Y. Xia, "Symmetry breaking during nanocrystal growth," Chem. Commun., vol. 53, no. 33, pp. 4530–4541, 2017, doi: 10.1039/c7cc01121k.

[123] P. Dandekar, Z. B. Kuvadia, and M. F. Doherty, "Engineering crystal morphology," Annu. Rev. Mater. Res., vol. 43, pp. 359–386, 2013, doi: 10.1146/annurev-matsci-071312-121623.

[124] C. Schmidt and J. Ulrich, "Morphology prediction of crystals grown in the presence of impurities and solvents - An evaluation of the state of the art," J. Cryst. Growth, vol. 353, no. 1, pp. 168–173, 2012, doi: 10.1016/j.jcrysgro.2012.05.001.

[125] Z. Xue, C. Yan, and T. Wang, "From Atoms to Lives: The Evolution of Nanoparticle Assemblies," Adv. Funct. Mater., vol. 29, no. 12, 2019, doi: 10.1002/adfm.201807658.

[126] G. Wulff, "XXV. Zur Frage der Geschwindigkeit des Wachsthums und der Auflösung der Krystallflächen," Zeitschrift für Krist. - Cryst. Mater., vol. 34, no. 1–6, pp. 449– 530, 1901, doi: 10.1524/zkri.1901.34.1.449.

[127] S. De Waele, K. Lejaeghere, M. Sluydts, and S. Cottenier, "Error estimates for density-functional theory predictions of surface energy and work function," Phys. Rev. B, vol. 235418, no. 23, pp. 1–13, 2016, doi: 10.1103/PhysRevB.94.235418.

[128] J. Andrés, L. Gracia, A. F. Gouveia, M. M. Ferrer, and E. Longo, "Effects of surface stability on the morphological transformation of metals and metal oxides

as investigated by first-principles calculations.," Nanotechnology, vol. 26, no. 40, p. 405703, 2015, doi: 10.1088/0957-4484/26/40/405703.

2. Aims

Present Doctoral Thesis covers a multidisciplinary field combining physics, chemistry, theoretical and computational chemistry, and materials science pushing the boundaries for finding and understanding the structure and properties, at atomic level, of two types of materials: glasses (Ba_2SiO_4, high-$BaSiO_3$, $Ba_4Si_6O_{16}$, $Ba_5Si_8O_{21}$, $Ba_6Si_{10}O_{26}$, high-$BaSi_2O_5$ and sanbornite (low-$BaSi_2O_5$)) and semiconductors ($PbMoO_4$, In_2O_3, ZrO_2, $CaWO_4$ and $SnMoO_4$/$SnWO_4$). We discuss recent advances for understanding, at atomic level, their structural, electronic, and optical properties. We also studied the doping processes, the formation of solid solution, and phase transitions induced by pressure, that play key roles in the further development of these materials for optoelectronic and photocatalytic applications.

Herein, a roadmap with specific objectives is presented to disclose the structure and properties of these different materials mentioned above, using a combination of experimental and theoretical results:

- To investigate the vibrational modes of barium silicates related with the phases presented in the BaO-SiO_2 system and to correlate the experimental (^{29}Si MAS NMR (*Magic-Angle Spinning*) and Raman spectroscopic) results and first-principle calculations, at the density functional theory (DFT) level, to allow not only the classification of the vibrational modes up to 1150 °C, but also to obtain information and structural changes undergone by these materials.
- To investigate the effects of SiO_4 connectivity on the spectroscopic signature of the Q^n units in Ba_2SiO_4, high-$BaSiO_3$, $Ba_4Si_6O_{16}$, $Ba_5Si_8O_{21}$, $Ba_6Si_{10}O_{26}$, high-$BaSi_2O_5$ and sanbornite (low-$BaSi_2O_5$), using the ^{29}Si magic spinning angle nuclear magnetic resonance (MAS NMR) and Raman spectra by identifying features associated with of contributions of the Q^n species within these structures.
- To analyze the effects of the La^{3+} dopant in the phase formation (rh-In_2O_3 vs bcc-In_2O_3) and support these findings by X-ray diffraction and Rietveld refinements, energy dispersive X-ray (EDX), Raman, and UV–vis spectroscopies, as well as PL emissions and investigate by first-principle calculation the structures of the two phases, based on DFT, to obtain their relative stabilities and structure differences at the atomistic level.
- To explain how the theoretical and experimental morphologies from FE-SEM images of the cubic (In_2O_3 and La^{3+}-doped In_2O_3) phase are rationalized based on

the Wulff construction by first-principle calculations. In addition, to demonstrate that the prepared In_2O_3 and La^{3+}-doped In_2O_3 films present electrocatalytic activity for water oxidation and contribute to broaden their possible applications.

- To characterize the PMO and $Pb_{1-2x}Ca_xSr_xMoO_4$ (x= 0.1, 0.2, 0.3, 0.4 and 0.5 (CSMO)) solid solutions (synthetized by the co-precipitation method) by x-ray diffraction (XRD), field emission electron microscopy (FE-SEM), Micro Raman (MR) and ultraviolet-visible (UV-Vis) spectroscopies and to determine the effect of their chemical composition on the morphology and photoluminescence (PL) emissions.
- To complement and rationalize experimental results by means of first principles calculation, to obtain the geometry, electronic structure, and properties of PMO and the solid solutions, and to apply a joint experimental and theoretical strategy that we developed to obtain a complete map of the morphologies
- To explore systematically the role of Tb^{3+} as a luminescence enhancer in ZrO_2:Tb^{3+}(x = 1, 2, 4 and 8 mol%) material, and to analyze in detail the relationship among the amount of Tb^{3+} in the ZrO_2 host lattice, PL emissions, and phase composition (cubic vs tetragonal) and to discuss the changes in the Raman vibrational frequencies associated to lattice structure and phase the transition.
- To discuss the geometries, electronic structures, and properties of both ZrO_2 and ZrO_2:6% Tb^{3+} systems by using density functional theory (DFT) calculations.
- To report a combined experimental and theoretical work to investigate the events that occur in the PL activity and their relationship with the excited electronic states of Eu-doped $CaWO_4$ crystals by use of first-principles quantum-mechanical calculations, at the density functional theory (DFT) level.

A schematic representation of the materials studied by experimental and theoretical methods in this Doctoral Thesis is presented in Figure 7.

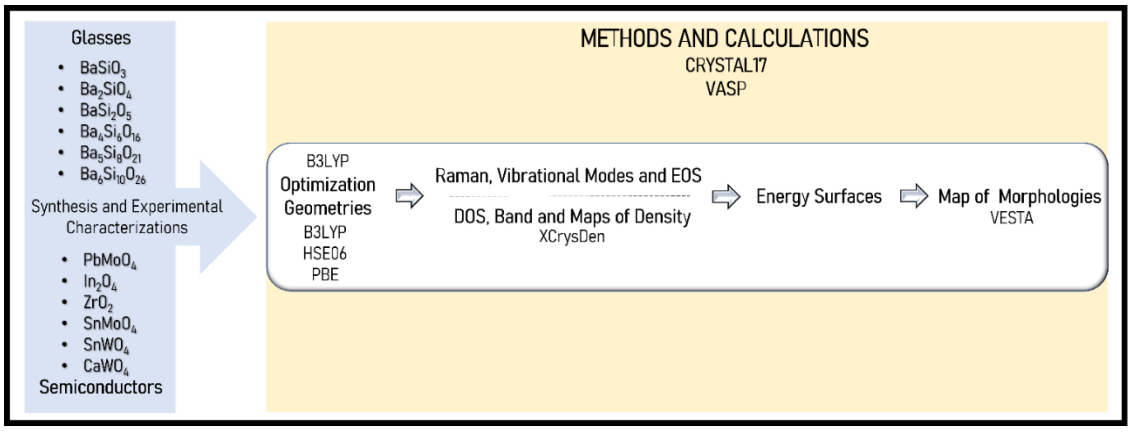

Figure 7: A schematic representation of the materials studied by experimental and theoretical methods in this Doctoral Thesis.

3. Computational methods

3.1. Theoretical methods

The interpretation at the atomic and molecular level requires the use of techniques that allow a greater clarification of the properties of materials, and that allow revolutionizing the field of Chemistry, Physics and Materials Science. One of the main tools for this description currently resides in computational simulations based on Quantum Mechanics, more precisely on the resolution of the Schrödinger equation (Equation 5), which allows the calculation of the electronic properties of any system by obtaining the respective function wave [130].

$$\hat{H}\Psi = E\Psi \qquad (5)$$

where Ψ represents the total wave function of the system, $\hat{H}$ the Hamiltonian operator an E the total energy of the system.

The Schrödinger wave equation can be defined for multielectronic systems, but it cannot be exactly solved for these cases, as the subsequent electrons introduce a complicated feature which is electron-electron repulsion, requiring the development of approximation methods [4].

3.1.1. DFT methodology

The (DFT – *Density Functional Theory*) appears as the basic idea, in which the electronic density ρ(r) at each point **r** determines the properties in the ground state of an atom, molecule or cluster, and refers to the works of Thomas, Fermi, Dirac in the beginning of the 20th century [131], on free electron gas in solids. Aiming to explain the electrical thermal conduction, these works constituted one of the most used methods in quantum calculations of the electronic structure of matter, and later improved by Slater years later [132]. Applied to electronic systems it is an alternative procedure to the solution of the Schrödinger equation, where the electronic energy functional is minimized with respect to electronic density.

The DFT has as its central focus the electronic density ρ(r), which makes possible to write Schrödinger's equation through an equation dependent on ρ. This electron density is not only the basis for the development of DFT, but a whole set of methods that study

atoms and molecules, which can be measured through experimental analyzes such as electron or X-ray diffraction, unlike the wave function. In addition to being an experimental observable, electron density is dependent only on 3 variables that define the spatial position and volume where the electron density is concentrated, simplifying the complex problem of solving eq.1 for multiple bodies (N) based, up to then, in dependent wave functions of 4N variables (3N spatial and N spin) [133].

The legitimization of the use of electronic density was then carried out with the publication of the two theorems proposed by Hohenberg and Kohn in 1964, which implemented important concepts for chemical description, where they demonstrate that the electronic density of a system determines the external potential and the number of electrons N and its approximation with ρ(r) allows us to say that the total energy will always be greater than or equal to the exact energy of the system [134].

• Hohenberg-Kohn (HK) Theorems

"The external potential v(r) is a unique functional of the electron density ρ(r) in addition to an additive constant".

In other words, the electron density of a system determines the external potential and the number of electrons N, that is, the Hamiltonian of the system, and by solving the Schrödinger equation, the ground state, and the excited state wave functions. Thus, the wave function is determined by the density ρ(r) of the ground state, with the properties of the system obtained as expectation values for the Hermitian operators. Therefore, energy is a functional of the ground state density: E=E[ρ] [134]. and can be written as follows:

$$E[\rho] = T[\rho] + V_{EE}[\rho] + V_{NE(BO)}[\rho] \quad (6)$$

where T[ρ] represent kinetic energy, $V_{NE}[\rho]$ the electron-core attraction energy (as a result of the Born-Oppenheimer approximation) and $V_{EE}[\rho]$ the electron-electron repulsion energy.

In the second theorem, the electronic density obeys the variational principle, which says that, given a specific electronic density, the energy will be greater than or equal to the exact energy,

$$T[\rho] + V_{EE}[\rho] + \int v_{NE}(r)\rho(r)dr = E[\rho_t] \geq E[\rho_0] \quad (7)$$

demonstrating that the ground-state energy can be obtained by the variational method, since the ground-state energy E[ρ0], minimized, corresponds to the ground-state electronic density (ρ0).

- **Kohn-Sham (KS) Method**

The Kohn-Sham (KS) method [5] proposes the execution of calculations based on the HK theorems, using a system of self-consistent monoelectronic equations, which can be solved by iterative methods similar to the Hartree-Fock (HF) equations, proposing that the energy by DFT has the functional as the form [135]:

$$\mathrm{E}[\psi_i] = \sum_{i=1}^{N} \langle \psi_i \left| -\frac{1}{2}\nabla^2 \right| \psi_i \rangle + \int \rho(r) v(r) dr + \int \frac{\rho(r_i)\rho(r_j)}{r_i - r_j} dr_i \, dr_j + E_{XC}[\rho] \qquad (8)$$

defining the first term as the kinetic energy functional of a system of non-interacting electrons whose density is the same as the density of real interacting electrons. And the second term, $E_{XC}[\rho(r)]$, called the exchange-correlation functional, is an overarching term to explain all other aspects of the real system, including the non-classical electron-electron interaction term (exchange and correlation) and also the residual part of the kinetic energy.

With the inclusion of the exchange and correlation term in the energy calculated by the DFT method, the Kohn-Sham equations were converted into exact ones, since they include all the components necessary for the description of the ground state. However, although the first HK theorem guarantees the existence of an exact functional of the electronic density, and the KS equations are solved in an iterative and self-consistent way (SCF) by varying the orbitals to minimize the energy expression, it is necessary the use of approximations to obtain the exchange and correlation functional.

3.1.1.1. Electron density functionals

Although the Kohn, Hohenberg and Sham theorems have shown that the energy of exchange and correlation can be defined as an electron density functional, which can be achieved by finding a self-consistent solution to a set of single-particle equations, this is completely unknown, requiring different approaches to its treatment. It is necessary to obtain an adequate approximation for the exchange-correlation functional:

- **Local-Density Approximation - LDA**

Proposed by Kohn and Sham in the same article [5], the LDA is a simple approximation and is based on the most used paradigm in Solid State Physics, the homogeneous electron gas. Also known in its localized spin form, LSDA, it presented serious problems when applied to real systems of interest that do not behave as homogeneous gas. However, for atoms or molecules, the LSDA/LDA approaches were very successful in describing structures in transition metal and solid-state complexes.

- **Generalized-Gradient Approximation - GGA**

Many of the quantitative deficiencies of LSDA/LDA can be corrected by employing GGA for the exchange-correlation energy. The inhomogeneity of the electron density in a finite system can be measured through its gradient, with this principle based on the GGA approximations. Despite depending on the density, it also depends on the density gradient, considering the inhomogeneity of the true distribution of electron density in a real system, making this approximation important, mainly for the energetic prediction of chemical reactions. The most used GGA correlation functionals are PBE, PBESOL, LYP (Lee-Yang-Parr) and PWGGA (Perdew-Wang) [136][137][138][139].

- **Hybrid Functionals**

Self-interaction, the possibility of interaction of electrons with themselves, is the main deficiency of local and semi-local functionals (LDA, LSDA, GGA). As a solution to this problem, it was proposed a correction to these functionals regarding the non-locality of E_{xc} for the system with non-interacting electrons, the replacement of part of the term of exchange of the semi-local functionals by the exact term from the Hartree-

method. Fock, a technique known as hybridization and which originates the called functional hybrids [130][140,141].

The physical principles by which hybrid functionals are based can be better understood in the fundamental structure of DFT, known as the adiabatic connection theorem, a method that allows the connection of a system of non-interacting electrons to the system of N-interacting electrons, so that the electronic density remains equal to the exact electronic density, using the adiabatic connection formalism as a practical tool for the construction of the functional. Proposing, from the linear interpolation between interacting and non-interacting regions, the so-called *Half-Half* Hybrid Functional [142], which indicates the potential benefits of using functionals that combine a fixed fraction of the exact exchange term with a fixed fraction of the semi-local exchange and correlation place:

$$E_{xc} = 0.5E_x^{exact} + 0.5E_{xc,1}^{LSDA}[n] \quad (9)$$

The methods most used today are hybrids, containing a mixture of GGA with Hartree-Fock, presenting a higher accuracy, compared to many traditional methods of Quantum Chemistry, keeping, however, a great computational simplicity. Its applications to crystalline systems described under periodic boundary conditions were employed when coded in the CRYSTAL program, enabling several observables such as the equilibrium structure, elastic constants and bulk modulus, thermochemical data, electric field gradients, phonon spectra and vibrational frequencies, be examined.

Among the most used functionals in computational chemistry is B3LYP, a GGA hybrid given by [139] is:

$$\mathrm{E_{xc}^{B3LYP}} = (1-\mathrm{a})\mathrm{E_x^{LSDA}} + \mathrm{aE_x^{exact}} + \mathrm{b}\Delta\mathrm{E_x^{B88}} + \mathrm{c}\Delta\mathrm{E_c^{LYP}} + (1-\mathrm{c})\mathrm{E_c^{VWN}} \quad (10)$$

in which the correlation functional of Lee, Yang and Parr, present the empirical parameters a = 0.20, b =0.72 and c = 0,81 [130][143].

However, this is not the only known hybrid functional, there are also other hybrid functionals that can be mentioned: B3PW (3 BECKE parameters for exchange and PWGGA for correlation), PBE0 (hybrid version of the PBEXC functional, with 25% of

Hartree-Fock exchange), PBESOL0 (same as PBE, but with PBESOL XC), B1WC, WC1LYP, B97H and PBE0-13 [130][141][144].

- **Basis set for Periodic Systems**

With the development of the SCF in computational routines, it is necessary basis set, which will be used to build the molecular orbitals that describe the system. As a simpler example, the bases Slater-Type Orbitals (STO) basis set [145] consist of Slater functions that mimic hydrogenoid functions and are restricted to molecular systems with a reduced number of atoms.

To overcome the limitations to a few atoms, more flexible functions such as Gaussian-type orbitals (GTO) can be used [146]. However, the GTO functions do not reproduce atomic conditions with the accuracy of STO, in the vicinity of the nucleus. Currently, there are several other naming and representation schemes for Gaussian base functions in the literature, named as Single-ζ (SZ – single zeta), Double- ζ (DZ – double zeta), Triple- ζ (TZ – triple zeta) e N- ζ (multiple zeta), where (ζ) represents the Slater coefficient.

3.2. Computational simulations

In practice, DFT methods are the first choice for the treatment in computational codes for solids with periodic models, presenting excellent results for ground state properties.

In this thesis, first-principles calculations were used to elucidate the structural, electronic and morphological properties implementing the CRYSTAL17 [15] and VASP [10] programs. CRYSTAL, and its latest commercial version (CRYSTAL-17), deals with 0D (molecules and clusters) and periodic systems in 1D (polymers, helices and nanotubes), 2D (slabs) and 3D (crystals) with HF and DFT Hamiltonians. It allows the study of the electronic structure of solids at Hartree-Fock and DFT level, allowing the use of different functionals and basis sets that best represent the studied material. Its main characteristics are in the simulations referring to structural, electronic, dielectric, vibrational, magnetic and elastic properties, making it a very useful program in the representation of periodic systems.

Vienna Ab initio Simulation Package (VASP) is a program for electronic structure calculations and quantum-mechanical molecular dynamics, from first principles. The

central quantities, like the one-electron orbitals, the electronic charge density, and the local potential are expressed in plane wave basis sets. The interactions between the electrons and ions are described using norm-conserving or ultrasoft pseudopotentials, or the projector-augmented-wave method. DFT is applied solving the Kohn-Sham equations, or within the Hartree-Fock (HF) approximation, solving the Roothaan equations. Hybrid functionals that mix the Hartree-Fock approach with density functional theory are implemented as well.

3.2.1. Calculations of the structural properties

For the calculations and optimization of the geometries and structures (*bulk* (3D)) of the materials in this study, we start from the geometry obtained by X-ray diffraction and Rietveld refinement, whose position of the different constituent atoms in the crystal lattice are known. In all the calculations of the most stable structure, it is necessary to minimize the total energy, by optimizing the lattice parameters and coordinates of the atoms. The convergence criteria used, and the methods were as follows:

- In the characterizations for barium silicates structures, DFT calculations of the lattice parameters and vibrational modes were done using Becke's three-parameter hybrid non-local exchange functional, combined with a Lee-Yang-Parr gradient-corrected correlation functional (B3LYP), implemented in the CRYSTAL17 package [15]. The atoms were centered and described using pseudopotential databases; [147], 88-31G* [148] and 8-411d11G [149](all-electron) for Ba, Si and O, respectively. Regarding the diagonalization of the density matrix, the reciprocal space net was described by a shrinking factor of 4, generated according to the Monkhorst–Pack scheme. The accuracy of the evaluation of the Coulomb and exchange series was controlled by five thresholds, whose adopted values were 10^{-7}, 10^{-7}, 10^{-7}, 10^{-7}, and 10^{-14}. The vibrational frequencies calculation was performed at the Γ point within the harmonic approximation, and the dynamic matrix was computed by the numerical evaluation of the first derivative of analytical atomic gradients.
- The structural and electronic properties of the PMO structure and $Pb_{1-2x}Ca_xSr_xMoO_4$ solid solutions were calculated using functional B3LYP,

implemented in the CRYSTAL17 package. The atoms were centered and described using pseudopotential databases Ca_pob_TZVP_2012, Sr_ECP28MDF_s411p411d11_Heifets_2013, Pb_ECP60MDF_doll_2011, 976-311 (d631) G and O-6-31G* (all-electron) for Ca, Sr, Pb, Mo and O, respectively. Regarding the diagonalization of the density matrix, the reciprocal space net was described by a shrinking factor of 4, generated according to the Monkhorst–Pack scheme. The accuracy of the evaluation of the Coulomb and exchange series was controlled by five thresholds, whose adopted values were 10^{-8}, 10^{-8}, 10^{-8}, 10^{-8}, and 10^{-16}. To simulate the substitution process and to obtain the ideal percentages presented in the experimental data, a 5×1×1 supercell, with a volume 5 times larger than the primitive cell and 60 atoms was used.

- To characterize the In_2O_3 and La^{3+}-doped In_2O_3 systems, all-electron basis sets were used to describe O atomic centers, a pseudopotential basis set for the in atom, (54) and an effective core potential (ECP) pseudopotential with 11 valence electrons described was used for the La^{3+} [150]. Regarding the density matrix diagonalization, the reciprocal space net was described by a shrinking factor of 4, corresponding to 36 k-points generated according to the Monkhorst–Pack scheme. The accuracy of the evaluation of the Coulomb and exchange series was controlled by five thresholds, whose adopted values were 10^{-8}, 10^{-8}, 10^{-8}, 10^{-8}, and 10^{-16}. A supercell of 80 atoms, corresponding to 2×2×1 conventional cells, was used to simulate the La^{3+}-doped In_2O_3 systems. A 12.50% substitution of In^{3+} ions by La^{3+} cations was performed to match the experimental value in which the rh-phase of In_2O_3 was formed.
- To characterize the Tb^{3+} in the ZrO_2 host lattice, the VASP package was used and the Kohn-Sham equations were solved by using the Perdew, Burke, and Ernzerhof (PBE) exchange-correlation functional [137], alongside including the effect of long-range interactions using Grimme's D3 semi-classical dispersion methods [151]. The electron-ion interaction was described via the projector-augmented-wave pseudo potentials and the plane-wave expansion was truncated at a cut-off energy of 520 eV. The Brillouin zone was sampled by using 4×4×4 Monkhorst-Pack special k-point grid to ensure geometrical and energetic convergence of the ZrO2 structures. Both cubic and tetragonal phases of ZrO_2 undoped and doped at 6% Tb substitution were tested. The valence electron density is defined by 12 ($4s^2 4p^6 5s^2 4d^2$) electrons for Zr atoms, 6 ($2s^2 2p^4$) electrons for O atoms and 19

($5s^2 5p^6 6s^2 4f^9$) electrons for Tb atoms. A supercell with 96 atoms was used to simulate an amount of Tb doping up to 6% for both systems, 2×2×2 and 2×2×4 for cubic and tetragonal phases, respectively. In addition, a large supercell with 192 atoms was used to simulate an amount of Tb doping up to 3% for both systems, 4×2×2 and 4×4×2 for cubic and tetragonal phases, respectively. Two Zr^{4+} were substituted by two Tb^{3+} and an oxygen vacancy was included to maintain the cell as electroneutral. The substitution process of Zr^{4+} by Tb^{3+} cations was done for both phases using structural models. The most energetically favorable arrangement can be selected to analyze theoretically the substitution process. The cell parameters and positions of all atoms were allowed to relax, and the conjugated gradient energy minimization method was used to obtain relaxed systems. This was achieved by setting a threshold value (i.e., 0.01 $eV \cdot Å^{-1}$) for the forces experienced by each atom.

- To study the effect of Eu-doped in the $CaWO_4$ structure, two models were constructed, the pure CW and CWE. All calculations were performed with the CRYSTAL17 package [15]. The computational method is based on the DFT associated with B3LYP hybrid functional 23,24. Ca, W, O, and Eu atomic centers were described by the Ag_HAYWSC-311d31G_apra_1991, W_cora_1996, and O_6-31d1_corno_2006 basis sets, respectively, which were obtained from the Crystal website [*https://www.crystal.unito.it/basis-sets.php*]. The diagonalization of the Fock matrix was performed using a 6×6×6 grid with 44 k-point grids in the reciprocal space. The thresholds controlling the accuracy of the calculation of the Coulomb and exchange integrals were set to 10^{-8}, 10^{-8}, 10^{-8}, 10^{-8}, and 10^{-16}, and the percentage of Fock/Kohn–Sham matrix mixing was set to 30. A full optimization process of the lattice parameters (a and c) and the internal atomic coordinates (x, y, and z) for the bulk was carried out until all force components were less than 10^{-5} eV/nm^2. From this optimized bulk structure, two periodic models, were built by selecting a 2×2×2 supercell: (1) the pure CW model of 192 atoms in the structure, composed by 32 Ca atoms, 32 W atoms and 128 O atoms and (2) the CWE model, in which two Ca^{2+} cations were replaced by two Eu^{3+} cations. To keep the electroneutrality of the system, a Ca^{2+} cation ghost was considered. This model contains 6.90% molar Eu in the structure.
    - The structural, electronic properties and EOS of $SnMoO_4$ and $SnWO_4$ bulk were simulated by means of periodic DFT using the CRYSTAL17 package. To

study the influence of different approximations for exchange and correlation on the DFT method, a complete structure optimization by using the HSE06 [152] and B3LYP [143] functionals. The atoms were described using pseudopotential bases set, Sn_ECP28MDF-411(51d) G_baranek_2013_$SnTiO_3$, W_cora_1996, 976-311 (d631) G and O-6-31G* (all-electron) for Sn, W, Mo, and O, respectively. The accuracy of the evaluation of the Coulomb and exchange series was controlled by five thresholds, whose adopted values were 10^{-7}, 10^{-7}, 10^{-7}, 10^{-7}, and 10^{-14} which assure a convergence in total energy better than 10^{-7} Hartree in all cases, whereas the percent of Fock/Kohn–Sham matrices mixing has been set to 40 (IPMIX= 40). For the calculations of the solid solutions, the substitution of W by Mo atoms was performed in a percentage of (0%, 25%, 50%, 75% and 100%), being the 0 and 100% the pure structures. The CRYSTAL program can perform an automated scan over the volume to compute energy E versus volume V curves that are then fitted to the third-order Birch−Murnaghan (BM) EOS [153]. For each volume, a full V-constrained geometry optimization was performed. As a result, the pressure dependence of the atomic and electronic structure was determined, such as zero pressure bulk modulus, B0, as well as the volume/pressure dependence of the total energy and enthalpy.

3.2.2. Calculations of the electronic properties

The study of the electronic properties of bulk and surfaces was carried out through the analysis of band structures, density of states (DOS) and projected DOS in atoms and atomic orbitals, by using the XCrysDen program. In the analysis of the energy band structures, the last 20 bands in the conduction band (CB) and the first 20 bands in the valence band (VB) were considered, according to the corresponding k points for each system in the Brillouin first zone [154]. Figure 8 presents an example of reciprocal lattices (dots) (a), the corresponding first Brillouin zone and the band structure obtained (c). The differences in energy generated between the BV and BC bands, the called band gap energy, was calculated for bulk and surfaces.

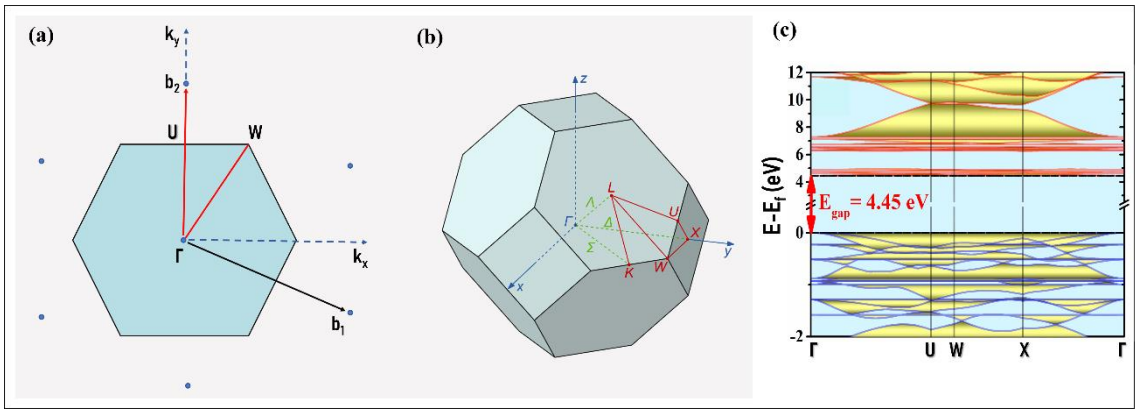

Figure 8: The reciprocal lattices (dots) (a), corresponding first Brillouin zone (b) and band (c).

3.2.3. Visualizations programs

The creation of the morphological maps was constructed according to Wulff's theorem using the program VESTA (Visualization for Electronic and Structural Analysis) [155], which made possible to create the nano-morphology (crystals) by means of the distances from the crystal center planes. This distance is directly proportional to the surface energy modulation.

The program XCrysDen (X-Window Crystalline Structures and Densities) [156] was used to help compiling structural and electronic data (Band structure and DOS), as well as the representation of contour maps for the electronic density distribution in the crystal structure. In addition, other remaining graphics were generated by the ORIGINPro program.

Figure 9: VESTA, ORIGINPro and XCrySDen programs layout.

References

[129] J. Ungelenk and C. Feldmann, "Synthesis of faceted β-$SnWO_4$ microcrystals with enhanced visible-light photocatalytic properties," Chem. Commun., vol. 48, no. 63, pp. 7838–7840, 2012, doi: 10.1039/c2cc33224h.

[130] A. D. Becke, "Perspective: Fifty years of density-functional theory in chemical physics," J. Chem. Phys., vol. 140, no. 18, 2014, doi: 10.1063/1.4869598.

[131] E. Fermi, "A statistical method for determining some properties of the atom. I.," Atti della Accad. Naz. dei Lincei, Cl. di Sci. Fis. Mat. e Nat. Rend., vol. 6, no. December, pp. 602–607, 1927.

[132] J. C. Slater, "A simplification of the Hartree-Fock method," Phys. Rev., vol. 81, no. 3, pp. 385–390, 1951, doi: 10.1103/PhysRev.81.385.

[133] G. Hautier, A. Jain, and S. P. Ong, "From the computer to the laboratory: Materials discovery and design using first-principles calculations," J. Mater. Sci., vol. 47, no. 21, pp. 7317–7340, 2012, doi: 10.1007/s10853-012-6424-0.

[134] P. Geerlings, F. De Proft, and W. Langenaeker, "Density Functional Theory: A Source of Chemical Concepts and a Cost - Effective Methodology for Their Calculation," Adv. Quantum Chem., vol. 33, no. C, pp. 303–328, 1998, doi: 10.1016/S0065-3276(08)60442-6.

[135] D. S. Sholl and J. A. Steckel, "What is Density Functional Theory?," Density Funct. Theory, pp. 1–33, 2009, doi: 10.1002/9780470447710.ch1.

[136] J. P. Perdew, K. Burke, and M. Ernzerhof, "Generalized gradient approximation made simple," Phys. Rev. Lett., vol. 77, no. 18, pp. 3865–3868, 1996, doi: 10.1103/PhysRevLett.77.3865.

[137] J. P. Perdew, M. Ernzerhof, and K. Burke, "Rationale for mixing exact exchange with density functional approximations," J. Chem. Phys., vol. 105, no. 22, pp. 9982–9985, 1996, doi: 10.1063/1.472933.

[138] J. P. Perdew et al., "Restoring the density-gradient expansion for exchange in solids and surfaces," Phys. Rev. Lett., vol. 100, no. 13, pp. 1–4, 2008, doi: 10.1103/PhysRevLett.100.136406.

[139] C. Lee, W. Yang, and R. G. Parr, "Development of the Colle-Salvetti correlation-energy formula into a functional of the electron density," Phys. Rev. B, vol. 37, no. 2, pp. 785–789, Jan. 1988, doi: 10.1103/PhysRevB.37.785.

[140] B. G. Janesko, T. M. Henderson, and G. E. Scuseria, "Screened hybrid density functionals for solid-state chemistry and physics," Phys. Chem. Chem. Phys., vol. 11, no. 3, pp. 443–454, 2009, doi: 10.1039/b812838c.

[141] C. Franchini, "Hybrid functionals applied to perovskites," J. Phys. Condens. Matter, vol. 26, no. 25, 2014, doi: 10.1088/0953-8984/26/25/253202.

[142] A. D. Becke, "A new mixing of Hartree-Fock and local density-functional theories," J. Chem. Phys., vol. 98, no. 2, pp. 1372–1377, 1993, doi: 10.1063/1.464304.

[143] A. D. Becke, “Density-functional thermochemistry. III. The role of exact exchange,” J. Chem. Phys., vol. 98, no. 7, pp. 5648–5652, 1993, doi: 10.1063/1.464913.

[144] C. Adamo and V. Barone, “Toward reliable density functional methods without adjustable parameters: The PBE0 model,” J. Chem. Phys., vol. 110, no. 13, pp. 6158–6170, 1999, doi: 10.1063/1.478522.

[145] J. C. Slater and G. F. Koster, “Simplified LCAO method for the periodic potential problem,” Phys. Rev., vol. 94, no. 6, pp. 1498–1524, 1954, doi: 10.1103/PhysRev.94.1498.

[146] A. Damascelli, “Probing the electronic structure of complex systems by ARPES,” Phys. Scr. T, vol. T109, pp. 61–74, 2004, doi: 10.1238/Physica.Topical.109a00061.

[147] E. O. Gomes et al., “Computational procedure to an accurate DFT simulation to solid state systems,” Comput. Mater. Sci., vol. 170, no. August, p. 109176, 2019, doi: 10.1016/j.commatsci.2019.109176.

[148] R. Nada, J. B. Nicholas, M. I. McCarthy, and A. C. Hess, “Basis sets for Ab initio periodic hartree-fock studies of zeolite/adsorbate interactions: He, Ne, and Ar in silica sodalite,” Int. J. Quantum Chem., vol. 60, no. 4, pp. 809–820, 1996, doi: 10.1002/(SICI)1097-461X(1996)60:4<809::AID-QUA3>3.0.CO;2-0.

[149] L. Valenzano, F. J. Torres, K. Doll, F. Pascale, C. M. Zicovich-Wilson, and R. Dovesi, “Ab initio study of the vibrational spectrum and related properties of crystalline compounds; the case of CaCO3 calcite,” Zeitschrift fur Phys. Chemie, vol. 220, no. 7, pp. 893–912, 2006, doi: 10.1524/zpch.2006.220.7.893.

[150] T. Bredow, K. Jug, and R. A. Evarestov, “Electronic and magnetic structure of ScMnO3,” Phys. Status Solidi Basic Res., vol. 243, no. 2, pp. 10–12, 2006, doi: 10.1002/pssb.200541403.

[151] S. Grimme, J. Antony, S. Ehrlich, and H. Krieg, “A consistent and accurate ab initio parametrization of density functional dispersion correction (DFT-D) for the 94 elements H-Pu,” J. Chem. Phys., vol. 132, no. 15, 2010, doi: 10.1063/1.3382344.

[152] A. V. Krukau, O. A. Vydrov, A. F. Izmaylov, and G. E. Scuseria, “Influence of the exchange screening parameter on the performance of screened hybrid functionals,” J. Chem. Phys., vol. 125, no. 22, 2006, doi: 10.1063/1.2404663.

[153] F. BIRCH, “Section of Geology and Mineralogy: Elasticity and Constitution of the Earth’S Interior*,” Trans. N. Y. Acad. Sci., vol. 14, no. 2 Series II, pp. 72–76, 1951, doi: 10.1111/j.2164-0947.1951.tb01059.x.

[154] L. Brillouin, “Les électrons libres dans les métaux et le role des réflexions de Bragg,” J. Phys. le Radium, vol. 1, no. 11, pp. 377–400, 1930, doi: 10.1051/jphysrad:01930001011037700.

[155] K. Momma and F. Izumi, “VESTA 3 for three-dimensional visualization of crystal, volumetric and morphology data,” J. Appl. Crystallogr., vol. 44, no. 6, pp. 1272–1276, 2011, doi: 10.1107/S0021889811038970.

[156] A. Kokalj, “XCrySDen-a new program for displaying crystalline structures and

electron densities," J. Mol. Graph. Model., vol. 17, no. 3–4, pp. 176–179, 1999, doi: 10.1016/S1093-3263(99)00028-5.

4. Results and discussion

This Doctoral Thesis is a summary of published articles, and articles in the publication stage or in the writing stage, in which the results are achieved through the joint use of experimental and theoretical works.

I- Title: Identifying and explaining vibrational modes of sanbornite (low-$BaSi_2O_5$) and $Ba_5Si_8O_{21}$: A joint experimental and theoretical study
Authors: Eduardo de Oliveira Gomes, Benjamin J.A. Moulton, Thiago R. Cunha, Lourdes Gracia, Paulo S. Pizani, Juan Andrés.
Journal: Spectrochimica Acta Part A: Molecular and Biomolecular Spectroscopy **2021**, 248, 119130. (Spectroscopy Q1)

II- Title: A theoretical and experimental investigation of hetero-versus homo connectivity in barium silicates
Authors: Benjamin J. A. Moulton, Eduardo de Oliveira Gomes, Thiago R. Cunha, Carsten Doerenkamp, Lourdes Gracia, Hellmut Eckert, Juan Andrés, Paulo S. Pizani.
Journal: American Mineralogist **2022** (*in press*). (Geophysics, Geochemistry and Petrology Q1)

III- Title: Joint theoretical and experimental study on the La doping process in In_2O_3: Phase transition and electrocatalytic activity
Authors: Samantha C. S. Lemos, Edson Nossol, John. L. Ferrari, Eduardo de Oliveira Gomes, Juan Andrés, Lourdes Gracia, Iván Sorribes, Renata C. Lima.
Journal: Inorganic Chemistry **2019**, 58, 17, 11738–11750. (Chemistry, Inorganic Q1)

IV- Title: Structure, electronic properties, morphology evolution, and photocatalytic activity in $PbMoO_4$ and $Pb_{1-2x}Ca_xSr_xMoO_4$ (x= 0.1, 0.2, 0.3, 0.4 and 0.5) solid solutions
Authors: Eduardo de Oliveira Gomes, Lourdes Gracia, Anderson A. G. Santiago, Ricardo L. Tranquilin, Fabiana V. Motta, Rafael A. C. Amoresi, Elson Longo, Mauricio R. D. Bomio, Juan Andrés.
Journal: Physical Chemistry Chemical Physics **2020,** 22, 25876-25891. (Physics, Atomic, Molecular & Chemical Q1)

V- Title: Integrated experimental and theoretical study on the phase transition and photoluminescent properties of ZrO_2: xTb^{3+} (x= 1, 2, 4 and 8 mol%)
Authors: Laura X. Lovisa, Eduardo de Oliveira Gomes, Lourdes Gracia, Anderson A. G. Santiago, M. Siu Li, Juan Andrés, Elson Longo, Mauricio R. D. Bomio, Fabiana V. Motta
Journal: Materials Research Bulletin **2022**, 145, 111532. (Mechanics of Materials and Mechanical Engineering Q1)

VI- Title: Photoluminescence emissions of $Ca_{1-x}WO_4$: xEu^{3+}: Bridging between experiment and DFT calculations
Authors: Amanda Fernandes Gouveia, Marcelo Assis, Lara Kelly Ribeiro, Aline Estefany Brandão Lima, Eduardo de Oliveira Gomes, Daniele Souza, Yara Gobato Galvão, Ieda Lucia Viana Rosa, Geraldo Eduardo da Luz Jr., Eva Guillamón, Elson Longo, Juan Andrés, Miguel Angel San-Miguel
Journal: Journal of Rare Earths **2021** (*in press*). (Chemistry Q2)

VII- Book chapter Title: Morphology-dependent properties in inorganic semiconductors: An experimental and theoretical approach
Authors: Amanda Fernandes Gouveia, Luis Henrique da Silveira Lacerda, Eduardo de Oliveira Gomes, Lourdes Gracia, Marcelo Assis, Camila Cristina de Foggi, Elson Longo, Juan Andrés, Miguel Angel San-Miguel
Book title: Advances in Material Research and Technology Series, (*pre-proof*)
Editorial: Springer (Series Ed.: Ikhmayies, Shadia Jamil)
https://www.springer.com/series/16426 ISSN: 2662-4761.

VIII- Title: Unveiling the relationship between the phase transition induced by pressure and the substitution processes along **α-** and **β-**$SnMo_{1-x}W_xO_4$ (x=0, 0.25. 05, 0.75 and 1) solid solutions (*drafting*).
Authors: Eduardo de Oliveira Gomes, Amanda F. Gouveia, Lourdes Gracia, Juan Andrés

4.1. Paper I and II (Barium silicates)

The barium silicates in general are found in nature or synthetic and usually have big and complex structures, presenting a challenge in the characterizations for researchers.

In the paper I, we report the analysis of vibrational properties of the sanbornite (low-$BaSi_2O_5$) and $Ba_5Si_8O_{21}$ structures using theoretical and experimental approaches, as well as results of high temperature experiments up to 1100–1150 °C. The crystal parameters derived from Rietveld refinement and calculations show excellent agreement, within 4%, while the absolute mean difference between the theoretical and experimental results for the IR and Raman vibrational frequencies was <6 cm^{-1}.

The sanbornite is composed of two layers: one of Q^3 species and one of BaO_9 polyhedra. Each of the Q^3 species are connected to adjacent tetrahedra via bridging oxygens (BO) at the O1 and O3 sites whereas the O2 oxygen is a non-bridging oxygen (NBO) which is only bonded to one Si and three Ba atoms and topologically, can be described as a 6^3 net or an infinite layer of six-membered tetrahedral rings. $Ba_5Si_8O_{21}$ presented 18 crystallographic sites. This phase is a rare silicate composed of quadruple Zwier chains that form ribbons that can be described topologically as $^2T2^3T6$ ribbons. In the $Ba_5Si_8O_{21}$ structure, the edge of each ribbon has Q2 species at the Si1 site. The remaining Si sites (Si2-Si4) are Q3 species, all of which have three BO and one NBO.

The theoretical calculations reproduced the experimental vibrational modes with a good agreement for both structures, the sanbornite (with 96 normal modes) and the $Ba_5Si_8O_{21}$ (with 204 normal modes *C2/c*). These results gave the detailed mode assignments, associated to specific Ba or Si sites or bonding configurations. Per example, stretching modes which are localized to specific Si-O bonds, show strong correlations with the bond length changes with temperature.

With this important introduction (paper I), in the paper II was analyzed the effects of connectivity on resonances in seven barium silicates: Ba_2SiO_4, high-$BaSiO_3$, $Ba_4Si_6O_{16}$, $Ba_5Si_8O_{21}$, $Ba_6Si_{10}O_{26}$, high-$BaSi_2O_5$ and sanbornite (low-$BaSi_2O_5$) using ^{29}Si MAS NMR and Raman spectroscopy. The connectivity is defined by the number of Si-O-Si bonds found around a central tetrahedron and described using the Q^n species notation, where n is the number of bridging oxygen (BO) atoms shared between tetrahedra and 4-n is the number of non-bridging oxygen (NBO) atoms bound to M cations. Using Rietveld refinement, the crystal lattice parameters were determined and with the ^{29}Si

magic spinning angle nuclear magnetic resonance (MAS NMR) and Raman spectra were identified features associated with each of the contributions of the Q^n species within these structures.

The Raman spectra of the barium silicates was found to be dominated by intense peaks in the 400-800 cm^{-1} and 800-1200 cm^{-1} ranges that correspond to the *bending* and *stretching* mode regions, respectively. The intense bands originated from the bending modes of the B4S6-BS2 phases display a doublet or triplet feature centered around ~530 cm^{-1} B4S6, B5S8, B6S10 and high-BS2 have similar unit cell symmetries, either $P2_1/c$ or C2/c, and similar intense bending mode frequencies. Despite the observed similarities in the spectra, the origins of these modes are quite distinct. For example, in low-BS2 the 535.5 cm^{-1} mode involves bending of the O3-Si-O2, where one oxygen is a BO and the other an NBO. In contrast, the 533.8 cm^{-1} mode of high-BS2 involves the bending of the Si3-O2-Ba2 bond angle.

These papers are a collaboration between the Laboratorio de Química Teórica y Computacional (QTC) and Center for Research, Technology and Education in Vitreous Materials, Department of Materials Engineering, Federal University of São Carlos (UFSCar). The syntheses and experimental characterizations described in this work were performed by Dr. Benjamin J. A. Moulton.

4.2. Paper III, IV, V and VI ($PbMoO_4$, In_2O_3, ZrO_2, $CaWO_4$)

Both In_2O_3 and ZrO_2 structures presented phase transitions as a result of doping with rare-earth metals, La^{3+} and Tb^{3+}, respectively.

In_2O_3 and La^{3+}-doped In_2O_3 nanostructures were synthesized through a facile and fast chemical route based on the microwave-assisted hydrothermal method combined with rapid thermal treatment in a microwave oven. The presence of the La^{3+} doping process modifies the size and morphology of the In_2O_3 nanostructures and stabilizes the rhombohedral (rh) In_2O_3 phase with respect to the most stable cubic (bcc) polymorph. A comparison of the results obtained from the Rietveld refinement shows that a percentage of 19.7% was achieved for the rh-In_2O_3 phase with La^{3+} doping.

A supercell of 80 atoms, corresponding to 2×2×1 conventional cells, was used to simulate the La^{3+}-doped In_2O_3 systems. An analysis of the results shows that the undoped bcc-In_2O_3 phase is more stable than the rh-In_2O_3 one; however, as the percent of La^{3+} doping content increases, the rh-phase is stabilized with respect to the bcc-structure. Substituting In^{3+} by La^{3+} cations in both positions 8b and 24d achieves an energy in which

the rh-In_2O_3 phase is more stable than the bcc-In_2O_3 phase when the doping percentage reaches the value of 12.5% at both 8b and 24d positions.

The (110), (100), (111), and (211) surfaces of the bcc-In_2O_3 phase were modeled using slab models with the calculated equilibrium geometries. According to the DFT calculations, the stability of the surfaces follows the order (100) < (211) < (110) < (111), with surface energies of 3.62, 2.29, 1.40, and 1.02 J m^{-2}, respectively. The analysis of the theoretical results revealed that the most stable morphology is an octahedron, in which only the (111) surface appears. From the energies obtained using the slab models, was possible to modulate the surface energies to find the morphology obtained experimentally. The Raman spectra of La^{3+}-doped In_2O_3 presented a strong band at 162 cm^{-1}, attributed to the A_{1g} symmetry of rh-In_2O_3, indicating the coexistence of cubic and rhombohedral phases of In_2O_3, which agrees with the X-ray diffraction characterization.

The calculated band structures and total and projected DOS on atoms for the pure bcc-In_2O_3, pure rh-In_2O_3, 12.5% La^{3+} bcc-In_2O_3, and 12.5% La^{3+} rh-In_2O_3, showed that doping of La^{3+} cations in the In_2O_3 matrix provides an increase in the indirect gap energy, which was the same behavior as that verified experimentally. This enhancement can be sensed more in rh-In_2O_3 (up to 4.11 eV) than in bcc-In_2O_3 (up to 3.82 eV) doped structures, due to the increase in electron density caused by the dopant.

In addition, the PL intensity decreased was observed from undoped In_2O_3 to La^{3+}-doped In_2O_3 nanostructures. This indicates that doping can alter the surface, generating trap states that should reduce the electron/hole recombination rates, improving the charge transfer processes, and consequently leading to a more efficient electrochemical performance.

This paper is a collaboration between the Laboratorio de Química Teórica y Computacional (QTC) and Institute of Chemistry of the Federal University of Uberlândia (UFU). The syntheses and experimental characterizations described in this work were performed on the supervision of Prof. Renata C. Lima and Dr. Samantha C. de Lemos.

ZrO_2 x mol% Tb^{3+} particles (x = 0,1,2,4 and 8%) were prepared by the complex polymerization (CP) method and characterized by XRD. The analysis of the peak intensities for the planes (202) and (004) for ZrO_2 compared to the ZrO_2:8% Tb samples showed that at 8% Tb the phase transition from zirconia to the cubic phase was already occurring, coexisting with the tetragonal phase, the latter in smaller amounts. The values of the lattice parameters "*a*" and "*c*" changed due to the increase in the concentration of Tb^{3+} in the ZrO_2. This discontinuity was associated with structural defects and distortions within the ZrO_2 lattice.

DFT calculations were carried out to investigate the doping process in cubic and tetragonal ZrO_2 phases. The results indicate that for pure ZrO_2 and 3% doped-ZrO_2 the tetragonal structure was more stable than cubic structure. The incorporation of 6% Tb^{3+} into the ZrO_2 structure increased the stability of the cubic phase relative to the tetragonal phase, and a more favorable substitution occurs in the cubic polymorph of ZrO_2 as the amount of Tb^{+3} increased. The transformation from the tetragonal phase to the cubic phase as a result of the introduction of Tb^{3+} ions into the ZrO_2 lattice was also observed by analyzing the Raman spectra. The bands located in the spectra in 147, 266, 317, 462 and 640 cm^{-1} are characteristic bands of the tetragonal phase and are represented by six active modes ($A_{1g} + 2B_{1g} + 3E_g$). The bands observed at 147, 266 and 462 cm^{-1} are assigned to E_g mode. The bands located at 317 and 640 cm^{-1} refer to the B_{1g} mode. In contrast, the cubic phase was clearly characterized by a relatively wide band between 533 and 664 nm centered on 625 cm^{-1}. Theoretical calculations of the Raman-active modes of pure tetragonal ZrO_2 yielded values of 149.4, 294.2, 301.5, 453.6, 611.5, and 650.9 cm^{-1} for the E_g, A_{1g}, B_{1g}, E_g, B_{1g}, and E_g modes, respectively. The case of pure cubic ZrO_2 (a unique mode which has T_{2g} symmetry) occurs at a wavenumber of 600.7 cm^{-1}.

The $E_{g(3)}$ mode in 462 cm^{-1} signalized the presence of a metastable tetragonal phase of ZrO_2 (t'- ZrO_2). This band is subtly verified in the Raman spectrum of the ZrO_2: 8% Tb sample, indicating the coexistence of the two phases: cubic (c- ZrO2) and metastable tetragonal (t'- ZrO_2). The t'- ZrO_2 phase is characterized by having a distorted shape of the cubic phase. Although, the relation of the lattice parameters is similar in both phases; in the t'- ZrO_2 phase, the oxygen ions are shifted alternately (zigzag aspect) along the z axis, assuming tetragonal symmetry.

This paper is a collaboration between the Laboratorio de Química Teórica y Computacional (QTC) and Laboratório de Síntese Química de Materiais (LSQM) of

the Department of Materiais of the Federal University of Rio Grande do Norte (UFRN). The syntheses and experimental characterizations described in this work were performed by Dr. Laura X. Lovisa under the supervision of Prof. Mauricio R. D. Bomio and Prof. Fabiana V. Motta.

$PbMoO_4$ (PMO) and $Pb_{1-2x}Ca_xSr_xMoO_4$ (x = 0.1, 0.2, 0.3, 0.4 and 0.5) solid solutions were successfully prepared, for the first time, by a simple co-precipitation method and a structural characterization of these samples was performed using X-ray diffraction with Rietveld refinement analysis. DFT calculations were performed to analyze the bulk and surfaces of PMO, $Ca_{0.5}Sr_{0.5}MoO_4$ (CSMO) and the solid solutions. The use of the Kröger–Vink notation allowed us to analyze the number of Pb–O breaking bonds in the exposed clusters in order to analyze the stability of studied surfaces. Therefore, different crystal morphologies were achieved by tuning the E_{surf} values of the different surfaces and were correlated with the experimental FE-SEM images (a faceted octahedron defined mainly by the (001), (011) and (112) surfaces, for the PMO sample).

The charge density maps showed that there is a higher electronic density around the Pb cations in relation to the Ca and Sr cations, allowing PMO to have a larger charge mobility, lower recombination rate (electron–hole), and greater dispersion in its bands, resulting in lower E_{gap} values of PMO compared to CSMO. In addition, the photocatalytic performance was tested *via* degradation of the RhB solution under UV light. Their analysis showed that with increasing concentration of the Ca/Sr cations (and consequently the decrease in the concentration of Pb cations), a reduction in the photodegradation process of the RhB can be observed. The kinetic constant was reduced from 1×10^{-2} min^{-1} to 1×10^{-3} min^{-1} in passing from PMO to CSMO, respectively. It was also found that the stability of the surfaces and their electronic properties are correlated with the presence of incomplete $[CaO_x]/[SrO_x]/[PbO_x]$ and distorted $[MoO_4]$ clusters as the reservoirs of holes and electrons, respectively, which act as the active sites in the photocatalytic activity.

This paper is a collaboration between the Laboratorio de Química Teórica y Computacional (QTC) and Laboratório de Síntese Química de Materiais (LSQM) of the Department of Materiais of the Federal University of Rio Grande do Norte (UFRN). The syntheses and experimental characterizations described in this work were performed by under the supervision of Prof. Mauricio R. D. Bomio and Prof. Fabiana V. Motta.

The $CaWO_4$ (CW) and $Ca_{1-x}WO_4:xEu^{3+}$ (CWE) samples were successfully synthesized by a simple co-precipitation method followed by microwave irradiation. XRD patterns of the samples showed the scheelite phase with tetragonal structure (space group $I4_{1a}$). DFT calculations were performed to analyze and decipher the geometry and electronic properties, thereby enabling a more accurate and direct comparison between theory and experiment for the CWE structure.

An analysis of electronic structures showed a direct electronic transition at the Γ-point in the Brillouin zone (figure 4.16). The CWE model had a lower band gap value (3.90 eV) when compared with the CW model (5.71 eV). This decrease of the band gap was due to the structural defect caused by the substitution of Ca^{2+} by Eu^{3+} cations, which involves the creation of new energy levels between the VB and CB. The FE-SEM was performed and the images of the CW and CWE samples showed the formation of microspheres and micro-dumbbells, with an average size of 4.05 ± 0.49 μm.

The PL emissions of the samples displayed that the pure CW has a broadband emission profile, characteristic of a multiphonic process, involving several intermediate energy states. The maximum emission of the CW sample was found in approximately 500 nm, in the cyan-green region, which were the result of internal charge transfers from the $[WO_4]$ clusters and oxygen vacancy (V_O) in the $[WO_4]$ and $[CaO_8]$ clusters. With the replacement of Ca^{2+} by Eu^{3+} cations, the appearance of specific transitions of Eu^{3+} was observed ($^5D_0 \rightarrow {}^7F_j$, j = 1, 2, 3, and 4), with maximum emission located at 596, 616, 659, and 704 nm, and these become more intense with the increased concentration of Eu^{3+} cations.

This paper is a collaboration between the Laboratorio de Química Teórica y Computacional (QTC) and the Centro de Desenvolvimento de Materiais Funcionais (CDMF), at the Universidade Federal de São Carlos (UFSCar). The syntheses and experimental characterizations described in this work were performed by Dr. Amanda Fernandes Gouveia under the supervision of Prof. Elson Longo.

4.3. Paper VII ($SnWO_4/SnMoO_4$)

This work is drafting nowadays, but we have some results. We performed an extensive structural optimization to identify the crystal structures and electronic properties of α- and β-$SnW_{1-x}Mo_xO_4$ (x=0, 0.25. 05, 0.75 and 1) solid solutions. The experimental data from the literature were used and compared with first-principles calculations on DFT, employing the hybrid functionals B3LYP and HSE06. The crystal lattice of α-$SnWO_4$ and α-$SnMoO_4$ present the orthorhombic structure (space group *Pnna*), and β-$SnMoO_4$ and β-$SnWO_4$ phases present a cubic structure (space group $P2_1/3$).

The computed cell parameters for cubic cell were found 7.131 Å and 7.073 Å, for β-$SnMoO_4$ and β-$SnWO_4$, respectively, and for α-$SnWO_4$ are a= 5.605 Å, b= 10.574 Å and c= 5.498 Å, while for α-$SnMoO_4$ are a= 5.597 Å, b= 10.717 Å and c= 5.423 Å. The parameters of solid solutions (α and β), in a 25%, 50% and 75% percentage of substitution of W by Mo atoms, were also calculated.

The results for the molybdates show that the beta phase is the most stable. However, for tungstates the most stable is the alpha phase in all range of studied volumes. The enthalpy variation values *(*ΔH*)* per formula unit with pressure can be observed for α-$SnMoO_4$ and β-$SnMoO_4$ phases for α-$SnWO_4$ and β-$SnWO_4$ *phases*. An analysis of these results suggests that a phase transition from β-$SnMoO_4$ to α-$SnMoO_4$ phase can be induced by applying pressure at approximately 2*GPa*, which corresponds to the intersection point of two curves. The bulk modulus (B_0) values were determined using the third-order *Birch−Murnaghan* EOS, obtaining B_0 values for β-$SnMoO_4$ and α-$SnMoO_4$ structures of 57.60 *GPa* and 41.93 *GPa*, respectively. For tungstates there is no indication of a phase transition but was determined the B_0 values of 69.47 *GPa* for α-$SnWO_4$ and 40.80 *GPa* for β-$SnWO_4$ phase.

The replacement of the W by Mo in solid solutions for 25%, 50% and 75% percentage implies an increase of the cell parameters, except for *b* parameter which tend to decrease for α solid solution. The exchange of *W* atoms by *Mo*, shows a phase transition at a percentage of substitution of the 57%. This result can be compared with the solid solution β-$SnW_{0.50}Mo_{0.50}O_4$, which presents an orthorhombic distortion as is noticeable by the cell parameters (a= 7.089 Å, b= 7.102 Å, c= 7.110 Å), providing evidence of a possible transition.

4.4. Book chapter

The design of new materials with tailored properties is the heart of materials research and nanotechnology and making them accessible for different applications. In this context, metal oxide semiconductors are an important area of research because almost all contemporary electronic technologies involve the use of these materials. Much research effort has focused on the synthesis of these inorganic semiconductors with controlled chemistry, size, shape, and composition driven by their intriguing, quantized behavior. They present themselves with marvelous morphology-dependent physical and chemical properties. They have attracted huge attention due to their unique material properties and their consequent theoretical and practical applications in chemistry, physics, materials science, biology, and medicine. This enormous progress has boosted new research due to their unanticipated novel properties, and consequently, a plethora of applications have stimulated further research efforts in this large field. To make possible the development of these technological applications, a complete understanding and rationalization, at the atomic level, of the physical and chemical, and thus the functions are of equal importance.

This chapter addresses these questions by presenting recent investigations performed by our research on different semiconductors. In particular, the metal oxides composed of Ag have been investigated by combining experimental studies and simulations based on first-principles calculations. The morphological modulations could be achieved by carefully analyzing the coordination environment surrounding the metals on the exposed surfaces at the morphology (defined here as the active sites where the electron transfer process involving O_2 and the bond making/-breaking processes associated to H_2O take place). From this analysis, an understanding of the mechanisms is obtained to explain the photocatalytic and biocide activity of semiconductors in advancing industrial and biomedical applications. Therefore, this strategy provided a gain of deep insight to modulate their geometric, electronic, and magnetic properties.

For this chapter of the book there was the collaboration of the QTC and the CDMF.

Prof. Dr. J. Andrés and Dr. Lourdes Gracia proposed the planning and helped in carrying out the calculations and in the final writing of these works. My participation has focused on carrying out the calculations in the QTC, analysis and discussion of the theoretical results, preparation of the figures and tables, the bibliographic review, and the writing.

5. Conclusions

In this Doctoral Thesis a set of published articles are collected in which the results are achieved through the joint use of experimental and theoretical works. By association of experimental and theoretical results, it was possible to deepen or understand the electronic and structures properties for seven (Ba_2SiO_4, high-$BaSiO_3$, $Ba_4Si_6O_{16}$, $Ba_5Si_8O_{21}$, $Ba_6Si_{10}O_{26}$, high-$BaSi_2O_5$ and sanbornite (low-$BaSi_2O_5$)) barium silicates structures and, crystalline, electronic, and morphological properties for semiconductors ($PbMoO_4$, In_2O_3, ZrO_2, $CaWO_4$ and $SnMoO_4$/$SnWO_4$). The main conclusions can be summarized as follows:

(i) Both Raman results and DFT-based calculations highlight that the stretching modes increase in frequency with increasing the number of BO atoms. Moreover, we may now refine 'the Q^n bands' as they are not related to the entire tetrahedral site but dominantly related to specific Si-O vibrations. While in the hetero-connected phases there are always extra vibrational modes related to the many Si-O bonds in these structures, which cause peaks to overlap, the most intense features correspond to the main structural units. Our results display clear structural trends, permitting future studies linking Raman frequencies to the specific distortions present for a given group of the Q^n species. Moreover, we hope this aids in further distinction among the major mineral groups. **(ii)** In_2O_3 and La^{3+}-doped In_2O_3 nanostructures were synthesized by a microwave-assisted hydrothermal method followed by microwave calcination. The Rietveld refinement provided information about the effect of the doping process of La^{3+} cations in the lattice parameters of the In_2O_3 matrix and determined the proportion of bcc- and rh-In_2O_3 polymorphs obtained in La^{3+}-doped In_2O_3 indicating the formation of the bcc-In_2O_3 structure for the undoped sample and a mixture of bcc- and rh-In_2O_3 structures for the La^{3+}-doped sample. The TEM images showed that the doping of La^{3+} induced the formation of cubelike particles with a larger size when compared to the undoped In_2O_3. Theoretical results indicated that for a La^{3+} substitution of 12.5%, the rh-In_2O_3 phase is more stable than the bcc-In_2O_3 phase, and the structural transformation was attributed to the changes in the In–O bond lengths, O–In–O bond angles, and the electronic redistribution induced by the La^{3+}-doping process. The analysis of PL intensity showed that a decreased from undoped In_2O_3 to La^{3+}-doped In_2O_3 nanostructures, although an increase could be observed in the blue emission for the doped sample, indicating that doping process can alter the surface, generating trap states that should reduce the

electron/hole recombination rates, improving the charge transfer processes, and consequently leading to a more efficient electrochemical performance.

(iii) The surface electronic properties of PMO and $Pb_{1-2x}Ca_xSr_xMoO_4$ (x = 0.1, 0.2, 0.3, 0.4 and 0.5) solid solutions (prepared for the first time by a co-precipitation method) showed that the (011) and (110) surfaces, that appear in the experimental FE-SEM images, enhanced photocatalytic activity. In particular, the specific local coordination of the Pb/Ca/Sr and Mo cations in the exposed surfaces can be correlated with the reservoirs of holes and electrons, respectively, which act as the active sites in the photocatalytic activity. The analyzed results found that the PL emission spectra of the samples showed predominant emission in the green-orange region, with predominantly shallow type defects for the most photoactive samples. **(iv)** The effect of the Tb^{3+} doping process on the luminescence performance and phase transition (cubic vs tetragonal) were investigated for ZrO_2:xTb^{3+} (x = 1, 2, 4 and 8 mol%) samples and an enhanced green emission was observed as Tb^{3+} was introduced to the ZrO_2 structure. Color purity was tunable from the addition of Tb^{3+}, reaching 80.5% for the ZrO_2:8 mol% Tb^{3+} sample, and the optimum concentration for maximum PL intensity was 2 mol% Tb^{3+}, indicating that the that this material can be a promising new green phosphor applicable to solid state lighting devices. **(v)** A deeper understanding of the effects caused by the Eu^{3+} cations in the $CaWO_4$ electronic structure, experimentally observed, were achieved by means of first-principles calculations. These findings allowed to discover a luminescent material in which by varying the Eu^{3+} cations concentration, the color emissions could be modulated, paving the way for the further design of $Ca_{1-x}WO_4$:xEu^{3+}-based materials for various applications as red-blue phosphors in different kinds of display devices.

6. Papers published, sent for publication and in the drafting phase

Spectrochimica Acta Part A: Molecular and Biomolecular Spectroscopy 248 (2021) 119130

Contents lists available at ScienceDirect

Spectrochimica Acta Part A: Molecular and Biomolecular Spectroscopy

journal homepage: www.elsevier.com/locate/saa

Identifying and explaining vibrational modes of sanbornite (low-$BaSi_2O_5$) and $Ba_5Si_8O_{21}$: A joint experimental and theoretical study

Eduardo O. Gomes [a], Benjamin J.A. Moulton [b,c], Thiago R. Cunha [b,c], Lourdes Gracia [a,1], Paulo S. Pizani [b,c], Juan Andrés [a,*]

[a] Departament de Química Física i Analítica, Universitat Jaume I, 12071 Castelló de la Plana, Spain
[b] CERTEV – Center for Research, Technology, and Education in Vitreous Materials, Department of Materials Engineering, Federal University of São Carlos, 13565 - 905 São Carlos-SP, Brazil[2]
[c] Universidade Federal de São Carlos, Departamento de Física, Rod. Washington Luis, Km 235, 13565-905 São Carlos, SP, Brazil

HIGHLIGHTS

- Experimental and theoretical vibrational modes of sanbornite (low-$BaSi_2O_5$) and $Ba_5Si_8O_{21}$.
- Temperature dependence of the Raman modes.
- The experimental results are correlated with first-principle calculations at DFT level.

GRAPHICAL ABSTRACT

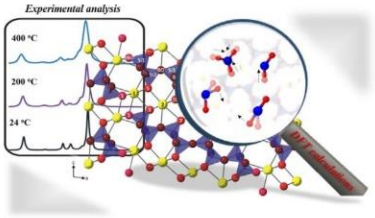

ARTICLE INFO

Article history:
Received 6 September 2020
Received in revised form 13 October 2020
Accepted 22 October 2020
Available online 24 November 2020

Keywords:
Barium silicates
Sanbornite
Low-$BaSi_2O_5$
$Ba_5Si_8O_{21}$
Raman spectroscopy
Rietveld refinement
DFT calculations

ABSTRACT

We report here the analysis of vibrational properties of the sanbornite (low-$BaSi_2O_5$) and $Ba_5Si_8O_{21}$ using theoretical and experimental approaches, as well as results of high temperature experiments up to 1100–1150 °C. The crystal parameters derived from Rietveld refinement and calculations show excellent agreement, within 4%, while the absolute mean difference between the theoretical and experimental results for the IR and Raman vibrational frequencies was <6 cm^{-1}. The temperature-dependent Raman study renders that both sanbornite and $Ba_5Si_8O_{21}$ display specific Ba and Si sites and their Ba—O and Si—O bonds. In the case of the stretching modes assigned to specific Si sites, the frequency dependence on the Si—O bond length exhibited very strong correlations. Both phases showed that for a change of 0.01 Å, the vibrational mode shifted 10 ± 2 cm^{-1}. These results are promising for using Raman spectroscopy to track *in situ* reactions under a wide variety of conditions, especially during crystallization.

1. Introduction

Barium silicates are extensively studied for their excellent material properties and device performance in a range of important technological applications [1–7] Sanbornite (low-$BaSi_2O_5$) is a uncommon mineral found in Big Creek, California (USA), and its hydrous analogue bigcreekite ($BaSi_2O_5{\cdot}4H_2O$) are rare examples where Ba is concentrated in a silicate phase [8–10]. On the other hand, $Ba_5Si_8O_{21}$ is a synthetic phase, displaying the rare characteristic of being an anhydrous phase containing ribbons (quadruple *zweier* chains) of silica tetrahedra surrounded by Ba cations which stabilize the stretched chains. Each ribbon is composed of two types of SiO_4 units that can be distinguished by the number of inter-tetrahedral linkages they contain. These can be

* Corresponding author.
E-mail address: andres@qfa.uji.es (J. Andrés).
[1] Permanent address: Department of Physical Chemistry, University of Valencia (UV), 46100 Burjassot, Spain.
[2] www.certev.ufscar.br.

https://doi.org/10.1016/j.saa.2020.119130
1386-1425/

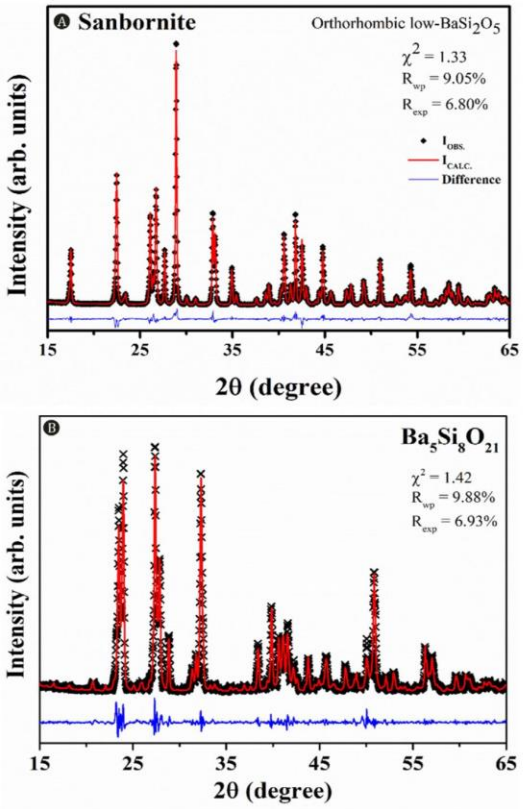

Fig. 1. Rietveld refinement of diffraction patterns for A) sanbornite and B) $Ba_5Si_8O_{21}$.

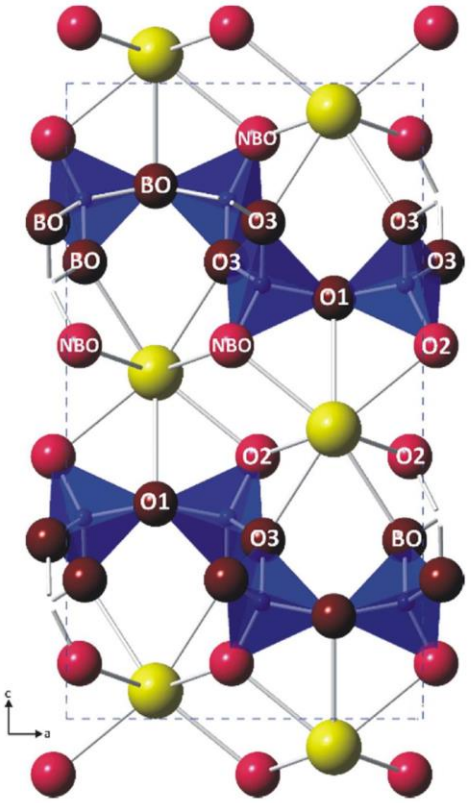

Fig. 2. A schematic representation of the sanbornite crystal structure. Ba are large yellow spheres (colour online). Blue Si-centered tetrahedra show dark red BO and lighter pink NBO. Site labels refer to those in Table 2. The directions defined by the a and c lattice parameters are drawn.

described as Q^n species where n is the number oxygens bonded to adjacent Si cations. In $Ba_5Si_8O_{21}$, the tetrahedra along the edges of the ribbons are only bonded to two adjacent tetrahedra, Q^2 species, whereas the tetrahedra which form the interior of the ribbon are connected to three adjacent tetrahedra, Q^3 species. Ultimately, $Ba_5Si_8O_{21}$ is distinct from sanbornite in the presence of the Q^2 species but comparable in that ribbon and sheets are dominantly composed of Q^3 species. Both structures have been discussed in considerable detail by Liebau and colleagues [11–14].

Sanbornite and $Ba_5Si_8O_{21}$ have received considerable attention in recent years due to their desirable formation as acicular aggregates, leading to a considerable strengthening of the glass-ceramics produced and due to their high thermal expansion, which has led to their wide investigation for solid-oxide fuel cell sealant materials [5,15]. In particular, sanbornite-based glasses display volume nucleation and thus have long been of interest to researchers looking into the fundamental process of crystallization [16–22]. When doped with rare-earth elements, these materials can be used as light emitting diode materials [23,24]. Although interesting behaviors have been shown, there is a lack of clarity regarding the origin and significance of the vibrational modes and their transitions during crystallization processes [21,25–28].

Vibrational spectroscopy is one of the most versatile techniques used in the investigation of the structure of oxides and oxide glasses. For the low symmetry materials, there may be several

Table 1
Crystal structural parameters of barium silicate phases in this study.

Phase	Formula	Space Group	Density[1] (g/cm³)		Cell Volume	a	b	c	β	Reference
			theoretical	experimental	(Å³)	(Å)	(Å)	(Å)	(degrees)	
Sanbornite low-$BaSi_2O_5$	$BaSi_2O_5$	Pmcn	3.77	3.70	481.25	7.688	4.629	13.523	90.00	[12]
					481.78	7.689	4.632	13.528	90.00	[15]
					483.02	7.695	4.636	13.538	90.00	This study - Rietveld
			3.632		500.84	7.778	4.684	13.744	90.00	This study - DFT
B5S8	$Ba_5Si_8O_{21}$	C2/c	3.925	3.93	2110.20	32.675	4.695	13.894	98.10	[11]
					2120.6	32.739	4.702	13.917	98.17	[15]
					2121.6	32.756	4.705	13.909	98.18	This study - Rietveld
			3.771		2200.3	33.284	4.738	14.097	98.29	This study - DFT

[1] Reported in [13].

bands calculated to lie near the position of a single observed feature. In such cases it is impossible to make an unambiguous assignment if the calculated intensities are so model-dependent that they cannot be used as an aid. Quantum-chemical computations predicting frequencies and spectral intensities are essential to complement the interpretation of experimental spectra, particularly for complex materials where the high density of states results in spectral complexity [26].

Despite the long history of using Raman and infrared spectroscopy, as well as the employ *ab initio* quantum mechanical methods [29,30], as appropriate tools to investigate the vibrational behavior and related properties (e.g. heat capacity), few crystalline phases of silicates have had detailed determination of their vibrational modes. Early studies have been subject to the limitations and *ad hoc* assumption used to determine the dominant spectral features [29].

The temperature effect on the phonon properties of both sanbornite (low-$BaSi_2O_5$) and $Ba_5Si_8O_{21}$ is unknown yet, and it is of great interest to study their vibrational properties at high-temperature. In this context, this work investigates the vibrational modes of these systems related with the phases presented in the BaO—SiO_2 system. The experimental results are correlated with first-principle calculations, at the density functional theory (DFT) level, which allows not only the classification of the vibrational modes up to 1150 °C, but also to obtain information and structural changes undergone by these materials. The application of the described strategy allowed us to reliably describe the low-$BaSi_2O_5$ and $Ba_5Si_8O_{21}$ materials.

2. Experimental and theoretical procedures

2.1. Sample preparation

High-purity reagents, $BaCO_3$ and SiO_2 (Sigma-Aldrich, >99.9%), where used to synthesize both low-$BaSi_2O_5$ and $Ba_5Si_8O_{21}$. Due to the impurities resulting from the stable phases differing by only ~3% BaO, the solid-state reaction procedure was followed. This entails grinding the powders in a highly vibrating mill (to ensure fine and evenly distributed grain sizes) and compression into tablets and then heat-treated for 30 h at 1340 and 1410 °C for low-$BaSi_2O_5$ and $Ba_5Si_8O_{21}$, respectively. Prior to heat treatment the polycrystalline tablets were calcined for 1 h at 1000 °C. Both phases have been confirmed by X-ray diffraction (XRD) measurements using Cu K_α radiation operating at 40 kV and a current of 20 mA in continuous scanning mode (0.5° min^{-1}) with a 2θ step of 0.02° between $10° \leq 2\theta \leq 80°$ on a Rigaku Ultima IV diffractometer. Rietveld refinement of the resulting patterns were done using the GSAS program [32,33]. A LabRAM HR800 was used to measure the Raman spectra operating a 532 nm diode laser of ~20 mW power on the sample. Spectra where taken using a 100x visible objective, a 100 μm pinhole, an 1800 gr/mm grating resulting in a frequency and lateral spatial resolution of ~0.5 cm^{-1} and <2 μm, respectively. Spectra are the average of 12 scans of a dwell time of five seconds. Spectra have been intensity normalized to the high frequency stretching region, although raw spectra have roughly equal intensity. Measured Raman active modes were curve fit using Lorentzian lineshapes to determine individual peak parameters. High temperature measurements were carried out on 40–60 mg polycrystalline monolithic chips heated using a Linkam stage and a 50× SLWD objective. Slightly longer spectra (10 s dwell time and 16 spectra were averaged) were taken as the furnace window cuts the measured intensity to roughly a third of ambient condition spectra.

2.2. Computational methods

DFT calculations of the lattice parameters and vibrational modes were done using Becke's three-parameter hybrid non-local exchange functional, combined with a Lee-Yang-Parr

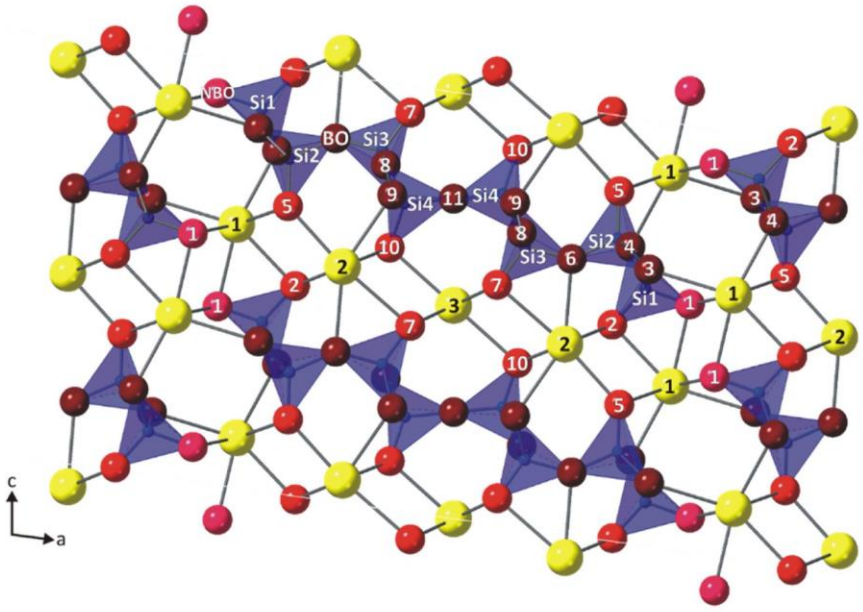

Fig. 3. A schematic representation of the unit cell showing structural features of $Ba_5Si_8O_{21}$. Site labels refer to those in Table 3 and colors follow those in Fig. 2. The directions defined by the a and c lattice parameters are drawn.

gradient-corrected correlation functional (B3LYP), implemented in the CRYSTAL17 package [34]. The atoms were centered and described using pseudopotential databases; [35], 88-31G* [36] and 8-411d11G [37] (all-electron) for Ba, Si and O, respectively. Regarding the diagonalization of the density matrix, the reciprocal space net was described by a shrinking factor of 4, generated according to the Monkhorst–Pack scheme. The accuracy of the evaluation of the Coulomb and exchange series was controlled by five thresholds, whose adopted values were 10^{-7}, 10^{-7}, 10^{-7}, 10^{-7}, and 10^{-14}. The vibrational frequencies calculation was performed at the Γ point within the harmonic approximation, and the dynamic matrix was computed by the numerical evaluation of the first derivative of analytical atomic gradients.

3. Results and discussion

3.1. XRD analysis

The XRD patterns of the synthesized samples are shown in Fig. 1. The crystal structure parameters are in agreement with the literature results, Table 1. The Rietveld refinement results are comparable to published results having a goodness-of-fit (χ^2) close to unity and R values below 10% [38]. The cell volumes for the measured and calculated structures of low-$BaSi_2O_5$ and $Ba_5Si_8O_{21}$ are less than 1% and 4% of the published values [11,12,15], respectively. Therefore, the simulations show a very good agreement with the experimental results of the measured structures.

Table 2
Experimental and calculated vibrational modes in sanbornite.

Mode	Infrared modes			Raman modes						
	Frequency cm^{-1}	Symmetry	Origin	Frequency	FWHM	Relative Intensity (%)	Frequency	Symmetry	Δυ	Origin[3]
υ_1	60.0	A_u	lattice	55.0	1.2	11	59.8	A_g	−4.8	O2-Ba
υ_2	66.1	B_{2u}	O2-Ba	70.1	3.5	14	71.5	B_{2g}	−1.4	Ba-O2-Si
υ_3	75.9	A_u	Ba-O2-Si	71.9	2.2	34	78.0	B_{3g}	−6.1	Ba-O2
υ_4				93.0	2.2	14	78.3	B_{1g}	14.7	SiO4
υ_5				98.6	1.8	1	99.5	A_g	−0.9	Ba-O2
υ_6	104.4	B_{1u}	Ba-O2	103.3	2.4	4	102.3	B_{3g}	1.0	lattice
υ_7							110.1	A_g		Ba-O2-Si
υ_8	120.3	B_{3u}	lattice				116,4	B_{2g}		Ba-O2
υ_9	126.3	B_{1u}	Si-O2	118.2	3.0	23	118.5	B_{1g}	−0.3	lattice
υ_{10}	134.8	B_{2u}	O1-Si-O2	122.0	6.7	6	125.1	B_{3g}	−3.1	Si-O2
υ_{11}	135.7	B_{3u}	lattice				126,8	A_g		O1-Si-O3
υ_{12}	137.5	B_{1u}	O1-Si-O3	148.5	6.0	3	159.6	B_{2g}	−11.1	Ba-O2
υ_{13}	182.5	B_{2u}	lattice	168.8	7.4	2	182.7	B_{3g}	−13.9	Si-O2
υ_{14}	198.7	A_u	Ba-O2	191.5	7.9	16	203.0	B_{1g}	−11.5	Ba-O2
υ_{15}	209.3	A_u	Ba-O2	224.0	10.4	19	216.9	A_g	7.1	Si-O3
υ_{16}	212.8	B_{1u}	lattice	247.4	6.0	6	236.3	B_{1g}	11.1	lattice
υ_{17}	253.8	B_{2u}	Ba-O2	267.4	7.2	5	259.9	B_{3g}	7.5	lattice
υ_{18}	259.3	B_{3u}	lattice				278.0	B_{2g}		Ba-O2,3-Si
υ_{19}	294.6	B_{1u}	Si-O2	292.3	12.6	5	299.3	A_g	−7.0	lattice
υ_{20}	312.8	B_{2u}	Si-O1-Si	315.7	5.0	11	322.2	B_{3g}	−6.5	Ba-O2
υ_{21}	325.5	B_{3u}	lattice	332.6	3.8	17	330.6	B_{1g}	2.0	O3-Si-O1
υ_{22}	327.6	A_u	O3-Si-O1	341.8	4.6	11	342.2	B_{2g}	−0.4	lattice
υ_{23}	372.0	B_{1u}	Ba-O2				355.3	A_g		Ba-O2
υ_{24}	389.1	A_u	O2-Si-O3				391.9	B_{3g}		lattice
υ_{25}	401.7	B_{2u}	lattice	386.1	5.2	3	392.9	B_{1g}	−6.8	O2-Si-O3
υ_{26}	438.9	B_{2u}	O1-Si-O2	431.5	6.3	0	438.6	B_{3g}	−7.1	O1-Si-O2
υ_{27}	453.9	B_{3u}	O3-Si-O1	453.0	3.2	1	457.0	B_{2g}	−4.1	SiO_4
υ_{28}	468.4	B_{1u}	O1-Si-O3	459.0	6.1	2	464.6	A_g	−5.6	O1-Si-O3
υ_{29}	473.1	A_u	O2,3-Si-O3	476.2	2.7	8	479.3	B_{1g}	−3.1	O2,3-Si-O3
υ_{30}	486.3	B_{1u}	O1-Si-O3	492.8	2.8	1	488.2	A_g	4.6	O1-Si-O3
υ_{31}	507.5	B_{3u}	O3-Si-O2				508.4	B_{2g}		O3-Si-O2
υ_{32}	535.6	B_{1u}	O3-Si-O2	535.5	8.2	66	534.5	A_g	1.0	O3-Si-O2
υ_{33}	538.7	B_{2u}	SiO_4				550.0	B_{3g}		SiO_4
υ_{34}	594.1	A_u	O3-Si-O2	597.2	5.9	7	594.4	B_{1g}	2.8	O3-Si-O2
υ_{35}	693.6	B_{2u}	Si-O1				703.8	B_{3g}		SiO_4
υ_{36}	758.8	B_{3u}	Si-O3				759.7	B_{2g}		O3-Si
υ_{37}	773.1	B_{1u}	SiO_4	756.5	9.4	1	760.6	A_g	4.1	SiO_4
υ_{38}	803.5	B_{2u}	Si-O3-Si				805.9	B_{3g}		Si-O3-Si
υ_{39}	971.1	B_{3u}	SiO_4				973.2	B_{1g}		O2,3-Si
υ_{40}	972.4	A_u	O3-Si-O2				973.6	B_{2g}		SiO_4
υ_{41}	980.5	B_{1u}	O3-Si-O2	986.6	9.6	2	980.4	A_g	6.2	O3-Si-O2
υ_{42}	1001.4	B_{3u}	O1-Si	1000.3	5.2	2	1004.1	B_{2g}	−3.7	O1-Si
υ_{43}	1035.6	A_u	SiO_4	1037.4	3.8	1	1046.1	B_{3g}	−8.7	O2,3-Si
υ_{44}	1047.7	B_{2u}	O2-Si				1053.4	B_{1g}		O2-Si
υ_{45}	1084.3	A_u	O1-Si	1077.9	4.5	100	1084.5	B_{1g}	−6.6	O1-Si
υ_{46}	1095.1	B_{3u}	SiO_4	1100.1	4.9	1	1096.3	A_g	3.8	O2-Si
υ_{47}	1095.3	B_{2u}	O3-Si				1113.2	B_{2g}		O1,2-Si
υ_{48}	1100.6	B_{1u}	O2-Si	1172.9	10.3	1	1193.0	B_{3g}	−20.1	O3-Si
			Mean A_g FWHM[1]	7.8				$\|\Delta\nu\|$[2]	5.8	
			Mean B_g FWHM[1]	5.3				max. Δυ	20.1	

[1] only modes contributing > 1% to the area were considered.
[2] $|\Delta\nu|$ is the absolute mean difference between theoretical and experimental frequency.
[3] Note O1 & O3 are BOs whereas O2 is a NBO (Fig. 2).

Table 3
Experimental and theoretical vibrational modes in $Ba_5Si_8O_{21}$*

Mode	Infrared modes			Raman Modes							
	Frequency cm^{-1}	Symmetry	Origin[2]	Frequency cm^{-1}	FWHM cm^{-1}	Relative Intensity (%)	Area %	Frequency cm^{-1}	Symmetry	Δυ	Origin[1]
υ_{-1}	−69.5	B_u	O10-Si4					−53.7	B_g		O10-Si4
υ_1	45.9	A_u	O2-Ba2-O10	51.8	3.2	5.4	<1	54.5	A_g	2.7	lattice
υ_2	55.5	B_u	Ba2-O1-Si1	57.1	1.8	5.8	<1	55.7	B_g	−1.4	O10-Ba2-O2,O6
υ_3	62.5	A_u	O5-Ba2-O7	59.9	2.1	4.1	<1	60.1	A_g	0.2	O6-Ba2-O10
υ_4	64.7	B_u	O2-Ba2-O5,6	65.4	2.9	19.2	1.2	73.0	B_g	7.6	Ba2-O6-Si3
υ_5	68.3	A_u	O4-Ba1-O2								
υ_6	70.2	B_u	O10-Ba3-O7	71.6	0.8	1.8	≪1	74.2	A_g	2.6	lattice
υ_7	73.2	B_u	O1-Ba1-O4,5								
υ_8	75.3	A_u	Ba2	76.8	4.2	14.8	1.3	80.2	B_g	3.4	O5-Ba1-Si1/O1
υ_9	81.4	A_u	Ba3-O10-Si4	81.8	4.0	23.0	2.0	85.9	A_g	4.1	lattice
υ_{10}	87.8	B_u	Ba3-O7-Si3	85.3	4.1	9.0	<1	87.7	B_g	2.4	lattice
υ_{11}	88.6	A_u	O2-Ba1-O4-Ba2-O10-Ba3	88.9	5.1	15.0	1.7	93.4	A_g	4.5	complex
υ_{12}	99.4	B_u	Ba3-O7	92.6	4.8	22.6	2.4	98.0	B_g	5.4	O1-Ba1-O2,5
υ_{13}	101.1	A_u	O2,5-Ba1-O1	98.3	5.6	8.5	1.0	101.7	B_g	3.4	Ba2-various O
υ_{14}	104.4	A_u	Ba lattice	102.5	3.9	18.6	1.6	101.8	A_g	−0.6	Si1-O2-Ba1,2-O10
υ_{15}	108.0	B_u	Ba1,3-various O-Si1	105.3	6.5	29.6	4.2	105.8	B_g	0.5	O1,4-Ba1-O2/Si1
υ_{16}	112.4	B_u	Ba2-O10-Ba3					106.0	A_g		Ba1-Si1 lattice
υ_{17}	114.0	B_u	Ba3-O7	114.4	8.2	7.6	1.4	115.5	B_g	1.1	Ba2-O10-Ba3
υ_{18}	115.1	A_u	Ba3-O7,10 & Si4-O11					117.2	A_g		O4-Ba1-O1
υ_{19}	118.6	A_u	O4-Ba1-O1	122.8	1.0	0.9	≪1	122.9	A_g	0.1	Si4-O11
υ_{20}	122.3	B_u	O10-Ba2-O2 & O10-Ba3-O7					133.8	B_g		Ba2-O10-Si4 & O7-Ba3-O10
υ_{21}	125.1	A_u	O5-Ba2-O10 & Si4-O11	132.8	6.0	9.2	1.2	134.0	A_g	1.2	O10-Ba2-O6
υ_{22}	130.1	A_u	O7-Ba3 & O10-Ba3	140.6	10.4	2.2	<1	141.6	B_g	1.0	O6-Ba2-O10-Ba3
υ_{23}	138.3	B_u	O7,10-Ba3 &O10-Ba3					143.6	A_g		lattice
υ_{24}	139.6	A_u	lattice	149.2	4.1	2.6	<1	154.4	B_g	5.2	lattice
υ_{25}	155.9	B_u	lattice	164.6	7.3	4.5	<1	160.9	A_g	−3.7	O1-Ba1-O2 & O5-Ba2
υ_{26}	166.4	A_u	lattice	168.6	9.2	8.7	1.8	167.7	B_g	−0.9	O4-Ba1-O2
υ_{27}	166.6	B_u	O4-Ba1-O2	186.0	10.5	6.7	1.6	176,8	A_g	−9.2	O1,5-Ba1,2
υ_{28}	188.5	A_u	Ba1,2 lattice	196.0	11.9	2.0	<1	196.2	B_g	0.2	lattice
υ_{29}	196.0	B_u	O5,6-Ba1,2-O1,2,6	209.1	8.6	5.6	1.0	208.1	A_g	−0.9	O1,4-Ba1,2-O1,2,5
υ_{30}	204.4	A_u	O4-B1-O2 & O4-Si2-O6					209.2	B_g		O1-Ba1-O4
υ_{31}	212.8	B_u	O2-Ba1-O1					217.7	B_g		O2-Ba1,2-O1,5
υ_{32}	217.7	B_u	O2-Ba1,2-O1,5					226.7	A_g		O1-Ba1 & O3-Si1-O4
υ_{33}	221.1	A_u	O2-Ba1 & O2-Ba2-O5					227.7	B_g		lattice
υ_{34}	229.4	A_u	lattice	241.5	12.8	29.9	8.4	233.1	A_g	−8.4	O2-Ba1 & O2,6-Ba2-O2,5
υ_{35}	233.7	B_u	lattice					250,8	A_g		O5-Ba1,2-O1,2
υ_{36}	243.2	B_u	lattice	257.7	10.0	14.6	3.2	255.1	B_g	−2.6	O5-Ba1,2-O1,10
υ_{37}	259.6	A_u	lattice					264.7	A_g		lattice
υ_{38}	266.6	B_u	lattice	273.6	9.8	16.3	3.5	274.5	B_g	0,9	lattice
υ_{39}	269.5	A_u	lattice	283.7	9.0	36.7	7.2	280.7	A_g	−3.0	lattice
υ_{40}	279.3	B_u	O7,10-Ba2,3-O2,7	297.8	8.3	5.5	1.0	299.6	B_g	1.9	O10-Ba2,3-O2,7
υ_{41}	290.8	A_u	lattice	306.6	9.7	8.3	1.8	300.4	A_g	−6.2	lattice
υ_{42}	296.4	A_u	O10-Ba2-O2 & Ba3-O7,10	316.3	8.9	8.6	1.7	310.6	B_g	−5.6	O2,5-Ba1,2-O1,5,10
υ_{43}	303.2	B_u	O1-Ba1,2-O1,5	324.8	5.8	2.9	<1	322.1	A_g	−2.7	Ba1,3-O1,5,7
υ_{44}	314.5	A_u	O7-Ba3-O10					322.2	B_g		Ba3-Si3-O7,9,10
υ_{45}	321.7	B_u	O9-Si3,4-O6,11					332.5	B_g		O1-Ba1-O5-Si1
υ_{46}	324.3	A_u	Ba2,3-O2,7,10					333.9	A_g		lattice
υ_{47}	330.4	B_u	all Ba rattle					350.0	A_g		lattice
υ_{48}	338.1	A_u	Ba2,3-O10-Si4	363.1	8.2	3.0	<1	361.7	A_g	−1.4	lattice
υ_{49}	359.5	A_u	lattice	375.2	8.4	3.9	<1	369.2	B_g	−6.0	lattice
υ_{50}	372.3	B_u	lattice					384.7	B_g		O11-Si4-O10
υ_{51}	381.1	A_u	O8-Si3-O7 & Si4-O11	393.7	9.8	2.1	<1	386.2	A_g	−7.5	Si4-O11
υ_{52}	383.1	B_u	O11-Si4-O10					400.1	B_g		O5-Si2-O6
υ_{53}	393.8	B_u	O5-Si2-O6	409.2	6.3	3.2	<1	406.8	A_g	−2.4	lattice
υ_{54}	413.5	A_u	O5-Si2-O4	430.4	5.4	4.5	<1	421.5	B_g	−8.9	O10-Si4-O11
υ_{55}	420.6	B_u	O10-Si4-O11								
υ_{56}	433.5	A_u	lattice	439.0	4.6	4.9	<1	444.9	A_g	5.9	O1-Si1-O2
υ_{57}	457.2	B_u	Si1-O1-Ba1	445.0	5.6	4.5	<1	451.1	B_g	6.1	O1-Si1-O2 & O10-Si4-O8
υ_{58}	463.9	A_u	Si4-O10-Ba2	449.4	6.3	3.9	<1	465.4	B_g	16.0	O4-Si1-O1
υ_{59}	464.0	B_u	O4-Si1-O1	468.6	4.6	10.7	1.1	467.4	A_g	−1.2	Si4-O10-Ba2

(*continued on next page*)

Table 3 (*continued*)

Mode	Infrared modes			Raman Modes							
	Frequency cm^{-1}	Symmetry	Origin[2]	Frequency cm^{-1}	FWHM cm^{-1}	Relative Intensity (%)	Area %	Frequency cm^{-1}	Symmetry	Δυ	Origin[1]
υ_{60}	481.4	B_u	O11-Si4-O8	471.0	6.2	5.9	<1	484.2	A_g	13.2	O1-Si1-O4 & O3-Si2-O5
υ_{61}	485.8	A_u	O3-Si2-O5	480.9	5.6	13.6	1.7	484.7	B_g	3.8	Si3-O8-Si4 & O11-Si4-O8
υ_{62}	490.8	A_u	O1-Si1-O4	501.8	8.1	21.7	3.9	488.7	A_g	−13.1	Si3-O6-Ba2
υ_{63}	498.4	B_u	O2-Si1-O4 & Si3-O6-Ba2	506.7	4.4	10.1	1.0	494.9	B_g	−11.8	O2-Si1-O2
υ_{64}	511.6	A_u	Si4-O8-Si3	516.7	3.8	2.9	<1	512.9	A_g	−3.8	Si4-O8-Si3
υ_{65}	522.7	B_u	Si1-O3-Si2 & O9-Si3-O6	523.6	4.7	14.5	1.5	523.9	B_g	0.2	Si1-O3-Si2 & O8-Si3-O9
υ_{66}	532.5	A_u	O8-Si4-O10	535.1	5.3	87.7	12.6	536.1	A_g	1.0	O7,9-Si3,4
υ_{67}	539.9	B_u	Si3,4-O8,9					545.0	B_g		Si3-O9-Si4
υ_{68}	540.7	A_u	Si3-O9-Si4	545.7	5.3	50.0	5.8	545.5	A_g	−0.2	O7-Si2-O5 & O9-Si3-O8
υ_{69}	555.4	B_u	O3-Si2-O4					555.6	B_g		O3,4-Si2-O5,6
υ_{70}	562.0	A_u	O4-Si1-Ba1 & O3-Si2-O4					564.5	A_g		O4-Si1-Ba1
υ_{71}	589.3	B_u	O4-Si1-O3	601.9	6.7	23.8	3.5	587.7	B_g	−14.3	O4-Si1-O3
υ_{72}	633.3	B_u	Si rattle	613.9	7.3	22.0	3.5	626.4	A_g	12.5	Si1-O4-Si2
υ_{73}	634.5	A_u	Si1-O4-Si2	632.1	6.5	3.1	<1	639.2	B_g	7.1	Si1-O4-Si2
υ_{74}	717.1	A_u	O8,10-Si4-O11					717.6	A_g		O8,10-Si4-O11
υ_{75}	735.6	B_u	Si1-O3,6-Si2					734.5	B_g		Si1-O3,6-Si2
υ_{76}	738.1	A_u	O3-Si1-Ba1	736.1	6.7	1.2	<1	739.6	A_g	3.5	O3-Si1-Ba1
υ_{77}	753.2	B_u	O4-Si2-O5	749.2	10.2	19.7	4.4	757.4	A_g	8.2	Si2-O4-Ba1 & O6-Si2-O3
υ_{78}	759.0	A_u	O4-Si2-O5					759.4	B_g		Si2-O4-Si1
υ_{79}	770.6	B_u	Si3-O8,9-Si4					774.2	A_g		Si3-O8,9-Si4
υ_{80}	781.6	A_u	Si3-O8,9-Si4					779.4	B_g		Si3-O8,9-Si4
υ_{81}	924.3	B_u	O3,4-Si2					925.3	B_g		O3,4-Si2
υ_{82}	924.4	A_u	O3,4-Si2	920.7	4.8	15.5	1.6	926.0	A_g	5.3	O3,4-Si2
υ_{83}	937.0	B_u	O2-Si1	924.0	7.2	32.2	5.1	934.1	A_g	10.1	O1,2-Si1
υ_{84}	941.9	A_u	O1-Si1					952.8	B_g		O1,2-Si1
υ_{85}	965.5	B_u	Si3-O9-Si4 & O9-Si4					966.2	B_g		Si3-O9-Si4 & O9-Si4
υ_{86}	966.5	A_u	Si3-O9-Si4 & O9-Si4	969.7	12.4	2.1	<1	967.2	A_g	−2.5	Si3-O9-Si4 & O9-Si4
υ_{87}	978.4	B_u	O8-Si3-O6, O8-Si4-O10	987.5	2.9	0.4	≪1	986.0	B_g	−1.4	O8-Si3-O6
υ_{88}	997.1	A_u	O4-Si1 & O7-Si3	1004,0	7.3	3.3	<1	1011.5	B_g	7.5	O6-Si2 & O10-Si4
υ_{89}	1008.4	B_u	O6-Si2 & O10-Si4	1011.3	4.7	12.8	1.3	1012.6	A_g	1.2	O1-Si1-O2
υ_{90}	1016.3	A_u	O2-Si1	1024.4	3.8	10.8	<1	1018.2	A_g	−6.1	O3,4-Si1-Ba1 & O7-Si3
υ_{91}	1023.7	A_u	O6-Si2 & O10-Si4	1027.6	8.6	13.6	2.6	1021.8	B_g	−5.8	O1,O2-Si1
υ_{92}	1028.4	B_u	O2-Si1					1042,8	A_g		O1-Si1
υ_{93}	1046.5	B_u	O1-Si1 & O7-Si3	1053.5	7.4	7.4	1.2	1045.5	B_g	−8.0	Si2-O6-Ba2 & O6,7-Si3
υ_{94}	1056.9	B_u	O6,7-Si3	1066.8	5.5	100	12.1	1064.7	B_g	−2.1	O7-Si3
υ_{95}	1064.5	A_u	O6-Si3	1069.6	5.7	44.1	5.5	1065.1	A_g	−4.5	O5-Si2
υ_{96}	1075.8	B_u	O3,5,-Si2 & O8-Si4	1075.3	4.5	63.7	6.3	1078.6	A_g	3.3	O8,10-Si4
υ_{97}	1078.0	A_u	O3,5-Si2 & O8-Si4					1085.6	A_g		O7-Si2
υ_{98}	1086.0	A_u	O7-Si3	1094.1	3.3	0.8	≪1	1107.6	B_g	13.5	Si1-O4-Si2
υ_{99}	1089.0	B_u	O5-Si2-O6	1099.4	5.2	1.2	≪1	1108.8	A_g	9.4	Si2-O6-Si3
υ_{100}	1129.5	A_u	Si4-O5,8	1130.4	8.4	0.1	≪1	1132.4	B_g	2.0	Si4-O11
υ_{101}	1178.8	B_u	Si4-O11	1171.1	11.0	0.7	<1	1197.9	B_g	26.8	Si4-O11
				Mean A_g FWHM	6.9				|Δν|	5.1	
				Mean B_g FWHM	7.0				max. Δυ	26.8	

* The symbols used are the same as in Table 2.
[1] - Note O1, O2, O5, O7 & O10 are NBO whereas O3, O4, O6, O8, O9 and O11 are BO. Si1 is the Q^2 whereas Si2-Si4 are Q^3 species (see Fig. 3).

Sanbornite is a phyllosilicate composed of two layers: one of Q^3 species and one of BaO_9 polyhedra (Fig. 2). Each of the Q^3 species are connected to adjacent tetrahedra *via* bridging oxygens (BO) at the O1 and O3 sites whereas the O2 oxygen is a non-bridging oxygen (NBO) which is only bonded to one Si and three Ba atoms. Topologically, sanbornite can be described as a 6^3 net or an infinite layer of six-membered tetrahedral rings [39]. The large size of the Ba cations distorts each sheet such that the NBO are sticking out towards the Ba cations. This results in a relationship between the layers were one BaO_9 polyhedron sits atop of two silica tetrahedra, and vice versa.

$Ba_5Si_8O_{21}$ has 18 crystallographic sites (Fig. 3) and as a consequence has a large number of Raman modes (Table 3). This phase is a rare silicate composed of quadruple zweier chains that form ribbons that can be described topologically as $^2T_2^3T_6$ ribbons [40]. In the $Ba_5Si_8O_{21}$ structure, the edge of each ribbon has Q^2 species

at the Si1 site. The remaining Si sites (Si2-Si4) are Q^3 species, all of which have three BO and one NBO. The Q^n species display distinct vibrational frequencies.

3.2. Vibrational modes

3.2.1. Low-$BaSi_2O_5$

The primitive cell of sanbornite (*Pmcn*) contains 32 atoms and therefore, 96 normal modes including the three acoustic translations (B_{1u}, B_{2u} & B_{3u}) (Fig. 2). The correlation method [41] allows for the determination of the vibrational modes at the center of the Brillouin zone, $\Gamma^{L-BaSi2O5}_{vibrational} = 13A^R_g + 11B^R_{1g} + 11B^R_{2g} + 13B^R_{3g} + 11A^{silent}_u + 12B^{IR}_{1u} + 12B^{IR}_{2u} + 10B^{IR}_{3u}$. There is no known published evaluation of the vibrational spectra despite the multiple Raman studies involving sanbornite [27,28,42]. However, theoretical results reproduce the experimental vibrational modes with an absolute mean deviation of <6 cm^{-1}, and the high degree of overlap in the measured peaks and the displacement from unity in the calculated frequencies yields a small potential for ambiguity. For example, the measured modes numbering 12 (148.5 cm^{-1}) through 17 (267 cm^{-1}) *could* correspond to the calculated modes at 182.7 through 278.0 cm^{-1}. The overall agreement found between measured and simulated frequencies suggests that the spectrum can be divided into four regions according to the predominant symmetry character of the modes: the essentially rigid rotational motions occur below 100 cm^{-1}; bending modes involving Ba—O polyhedral from 100 to 400 cm^{-1}; intra- or inter-tetrahedral bending modes

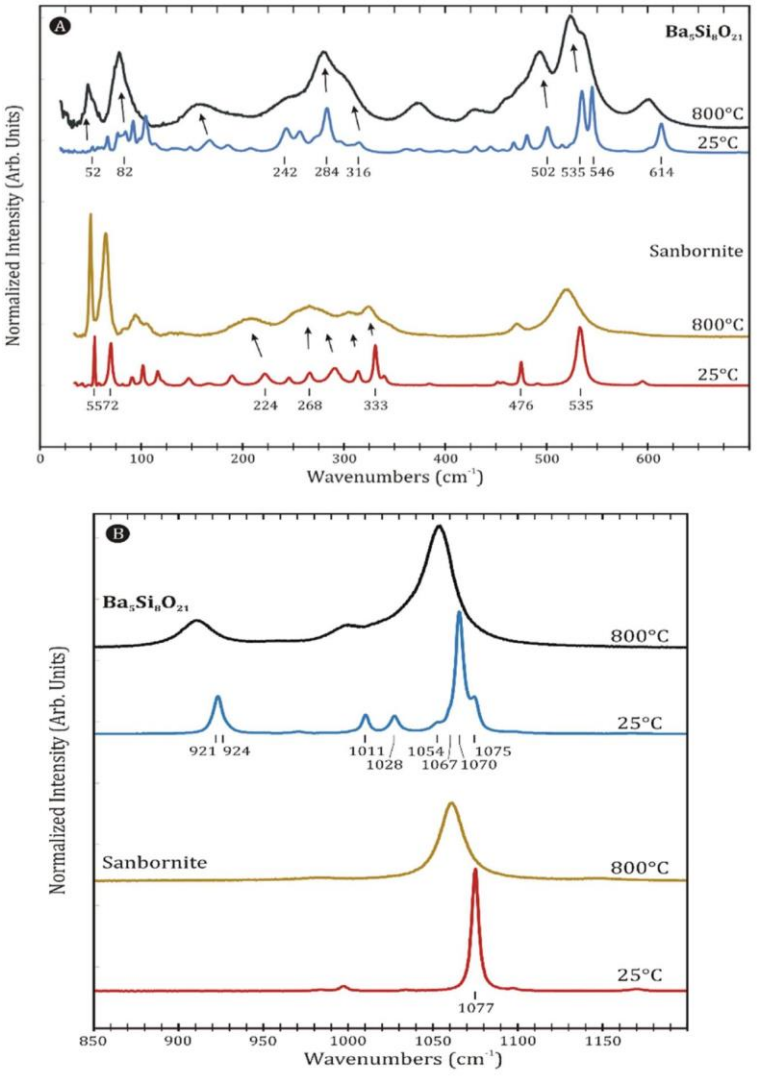

Fig. 4. Spectra of sanbornite and $Ba_5Si_8O_{21}$ at 25°C and 800 °C. A) the low frequency region and B) the high frequency stretching modes. Arrows highlight the vibrational modes.

(O—Si—O, Si—O—Si), with varying degree of Ba participation, at the range 400–760 cm^{-1}; the stretching mode region found >800 cm^{-1}. However, there are several stretching modes around 118 and 160 cm^{-1} and bending modes in the stretching region. Modes described as *lattice* involve significant movement of both the BaO_9 and SiO_4 sublattices. The complete list of mode symmetries and cations involved are reported in Table 2.

An analysis of the theoretical results of Table 2 shows that there is no distinction in either the relative intensities, the linewidths, or symmetry of modes involving a particular site (whether Si or Ba). Apart from the frequency distinctions there is no physically measurable parameter that distinguishes modes involving Si from Ba, nor distinguishing BO from NBO behavior.

3.2.2. $Ba_5Si_8O_{21}$

The primitive cell of $Ba_5Si_8O_{21}$ (*C2/c*) contains 68 atoms and consequently 204 normal modes including the acoustic modes (A_u + $2B_u$). The vibrational modes at Brillouin zone center can be composed as: $\Gamma_{vibratinal}^{Ba5Si8O21} = 49A_g^R + 50B_g^R + 51A_u^{IR} + 51B_u^{IR}$. The theoretical results reproduce the experimental observed modes slightly better than for sanbornite with a lower absolute mean deviation of <5.1 cm^{-1}. It is important to remark that numerous vibrational modes leave some ambiguity, especially at lower frequencies where many modes overlap. Note that the Ba3 and O11 sites (Fig. 3) are found at the Wycoff sites 4a and 4e, respectively, and consequently, the correlation method would infer that the Ba3 is not Raman active and that O11 site would only contribute to three modes. Fortunately, our simulation shows that this inference is somewhat misleading. An analysis of the results of Table 3 renders that the Ba3 site contributes to at least six modes whereas the O11 site contributes to multiple modes included several pure Si4-O11 stretching modes with values larger than 1100 cm^{-1}. This result highlights the necessity of *ab initio* simulations in determining the origin of the Raman modes. As with sanbornite, the spectra can be divided into four regions with small shifts in the limits (Fig. 4). The essentially rigid rotational motions occur below 100 cm^{-1}; bending modes involving Ba—O polyhedral from 100 to 370 cm^{-1}; intra- or inter-tetrahedral bending modes (O—Si—O, Si—O—Si), with varying degree of Ba participation, found from 370 to 780 cm^{-1}; the stretching mode region found >900 cm^{-1}.

The same caveats noted above apply to our analysis of $Ba_5Si_8O_{21}$, however, given the complexity of the spectra we emphasize that the agreement is excellent. The above modes are discussed in more detail below along with some correlations to their crystal chemical properties.

3.3. Temperature dependence of Raman modes

In general, as temperature increases, a thermal expansion takes place with concomitant increase of the crystal volume by lengthening bonds and increasing the inter-tetrahedral angles. These changes should be recorded in the frequencies of the vibrational modes. Twenty of the 33 measured modes found for sanbornite (Table 2) have been consistently identified up to 1150 °C, and therefore, can be related to its thermal expansion. Table 4 includes the ambient position center (ν_0) and linewidth (W_0) and their temperature dependences ($\delta\nu/\delta T$ and $\delta W/\delta T$, respectively) as well as a confidence indicator whether regression well ($R^2 > 0.9$) to weakly

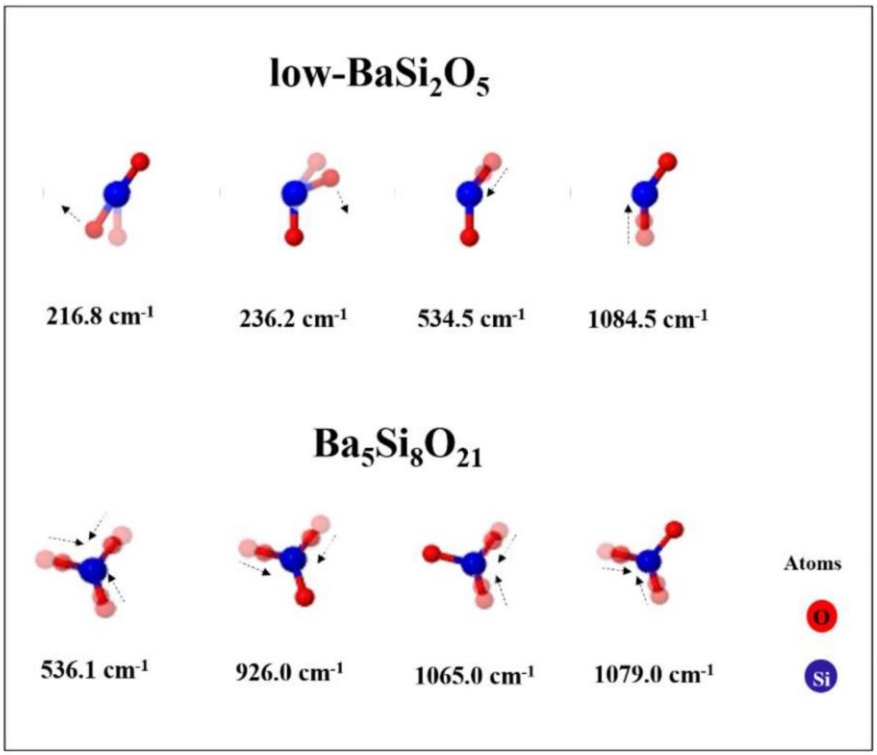

Fig. 5. Vibrational modes of the tetrahedral group (SiO_4) for low-$BaSi_2O_5$: 216.8, 236.2, 534.5 and 1084.5 cm^{-1} and $Ba_5Si_8O_2$: 536.1, 926.0, 1065.0 and 1079.0 cm^{-1}.

Table 4
Values of thermal effects on the mode parameters for sanbornite.

Mode	Center (C)		Shift	Linewidth[1]		% of Variance[2]		γ_P[3]
	υ_0	T_{max}	10^3 $\delta\upsilon/\delta T$	W_0	10^3 $\delta W/\delta T$	υ	W	
υ_1	55.0	1150	−6.5	0.9	1.7	h	m	3.22
υ_3	71.9	1150	−8.6	3.0	4.5	h	h	3.26
υ_6	103.3	1150	−9.9	3.9	4.8	h	l	2.61
υ_9	118.2	1150	−13.5	4	n.d.	h		3.11
υ_{12}	148.5	925	−20.6	5	n.d.	h		3.78
υ_{15}	224.0	1150	−11.4	12.5	14.7	m	m	1.39
υ_{16}	247.4	1150	3.4	4.1	24.6	l	h	−0.37
υ_{17}	267.4	1150	−2.3	8.2	15.7	l	h	0.23
υ_{19}	292.3	1150	−11.3	13	n.d.	h		1.05
υ_{20}	315.7	1150	−13.3	4.6	19.8	h	h	1.15
υ_{21}	332.6	1150	−10.0	2.8	17.9	h	vh	0.82
υ_{22}	341.8	1150	2.9	4.3	14.4	m	h	−0.23
υ_{29}*	476.2	1150	−7.2	3.0	7.7	h	h	0.41
υ_{32}	535.5	1150	−19.0	8.7	26.6	h	vh	0,97
υ_{34}	597.2	1150	−30.0	9.7	10.8	m	l	1.37
υ_{37}	756.5	1150	−20.8	12.2	9.9	h	l	0.75
υ_{42}	1000.3	1150	−25.8	n.d.				0.70
υ_{45}	1077.9	1150	−19.7	2.8	18.4	h	h	0.50
υ_{48}	1172.9	1150	−31.7	20–40	n.d.	h		0.74

* FWHM deviates from linearity around 800 °C
[1] W = full-width at half-maximum; n.d. = not determined
[2] % of variance explained by regression model: v = very; h = high, $R^2 > 0.9$; m = moderate, $R^2 > 0.75$; l = low, $R^2 > 0.5$
[3] $\gamma_P = (-1/\alpha\upsilon_0)(\delta\upsilon/\delta T)_P$, where α is the room temperature volume expansion coefficient (3.67×10^{-5} /K) determined from the structural data of [15].

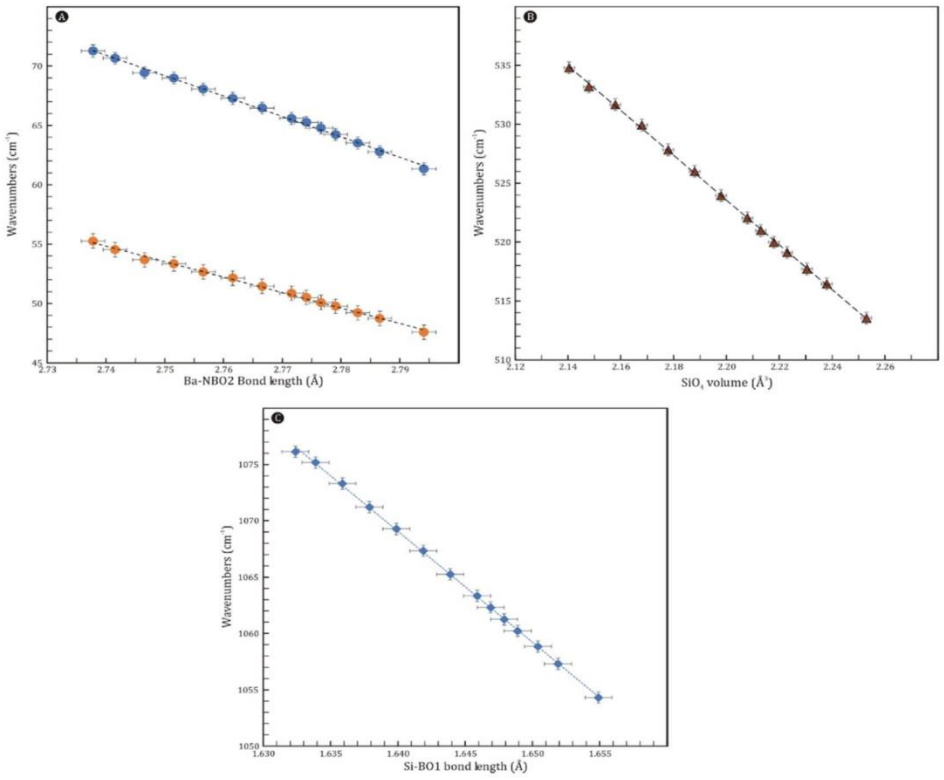

Fig. 6. Frequency dependence on the bond length or tetrahedron volume derived from crystal structural parameters of low-$BaSi_2O_5$ determined to 1100 °C. A) Shows the Ba-O2 vibrational modes at 55.0 ($\upsilon_1 = -130.4(d_{Ba-NBO}) + 411.5$, R^2 = 0.9968) and 71.9 cm^{-1} ($\upsilon_3 = -172.1(d_{Ba-NBO}) + 541.6$, R^2 = 0.9972). B) Shows the 535.5 cm^{-1} bending mode versus SiO_4 volume ($\upsilon_{32} = -190.1(SiO_4\,volume) + 941.8$, R^2 = 0.9995). C) Shows the 1077.9 cm^{-1} versus Si—O1 bond length ($\upsilon_{45} = -984.4(d_{Si-O1}) + 2683.5$, R^2 = 0.9995).

describes the mode trend. Modes not included in this table were not well constrained or too weak to follow as the temperature increases.

Raman modes are related to specific bonds, and/or groups of bonds, that can be characterized by their crystal chemical properties. For instance, the Ba—O2 bonds are solely responsible for vibrational modes at 55.0, 71.9, 148.5, and 315.7 cm^{-1}, however, not all are well defined. Using the thermal expansion data of Gorelova et al., [15], combined with our *in situ* high temperature data reported here allows us to determine the mode dependence on various crystal structure parameters.

In Fig. 4, representative spectra at room temperature and 800 °C were chosen to show the temperature dependence of the modes. At higher temperatures, >800 °C, the distinctions between overlapping modes are lost due to homogeneous broadening. The vibrational modes with very low values of frequency at 55.0 (υ_1) and 71.9 cm^{-1} (υ_3) are well defined, and become increasingly so, at higher temperatures (Fig. 4a). The low frequency bands are related to rigid motions of the Ba—O2 bonds and, therefore relate directly to the bond length and indirectly to the volume of the BaO_9 polyhedron (Fig. 5). Although they both have slightly different dependencies, they are similar at roughly ~1.5 cm^{-1} for bond length change of 0.01 Å (Fig. 6a). A difference quite easily measured given the resolution of our Raman spectrometer. Likewise, the 1077.9 cm^{-1} (υ_{45}) stretching mode of the O1 away from the central Si atom shows an even stronger correlation with the bond length (Fig. 6c). This stretching mode is much more sensitive to a changing bond length in that for every 0.01 Å the frequency shifts by −9.8 cm^{-1}. This bond length shift is very similar but even more strongly correlated than that found for the Si—O stretching modes and bond lengths in forsterite (Mg_2SiO_4) [30]. Another intense mode is found at 535.5 cm^{-1} (υ_{32}) at ambient temperatures. This mode is related predominantly to the bending motion of the Si perpendicular the face joined by adjacent bridging (two O3) and non-bridging (O2) oxygens. Ultimately, this vibrational mode can be correlated to the overall volume of the SiO_4 tetrahedron (Fig. 3b). In this case, a 1% volume change corresponds to a 1.9 shift in wavenumbers. Further generalization of these relationships may permit Raman spectroscopy to be used *in situ* to probe crystal chemical properties, especially, during chemical reactions (e.g. crystallization), where the origin of the vibrational mode is known.

The $Ba_5Si_8O_{21}$ spectra has a high number of vibrational modes which has the advantage of permitting quite well-constrained temperature dependence of the peak positions. However, the corollary is that this co-dependence becomes a disadvantage when one mode in a series of overlapping mode becomes poorly constrained such that it degrades the fit of all overlapping modes. Ultimately, of the 70 modes observed at ambient conditions, 28 were reliable characterized to temperatures above 800 °C (see Table 5). The temperature-dependent Raman study of the $Ba_5Si_8O_{21}$ was performed to obtain information on structural changes induced by temperature, and the wavenumber versus temperature plots are

Table 5
Values of thermal effects on the mode parameters for $Ba_5Si_8O_{21}$*

Mode	Center (C)		Shift	Linewidth		% of Variance		γ_P[1]
	ν_0	T_{max}	10^3 $\delta\nu/\delta T$	W_0	10^3 $\delta W/\delta T$	ν	W	
υ_1	52.0	1100	−5.3	1.5	5.7	h	h	3.80
υ_2	56.6	800	−4.3	2.4	4.3	h	vl	2.83
υ_6	76.6	1100	−3.8	2.7	5.3	m	m	1.85
υ_{10}	83.9	1000	−6	5.8	3.5	h	m	2.66
υ_{12}	92.0	1100	−6.9	4	8.2	m	m	2.79
υ_{13}	98.0	800	−1.8	4.2	7.5	l	l	0.68
υ_{15}	104.5	600	0.8	6.2	n.d.	m	l	−0.29
υ_{19}	131.3	600	−8.1	5	n.d.	h	l	2.30
υ_{26}	166.3	1100	−17.8	12	n.d.	h	l	3.99
υ_{27}	185.4	1000	−23.9	13.8	13.8	h	l	4.80
υ_{29}	211.1	1000	−31.3	9.7	27.4	h	h	5.53
υ_{34}	241.0	1100	−0.4	10.7	29.2	vl	h	0.06
υ_{36}	256.2	800	−6.8	10.5	23.8	l	m	0.99
υ_{39}	282.8	1100	−3.8	8.2	24.8	m	vh	0.50
υ_{41}	305.3	1100	−4.5	9.9	18.1	vl	m	0.55
υ_{42}	315.4	400	−11.3	7.1	20.6	h	h	1.34
υ_{48}	362.0	600	10.1	4.9	8.3	h	l	−1.04
υ_{49}	376.0	1100	−3.6	5.9	19.3	l	m	0.36
υ_{51}	393.9	600	−10.4	7.9	17.7	m	h	0.98
υ_{54}	430.2	1100	−3.3	3.8	11.9	vl	m	0.29
υ_{57}	445.1	800	−11.5	9	8.4	h	l	0.96
υ_{59}	468.5	1000	−11.8	3.1	17	h	h	0.94
υ_{61}	481.6	1100	−11	4.9	19.3	m	h	0.85
υ_{62}	501.8	1100	−11.4	7.3	19.6	h	h	0.85
υ_{66}	535.6	1100	−17.2	6.6	16.2	vh	vh	1.20
υ_{68}	546.0	1100	−11.3	3.9	24.8	vh	vh	0.77
υ_{71}	600.8	1000	−11.8	5	19	m	h	0.73
υ_{72}	613.8	1100	−14.3	8.2	13.8	h	m	0.87
υ_{82}	923.6	500	−18.7	6.2	12.6	h	h	0.75
υ_{83}	928.1	1100	−21	6.5	19.7	vh	h	0.84
υ_{86}	972.2	1100	−22	9.9	23.2	h	h	0.84
υ_{89}	1010.8	1100	−14.5	2.1	27.9	vh	h	0.53
υ_{91}	1027.5	500	−12	6.8	28.5	h	m	0.44
υ_{93}	1053.8	1100	−25.4	4.6	34.2	h	l	0.90
υ_{95}	1066.6	1100	−16	5.6	18	vh	vh	0.56
υ_{96}	1075.1	500	−21.6	4.7	4.5	vh	l	0.75

* Parameters described as in Table 4.
[1] Isobaric mode-Grüneisen parameter calculated using α, the room temperature volume expansion coefficient, determined as 2.68×10^{-5} /K from the structural data of [15].

presented in Fig. 7. We can observe that the Raman spectra remain nearly unchanged during the heating of the sample.

Notable among these modes are those that are similar to those in sanbornite, specifically those centered at 57, ~500, 900–1070 cm^{-1}, which are related to Si—O—Ba bending, and Ba—O and Si—O stretching motions, respectively. Unlike sanbornite, $Ba_5Si_8O_{21}$ does not have modes predominantly associated with specific Ba-Oxygen bonding. The mode at 56.6 cm^{-1} (ν_2) involves rigid motion of the Ba2 site combined with the two opposing oxygens, O2 and O10, on adjacent tetrahedral ribbons. The linear correlation to the Ba2—O* distance is weaker (Fig. 8a) than observed for sanbornite (Fig. 6a). This is explained by the overlap of ν_2 mode with adjacent ν_1 and ν_3 modes. Likewise, the remaining modes involve more than one oxygen and often both Si and Ba. For instance, the bending modes at 468.5 (ν_{59}) and 501.8 cm^{-1} (ν_{62}) involve Si4-O10-Ba2 and Si3-O6-Ba2, respectively (Table 3). Both should therefore be sensitive to the twisting of the adjacent tetrahedra with thermal expansion which is concentrated along the ribbon length rather than perpendicular to it [15]. Fig. 8b shows the frequency dependence of these modes correlated to their respective Si—O and Ba—O bond lengths. They show excellent correlation in either case. This change is significant, because often shifts in bending modes are associated with changes in bond angles, however, in this case, the Si4-O10-Ba2 and Si3-O6-Ba2 angles change less than 1 degree between room temperature and 1000 °C, whereas these modes show large frequency displacements, both approximately −1 cm^{-1} for every 100 °C. These bending mode correlations are stronger than recent correlations found for orthoenstatite [29]. Ultimately, however, knowing the pressure dependence as well as the temperature dependence reported here would provide a more rigorous understanding of the volume dependence and consequently the thermodynamics of these phases.

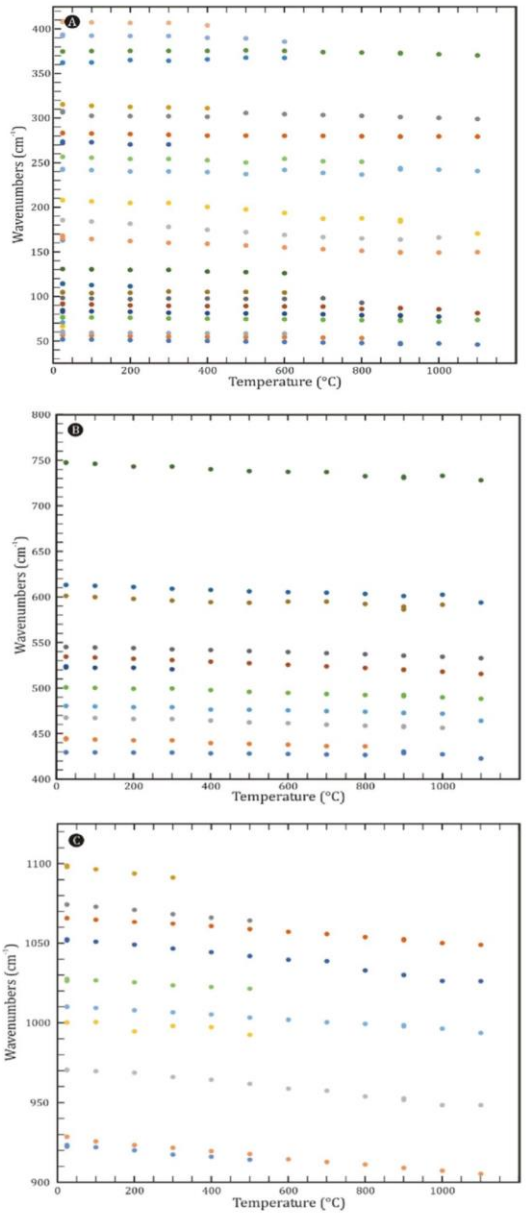

Fig. 7. Temperature dependence of vibrational modes for $Ba_5Si_8O_{21}$ highlighting the A) low frequency, B) middle frequency, and C) high frequency mode behavior.

Finally, the stretching modes at 928.1 (ν_{83}) and 1066.6 (ν_{95}) cm^{-1} are uniquely associated with the Si1 (Q^2) and adjacent Si2 (Q^3) sites, respectively, and clearly persist to the highest temperatures investigated here (Figs. 4, 7). The Si1 mode involves both stretching of both adjacent oxygens, O1 and O2, away from the central silicon, whereas, the Si2 mode localized to the O5—S2 bond. Both of these peaks overlap with adjacent modes although the ν_{95} mode suffers more from this issue. The high frequency B_g modes are quite sensitive to orientation, however, as this experiment was conducted on the same site, we can be certain that the same ν_{95} mode was followed throughout our high-temperature experiment. In the Si1 case, the average of the short, Si1-O1, and the long, Si1-O2, bond lengths are plotted against the frequency shift (Fig. 8c). The strong correlations in both the peak center and linewidth affirm this interpretation (Table 5). In both cases, there is a strong correlation between the bond length and the frequency of these modes. Although not identical, nor should they be expected to be identical, they are similar. They indicate that a 0.01 Å change in bond length corresponds to a shift of 10 ± 2 cm^{-1}.

4. Conclusions

The prominent phases of silicate: sanbornite and $Ba_5Si_8O_{21}$ have become ever more important for industrial applications and hold promise in understanding crystal nucleation and growth processes. Though widely used, Raman spectroscopy remains limited by an inability to make detailed mode assignments and consequently, clear and confident interpretations remain few and far between. This issue is largely overcome with *ab initio* calculations of vibrational frequencies, as done here. The vibrational mode assignments and their relation to the structural features has been reported in detail for both sanbornite and $Ba_5Si_8O_{21}$.

In addition, we report the temperature dependence of the Raman modes. Given the detailed mode assignments, associated to specific Ba or Si sites or bonding configurations have been revealed. Several examples, particularly of the stretching modes which are localized to specific Si—O bonds show strong correlations with the bond length changes up to 1100 °C. These relationships should be pursued to high pressures so that a complete thermodynamic model can be made. Finally, if the frequency dependence on some of these crystal chemical parameters can be

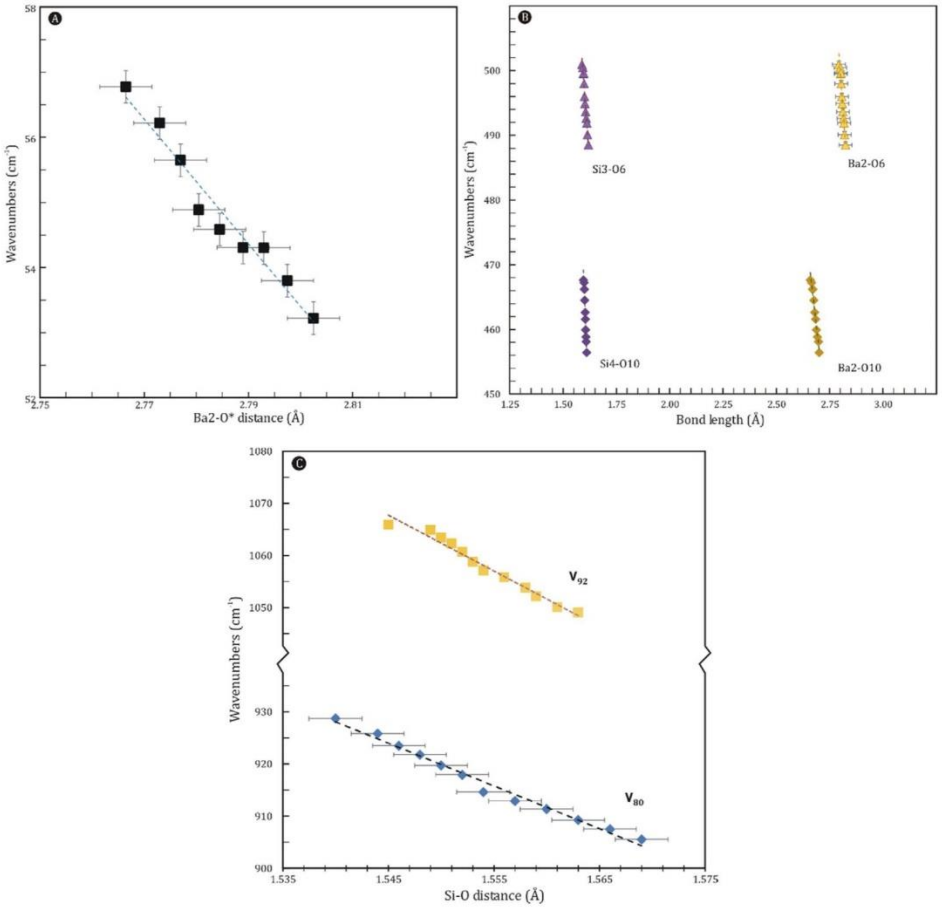

Fig. 8. $Ba_5Si_8O_{21}$ frequency dependence of the crystal chemical parameters. A) Frequency υ_2 versus Ba2—O* length, where O* is the mean bond lengths to the two oxygens (O6 and O10) involved in this motion. The dependence is described as −95.7 (Ba—O) + 321.5 (R^2 = 0.96). B) Comparison of the mode shift to the Si—O and Ba—O bond lengths involved in the 468.5 cm^{-1} (v_{59}) and 501.8 cm^{-1} (v_{62}). (R^2 = 0.96–0.98). C) The Si—O stretching frequencies versus bond lengths for the Si1 at 928.1 cm^{-1} (v_{83}) and the main Si2 band at 1066.6 cm^{-1} (v_{95}).

generalized more broadly, *in situ* Raman experiments may lead to critical insights into *in situ* reactions, including crystallization and catalysis. Finally, we hope that this type of research can be considered a clear example of how the joint use of first principle calculations and experimental measurements of vibrational modes is an appropriate strategy to disclose the structure of complex oxide-based materials

CRediT authorship contribution statement

Eduardo O. Gomes: Conceptualization, Methodology, Validation, Formal analysis, Investigation, Writing - original draft. **Benjamin J.A. Moulton:** Conceptualization, Methodology, Validation, Formal analysis, Investigation, Writing - original draft. **Thiago R. Cunha:** Formal analysis, Investigation, Writing - original draft. **Lourdes Gracia:** Conceptualization, Methodology, Validation, Formal analysis, Investigation, Writing - original draft, Project administration. **Paulo S. Pizani:** Resources, Supervision, Project administration, Funding acquisition. **Juan Andrés:** Resources, Writing - review & editing, Project administration, Funding acquisition.

Declaration of Competing Interest

The authors declare that they have no known competing financial interests or personal relationships that could have appeared to influence the work reported in this paper.

Acknowledgements

EOG acknowledges Generalitat Valenciana for the Santiago Grisolia program (2018/064). EOG and JA acknowledge financial support from Universitat Jaume I, for project UJI-B2019-30, and Ministerio de Ciencia, Innovación y Universidades (Spain) project PGC2018-094417-B-I00. We also wish to thank the Servei d'Informática, Universitat Jaume I, for their generous allocation of computer time. BJAM and TRC thank the São Paulo Research Foundation (FAPESP) for funding through grant numbers 2016/18567-5 and 2019/12383-8. PSP appreciates the support of CNPq and CAPES. We especially thank FAPESP for the CEPID project funding (no. 2013/07793-6) which made this a reality. Finally, we are thankful to Valmor Mastelaro for making this collaboration possible.

References

[1] R. Trejo, E. Lara-Curzio, A. Shyam, M.J. Kirkham, V. Garcia-Negron, Y. Wang, Physical and mechanical properties of barium alkali silicate glasses for SOFC sealing applications, Int. J. Appl. Glas. Sci. 3 (2012) 369–379, https://doi.org/10.1111/ijag.12004.

[2] J.H. Park, J.S. Kim, J.T. Kim, Luminescent properties of $BaSi_2O_5:Eu^{2+}$ phosphor film fabricated by spin-coating of Ba-Eu precursor on SiO_2 glass, J. Opt. Soc. Korea. 18 (2014) 45–49, https://doi.org/10.3807/JOSK.2014.18.1.045.

[3] F. Xiao, Y.N. Xue, Q.Y. Zhang, Bluish-green color emitting $Ba_2Si_3O_8:Eu^{2+}$ ceramic phosphors for white light-emitting diodes, Spectrochim. Acta - Part A Mol. Biomol. Spectrosc. 74 (2009) 758–760, https://doi.org/10.1016/j.saa.2009.08.011.

[4] M. Zhang, J. Wang, Q. Zhang, W. Ding, Q. Su, Optical properties of $Ba_2SiO_4:Eu^{2+}$ phosphor for green light-emitting diode (LED), Mater. Res. Bull. 42 (2007) 33–39, https://doi.org/10.1016/j.materresbull.2006.05.011.

[5] M. Kerstan, C. Rüssel, Barium silicates as high thermal expansion seals for solid oxide fuel cells studied by high-temperature X-ray diffraction (HT-XRD), J. Power Sources. 196 (2011) 7578–7584, https://doi.org/10.1016/j.jpowsour.2011.04.035.

[6] S. Lin, H. Lin, Q. Huang, Y. Cheng, J. Xu, J. Wang, X. Xiang, C. Wang, L. Zhang, Y. Wang, A Photostimulated BaSi2O5:Eu2+, Nd3+ Phosphor-in-Glass for Erasable-Rewritable Optical Storage Medium, Laser Photon. Rev. 13 (2019) 1900006, https://doi.org/10.1002/lpor.201900006.

[7] J.K. Park, M.A. Lim, K.J. Choi, C.H. Kim, Luminescence characteristics of yellow emitting $Ba_3SiO_5:Eu^{2+}$ phosphor, J. Mater. Sci. 40 (2005) 2069–2071, https://doi.org/10.1007/s10853-005-1237-z.

[8] R.M. Douglass, The crystal structure of sanbornite, $BaSi_2O_5$, Am. Mineral. 43 (1958) 517–536.

[9] R.E. Walstrom, J.F. Leising, Barium minerals of the Sanbornite Deposits, Axis. 1 (2005) 1–18. http://www.mineralogicalrecord.com.

[10] L.C. Basciano, L.A. Groat, A.C. Roberts, J.D. Grice, G.E. Dunning, E.E. Foord, I.M. Kjarsgaard, R.E. Walstrom, Kampfite, a new barium silicate carbonate mineral species from Fresno County, California, Can. Mineral. 39 (2001) 1053–1058, https://doi.org/10.2113/gscanmin.39.4.1053.

[11] K.F. Hesse, F. Liebau, Crystal chemistry of silica-rich Barium silicates I: Refinement of the crystal structures of $Ba_4[Si_6O_{16}]$, $Ba_5[Si_8O_{21}]$ and $Ba_6[Si_{10}O_{26}]$, silicates with triple, quadruple and quintuple chains, Zeitschrift Fur Krist. - New Cryst. Struct. 153 (1980) 3–17, https://doi.org/10.1524/zkri.1980.0002.

[12] K.F. Hesse, F. Liebau, Crystal chemistry of silica-rich Barium silicates III: Refinement of the crystal structures of the layer silicates $Ba_2[Si_4O_{10}]$ (l), (Sanbornite), and $Ba_2[Si_4O_{10}]$ (h), Zeitschrift Fur Krist. - New Cryst. Struct. 153 (1980) 33–41, https://doi.org/10.1524/zkri.1980.0004.

[13] F. Liebau, Structural Chemistry of Silicates, 1st ed., Springer Berlin Heidelberg, Berlin, Heidelberg, 1985. doi:10.1007/978-3-642-50076-3.

[14] M. Czank, P.R. Buseck, Crystal chemistry of silica-rich barium silicates, Zeitschrift Für Krist. - Cryst. Mater. 153 (1980) 19–32, https://doi.org/10.1524/zkri.1980.0003.

[15] L.A. Gorelova, R.S. Bubnova, S.V. Krivovichev, M.G. Krzhizhanovskaya, S.K. Filatov, Thermal expansion and structural complexity of Ba silicates with tetrahedrally coordinated Si atoms, J. Solid State Chem. 235 (2016) 76–84, https://doi.org/10.1016/j.jssc.2015.12.012.

[16] S. Sen, T. Mukerji, A generalized classical nucleation theory for rough interfaces: Application in the analysis of homogeneous nucleation in silicate liquids, J. Non. Cryst. Solids. 246 (1999) 229–239, https://doi.org/10.1016/S0022-3093(99)00093-9.

[17] A.M. Rodrigues, D.R. Cassar, V.M. Fokin, E.D. Zanotto, Crystal growth and viscous flow in barium disilicate glass, J. Non. Cryst. Solids. 479 (2018) 55–61, https://doi.org/10.1016/j.jnoncrysol.2017.10.007.

[18] V.M. Fokin, E.D. Zanotto, N.S. Yuritsyn, J.W.P. Schmelzer, Homogeneous crystal nucleation in silicate glasses: A 40 years perspective, J. Non. Cryst. Solids. 352 (2006) 2681–2714, https://doi.org/10.1016/j.jnoncrysol.2006.02.074.

[19] X. Xia, I. Dutta, J.C. Mauro, B.G. Aitken, K.F. Kelton, Temperature dependence of crystal nucleation in $BaO{\cdot}2SiO_2$ and $5BaO{\cdot}8SiO_2$ glasses using differential thermal analysis, J. Non. Cryst. Solids. 459 (2017) 45–50, https://doi.org/10.1016/j.jnoncrysol.2016.12.032.

[20] L. Cai, R.E. Youngman, D.E. Baker, A. Rezikyan, M. Zhang, B. Wheaton, I. Dutta, B.G. Aitken, A.J. Allen, Nucleation and early stage crystallization in barium disilicate glass, J. Non. Cryst. Solids. 548 (2020), https://doi.org/10.1016/j.jnoncrysol.2020.120330 120330.

[21] Y. Takahashi, M. Osada, H. Masai, T. Fujiwara, Structural heterogeneity and homogeneous nucleation of $1BaO{\cdot}2SiO_2$ glass, Appl. Phys. Lett. 94 (2009), https://doi.org/10.1063/1.3142394 211907.

[22] E.D. Zanotto, P.F. James, Experimental test of the general theory of transformation kinetics: Homogeneous nucleation in a $BaO{\cdot}2SiO_2$ glass, J. Non. Cryst. Solids. 104 (1988) 70–72, https://doi.org/10.1016/0022-3093(88)90183-4.

[23] A. Herrmann, A. Simon, C. Rüssel, Preparation and luminescence properties of Eu2-doped $BaSi_2O_5$ glass-ceramics, J. Lumin. 132 (2012) 215–219, https://doi.org/10.1016/j.jlumin.2011.08.024.

[24] P. Wang, X. Xu, D. Zhou, X. Yu, J. Qiu, Sunlight Activated Long-Lasting Luminescence from $Ba_5Si_8O_{21}:Eu^{2+}$, D^{y3}+ Phosphor, Inorg. Chem. 54 (2015) 1690–1697, https://doi.org/10.1021/ic5026312.

[25] Y. Takahashi, H. Masai, M. Osada, R. Ihara, T. Fujiwara, Formation of spherulite and metastable phase in stoichiometric $Ba_2Si_3O_8$ glass, J. Ceram. Soc. Japan. 118 (2010) 955–958, https://doi.org/10.2109/jcersj2.118.955.

[26] B.J.A. Moulton, A.M. Rodrigues, P.S. Pizani, D.V. Sampaio, E.D. Zanotto, A Raman investigation of the structural evolution of supercooled liquid barium disilicate during crystallization, Int. J. Appl. Glas. Sci. 9 (2018) 510–517, https://doi.org/10.1111/ijag.12356.

[27] B.J.A. Moulton, A.M. Rodrigues, D.V. Sampaio, L.D. Silva, T.R. Cunha, E.D. Zanotto, P.S. Pizani, The origin of the unusual DSC peaks of supercooled barium disilicate liquid, CrystEngComm. 21 (2019) 2768–2778, https://doi.org/10.1039/c8ce02054j.

[28] L.L. Evaristo, B.J.A. Moulton, P.S. Pizani, S. Buchner, Effect of high pressure on the structure of barium disilicate glass-ceramics, J. Non. Cryst. Solids. 550 (2020), https://doi.org/10.1016/j.jnoncrysol.2020.120380 120380.

[29] C. Stangarone, M. Tribaudino, M. Prencipe, P.P. Lottici, Raman modes in Pbca enstatite ($Mg_2Si_2O_6$): an assignment by quantum mechanical calculation to interpret experimental results, J. Raman Spectrosc. 47 (2016) 1247–1258, https://doi.org/10.1002/jrs.4942.

[30] C. Stangarone, U. Böttger, D. Bersani, M. Tribaudino, M. Prencipe, Ab initio simulations and experimental Raman spectra of Mg_2SiO_4 forsterite to simulate Mars surface environmental conditions, J. Raman Spectrosc. 48 (2017) 1528–1535, https://doi.org/10.1002/jrs.5127.

[32] H.M. Rietveld, Line profiles of neutron powder-diffraction peaks for structure refinement, Acta Crystallogr. 22 (1967) 151–152, https://doi.org/10.1107/S0365110X67000234.

[33] A.C. Larson, R.B. Von Dreele, General Structure Analysis System (GSAS), Los Alamos Natl. Lab. Rep. LAUR. 748 (2004) 86–748, https://doi.org/10.1103/PhysRevLett.101.107006.

[34] R. Dovesi, A. Erba, R. Orlando, C.M. Zicovich-Wilson, B. Civalleri, L. Maschio, M. Rérat, S. Casassa, J. Baima, S. Salustro, B. Kirtman, Quantum-mechanical condensed matter simulations with CRYSTAL, Wiley Interdiscip. Rev. Comput. Mol. Sci. 8 (2018), https://doi.org/10.1002/wcms.1360 e1360.

[35] M.D. Towler, BARIUM BASIS SETS FOR THE CRYSTAL PROGRAM, (1996). https://vallico.net/mike_towler//basis_sets/Ba_basis.txt.

[36] R. Nada, J.B. Nicholas, M.I. McCarthy, A.C. Hess, Basis sets for ab initio periodic Hartree—Fock studies of zeolite/adsorbate interactions: He, Ne, and Ar in silica sodalite, Int. J. Quantum Chem. 60 (1996) 809–820, https://doi.org/10.1002/(SICI)1097-461X(1996)60:4<809::AID-QUA3>3.3.CO;2-F.

[37] L. Valenzano, F.J. Torres, K. Doll, F. Pascale, C.M. Zicovich-Wilson, R. Dovesi, Ab Initio Study of the Vibrational Spectrum and Related Properties of Crystalline Compounds; the Case of CaCO3 Calcite, Zeitschrift Für Phys. Chemie. 220 (2006) 893–912, https://doi.org/10.1524/zpch.2006.220.7.893.

[38] L.B. McCusker, R.B. Von Dreele, D.E. Cox, D. Louër, P. Scardi, Rietveld refinement guidelines, J. Appl. Crystallogr. 32 (1999) 36–50, https://doi.org/10.1107/S0021889898009856.

[39] F.C. Hawthorne, Y.A. Uvarova, E. Sokolova, A structure hierarchy for silicate minerals: sheet silicates, Mineral. Mag. 83 (2019) 3–55, https://doi.org/10.1180/mgm.2018.152.

[40] M.C. Day, F.C. Hawthorne, A structure hierarchy for silicate minerals: chain, ribbon, and tube silicates, Mineral. Mag. 84 (2020) 165–244, https://doi.org/10.1180/mgm.2020.13.

[41] W.G. Fateley, F.R. Dollish, N.T. McDevitt, F.F. Bentley, Infrared and Raman Selection Rules for Lattice Vibrations: The Correlation Method, John Wiley & Sons, Inc., Toronto, 1972.

[42] Y. Takahashi, R. Ihara, T. Fujiwara, M. Osada, Crystallization and Morphology of Glassy Sanbornite, Key Eng. Mater. 485 (2011) 301–304, https://doi.org/10.4028/www.scientific.net/KEM.485.301.

This is the peer-reviewed, final accepted version for American Mineralogist, published by the Mineralogical Society of America.
The published version is subject to change. Cite as Authors (Year) Title. American Mineralogist, in press.
DOI: https://doi.org/10.2138/am-2021-7910. http://www.minsocam.org/

Word Count: 9382 **REVISION #3 MANUSCRIPT 7910R3**

A theoretical and experimental investigation of hetero- versus homo-connectivity in barium silicates

Benjamin J. A. Moulton[a,b], Eduardo O. Gomes[c], Thiago R. Cunha[a,b], Carsten Doerenkamp[d], Lourdes Gracia[c,e], Hellmut Eckert[d,f], Juan Andrés[c], and Paulo S. Pizani[a,b]

[a] *Universidade Federal de São Carlos, Departamento de Física, Rod. Washington Luis, Km 235 13565-905 São Carlos, SP, Brazil*

[b] *CERTEV — Center for Research, Technology, and Education in Vitreous Materials, Department of Materials Engineering, Federal University of São Carlos, 13565 - 905 São Carlos-SP, Brazil: www.certev.ufscar.br*

[c] *Departament de Química Física i Analítica, Universitat Jaume I, 12071, Castelló de la Plana, Spain*

[d] *Institute of Physics in São Carlos, University of São Paulo, São Carlos, SP 13566-590, Brazil.*

[e] *Department of Physical Chemistry, University of Valencia (UV), 46100 Burjassot, Spain*

[f] *Institute of Physical Chemistry, Westfälische Wilhelms-Universität Münster, Corrensstrasse 28/30, 48149, Münster, Germany.*

Abstract

Barium silicates may be found in contact aureoles and are used in several important technologies (e.g. LEDs). The BaO-SiO_2 system stabilizes 13 crystalline phases with different silicate tetrahedral and connectivity profiles. Aside from phases composed of a single structural unit (isolated or homo-connected tetrahedra) one encounters the relatively rare case of hetero-connected tetrahedra in which varying proportions of several Q^n species are linked together. Here, we analyze the ^{29}Si MAS NMR and Raman spectroscopic manifestations of the connectivities in seven barium silicates: Ba_2SiO_4, high-$BaSiO_3$, $Ba_4Si_6O_{16}$, $Ba_5Si_8O_{21}$, $Ba_6Si_{10}O_{26}$, high-$BaSi_2O_5$ and sanbornite (low-$BaSi_2O_5$). The structures and purity of these phases were confirmed by Rietveld refinement. From the Raman spectroscopic database on 144 predominantly homo-connected crystalline silicates, the mean Q^n mode frequencies ($\nu_{Qn} \pm 1\sigma$) are found at 827.7 (±13.8) cm^{-1} for Q^0, 905.3 (±22.1) cm^{-1} for Q^1, 993.5 (±25.9) cm^{-1} for Q^2, and 1068.4 (±17.6) cm^{-1} for Q^3 units. Experimentally, homo-connected barium silicates show good agreement with these values whereas the hetero-connected phases show a wider range of ν_{Q2} than of ν_{Q3} frequencies. While the ^{29}Si NMR chemical shifts of the barium silicates are in agreement with known structural trends, those measured for the Q^2 resonances remain essentially constant, which may be caused by the lattice distortion around the large Ba^{2+} cations. To complement and rationalize experimental measurements, first-principles calculations, at the

density functional theory level, have reproduced measured frequencies within a mean absolute deviation of less than 7 cm^{-1}. Our work highlights how the results provided by ^{29}Si NMR and Raman spectroscopies, and *ab initio* calculations can be combined to rationalize the structure of complex systems. Present findings also shed light on the vibrational modes that may be used to track bond lengths *in situ* at extreme conditions and the behavior of homo- versus hetero-connectivity, revealing clear implications for evaluating silicate glasses and melts where hetero-connectivity is the rule rather than the exception.

Keywords: Barium silicates, Ba_2SiO_4, high-$BaSiO_3$, $Ba_4Si_6O_{16}$, high-$Ba_5Si_8O_{21}$, $Ba_6Si_{10}O_{26}$, high-$BaSi_2O_5$ and low-$BaSi_2O_5$, ^{29}Si MAS NMR and Raman spectroscopies, X-ray diffraction, density functional theory calculations.

1 Introduction

During the last decade, the study of barium silicates represents an exceptional part in a wide field of crystallographic and material science because of their applications in different fields. For example, barium silicate-based ceramics are used as solid-oxide sealant materials (e.g. Namwong et al. 2010), erasable-writable optical storage devices (Lin et al. 2019), and, when doped with rare-earth elements, as light emitting diode materials (Xiao et al. 2009; Chen et al. 2015). Barium silicates are built of SiO_4^{n-} tetrahedra, the fundamental building blocks of almost all silicate minerals and liquids (Liebau 1985). Its remarkable stability through the transition from the solid into the liquid state is central to understanding and predicting the properties of silicate crystals, glasses, and melts. The modified random network model of silicate liquids describes them as having two entangled subnetworks: one constructed from interconnected silica tetrahedra and one comprised of ill-defined modifier-oxygen polyhedra (MO_x, where M = K, Ba, etc.) (c.f. Greaves 1985). The silica subnetwork contains tetrahedra that may be connected by up to four additional tetrahedra units. Connectivity is defined by the number of Si-O-Si bonds found around a central tetrahedron and described using the Q^n species notation, where n is the number of bridging oxygen (BO) atoms shared between tetrahedra and 4-n is the number of non-bridging oxygen (NBO) atoms bound to M cations (c.f. Calas et al. 2006). Most crystalline silicates are

63 built from a single Q^n species, whereas in silicate liquids and glasses have two or more Q^n
64 species that are assumed to be randomly linked. Sanbornite, low-$BaSi_2O_5$, is an uncommon
65 mineral composed of Q^3 units and can be found in the metamorphic aureole associated with a
66 migmatite and granodiorite pluton at Big Creek, California, USA (Douglass 1958; Walstrom and
67 Leising 2005).

68 Barium silicates stabilize a wide range of structures from neso- (Q^0), ino- (Q^2), and phyllo-
69 (Q^3) silicates including Ba_2SiO_4, $BaSiO_3$, and $BaSi_2O_5$ which are built from a single Q^n species
70 (Eskola 1922; Roth and Levin 1959; Oehlschlegel 1975; Shukla et al. 2018). When bonding is
71 between Q^n of equal n, e.g. Q^3-Q^3, we refer to this as *homo-connectivity*. Also present are
72 $Ba_4Si_6O_{16}$, $Ba_5Si_8O_{21}$, and $Ba_6Si_{10}O_{26}$ which are uncommon non-hydrous crystal structures built
73 from both Q^2 and Q^3 species, which are also interconnected (Liebau 1985). In this
74 mineralogically rare situation, where Q^n are bound to $Q^{n\pm1}$, e.g. Q^2-Q^3 linkages, we refer to this
75 as *hetero-connectivity* (Fig. 1). By far the most common hetero-connective mineral phases are
76 found within the amphibole group (e.g. tremolite, $Ca_2Mg_5Si_8O_{22}(OH)_2$), which have complex
77 chemistry including hydroxyl groups. The three hetero-connective phases, $Ba_6Si_{10}O_{26}$, $Ba_5Si_8O_{21}$,
78 and $Ba_4Si_6O_{16}$, have Q^2:Q^3 ratios that increase with increasing Ba content from 1:4 to 1:3 to 1:2,
79 respectively (Table 1). Beyond their structures (Hesse and Liebau 1980a) and thermal expansion
80 behavior (Gorelova et al. 2016), little is known about these hetero-connected phases. In contrast,
81 the structure and properties of the homo-connected phases Ba_2SiO_4 (Q^0), high-$BaSiO_3$ (Q^2), and
82 the two Q^3 polymorphs, sanbornite (orthorhombic low-$BaSi_2O_5$) and monoclinic high-$BaSi_2O_5$,
83 have been the focus of many studies using X-ray diffraction (Grosse and Tillmanns 1974a,
84 1974b; Hesse and Liebau 1980a, 1980b; Cormier et al. 1999; Schlenz et al. 2002; Denault et al.
85 2015; Gorelova et al. 2016), nuclear magnetic resonance (NMR) (^{29}Si: Smith et al., (1983), ^{17}O:
86 Thompson et al., (2012)), Raman (Takahashi et al. 2010; Moulton et al. 2019), Si *K*-edge and Ba
87 L_3-edge XANES, X-ray photoemission (XPS) (Bender et al., 2002;), and atomic force
88 microscopy (Schlenz et al. 2002).

89 Advances of experimental characterization techniques, especially solid-state NMR and
90 Raman spectroscopy, and first-principles calculations have significantly improved the
91 understanding of the structures of these systems. This study expands upon our recent analysis of
92 the vibrational modes of sanbornite and $Ba_5Si_8O_{21}$ (Gomes et al. 2021) and here we investigate

This is the peer-reviewed, final accepted version for American Mineralogist, published by the Mineralogical Society of America.
The published version is subject to change. Cite as Authors (Year) Title. American Mineralogist, in press.
DOI: https://doi.org/10.2138/am-2021-7910. http://www.minsocam.org/

93 the effects of SiO_4 connectivity on the spectroscopic signature of the Q^n units in Ba_2SiO_4, high-
94 $BaSiO_3$, $Ba_4Si_6O_{16}$, $Ba_5Si_8O_{21}$, $Ba_6Si_{10}O_{26}$, high-$BaSi_2O_5$ and sanbornite (low-$BaSi_2O_5$). As a
95 first step, the crystal lattice parameters were determined using Rietveld refinement of powder
96 diffraction and first-principles calculations. Second, the ^{29}Si magic spinning angle nuclear
97 magnetic resonance (MAS NMR) and Raman spectra were used to identify features associated
98 with each of the contributions of the Q^n species within these structures. Finally, an evaluation of
99 the vibrational modes and their origin is reported based on simulation results using *ab initio*
100 calculations at the density functional level of theory (e.g. Gomes et al. 2019). The theoretical and
101 experimental results are in excellent agreement and clearly reveal the differences between homo-
102 and hetero-connectivity in barium silicates. We conclude by emphasizing some of the
103 implications for the interpretation of Raman spectra of silicate liquids and glasses (e.g. Moulton
104 et al. 2018), where hetero-connectivity is the rule rather than the exception.

105 Ba_2SiO_4 is composed of isolated tetrahedra (Q^0 species) surrounded by Ba^{2+} cations which
106 form an arcanite-type (β-K_2SO_4) structure (McGinnety 1972). The composition range $BaSiO_3$-
107 $BaSi_2O_5$, including the hetero-connective phases, form a series with the general formula
108 $Ba_{m+1}Si_{2m}O_{5m+1}$. Here m = 1, 3, 4, 5, or ∞, and is the number of silica tetrahedra which form the
109 *zweier* single chains, m = 1, ribbons or *zweier* triple–quintuple chains, for m = 3-5, and
110 ultimately, sheets, for m = ∞ (Fig. 1); e.g. sanbornite (Hesse and Liebau 1980a, 1980b). Ba^{2+} is
111 able to stabilize these structures due to its low electronegativity, 0.89, and large ionic radius, 1.35
112 Å (Brown and Altermatt 1985; Gagné and Hawthorne 2015). As a result, barium silicates can be
113 formed with a wide range of topologies. In fact, Liebau (1985) noted that the Ba- and Si-
114 substructures stretch and twist so that the diameter of one BaO_x polyhedron is approximately
115 equal to Si-Si distance. This produces an internal strain on these tetrahedra making these chains
116 quite stretched compared to other, smaller alkaline-earth-bearing inosilicates. This is the
117 explanation of why no Q^1 phase, e.g. $Ba_3Si_4O_{11}$, is known, because the extreme strain is more
118 than can be accommodated by stretching or twisting adjacent tetrahedra (Liebau 1985). The
119 topologies of the barium silicates and how they compare to other silicate groups are further
120 discussed in recent articles (Hawthorne et al. 2019; Day and Hawthorne 2020).

2 Experimental and theoretical procedures

2.1 Synthesis of barium silicate powders

Batches of 3-5 g of high-purity SiO_2 and $BaCO_3$ (Sigma-Aldrich, >99.9%) reagents where used to synthesize the crystalline xBaO·(1-x)SiO_2 (x = 0.33, 0.375, 0.385, 0.40, 0.50, and 0.66) phases. The solid-state reaction procedure of Gorelova et al., (2016) was followed where between successive heat treatments the samples were repeatedly ground and pressed into tablets. Heat treatment protocols comprised two steps prior to the final temperature: a low-temperature heating step (1 h at 500°C) for removing polyvinyl butyral (used as a binder material to increase the density) of the pellets, followed by calcination for 1 h at 1000°C. The crystalline samples where ground using a mixture of sample plus ZrO_2 balls in a high-energy vibrating mill for 2 h. The milled powders produce very-fine and evenly distributed grain sizes resulting in an improved compositional homogeneity. This is critical to reduce the number of phases present in this system where the compositions of stable phases differ by only a few mole percent.

2.2 Characterization of the samples

All the crystal structures have been confirmed using X-ray diffraction (XRD). XRD measurements were made on a Rigaku Ultima IV machine using Cu K_α radiation operating at 40 kV and a current of 20 mA using continuous scanning mode (0.5° min^{-1}) with a 2θ step of 0.02° between $10° \leq 2\theta \leq 80°$. The diffraction patterns were refined using the GSAS program (Rietveld 1967; Larson and Von Dreele 2004) and show that the crystalline phases are of high purity and contain <1% of any impurity.

The Raman spectra were taken on a LabRAM HR800 spectrometer using a 532 nm wavelength laser which supplied ~20 mW on the sample. Spectra were taken using a 100X visible objective (lateral spatial resolution ~1 μm), 100 μm pinhole, and an 1800 gr/mm grating between 10 – 1600 cm^{-1} or greater range (resolution ≤0.5 cm^{-1}). Raman spectra of the crystalline phases were measured using 12 accumulations and a dwell time of 5 s. Reported spectra below are normalized to the intensity of the most intense band, representing the symmetric stretching mode. In order to characterize the vibrational modes, the spectra first had a flat baseline removed, except near the laser line, and were then curve fit using Lorentzian lineshapes to determine the mode character. This procedure yielded excellent fits to the spectra overall.

The solid-state ^{29}Si MAS NMR spectra were recorded with an Agilent DD2 spectrometer operating at 5.64 T. The measurements were conducted in a 7.5 mm MAS-NMR probe, using $\pi/2$ pulses of 5.5 μs length, a rotation frequency of 5.0 kHz and a relaxation delay of up to 30 000 s, depending on relaxation characteristics, ensuring quantitatively reliable detection. The chemical shifts are reported relative to tetramethylsilane using $CaSiO_3$ as a secondary reference (δ = –71.33 ppm). All line shape deconvolutions were done using the DMFIT software (Massiot et al. 2002).

2.3 Computational methods and model systems

Density functional theory (DFT) level calculations of the lattice parameters and vibrational modes were carried out using Becke's three-parameter hybrid non-local exchange functional, combined with a Lee-Yang-Parr gradient-corrected correlation functional (B3LYP), implemented in the CRYSTAL17 package (Dovesi et al. 2018). The centered atoms were described using pseudopotential databases: (Towler 1996), 88-31G* (Nada et al. 1996) and 8-411d11G (Valenzano et al. 2006) (all-electron) for Ba, Si and O, respectively. In relation to the diagonalization of the density matrix, the reciprocal space net was described using a shrinking factor of 4 and generated according to the Monkhorst–Pack scheme. The accuracy of the evaluation of the Coulomb and exchange series was controlled by five thresholds at values of 10^{-7}, 10^{-7}, 10–7, 10^{-7}, and 10^{-14}. The vibrational frequencies calculation was performed at the Γ point within the harmonic approximation, and the dynamic matrix was computed by the numerical evaluation of the first derivative of analytical atomic gradients. The optimized structural parameters of the crystal structures are reported in Table 1. We have used the same procedure here as in our initial works, first on $BaMoO_3$ (Gomes et al. 2019) and more recently on sanbornite and $Ba_5Si_8O_{21}$ (Gomes et al. 2021).

3 Results

The results of the bulk structural analysis from experimental measurements and first principle calculations are reported before discussing the Raman and ^{29}Si MAS NMR spectra. For simplicity the phases are referred to by their $BaO:SiO_2$ molar ratios, as indicated in the ID of Table 1. For example, monoclinic $Ba_4Si_6O_{16}$ is denoted **B4S6**.

This is the peer-reviewed, final accepted version for American Mineralogist, published by the Mineralogical Society of America.
The published version is subject to change. Cite as Authors (Year) Title. American Mineralogist, in press.
DOI: https://doi.org/10.2138/am-2021-7910. http://www.minsocam.org/

3.1 Crystal structures determined by XRD

The crystal cell dimensions, β angles and volumes are reported in Table 1. An example of the Rietveld refinement of B6S10 is provided in Figure 2. Individual refinements are shown in the supplementary material, Section S2 (Fig. S1). The cell volumes of the barium silicates derived from Rietveld refinements are within <1% of reported values (Grosse and Tillmanns 1974b, 1974a; Hesse and Liebau 1980a, 1980b). The relaxed cell volumes of the DFT simulations reproduce the reported values within <4%. Therefore, the experimental and calculated crystal structures are in good agreement.

3.2 ^{29}Si NMR results

Single sharp peaks are observed at -93.1 ppm for low-BS2, -80.0 ppm for high-BS, and -70.1 ppm for B2S (Fig. 3), in agreement with published values (Smith et al. 1983; Mägi et al. 1984; Murdoch et al. 1985). The hetero-connected barium silicates show a range of chemical shift values consistent with those expected for other Q^2- and Q^3-bearing phases (Table 2). In samples containing multiple Si sites, the relative peak areas are in excellent agreement with the expected proportions. The NMR spectra of the hetero-connected B4S6, B5S8, and B6S10 phases are reported here for the first time.

3.3 Raman spectra and their vibrational mode assignments

The Raman spectra of the barium silicates are dominated by intense peaks in the 400-800 cm^{-1} (Fig. 4a) and 800-1200 cm^{-1} (Fig. 4b) ranges that correspond to the *bending* and *stretching* mode regions, respectively (c.f. Gomes et al. 2021). Table 3 summarizes the observed high-intensity Raman peaks. A detailed discussion of all modes is beyond the focus of this work; however, a full analysis of all vibrational modes is provided in supplementary material Sections S3 and S4. In Table 4 a complete mode analysis of Ba_2SiO_4 is provided as an example. Given the numerous vibrational modes (e.g. Table S3) and the small frequency differences among them, further refinement of our interpretation through polarized or oriented single crystal investigations should be possible. Given the complexity of the Raman spectra (Fig. S2), we emphasize that the overall agreement between theoretical and experimental values is excellent.

An analysis of the results for high-BS renders that the intense band at 599.8 cm^{-1} is associated with Si-O1-Si bending motion (Table S2). The symmetry of high-BS, $P2_12_12_1$, is unique among the phases studied and the 599.8 cm^{-1} band is displaced from those belonging to

the bending modes of the other phases. The intense bands originating from the bending modes of the B4S6-BS2 phases display a doublet or triplet feature centered around ~530 cm^{-1} (Fig. 4a). B4S6, B5S8, B6S10 and high-BS2 have similar unit cell symmetries, either $P2_1/c$ or C2/c, and similar intense bending mode frequencies. Despite the observed similarities in the spectra, the origins of these modes are quite distinct. For example, in low-BS2 the 535.5 cm^{-1} mode involves bending of the O3-Si-O2, where one oxygen is a BO and the other a NBO (Table S7). In contrast, the 533.8 cm^{-1} mode of high-BS2 involves the bending of the Si3-O2-Ba2 bond angle (Table S6). As the origin of the intense bending modes is structure dependent, any generalizations regarding relationships between mode frequency and crystal chemical properties, such as the mean inter-tetrahedral angle, should be treated with caution, except in cases where the mode originates in the actual bending of Si-O-Si bond angles.

The higher frequency region (>800 cm^{-1}) consists of Si-O stretching modes that are often attributed to Q^n species (Fig 4b). In early studies which applied the central force model to Q^n species generated symmetric (υ_1-type) and antisymmetric (υ_3-type) stretching modes, any deviation from tetrahedral symmetry was thought to produce vibrational coupling between these modes (c.f. McMillan 1984). Vibrational coupling of υ_1- and υ_3-type modes was expected to produce frequency shifts and changes in the relative intensities of the peaks particularly in nesosilicates (Piriou and McMillan 1983). Lam et al., (1990) challenged these inferences using lattice dynamic calculations to reproduce the trends in the stretching modes of forsterite. However, as Dowty (1987) emphasizes, the term *mode coupling* has been inconsistently applied. Furthermore, the success of central force calculations in reproducing the mode frequencies has been lessened by the model dependence of these calculations. More recent DFT-based approaches (e.g. Zicovich-Wilson et al. 2004; Aliatis et al. 2015; Stangarone et al. 2017; Gomes et al. 2019, 2021) have found excellent agreement between experimental and simulated spectra without such model dependence. The results herein overwhelmingly confirm that most of the high-frequency peaks originate from specific and singular Si-O stretching vibrations regardless of the structural type or unit.

In the high-frequency region, the most intense peaks correspond to Si-O stretching modes are characteristic of the Q^n species (e.g. McMillan 1984; Nesbitt et al. 2017a, 2018, 2020). The barium silicate structures contain Q^0, as well as homo-connected Q^2 and Q^3 species, show

239 stretching modes that shift from 823.8 cm^{-1} in B2S to 963.9 cm^{-1} for high-BS to 1077.7 cm^{-1} for
240 low-BS2 (Fig. 4b). The 964 cm^{-1} peak of high-BS originates from symmetric stretching motions
241 of the O3 and O2 sites away from the central Si. In contrast, the 823.7 cm^{-1} peak of B2S and the
242 1077.9 cm^{-1} peak of low-BS2 both involve the elongation of the Si-O1 bonds in their respective
243 structures. The hetero-connected phases show intense peaks around ~1065 cm^{-1} that shift to
244 higher frequencies with increasing proportion of Q^3 species. The intense high-frequency peaks of
245 B6S10, B5S8 and B4S6 are found at 1069.2, 1066.8 and 1061.0 cm^{-1}, respectively. Simulations
246 of the stretching modes lead us to conclude that the B4S6 mode at 1061.0 cm^{-1} originates from
247 Si3-O8 bond stretching (Table S3) whereas the B5S8 mode at 1066.8 cm^{-1} comes from Si3-O7
248 bond stretching (Table S4). Both of these belong to Q^3 sites which are bonded to Q^3 only.
249 Consequently, the Q^3 units do not need to be directly bonded to the Q^2 site to induce a frequency
250 shift. This indicates that the electron density is spread across the tetrahedral ribbon.

251 These hetero-connected phases display two other features that are characteristic of their
252 spectra. First, the main peaks overlap strongly with adjacent peaks, and, second, they display
253 other peak(s) centered near 925 cm^{-1} (Fig. 4b). The former feature may be expected as the
254 hetero-connected phases have three or more Si sites and many O sites. Peaks at comparable
255 wavenumbers (928.1, 924.0 and 921.3 cm^{-1}) are observed for B6S10, B5S8 and B4S6,
256 respectively, i.e., at slightly lower wavenumbers than the 963.9 cm^{-1} peak of high-BS. Again,
257 simulations lead us to conclude that the B4S6 mode, at 928.1cm^{-1}, originates from Si1-O2
258 stretching (Table S3) whereas the B5S8 mode, at 924.0 cm^{-1}, involves simultaneous stretching of
259 the Si1 away from both the O1 and O2 sites (Table S4). The trend here is that as the proportion
260 of Q^2 increases, the vibrational frequency of the Q^2 unit increases. This is the same as for the Q^3
261 units whose frequencies also increase with increasing proportion of Q^3. In both cases, the shift is
262 toward the frequency observed in the homo-connected structures.

263 The above findings correspond to the high intensity Raman modes that are obvious in the
264 spectra, however, other vibrational modes may provide insights in future studies. Full analysis of
265 the vibrational modes in the complete spectra for B2S is reported in Table 4 whereas the
266 remaining mode analysis of high-BS, B4S6, B5S8, B6S10, high-BS2, and low-BS2 are presented
267 in Table S2, Table S3, Table S4, Table S5, Table S6 and Table S7, respectively. Calculated
268 values reproduce the mode frequencies of the measured spectra with a mean absolute deviation

of <7 cm^{-1}. However, the experimental Raman spectra usually reveal only two thirds the number of expected normal modes, and consequently, there is always some ambiguity even in polarized single crystal studies (e.g. Chopelas 1991). We hope that reporting the complete mode analysis will provide insights in future studies (e.g. in studying the effects of dopants or *in situ* reactions).

4 Discussion

4.1 NMR chemical shifts and structural attributes

The most successful empirical model of the ^{29}Si NMR chemical shifts comes from Sherriff and Grundy (1988). The predictive capacity of this model is very good with $\delta_{measured}$-$\delta_{predicted}$ <2 ppm for a wide range of silicates and aluminosilicates. The isotropic chemical shift (δ) is predicted from:

$$\delta = 650.08\chi'' - 56.06 \quad (1)$$

where

$$\chi'' = \sum s((1 - 3\cos^2\theta)/3R^3)\left(\frac{\cos\alpha}{\cos\alpha - 1}\right) \quad (2)$$

Here s is the bond valence of the M-O bond, R is half the distance between the O and the second neighbour (M), and θ and α are the Si-O-M and O-M-Si angles, respectively (Sherriff and Grundy 1988). The summation includes all the second-nearest neighbors. In the present case the measured shifts are not well reproduced when all the second neighbours are included, possibly due to the high coordination number of Ba^{2+} cations. Therefore, we have tested two different constraints in calculating χ'': (i) using a cut-off distance of 3.7 Å for second neighbours (or 3.8 Å when an additional neighbour was found at the limit) or (ii) considering only the two closest second next nearest neighbours (2 NNN). Both constraints result in fewer second neighbour Ba cations being included in the calculation of χ'', and both reproduce many of the chemical shifts reasonably well, while they fail for others (see Table 5). We also find that the second constraint produces worse predictive accuracy for low-silica compositions. Overall, our results indicate that even under these constraints, χ'' does not correctly account for the influence of Ba-O bonding on the ^{29}Si chemical shifts.

The reason for the success of the Sherriff and Grundy model is that it incorporates many of the crystal chemical parameters which had already been empirically shown to have a strong

This is the peer-reviewed, final accepted version for American Mineralogist, published by the Mineralogical Society of America.
The published version is subject to change. Cite as Authors (Year) Title. American Mineralogist, in press.
DOI: https://doi.org/10.2138/am-2021-7910. http://www.minsocam.org/

297 influence on the chemical shift, for example, the connectivity (Lippmaa et al., 1980; Smith et al.,
298 1983), the Si-O bond length (Grimmer and Radeglia, 1984), the bond strength (Mägi et al.,
299 1984), the mean inter-tetrahedral angle (Dupree and Pettifer, 1984), the electronegativity (Janes
300 and Oldfield, 1985), and the σ orbital hybridization (Engelhardt and Radeglia, 1984). Despite
301 this success, there were hints that covalency effects of non-silica second neighbours were not
302 well incorporated. For instance, Si-poor phases, e.g., nesosilicates, are somewhat less well
303 described by this model than more siliceous ones. In the original report the calculation for
304 forsterite yields a chemical shift of -67.8 ppm whereas it is measured at -62.0 ppm, which is a
305 two-to-three times worse agreement than observed for the majority of the silicates studied. More
306 recently, *ab initio* methods have been more successful at predicting the chemical shifts of
307 Mg_2SiO_4 polymorphs (e.g. Ashbrook et al. 2007), although no additional insight regarding the
308 chemical shielding of the silicate tetrahedra was offered beyond the original empirical trends.
309 Given the constraints discussed above, the experimental chemical shifts are in good agreement
310 with those predicted by the Sherriff and Grundy model (**SG88**), with $\delta_{measured}$-$\delta_{predicted}$ values
311 usually <5 ppm but as large as 12 ppm in B2S (Table 5) without any indication of systematic
312 discrepancies.

313 Although several factors affect the chemical shift, strong linear correlations with the inter-
314 tetrahedral angle have been found for three Q^3-bearing alkali phyllosilicates (De Jong et al.
315 1998), however, for barium silicates the correlation between chemical shift and inter-tetrahedral
316 angle is clearly nonlinear (Fig. 5). For hetero-connective structures, the Q^3 chemical shift appears
317 to be more sensitive to smaller inter-tetrahedral angles (<140˚) than to large ones (Table 6). In
318 contrast, the Q^2 chemical shifts considered here are almost independent of inter-tetrahedral angle.
319 Ultimately, there is an influence of mean inter-tetrahedral angle on the chemical shift, but other
320 factors need to be taken into consideration, e.g., steric limits, as the linear regressions of figure 4
321 are weak (R^2 = ~0.7).

322 The extreme shifts displayed by the barium silicate Q^2 species are more evident when the
323 overall trends between the Q^n units and chemical shift are shown (Fig. 6). This data is compiled
324 from the literature (see supplemental materials; Smith et al. 1983; Mägi et al. 1984; Kinsey et al.
325 1985; Murdoch et al. 1985; Sherriff and Grundy 1988; De Jong et al. 1998; Ashbrook et al.
326 2007). For the barium silicates which have highly strained Q^2 sites, their chemical shift is

327 essentially at the extreme positive end, near -80 ppm, of the distribution of literature values. The
328 remaining Q^0 and Q^3 peaks of the barium silicates are situated near the grand mean chemical
329 shift defined by the range of literature values for these Q^n species. Although the above discussion
330 takes the perspective of the Q^n species above, we would point out that broadly the Q^n species
331 correspond to crystal groups within the structural hierarchy hypothesis (Hawthorne et al. 2019):
332 cluster silicates (Q^{0-1}), chain-ribbon silicates (Q^{2-3}), sheet silicates (Q^3) and framework silicates
333 (Q^4).

334 ## 4.2 Si-O stretching frequency versus connectivity

335 The stretching vibrations of the barium silicates have been plotted alongside our analysis of
336 values taken from the RRUFF database (Lafuente et al. 2015) and published studies on the
337 *nesosilicates* (Q^0 – Handke and Urban 1982; Piriou and McMillan 1983; Chopelas 1991;
338 Mohanan et al. 1993; Voronko et al. 2006; Bispo et al. 2017), the *sorosilicates* (Q^1 - Tarte et al.
339 1973; Gabelica-Robert and Tarte 1979, 1981; Nesbitt et al. 2018), the *inosilicates* (Brawer and
340 White 1975; Konijnendijk and Stevels 1976; Richet et al. 1998; Huang et al. 2000; Tribaudino et
341 al. 2012, 2019; Mantovani et al. 2015; Nesbitt et al. 2018) and the *phyllosilicates* (Q^3 –Brawer
342 and White 1975; Konijnendijk and Stevels 1976; McKeown and Bell 1998; Moulton et al. 2019)
343 in Figure 7. The stretching modes of the phases in figure 7 were established either, because prior
344 mode analysis has been reported, or, the modes were identified due to their intensity – usually
345 ~10 times stronger than adjacent bands in spectra. Although clear trends are found, this was not a
346 trivial task as the stretching modes often give rise to less intense Raman bands than the bending
347 modes for both the phyllosilicates (e.g. Wang et al. 2015) and double chain amphiboles (e.g.
348 tremolite-actinolite group – Apopei and Buzgar 2010; Ott and Williams 2020). These values
349 should be taken with caution because they are only a subset within the diversity of modes in
350 these spectra.

351 As with ^{29}Si chemical shifts, the extreme values for the Si-O stretching frequencies of the Q^n
352 species somewhat overlap. For example, the ranges of stretching frequencies assigned to Q^2 and
353 Q^3 units overlap in the 1010-1035 cm^{-1} region (Fig. 7). This region usually corresponds to
354 differences in composition and crystal symmetry. For example, Handke and Urban, (1982) report
355 the alkaline earth orthosilicate series, Be_2SiO_4-Ba_2SiO_4, where all intense stretching modes range
356 from 810 to 840 cm^{-1} except for beryllium-nesosilicate which has a value of 880 cm^{-1}, closer to

This is the peer-reviewed, final accepted version for American Mineralogist, published by the Mineralogical Society of America.
The published version is subject to change. Cite as Authors (Year) Title. American Mineralogist, in press.
DOI: https://doi.org/10.2138/am-2021-7910. http://www.minsocam.org/

the typical Q^1 frequency. The reason for this is that Be^{2+} cation is much smaller and more strongly electronegative than the other alkaline earth elements and consequently it crystallizes in the hexagonal phenakite-type structure, rather than other olivine group minerals with larger and more electropositive cations Mg^{2+} to Ba^{2+} which crystallize to orthorhombic or monoclinic structures at ambient conditions.

144 Raman spectra give a grand mean ν_{Qn} ($\pm\sigma$) frequency of 827.7 ($\pm$13.8) cm^{-1} for Q^0, 905.3 ($\pm$22.1) cm^{-1} for Q^1, 993.5 ($\pm$25.9) cm^{-1} for Q^2, and 1068.4 ($\pm$17.6) cm^{-1} for Q^3 (Fig. 7). For the homo-connected barium silicates, the main stretching frequencies are well within their respective Q^n ranges, although the Q^2 mode of BS is near the lower end of the range of Q^2 frequencies. This is consistent with above NMR results, where the Q^2 units also resonate towards the extreme end of the Q^2 chemical shifts. Above it was shown that the intense high-frequency peaks are usually related to individual Si-O stretching motions. Therefore, it is somewhat surprising that the trends in the high-intensity stretching modes are so distinct. Nonetheless, the trend is evidently robust (Fig. 7). The effects of crystal symmetry within each of the Q^n species structural groups deserves further consideration. Although the high-frequency modes originate from different bonds, the relative bond strength of the tetrahedron, related to the number of next-nearest-neighbour Si, or other tetrahedral elements, controls the values of the vibrational frequency.

4.2.1 The effect of hetero-connectivity on the stretching mode frequencies

Raman spectra of the anhydrous hetero-connected siliceous phases are rare. The series from B4S6 to B6S10 which form triple-, quadruple- and quintuple-chains containing Q^2:Q^3 ratios from 1:2 to 1:4 (Fig. 1). This series represents a rare opportunity to compare the vibrational spectra of these phases of relatively simple (e.g., anhydrous, low symmetry) and comparable chemistry (e.g. only containing Ba, Si, and O). As a result, the main structural differences associated with the localized Si-O stretching modes are related to their local bonding environments. The DFT-based simulations allow us to unveil the origin of the vibrational modes (e.g., Table 4). An analysis of these results renders that the hetero-connected phase s have a second moderately intense band near 925 cm^{-1}, which is related to the Q^2 site and another peak near 1070 cm^{-1} related to the Q^3 site (Fig. 4B). The observed shift of the former feature from 921.3 in B6S10 to 928.1 cm^{-1} in B4S6, is likewise observed in the Q^3 modes which shift from

1061 to 1069 cm^{-1}, respectively. In both the Q^2 and Q^3 cases, the shift reflects a trend towards the frequencies of the homo-connected Q^n species. It is also important to note that the relative intensity of the Q^2 peak compared to that of the Q^3 peak does not increase with increasing Q^2 content. Nonetheless, we may conclude that for barium silicates the Q^2 and Q^3 modes shift systematically to higher frequencies with increasing proportion of their respective Q^n contents. However, this also depends on how distorted these Q^n species are to begin with as Q^2 is already at the extreme end of the range of Q^2–related Si-O-Si bond angles. Next, we test these trends as compared to other hetero-connected phases, tremolite and xonotlite.

4.3 Comparison to other hetero-connected phases: Tremolite & Xonotlite

To reinforce the finding above, we compare the results on two phases that have similar chemistry, 'simple' alkaline-earth-bearing silicates, by analyzing available structural and spectroscopic data. The first mineral considered is the amphibole endmember tremolite, $Ca_2Mg_5Si_8O_{22}(OH)_2$, which has two tetrahedral sites, one Q^2 and one Q^3 in equal proportion. The second mineral is xonotlite ($Ca_6Si_6O_{17}(OH)_2$), which has a Q^2:Q^3 ratio of 2:1. Tremolite contains a double chain where *every other* tetrahedron is a Q^3 unit which links the two chains forming six-membered rings (Hawthorne and Grundy 1976; Gibbs et al. 2005; Antao et al. 2008). Xonotlite also has double chains but with *every third* tetrahedron is crosslinked by a Q^3 site (Brown 1978; Kudoh and Takéuchi 1979; Hejny and Armbruster 2001). Their Raman and ^{29}Si MAS NMR spectra have been reported (Mägi et al., 1984; Apopei and Buzgar, 2010; Frost et al., 2012) and their stretching mode positions have been included in figures 6 and 7.

In terms of ^{29}Si MAS NMR, both xonotlite and tremolite show Q^2 chemical shifts near the average value observed for crystalline compounds containing Q^2 species, at -87 ppm (Fig. 6). The chemical shift of the Q^3 species in xonotlite adopts a near-extreme value at -97.6 ppm whereas in tremolite this peak is found at -92.2 ppm. Xonotlite shows a Q^2-Q^3 peak separation of 11 ppm, comparable to the separation observed in the hetero-connected barium silicates whereas the separation is only ~5 ppm for tremolite (Table 5). Tremolite, containing the smaller Mg cation, does not appear to show a large distortion of the tetrahedral ribbons whereas the Ca-rich xonotlite is considerably distorted and shows a large separation between Q^2 and Q^3 peaks. Apparently, the influence of the hydroxyl groups on the chemical shielding is smaller than the distortion produced simply from having large counterions like Ca^{2+} or Ba^{2+} cations. This

This is the peer-reviewed, final accepted version for American Mineralogist, published by the Mineralogical Society of America.
The published version is subject to change. Cite as Authors (Year) Title. American Mineralogist, in press.
DOI: https://doi.org/10.2138/am-2021-7910. http://www.minsocam.org/

417 comparison suggests that the Q^3 site of xonotlite is considerably strained whereas it is the Q^2
418 sites in the hetero-connected barium silicates, which appears to be strained (e.g. note the
419 tetrahedra volumes in Table 6).

420 In terms of Raman spectra, xonotlite and tremolite show similar behavior as B4S6, B5S8
421 and B6S10 (Fig. 7). The wavenumbers observed for the Q^2 unit of xonotlite (962.5 cm^{-1}) and BS
422 are essentially equal whereas that of the Q^3 band is found to be slightly lower (1044 cm^{-1}) than
423 those in the barium-containing phases (~1070 cm^{-1}). In view of the previously discussed trends
424 this shift is expected given that there are more Q^2 than Q^3 units in the xonotlite structure. In
425 contrast, the intense Raman bands of Q^2, at 929 cm^{-1}, and the Q^3 mode, at 1059 cm^{-1}, of tremolite
426 appear at very similar frequencies as those observed in the hetero-connected barium phases. This
427 is expected as tremolite has equal proportions of Q^2 and Q^3 units and thus can be considered
428 structurally similar to the B4S6 phase.

429 In summary, the general trends found among anhydrous barium silicates are consistent with
430 other hetero-connective phases with some subtle differences related to the distortion among sites
431 within each structure. This comparison shows a more systematic behavior of Raman modes in
432 hetero-connected phases whereas the relationship between ^{29}Si chemical shifts and local
433 geometry appears to be more complex. Understanding the subtleties highlighted here will
434 hopefully lead us to a better understanding of why the clear trends in NMR peaks of the alkali
435 silicate glasses are better reproduced than those of alkaline earth silicates glasses (e.g. Pedone et
436 al. 2010; Charpentier et al. 2013).

437 ### 4.4 On the complementary nature of NMR and Raman measurements

438 The above results of barium silicates point out important differences between the Q^n group
439 signatures in NMR and Raman spectroscopy. The inferences of one are not directly applicable to
440 the other, nor vice versa. In fact, while the correlations between vibrational wavenumber or
441 chemical shifts with the type of structural group have a well-established positive correlation (Fig.
442 6,7), structural trends *within a Q^n group* are essentially orthogonal (dashed lines in Fig. 8) to the
443 general trend. For example, in the present barium silicates the ^{29}Si chemical shifts of the Q^3
444 units show a broad distribution across ~10 ppm whereas the Q^2 peaks shift over a much narrower
445 range, only ~2 ppm. In contrast, the Raman mode wavenumbers display the opposite behavior.
446 For the Q^2 stretching modes, variations on the order of ~40 cm^{-1} are observed whereas the Q^3

This is the peer-reviewed, final accepted version for American Mineralogist, published by the Mineralogical Society of America.
The published version is subject to change. Cite as Authors (Year) Title. American Mineralogist, in press.
DOI: https://doi.org/10.2138/am-2021-7910. http://www.minsocam.org/

447 modes only spread across half this range, ~20 cm^{-1}. These differences arise because the Q^n
448 chemical shifts are strongly influenced by the second nearest neighbours, whereas the vibrational
449 modes associated with the Q^n units are highly localized, often to specific Si-O bonds. As a result
450 of this behavior, the main bands in the Raman spectra do shift systematically in frequency, even
451 in the hetero-connected cases, whereas the ^{29}Si isotropic chemical shifts show a non-linear
452 behavior when a distribution of Q^n species are present. Overall, the origins of the Raman bands
453 of mineral phases remain poorly known and key mineral groups should be targeted in future
454 studies that combine quantum mechanical and experimental approaches (e.g. this study;
455 Stangarone et al. 2016; Gomes et al. 2021). This work emphasizes the complementary
456 information available using both spectroscopic techniques.

457 # 5 Implications

458 ## 5.1 Raman modes of Q^n species in silicate glasses and melts

459 Both Raman results and DFT-based calculations highlight that the stretching modes increase
460 in frequency with increasing the number of BO atoms (McMillan 1984; Rossano and Mysen
461 2012; Nesbitt et al. 2017b; Gomes et al. 2021). Moreover, we may now refine 'the Q^n bands' as
462 they are not related to the entire tetrahedral site but dominantly related to specific Si-O
463 vibrations. While in the hetero-connected phases there are always extra vibrational modes related
464 to the many Si-O bonds in these structures, which cause peaks to overlap, the most intense
465 features correspond to the main structural units. Our results display clear structural trends,
466 permitting future studies linking Raman frequencies to the specific distortions present for a given
467 group of the Q^n species. Moreover, we hope this aids in further distinction among the major
468 mineral groups.

469 When investigating unpolarized Raman spectra it is typically assumed that the most intense
470 features have A_g symmetry. However, the barium silicates show that the intense Raman peaks
471 display usually, but not exclusively, of A_g symmetry. For example, the vibrational modes of the
472 Q^n species discussed above for BS, B5S8, and H-BS2 are indeed A_g modes (e.g., Fig. 4B),
473 however, the intense high-frequency modes in B2S and low-BS2 have B_{3g} and B_{1g} symmetries,
474 respectively (see tables in supplementary material). This may lead to the misconception that
475 similar intensities are produced from similar structural origins. The phases studied above provide
476 no clear correspondence between any peak characteristic and its structural origin. Therefore, we

477 recommend that future experimental studies focus on polarized spectra in combination with *ab*
478 *initio* simulations to disclose this dichotomy.

479 Assuming that the vibrational modes in the crystalline phase have similar origins to those in
480 the glass (c.f. Brawer and White 1975), as has been demonstrated in the case of $BaSi_2O_5$
481 (Moulton et al. 2018), we offer several critical comments. First, the spectra of barium silicates
482 show that the intense stretching modes may originate from the bonds between Si and either BO
483 or NBO atoms, or both. This inference was also reported in simulations of Na-silicate glasses
484 (Kilymis et al. 2019). This information should be used to offer more circumspect mode
485 assignments for glass spectra as the stretching modes can be assigned to the Q^n species but
486 attributions to bonds between Si and specific oxygen atoms, or the whole tetrahedron, should be
487 treated with skepticism unless they are traced directly from bands having a known origin in an
488 isochemical crystal phase. Likewise, assignments relating antisymmetric versus symmetric
489 stretching modes appear to no longer be justified for the high-frequency modes, which tend to be
490 localized to specific bonds and not on the entire tetrahedron. Second, B_g and other lower-
491 symmetry modes can have high Raman scattering intensities. This insight may be important in
492 polarized studies of silicate glasses and melts which show that the depolarization ratio changes as
493 the frequencies deviate from the main Q^n peak center (e.g. Kalampounias et al. 2006, 2009).
494 Therefore, non-A_g modes, comparable to those described here, may provide an explanation for
495 the 'extra peaks' needed to fit the glass spectrum.

496 Finally, the present findings may serve as a guide for more refined and insightful
497 interpretation of Raman spectra in silicates. For instance, the degree of site distortion, as
498 indicated by the Si-O bond lengths and inter-tetrahedral angles, appears to be related to the
499 frequency within the range observed for individual Q^n units. For example, the Q^2 peak positions
500 in both the NMR and Raman spectra above are very close to the limit of the expected Q^2 range
501 and we know that the Q^2-bearing phase, BS, is at the limit of structural stability for the binary
502 barium silicates. When vibrational modes approach these limits, the structure suffers a symmetry
503 breaking process to accommodate a new lower energy configuration.

504

6 Acknowledgements

BJAM, TRC and CD are grateful to the São Paulo Research Foundation (FAPESP) for funding this research through post doctoral fellowship grants: 2016/18567-5, 2019/12383-8 and 2017/06649-0. The work was further supported by FAPESP grant number 2013/07793-6. We appreciate the support of CNPq and CAPES support to PSP. BJAM would like to thank Harold Lozano (NMR experiments), Millena Logrado (precursor NMR data reduction), and Valmor Mastelaro for making this collaboration possible. EOG acknowledges Generalitat Valenciana for the Santiago Grisolia program (2018/064). EOG and JA acknowledge financial support from Universitat Jaume I, for project UJI-B2019-30. EOG, JA, and LG appreciate support from the Ministerio de Ciencia, Innovación y Universidades (Spain) project PGC2018-094417-B-I00. We also wish to thank the Servei d'Informática, Universitat Jaume I, for their generous allocation of computer time. We would like to thank Mario Tribaudino and the referees for their critical comments which have and will continue to improve this research.

7 References

Aliatis, I., Lambruschi, E., Mantovani, L., Bersani, D., Andò, S., Diego Gatta, G., Gentile, P., Salvioli-Mariani, E., Prencipe, M., Tribaudino, M., and others (2015) A comparison between ab initio calculated and measured Raman spectrum of triclinic albite (NaAlSi3O8). Journal of Raman Spectroscopy, 46, 501–508.

Antao, S.M., Hassan, I., Wang, J., Lee, P.L., and Toby, B.H. (2008) State-of-the-art high-resolution powder X-ray diffraction (HRPXRD) illustrated with Rietveld structure refinement of quartz, sodalite, tremolite, and meionite. The Canadian Mineralogist, 46, 1501–1509.

Apopei, A.I., and Buzgar, N. (2010) The Raman study of amphiboles. Al. I. Cuza Iasi Geologie, 56, 57–83.

Ashbrook, S.E., Le Pollès, L., Pickard, C.J., Berry, A.J., Wimperis, S., and Farnan, I. (2007) First-principles calculations of solid-state 17O and 29Si NMR spectra of Mg2SiO4 polymorphs. Physical Chemistry Chemical Physics, 9, 1587–1598.

Bender, S., Franke, R., Hartmann, E., Lansmann, V., Jansen, M., and Hormes, J. (2002) X-ray absorption and photoemission electron spectroscopic investigation of crystalline and amorphous barium silicates. Journal of Non-Crystalline Solids, 298, 99–108.

Bispo, A.G., Ceccato, D.A., Lima, S.A.M., and Pires, A.M. (2017) Red phosphor based on Eu 3+ -isoelectronically doped Ba 2 SiO 4 obtained via sol-gel route for solid state lightning. RSC Advances, 7, 53752–53762.

Brawer, S.A., and White, W.B. (1975) Raman spectroscopic investigation of the structure of

539 silicate glasses: I. The binary alkali silicates. The Journal of Chemical Physics, 63, 2421–
540 2432.

541 Brown, I.D., and Altermatt, D. (1985) Bond-valence parameters obtained from a systematic
542 analysis of the Inorganic Crystal Structure Database. Acta Crystallographica Section B
543 Structural Science, 41, 244–247.

544 Brown, P.A. (1978) Xonotlite: a New Occurrence At Rose Blanche, Newfoundtand. Canadian
545 Mineralogist, 16, 67–672.

546 Calas, G., Henderson, G.S., and Stebbins, J.F. (2006) Glasses and melts: linking geochemistry to
547 materials science. Elements, 2, 265–268.

548 Charpentier, T., Menziani, M.C., and Pedone, A. (2013) Computational simulations of solid state
549 NMR spectra: A new era in structure determination of oxide glasses. RSC Advances, 3,
550 10550–10578.

551 Chen, M., Xia, Z., Molokeev, M.S., and Liu, Q. (2015) Insights into Ba4Si6O16 structure and
552 photoluminescence tuning of Ba4Si6O16:Ce3+,Eu2+ phosphors. Journal of Materials
553 Chemistry C, 3, 12477–12483.

554 Chopelas, A. (1991) Single crystal Raman spectra of forsterite, fayalite, and monticellite.
555 American Mineralogist, 76, 1101–1109.

556 Cormier, L., Gaskell, P.H., and Creux, S. (1999) Comparison of the low-Q features in diffraction
557 data for silicate glasses and crystals containing Sr or Ba. Journal of Non-Crystalline Solids,
558 248, 84–91.

559 Day, M.C., and Hawthorne, F.C. (2020) A structure hierarchy for silicate minerals: chain, ribbon,
560 and tube silicates. Mineralogical Magazine, 84, 165–244.

561 De Jong, B.H.W.S., Supèr, H.T.J., Spek, A.L., Veldman, N., Nachtegaal, G., and Fischer, J.C.
562 (1998) Mixed Alkali Systems: Structure and 29Si MAS NMR of Li2Si2O5 and K2Si2O5.
563 Acta Crystallographica Section B: Structural Science, 54, 568–577.

564 Denault, K.A., Brgoch, J., Kloß, S.D., Gaultois, M.W., Siewenie, J., Page, K., and Seshadri, R.
565 (2015) Average and local structure, debye temperature, and structural rigidity in some oxide
566 compounds related to phosphor hosts. ACS Applied Materials and Interfaces, 7, 7264–7272.

567 Douglass, R.M. (1958) The crystal structure of sanbornite, BaSi2O5. American Mineralogist, 43,
568 517–536.

569 Dovesi, R., Erba, A., Orlando, R., Zicovich-Wilson, C.M., Civalleri, B., Maschio, L., Rérat, M.,
570 Casassa, S., Baima, J., Salustro, S., and others (2018) Quantum-mechanical condensed
571 matter simulations with CRYSTAL. Wiley Interdisciplinary Reviews: Computational
572 Molecular Science, 8, e1360.

573 Dowty, E. (1987) Vibrational interactions of tetrahedra in silicate glasses and crystals - I.
574 calculations on ideal silicate-aluminate-germanate structural units. Physics and Chemistry
575 of Minerals, 14, 80–93.

576 Eskola, P. (1922) The silicates of strontium and barium. American Journal of Science, 5–4, 331–

375.

Frost, R.L., Mahendran, M., Poologanathan, K., and Xi, Y. (2012) Raman spectroscopic study of the mineral xonotlite Ca6Si6O17(OH)2 - A component of plaster boards. Materials Research Bulletin, 47, 3644–3649.

Gabelica-Robert, M., and Tarte, P. (1979) Vibrational spectrum of akermanite-like silicates and germanates. Spectrochimica Acta Part A: Molecular Spectroscopy, 35, 649–654.

——— (1981) Vibrational spectrum of fresnoite (Ba2TiOSi2O7) and isostructural compounds. Physics and Chemistry of Minerals, 7, 26–30.

Gagné, O.C., and Hawthorne, F.C. (2015) Comprehensive derivation of bond-valence parameters for ion pairs involving oxygen. Acta Crystallographica Section B Structural Science, Crystal Engineering and Materials, 71, 562–578.

Gibbs, G. V., Cox, D.F., Ross, N.L., Crawford, T.D., Burt, J.B., and Rosso, K.M. (2005) A mapping of the electron localization function for earth materials. Physics and Chemistry of Minerals, 32, 208–221.

Gomes, E.O., Fabris, G.S.L., Ferrer, M.M., Motta, F. V., Bomio, M.R.D., Andres, J., Longo, E., and Sambrano, J.R. (2019) Computational procedure to an accurate DFT simulation to solid state systems. Computational Materials Science, 170, 109176.

Gomes, E.O., Moulton, B.J.A., Cunha, T.R., Gracia, L., Pizani, P.S., and Andrés, J. (2021) Identifying and explaining vibrational modes of sanbornite (low-BaSi2O5) and Ba5Si8O21: A joint experimental and theoretical study. Spectrochimica Acta Part A: Molecular and Biomolecular Spectroscopy, 248, 119130.

Gorelova, L.A., Bubnova, R.S., Krivovichev, S. V., Krzhizhanovskaya, M.G., and Filatov, S.K. (2016) Thermal expansion and structural complexity of Ba silicates with tetrahedrally coordinated Si atoms. Journal of Solid State Chemistry, 235, 76–84.

Greaves, G.N. (1985) EXAFS and the structure of glass. Journal of Non-Crystalline Solids, 71, 203–217.

Grosse, H.-P., and Tillmanns, E. (1974a) Barium metasilicate BaSiO3 (h). Crystal Structure Communications, 3, 603–605.

——— (1974b) Barium orthosilicate Ba2SiO4. Crystal Structure Communications, 3, 599–601.

Handke, M., and Urban, M. (1982) IR and Raman spectra of alkaline earth metals orthosilicates. Journal of Molecular Structure, 79, 353–356.

Hawthorne, F.C., and Grundy, H.D. (1976) The Crystal Chemistry of the Amphiboles: IV. X-ray and Neurton refinements of the crystal structure of tremolite. Canadian Mineralogist, 14, 334–345.

Hawthorne, F.C., Uvarova, Y.A., and Sokolova, E. (2019) A structure hierarchy for silicate minerals: sheet silicates. Mineralogical Magazine, 83, 3–55.

Hejny, C., and Armbruster, T. (2001) Polytypism in xonotlite Ca6Si6O17(OH)2. Zeitschrift fur Kristallographie, 216, 396–408.

615 Hesse, K.F., and Liebau, F. (1980a) Crystal chemistry of silica-rich Barium silicates I:
616 Refinement of the crystal structures of Ba4[Si6O16], Ba5[Si8O21] and Ba6[Si10O26],
617 silicates with triple, quadruple and quintuple chains. Zeitschrift fur Kristallographie - New
618 Crystal Structures, 153, 3–17.

619 ——— (1980b) Crystal chemistry of silica-rich Barium silicates III: Refinement of the crystal
620 structures of the layer silicates Ba2[Si4O10] (I), (Sanbornite), and Ba2[Si4O10] (h).
621 Zeitschrift fur Kristallographie - New Crystal Structures, 153, 33–41.

622 Huang, E., Chen, C.H., Huang, T., Lin, E.H., and Xu, J.A. (2000) Raman spectroscopic
623 characteristics of Mg-Fe-Ca pyroxenes. American Mineralogist, 85, 473–479.

624 Kalampounias, A.G., Yannopoulos, S.N., and Papatheodorou, G.N. (2006) Temperature- induced
625 structural changes in glassy, supercooled, and molten silica from 77 to 2150 K. J. Chem.
626 Phys., 124, 14504.

627 Kalampounias, A.G., Nasikas, N.K., and Papatheodorou, G.N. (2009) Glass formation and
628 structure in the MgSiO3–Mg2SiO4 pseudobinary system: From degraded networks to
629 ioniclike glasses. The Journal of Chemical Physics, 131, 114513.

630 Kilymis, D., Ispas, S., Hehlen, B., Peuget, S., and Delaye, J.M. (2019) Vibrational properties of
631 sodosilicate glasses from first-principles calculations. Physical Review B, 99, 1–14.

632 Kinsey, R.A., Kirkpatrick, R.J., Hower, J., Smith, K.A., and Oldfield, E. (1985) High Resolution
633 Aluminum-27 and Silicate-29 Nuclear Magnetic resonance spectroscopic study of layer
634 silicates, including clay minerals. American Mineralogist, 70, 537–548.

635 Konijnendijk, W.L., and Stevels, J.M. (1976) Raman scattering measurements of silicate glasses
636 and compounds. Journal of Non-Crystalline Solids, 21, 447–453.

637 Kudoh, Y., and Takéuchi, Y. (1979) Polytypism of xonotlite: (I) Structure of an A-1 polytype.
638 Mineralogical Journal, 9, 349–373.

639 Lafuente, B., Downs, R.T., Yang, H., and Stone, N. (2015) The power of databases: the RRUFF
640 project., 1–30 p. (T. Armbruster & R.M. Danisi, Eds.)Highlights in Mineralogical
641 Crystallography Vol. pp. 1-30. W. De Gruyter.

642 Lam, P.K., Yu, R., Lee, M.W., and Sharma, S.K. (1990) Structural distortions and vibrational
643 modes in Mg2SiO4. American Mineralogist, 75, 109–119.

644 Larson, A.C., and Von Dreele, R.B. (2004) General Structure Analysis System (GSAS). Los
645 Alamos National Laboratory Report LAUR, 748, 86–748.

646 Liebau, F. (1985) Structural Chemistry of Silicates, 1st ed., 347 p. Springer Berlin Heidelberg,
647 Berlin, Heidelberg.

648 Lin, S., Lin, H., Huang, Q., Cheng, Y., Xu, J., Wang, J., Xiang, X., Wang, C., Zhang, L., and
649 Wang, Y. (2019) A Photostimulated BaSi2O5 :Eu2+ ,Nd3+ Phosphor-in-Glass for Erasable-
650 Rewritable Optical Storage Medium. Laser & Photonics Reviews, 13, 1900006.

651 Mägi, M., Lippmaa, E., Samoson, A., Engelhardt, G., and Grimmer, A.R. (1984) Solid-state
652 high-resolution silicon-29 chemical shifts in silicates. Journal of Physical Chemistry, 88,

1518–1522.

Mantovani, L., Tribaudino, M., Aliatis, I., Lambruschi, E., Lottici, P.P., and Bersani, D. (2015) Raman spectroscopy of CaCoSi2O6–Co2Si2O6 clinopyroxenes. Physics and Chemistry of Minerals, 42, 179–189.

Massiot, D., Fayon, F., Capron, M., King, I., Le Calvé, S., Alonso, B., Durand, J.O., Bujoli, B., Gan, Z., and Hoatson, G. (2002) Modelling one- and two-dimensional solid-state NMR spectra. Magnetic Resonance in Chemistry, 40, 70–76.

McGinnety, J.A. (1972) Redetermination of the structures of potassium sulphate and potassium chromate: the effect of electrostatic crystal forces upon observed bond lengths. Acta Crystallographica Section B Structural Crystallography and Crystal Chemistry, 28, 2845–2852.

McKeown, D.A., and Bell, M.I. (1998) Linked four-membered silicate rings: Vibrational analysis of Gillespite: BaFeSi4O10 and implications for glass structure. Physics and Chemistry of Minerals, 25, 273–281.

McMillan, P. (1984) Structural studies of silicate glasses and melts--applications and limitations of Raman spectroscopy. American Mineralogist, 69, 622–644.

Mohanan, K., Sharma, S.K., and Bishop, E.C. (1993) A Raman spectral study of forsterite-monticellite solid solutions. American Mineralogist, 78, 42–48.

Moulton, B.J.A., Rodrigues, A.M., Pizani, P.S., Sampaio, D.V., and Zanotto, E.D. (2018) A Raman investigation of the structural evolution of supercooled liquid barium disilicate during crystallization. International Journal of Applied Glass Science, 9, 510–517.

Moulton, B.J.A., Rodrigues, A.M., Sampaio, D. V., Silva, L.D., Cunha, T.R., Zanotto, E.D., and Pizani, P.S. (2019) The origin of the unusual DSC peaks of supercooled barium disilicate liquid. CrystEngComm, 21, 2768–2778.

Murdoch, J.B., Stebbins, J.F., and Carmichael, I.S.E. (1985) High resolution ^29Si NMR study of silicate and aluminosilicate glasses: the effect of network-modifying cations. American Mineralogist, 70, 332–343.

Nada, R., Nicholas, J.B., McCarthy, M.I., and Hess, A.C. (1996) Basis sets for ab initio periodic Hartree—Fock studies of zeolite/adsorbate interactions: He, Ne, and Ar in silica sodalite. International Journal of Quantum Chemistry, 60, 809–820.

Namwong, P., Laorodphan, N., Thiemsorn, W., Jaimasith, M., Wannakon, A., and Chairuangsri, T. (2010) A barium-calcium silicate glass for use as seals in planar SOFCs. Chiang Mai Journal of Science, 37, 231–242.

Nesbitt, H.W., Henderson, G.S., and Bancroft, G.M. (2017a) Electron densities over Si and O atoms of tetrahedra and their impact on Raman stretching frequencies and Si-NBO force constants. Chemical Geology, 461, 65–74.

——— (2017b) Electron densities over Si and O atoms of tetrahedra and their impact on Raman stretching frequencies and Si-NBO force constants. Chemical Geology, 461, 65–74.

Nesbitt, H.W., Bancroft, G.M., and Henderson, G.S. (2018) Temperature dependence of Raman shifts and line widths for Q0 and Q2 crystals of silicates, phosphates, and sulfates. American Mineralogist, 103, 966–976.

Nesbitt, H.W., Henderson, G.S., Bancroft, G.M., and Neuville, D.R. (2020) Spectral Resolution and Raman Q and Q cross sections. Chemical Geology, 562, 120040.

Oehlschlegel, G. (1975) Crystallization of Glasses in the System BaO*2SiO2-2BaO*3SiO2. Journal of the American Ceramic Society, 58, 148–149.

Ott, J.N., and Williams, Q. (2020) Raman spectroscopic constraints on compression and metastability of the amphibole tremolite at high pressures and temperatures. Physics and Chemistry of Minerals, 47, 27.

Pedone, A., Charpentier, T., and Menziani, M.C. (2010) Multinuclear NMR of CaSiO3 glass: simulation from first-principles. Physical Chemistry Chemical Physics, 12, 6054–6066.

Piriou, B., and McMillan, P.F. (1983) The high-frequency vibrational spectra of vitreous and crystalline orthosilicates. American Mineralogist, 68, 426–443.

Richet, P., Mysen, B.O., and Ingrin, J. (1998) High-temperature X-ray diffraction and Raman spectroscopy of diopside and pseudowollastonite. Physics and Chemistry of Minerals, 25, 401–414.

Rietveld, H.M. (1967) Line profiles of neutron powder-diffraction peaks for structure refinement. Acta Crystallographica, 22, 151–152.

Rossano, S., and Mysen, B. (2012) Raman spectroscopy of silicate glasses and melts in geological systems. European Mineralogical Union Notes in Mineralogy, 12, 321–366.

Roth, R.S., and Levin, E.M. (1959) Phase equilibria in the subsystem barium disilicate - dibarium trisilicate. Journal of Research of the National Bureau of Standards, 62, 193.

Schlenz, H., Kirfel, A., Schulmeister, K., Wartner, N., Mader, W., Raberg, W., Wandelt, K., Oligschleger, C., Bender, S., Franke, R., and others (2002) Structure analyses of Ba-silicate glasses. Journal of Non-Crystalline Solids, 297, 37–54.

Sherriff, B.L., and Grundy, H.D. (1988) Calculations of 29Si MAS NMR chemical shift from silicate mineral structure. Nature, 332, 819–822.

Shukla, A., Jung, I.-H., Decterov, S.A., and Pelton, A.D. (2018) Thermodynamic evaluation and optimization of the BaO-SiO2 and BaO-CaO-SiO2 systems. Calphad, 61, 140–147.

Smith, K.A., Kirkpatrick, R.J., and Henderson, D.M. (1983) High-resolution silicon-29 nuclear magnetic resonance study of rock-forming silicates. American Mineralogist, 68, 1206–1215.

Stangarone, C., Tribaudino, M., Prencipe, M., and Lottici, P.P. (2016) Raman modes in Pbca enstatite (Mg2Si2O6): an assignment by quantum mechanical calculation to interpret experimental results. Journal of Raman Spectroscopy, 47, 1247–1258.

Stangarone, C., Böttger, U., Bersani, D., Tribaudino, M., and Prencipe, M. (2017) Ab initio simulations and experimental Raman spectra of Mg2SiO4 forsterite to simulate Mars

729 surface environmental conditions. Journal of Raman Spectroscopy, 48, 1528–1535.

730 Takahashi, Y., Osada, M., Masai, H., and Fujiwara, T. (2010) Transmission electron microscopy
731 and in situ Raman studies of glassy sanbornite: An insight into nucleation trend and its
732 relation to structural variation. Journal of Applied Physics, 108, 63507.

733 Tarte, P., Pottier, M.J., and Procès, A.M. (1973) Vibrational studies of silicates and germanates-
734 V. I.R. and Raman spectra of pyrosilicates and pyrogermanates with a linear bridge.
735 Spectrochimica Acta Part A: Molecular Spectroscopy, 29, 1017–1027.

736 Thompson, L.M., McCarty, R.J., and Stebbins, J.F. (2012) Estimating accuracy of 17O NMR
737 measurements in oxide glasses: Constraints and evidence from crystalline and glassy
738 calcium and barium silicates. Journal of Non-Crystalline Solids, 358, 2999–3006.

739 Towler, M.D. (1996) Barium basis sets for the CRYSTAL program.

740 Tribaudino, M., Mantovani, L., Bersani, D., and Lottici, P.P. (2012) Raman spectroscopy of
741 (Ca,Mg)MgSi2O6 clinopyroxenes. American Mineralogist, 97, 1339–1347.

742 Tribaudino, M., Stangarone, C., Gori, C., Mantovani, L., Bersani, D., and Lottici, P.P. (2019)
743 Experimental and calculated Raman spectra in Ca–Zn pyroxenes and a comparison between
744 (CaxM2+1−x)M2+Si2O6 pyroxenes (M2+ = Mg, Co, Zn, Fe2+). Physics and Chemistry of
745 Minerals, 46, 827–837.

746 Valenzano, L., Torres, F.J., Doll, K., Pascale, F., Zicovich-Wilson, C.M., and Dovesi, R. (2006)
747 Ab Initio Study of the Vibrational Spectrum and Related Properties of Crystalline
748 Compounds; the Case of CaCO3 Calcite. Zeitschrift für Physikalische Chemie, 220, 893–
749 912.

750 Voronko, Y.K., Sobol, A.A., and Shukshin, V.E. (2006) Raman spectra and structure of silicon-
751 oxygen groups in crystalline, liquid, and glassy Mg 2SiO 4. Inorganic Materials, 42, 981–
752 988.

753 Walstrom, R.E., and Leising, J.F. (2005) Barium minerals of the Sanbornite Deposits. Axis, 1, 1–
754 18.

755 Wang, A., Freeman, J.J., and Jolliff, B.L. (2015) Understanding the Raman spectral features of
756 phyllosilicates. Journal of Raman Spectroscopy, 46, 829–845.

757 Xiao, F., Xue, Y.N., and Zhang, Q.Y. (2009) Bluish-green color emitting Ba2Si3O8:Eu2+
758 ceramic phosphors for white light-emitting diodes. Spectrochimica Acta - Part A: Molecular
759 and Biomolecular Spectroscopy, 74, 758–760.

760 Zicovich-Wilson, C.M., Pascale, F., Roetti, C., Saunders, V.R., Orlando, R., and Dovesi, R.
761 (2004) Calculation of the vibration frequencies of α-quartz: The effect of Hamiltonian and
762 basis set. Journal of Computational Chemistry, 25, 1873–1881.

763

764

765 **Figure captions:**

766 **Figure 1:** Structural features of the barium silicate phases showing homo-connected (top) and
767 hetero-connected (bottom) phases. Below each structure is their composition and Q^n species. For
768 the hetero-connected phases black triangles representing the tetrahedra across the ribbon
769 structure, are labelled with both their Q^n species (left-side triangles) and Si site number (right-
770 side). The structures contain Si (small blue), Ba (yellow), bridging oxygen (brown) and non-
771 bridging oxygens (red). Ba cations have been omitted for clarity in the hetero-connected
772 structures.

773

774 **Figure 2:** Diffractogram and Rietveld refinement of B6S10. The 'x' symbols are the
775 experimental measured values, the red solid line represents the calculated intensities from
776 Rietveld refinement and the blue solid line at the bottom is the residual curve between them.

777

778 **Figure 3:** ^{29}Si MAS NMR spectra of crystalline phases. Dashed lines are placed at -93.1 (homo-
779 connected Q^3) and -80.0 ppm (homo-connected Q^2). The weak additional resonances observed in
780 sample B5S8 arise from minor impurities of B6S10.

781

782 **Figure 4:** Representative Raman spectra of the bending (a) and stretching (b) regions of
783 crystalline barium silicates. Black marks below spectra indicate the theoretically calculated
784 frequency of the mode. Spectra are in the same order in both panels. Numbers inside triangles
785 correspond to vibrations depicted to the righthand side.

786

787 **Figure 5:** Chemical shift versus inter-tetrahedral angle for phases with Q^2 and Q^3 species. Error
788 bars are smaller than the symbols.

789

790 **Figure 6:** ^{29}Si MAS NMR chemical shift versus composition. Homo-connected barium silicate
791 are shown as hollow red circles. Hetero-connected barium silicates are shown as filled circles in
792 green for Q^3 and blue for Q^2. The data sources are reported in supplemental materials section
793 S5.1. Structural units are plotted by O:Si ratio showing Q^0 as 'X', Q^1 as squares, Q^2 as '+', Q^3 as
794 triangles and Q^4 as '—'. Lighter shades of these symbols indicate Al-bearing phases. Hetero-
795 connected tremolite and xonotlite are shown as purple diamonds.

796

797 **Figure 7:** Raman scattering wavenumber of the Si-O stretching modes versus composition. Peak
798 positions from this study are plotted as circles (open for homo-connected Q^n species; solid green
799 (Q^3) or blue (Q^2) for hetero-connected Q^n phases). Database values are for nesosilicates, Q^0,
800 (blue x), sorosilicates, Q^1, (orange squares), inosilicates, Q^2, (grey +), and phyllosilicates, Q^3

(yellow triangles). Purple diamonds refer to tremolite and xonotlite. The central lines and bars on the righthand side correspond to the mean Q^n position and $\pm 1\sigma$ of their distribution.

Figure 8: Raman wavenumber versus ^{29}Si chemical shift for the barium silicate phases. Note the trends within Q^2 and Q^3 resonances which are orthogonal to the general positive correlation observed for the Q^n species with chemical and Raman shifts.

This is the peer-reviewed, final accepted version for American Mineralogist, published by the Mineralogical Society of America.
The published version is subject to change. Cite as Authors (Year) Title. American Mineralogist, in press.
DOI: https://doi.org/10.2138/am-2021-7910. http://www.minsocam.org/

Table 1: Values of crystal structural parameters .

Phase ID	Phase Formula	BaO mol. %	O:Si	ICSD[1]	Space Group		Density (g/cm^3) theoretical	Density (g/cm^3) experimental	Cell Volume Å^3	a Å	b Å	c Å	β °	# of Sites (Wyckoff)	Ba CN_{PFU}[2]	Reference[3]
				6246			5.49		444.02	5.805	10.200	7.499	90.00			[i]
				291355			5.466		445.56	5.810	10.217	7.506	90.00	Ba: 2 (4 c)		[ii]
B2S	Ba_2SiO_4	66.6	4		Pmcn	62			444.76	5.807	10.209	7.503	90.00	Si: 1 (4 c)	9.5	[iii]
							5.464		**445.81(2)**	**5.811**	**10.220**	**7.507**	**90.00**			**This study - Rietveld**
							5.303		**460.62**	**5.861**	**10.358**	**7.586**	**90.00**			**This study - DFT**
				6245			4.44		319.46	4.580	5.611	12.431	90.00			[iv]
high-BS	$BaSiO_3$	50	3		$P2_12_12_1$	19			320.30	4.584	5.616	12.443	90.00	Ba: 1 (4 a)	8	[iii]
							4.419		**320.79(1)**	**4.585**	**5.619**	**12.450**	**90.00**	Si: 1 (4 a)		**This study - Rietveld**
							4.277		**322.13**	**4.616**	**5.692**	**12.260**	**90.00**			**This study - DFT**
				100310			3.98	3.97	813.54	12.477	4.685	13.944	93.54			[v]
B4S6	$Ba_4Si_6O_{16}$	40	2.67		$P2_1/c$	14			814.0	12.483	4.686	13.943	93.53	Ba: 2 (4 e)	8.5	[iii]
							3.976		**813.46(6)**	**12.477**	**4.685**	**13.943**	**93.58**	Si: 3 (4 e)		**This study - Rietveld**
							3.838		**844.11**	**12.652**	**4.725**	**14.147**	**93.73**			**This study - DFT**
				100311			3.925	3.93	2110.20	32.675	4.695	13.894	98.10			[v]
									2120.6	32.739	4.702	13.917	98.17	Ba: 1+2 (8 f, 4 a)	8	[iii]
B5S8	$Ba_5Si_8O_{21}$	38.5	2.63		C2/c	15									(*7.6)	Rietveld - [vii]
							3.905		**2121.6(2)**	**32.756**	**4.705**	**13.909**	**98.18**	Si: 4 (8 f)		DFT - [vii]
							3.771		**2200.25**	**33.284**	**4.738**	**14.097**	**98.29**			
				100312			3.882	3.88	1301.03	20.196	4.707	13.842	98.61	Ba: 3 (4 e)	8.33	[v]
B6S10	$Ba_6Si_{10}O_{26}$	37.5	2.6		$P2_1/c$	14	**3.876**		**1303.28(7)**	**20.210**	**4.707**	**13.856**	**98.63**	Si: 5 (4 e)		**This study - Rietveld**
				100314			3.74	3.74	1457.96	23.195	4.658	13.613	97.57			[vi]
									1459.0	23.193	4.659	13.622	97.56	Ba: 2 (4 a, 8 f)	8.67	[iii]
high-BS2	$BaSi_2O_5$	33.3	2.5		C2/c	15	**3.720**		**1465.17(7)**	**23.232**	**4.665**	**13.637**	**97.55**	Si: 3 (8 f)		**This study - Rietveld**
							3.604		**1513.92**	**23.466**	**4.702**	**13.842**	**97.61**			**This study - DFT**
				100313			3.77	3.70	481.25	7.688	4.629	13.523	90.00			[vi]
Sanbornite (low-BS2)	$BaSi_2O_5$	33.3	2.5		Pmcn	62			481.78	7.690	4.632	13.528	90.00	Ba: 1 (4 c)	9	[iii]
							3.762		**482.94(2)**	**7.696**	**4.636**	**13.538**	**90.00**	Si: 1 (8 d)		Rietveld - [vii]
							3.632		**500.84**	**7.778**	**4.684**	**13.744**	**90.00**			DFT - [vii]

* Note that Rietveld model standard deviation, when not shown (e.g. lattice parameters), are less than ±1 of the last decimal place reported.

[1] International Crystal Structure Database (ICSD) available: https://www.fiz-karlsruhe.de/; densities also come from the data reported in ICSD.

[2] PFU - per formula unit. For example, high-BS2 has two sites with different multiplicity: CN_{PFU} = (4*8 + 8*9)/12 = 8.67). Ba-O cutoff radius is 3.3 Å. Ba CN = 7.6 for B5S8 if the two O at 3.27 Å are excluded.

[3] references: [i] Grosse & Tillmanns, 1974b; [ii] Denault et al., 2015; [iii] Gorelova et al., 2016; [iv] Grosse & Tillmanns, 1974a; [v] Hess & Liebau, 1980b; [vi] Hess & Liebau, 1980a; [vii] Gomes et al., 2021.

This is the peer-reviewed, final accepted version for American Mineralogist, published by the Mineralogical Society of America.
The published version is subject to change. Cite as Authors (Year) Title. American Mineralogist, in press.
DOI: https://doi.org/10.2138/am-2021-7910. http://www.minsocam.org/

Table 2: Values of peak parameters obtained by ˇ˘Si MAS NMR spectroscopy .

Si Site		1		2		3		4		5		
Phase	**Q^n**	Shift ppm	Area %	Shift ppm	Area %	Shift ppm	Area %	Shift ppm	Area %	Shift ppm	Area %	**Reference[1]**
low-BS2	Q^3	-93.11 -93.5	100									[i]
high-BS2	Q^3	-93.03	66.5	-92.11	33.5							
B6S10	Q^4-$4Q^3$	-93.02	19.7	-92.18	20.3	-88.84	18.9	-87.97	20.2	-81.37	21.0	
B5S8	Q^4-$3Q^3$	-94.14	23.9			-89.60	52.2			-81.42	23.9	
B4S6	Q^4-$2Q^3$	-92.18	35.8	-91.22	32.1					-81.20	32.1	
high-BS	Q^2									-80.00 -80	100	[ii]
B2S	Q^0									-70.12 -70.3	100	[iii]

*** Notes: i) frequency resolution is 0.03 ppm; ii) peak FWHM fixed to the value of L-BS2 = 1.11 ppm.**

[1] References: [i] Murdoch et al., 1985; [ii] Smith et al., 1985; [iii] Mägi et al., 1984.

This is the peer-reviewed, final accepted version for American Mineralogist, published by the Mineralogical Society of America.
The published version is subject to change. Cite as Authors (Year) Title. American Mineralogist, in press.
DOI: https://doi.org/10.2138/am-2021-7910. http://www.minsocam.org/

Table 3: Values of peak parameters obtained by Raman spectroscopy .

		***Bending* region**				***Stretching* region**						
Phase	Q^n	Center cm^{-1}	FWHM cm^{-1}	Center cm^{-1}	FWHM cm^{-1}	Center cm^{-1}	FWHM cm^{-1}	Center cm^{-1}	FWHM cm^{-1}	Center cm^{-1}	FWHM cm^{-1}	**Note**[1]
low-BS2	Q^3	**535.5**	**8.2**					**1077.9**	4.5			this study
	Q^3	535.2	8.5					1076.8	4.6			1
Sanbornite	Q^3	535.1	8.8					1076.9	4.6			1
high-BS2	Q^3	**533.8**	**8.5**					**1079.5**	5.2			this study
	Q^3	533.5	8.8					1079.2	5.4			1
B6S10	Q^2:4Q^3	**534.7**	**7.0**	544.3	5.4	**921.3**	7.9	**1069.2**	6.3	1075.3	4.5	this study
σ		0.1	0.6	0.5	0.9	0.1	0.5	**0.2**	0.3	0.1	0.3	
B6S10	Q^2:4Q^3	535.6	6.5	546.1	4.9	924.6	6.2	1067.0	5.5	1075.3	6.8	1
B5S8	Q^2:3Q^3	**535.1**	**6.6**	545.7	5.3	**924.0**	7.2	**1066.8**	5.5	1075.3	4.5	this study
		535.6	6.0	545.8	4.4	923.6	6.4	1065.6	5.5			1
B4S6	Q^2:2Q^3	**532.0**	**5.5**	549.1	5.1	**928.1**	6.6	**1061.0**	5.0	1049.9	7.3	this study
high-BS	Q^2	**599.8**	**9.7**			**964.0**	8.3					this study
B2S[3]	Q^0					**823.7**	3.2	858.4	6.2			this study

[1] 1 come from Moulton et al., 2019 based on a 'local' fit and samples of H-BS2, B5S8 and B6S10 were those of Gorelova et al., (2016).

[2] σ values were calculated from the mean of three spectra. Exemplar σ are reported for B6S10 as these values are typical for all fits and larger than phases with fewer Si sites.

[3] Ba_2SiO_4 values were also measured as 822 cm^{-1} by Bispo Jr. et al. (2017) & as 819 cm^{-1} by Handke & Urban, (1982).

* All results were reproduced using 532 and 633 nm lasers & are reproducible within <1.5 cm^{-1}.

This is the peer-reviewed, final accepted version for American Mineralogist, published by the Mineralogical Society of America.
The published version is subject to change. Cite as Authors (Year) Title. American Mineralogist, in press.
DOI: https://doi.org/10.2138/am-2021-7910. http://www.minsocam.org/

Table 4: Experimental and theoretical vibrational modes in barium orthosilicate, Ba_2SiO_4[1].

Raman Modes

Mode	Measured				Theoretical			
	Frequency cm^{-1}	FWHM cm^{-1}	Relative Intensity (%)	Area %	Frequency cm^{-1}	Δν cm^{-1}	Symmetry	Origin[2]
ν_1					56.9		B_{2g}	O1-Ba2,1
ν_2	59.2	1.6	29.1	4.5	63.2	3.9	A_g	Ba1-Ba2
ν_3	68.6	4.2	6.8	2.8	69.1	0.5	B_{1g}	Ba1-Ba2-O2
ν_4	73.0	2.8	9.8	2.6	75.4	2.4	B_{3g}	Ba2-Ba1
ν_5					76.7		B_{2g}	O2-Ba2,1
ν_6	86.4	3.8	9.6	3.6	89.1	2.8	A_g	Ba2-Ba1
ν_7	89.7	3.6	20.1	7.1	92.8	3.1	B_{1g}	Ba1,2
ν_8					96.2		A_g	Ba1-Si
ν_9					105.0		B_{2g}	Ba1-Ba2
ν_{10}	108.9	1.2	9.5	1.1	105.5	-3.4	B_{3g}	Ba1,2
ν_{11}					121.9		A_g	Ba2-O1
ν_{12}	132.2	3.7	0.8	0.3	137.3	5.1	B_{1g}	lattice
ν_{13}					141.9		B_{3g}	O2,3-Ba2
ν_{14}	158.8	7.9	1.5	1.2	158.2	-0.6	A_g	O2-Ba2-O2
ν_{15}					158.4		B_{3g}	Ba2
ν_{16}					159.1		B_{2g}	O2-Ba2
ν_{17}	169.0	6.2	4.8	2.9	169.7	0.7	B_{1g}	O2-Ba2-O2
ν_{18}	181.9	5.8	16.4	9.4	186.0	4.1	B_{3g}	lattice
ν_{19}	195.6	13.8	2.8	3.8	200.4	4.8	B_{2g}	O3-Ba1-Ba2
ν_{20}	207.9	5.1	12.5	6.2	210.4	2.5	A_g	lattice
ν_{21}					213.8		B_{3g}	O2-Ba2-Ba1
ν_{22}					218.6		B_{1g}	O3-Ba1-Ba2
ν_{23}					223.4		A_g	lattice
ν_{24}					258.3		B_{3g}	O1-Ba2,1
ν_{25}	347.5	6.8	0.5	0.3	363.6	16.1	A_g	O1-Ba2
ν_{26}	370.3	10.4	4.6	4.7	377.4	7.1	B_{1g}	lattice
ν_{27}					390.6		B_{2g}	lattice
ν_{28}					393.6		B_{3g}	lattice
ν_{29}	490.3	3.3	1.8	0.6	517.3	27.0	A_g	O3-Si-Ba1
ν_{30}	497.4	3.5	15	5	519.7	22.3	B_{3g}	lattice
ν_{31}	520.7	3.5	1.5	0.5	525.9	5.2	B_{1g}	SiO4
ν_{32}					526.9		B_{2g}	SiO4
ν_{33}					552.8		A_g	lattice
ν_{34}					569.6		B_{3g}	O2-Si-O3
ν_{35}	815.3	6.9	1.1	0.8	827.9	12.6	A_g	O1-Si
ν_{36}	823.7	3.2	100	32	833.4	9.7	B_{3g}	O1-Si
ν_{37}	854.0	3.2	2.0	1	863.3	9.3	A_g	O2-Si-O1
ν_{38}	858.4	6.2	8.4	4.5	876.4	18.0	B_{3g}	SiO4
ν_{39}	867.0	3.4	2.0	0.7	895.5	28.5	B_{1g}	O2-Si
ν_{40}	887.8	5.0	3.9	1.9	895.6	7.8	B_{2g}	O2-Si
ν_{41}	910.2	5.1	6.0	3.0	942.2	32.0	A_g	O2-Si
ν_{42}					966.4		B_{3g}	O3-Si
Mean A_g FWHM*		5.0			|Δν|[3]	7.5		
Mean B_g FWHM*		5.5			maximum Δν	32.0		

* Only modes contributing >1% area were considered.

[1] Note that all O are NBO and the Si site is a Q^0 species.

[2] Mode origin are labelled as 'lattice' where they involve both BaO_x & SiO_4.

[3] |Δν| is the absolute mean difference between theoretical and experimental frequency.

This is the peer-reviewed, final accepted version for American Mineralogist, published by the Mineralogical Society of America.
The published version is subject to change. Cite as Authors (Year) Title. American Mineralogist, in press.
DOI: https://doi.org/10.2138/am-2021-7910. http://www.minsocam.org/

Table 5: Theoretical versus experimental (Exp) ^{29}Si MAS NMR chemical shift frequencies.

Si Site	low-$BaSi_2O_5$			high-$BaSi_2O_5$			$Ba_6Si_{10}O_{26}$			$Ba_5Si_8O_{21}$			$Ba_4Si_6O_{16}$			Tremolite[a]	Xonotlite[a]	high-$BaSiO_3$			Ba_2SiO_4		
	Exp	SG88[b]		Exp	SG88		Exp	SG88		Exp	SG88		Exp	SG88		Exp	Exp	Exp	SG88		Exp	SG88	
		3.7 Å	2 NNN		3.7 Å	2 NNN		3.7 Å	2 NNN		3.7 Å	2 NNN		3.7 Å	2 NNN				3.7 Å	2 NNN		3.7 Å	2 NNN
1							**-81.4**	-73.5	-82.4	**-81.4**	-80.4	-83.5	**-81.2**	-73.8	-78.3	-87.8	-86.8	**-80.0**	-72.4	-72.4	**-70.1**	-61.6	-57.6
2							**-88.0**	-88.2	-97.3														
3				**-92.1**	-87.6	-92.4	**-88.8**	-88.8	-88.8	**-89.6**	-91.7	-91.7											
4				**-93.0**	-90.6	-95.4	**-92.2**	-90.9	-98.3	**-89.6**	-92.0	-90.2	**-91.2**	-85.8	-102.5								
5	**-93.1**	-86.3	-87.8	**-93.0**	-91.5	-96.1	**-93.0**	-96.8	-100.0	**-94.1**	-93.0	-96.9	**-92.2**	-92.3	-99.9	-92.2	-97.8						

[a] - chemical shift of tremolite and xonotlite are from Mägi et al., 1984

[b] - SG88 derived values come from the empirical model of Sherriff & Grundy (1988) where the NNN have been limited to either, neighbours up to 3.7 Å (3.7 Å), or two next-nearest neighbours (2 NNN)

This is the peer-reviewed, final accepted version for American Mineralogist, published by the Mineralogical Society of America.
The published version is subject to change. Cite as Authors (Year) Title. American Mineralogist, in press.
DOI: https://doi.org/10.2138/am-2021-7910. http://www.minsocam.org/

Table 6: Values of Si site parameters.

Phase	Q^n	Site Parameter		
		Si-O (Å)	Avg. Si-O-Si (°)	Volume (Å^3)
B2S	0	**1.633**	n/a	**2.230**
Ba_2SiO_4	0	1.638	n/a	**2.250**
B-BS	2	**1.623**	**128.2**	**2.165**
B2S3	2	**1.636**	**129.7**	**2.219**
$Ba_4Si_6O_{16}$	3	**1.620**	**135.8**	**2.157**
	3	**1.617**	**139.1**	**2.146**
mean		1.624	134.9	2.174
B5S8	2	**1.623**	**132.2**	**2.118**
$Ba_5Si_8O_{21}$	3	**1.604**	**134.8**	**2.045**
	3	**1.612**	**135.6**	**2.123**
	3	**1.608**	**146.5**	**2.212**
mean		1.612	137.3	2.125
B3S5	2	**1.647**	**131.0**	**2.251**
$Ba_6Si_{10}O_{26}$	3	**1.624**	**133.8**	**2.181**
	3	**1.614**	**134.1**	**2.128**
	3	**1.608**	**138.6**	**2.104**
	3	**1.606**	**142.3**	**2.098**
mean		1.620	136.0	2.152
H-BS2	3	**1.619**	**137.6**	**2.151**
$BaSi_2O_5$	3	**1.616**	**138.5**	**2.152**
	3	**1.616**	**138.1**	**2.146**
mean		1.617	138.1	2.150
Sanbornite	3	**1.614**	**138.6**	2.140
Low-Quartz[1]	4	**1.608**	**143.8**	2.134

[1] low-quartz values determined from Antao & Hassan, (2008).

This is the peer-reviewed, final accepted version for American Mineralogist, published by the Mineralogical Society of America.
The published version is subject to change. Cite as Authors (Year) Title. American Mineralogist, in press.
DOI: https://doi.org/10.2138/am-2021-7910. http://www.minsocam.org/

Fig 1

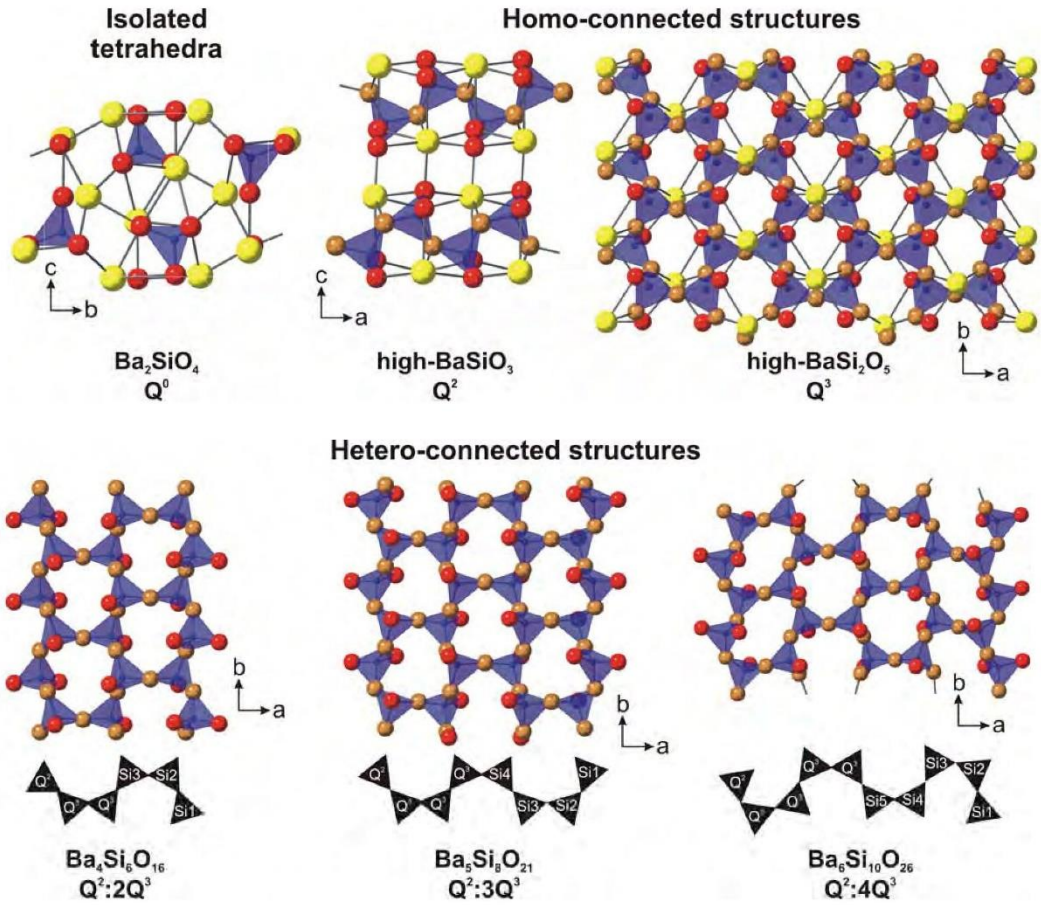

Fig 2

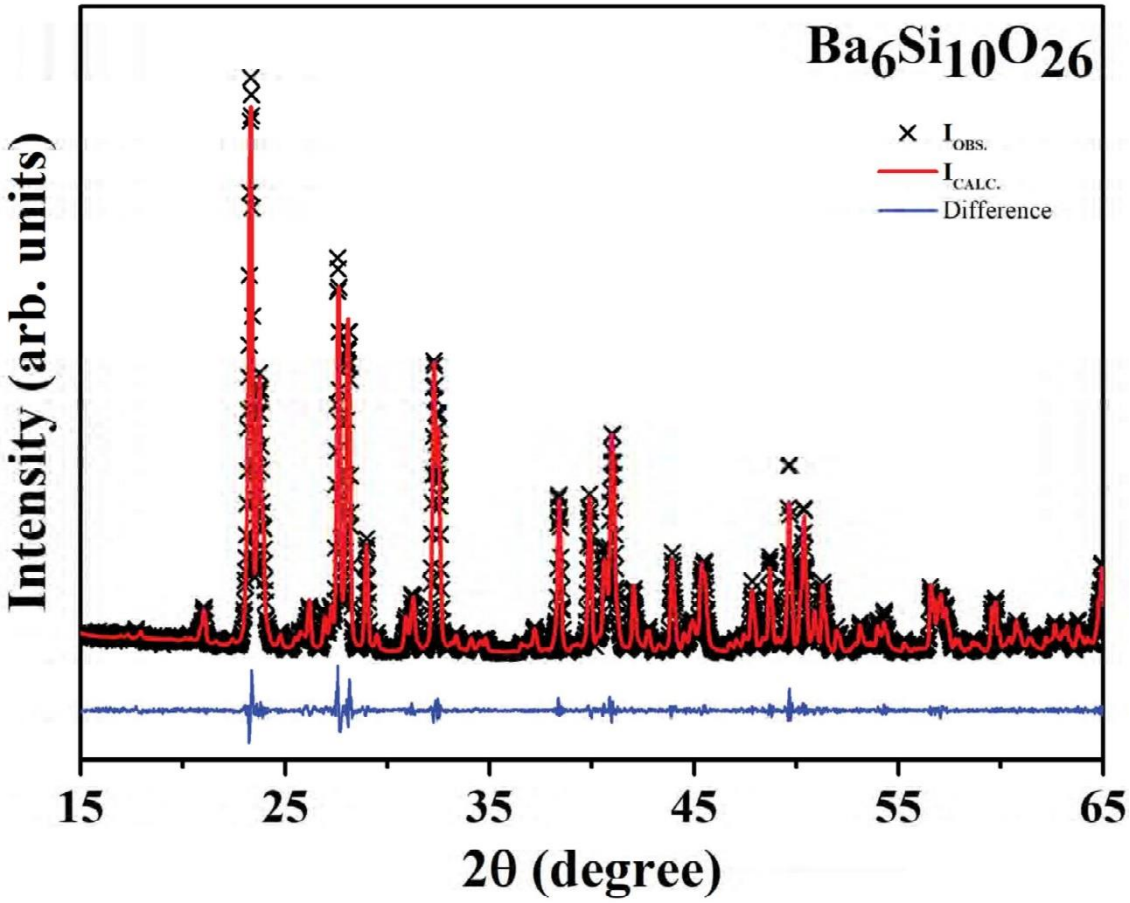

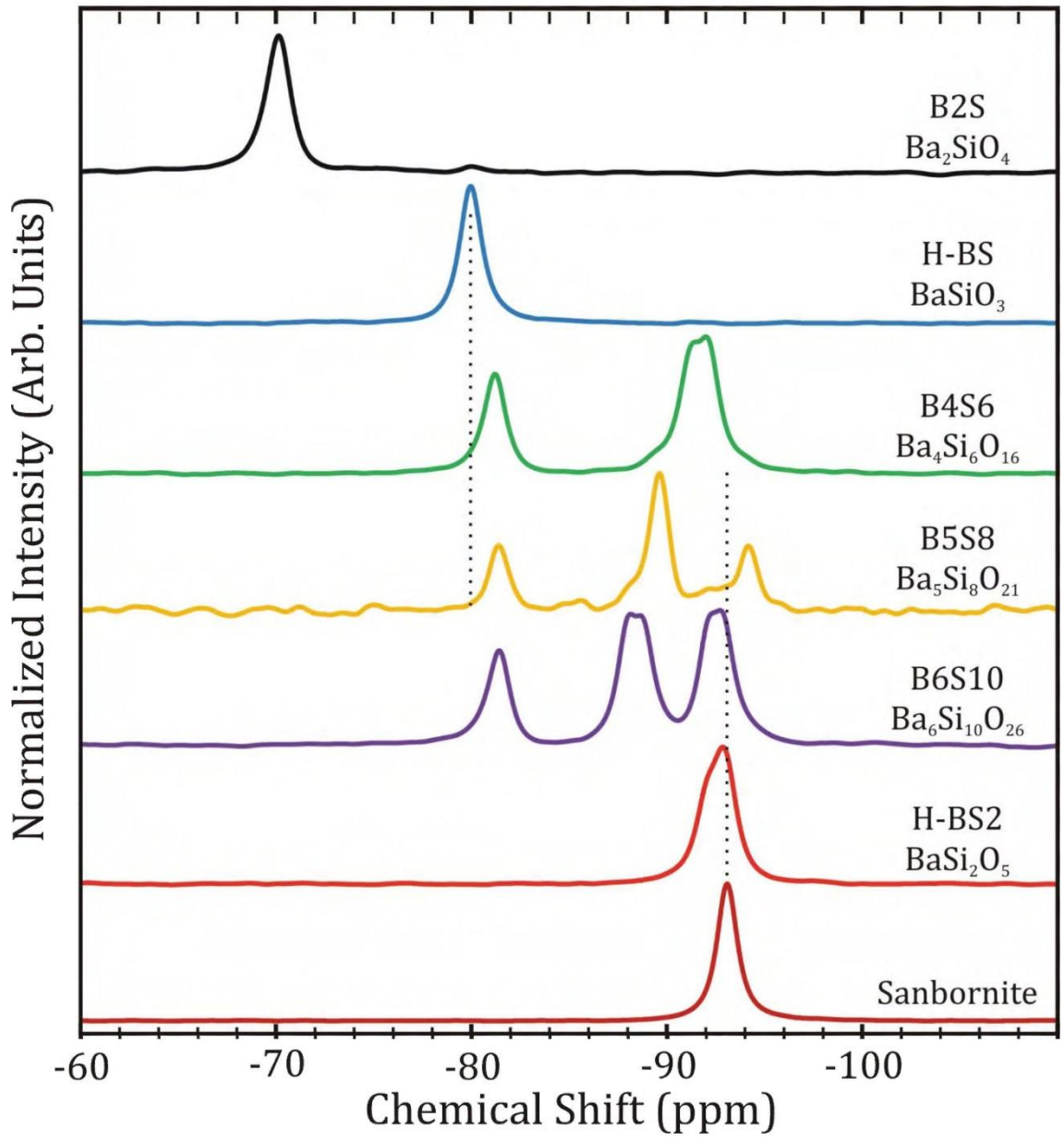

Fig 3 - NMR spectra

FIG 4A

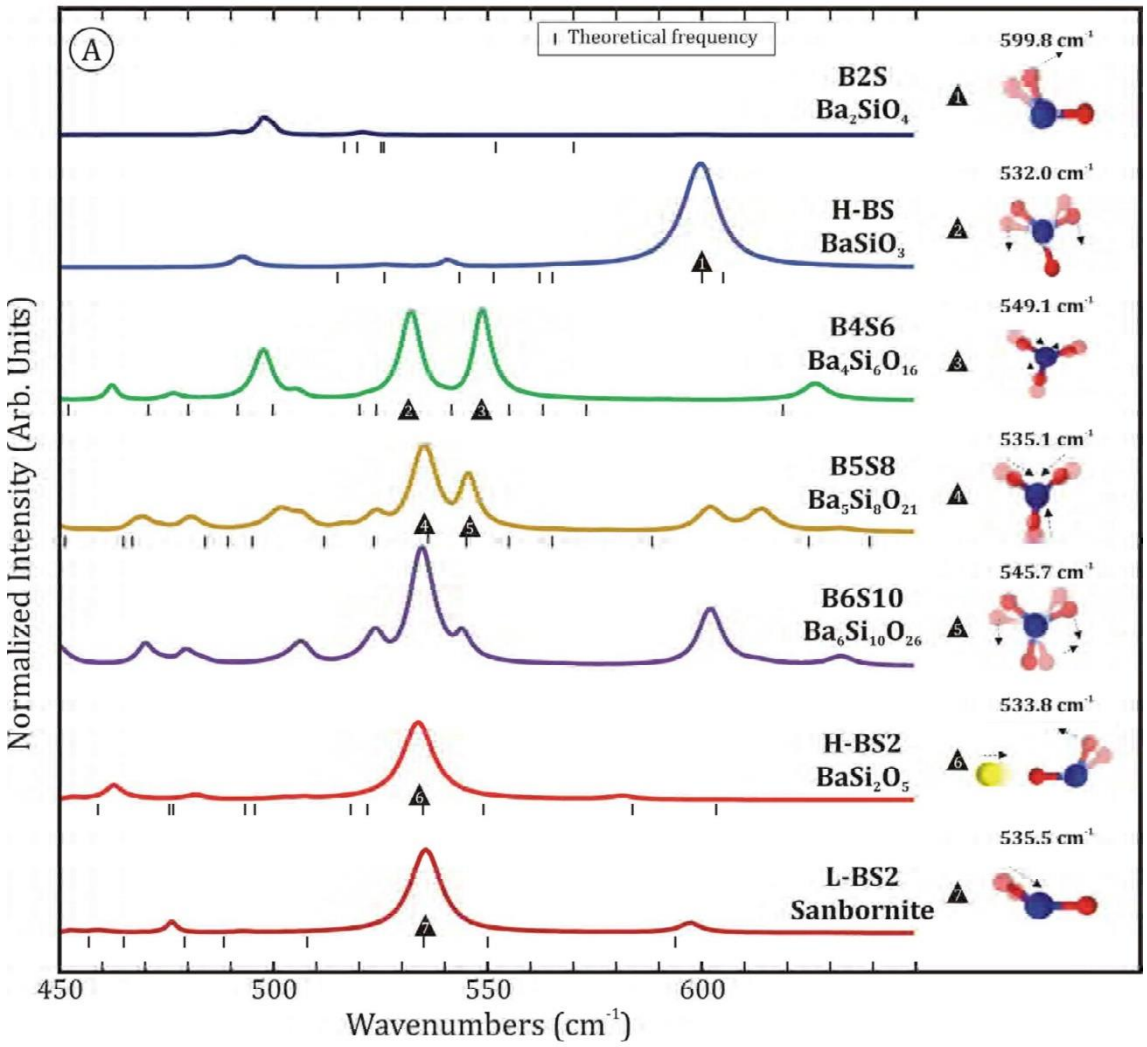

FIG 4B

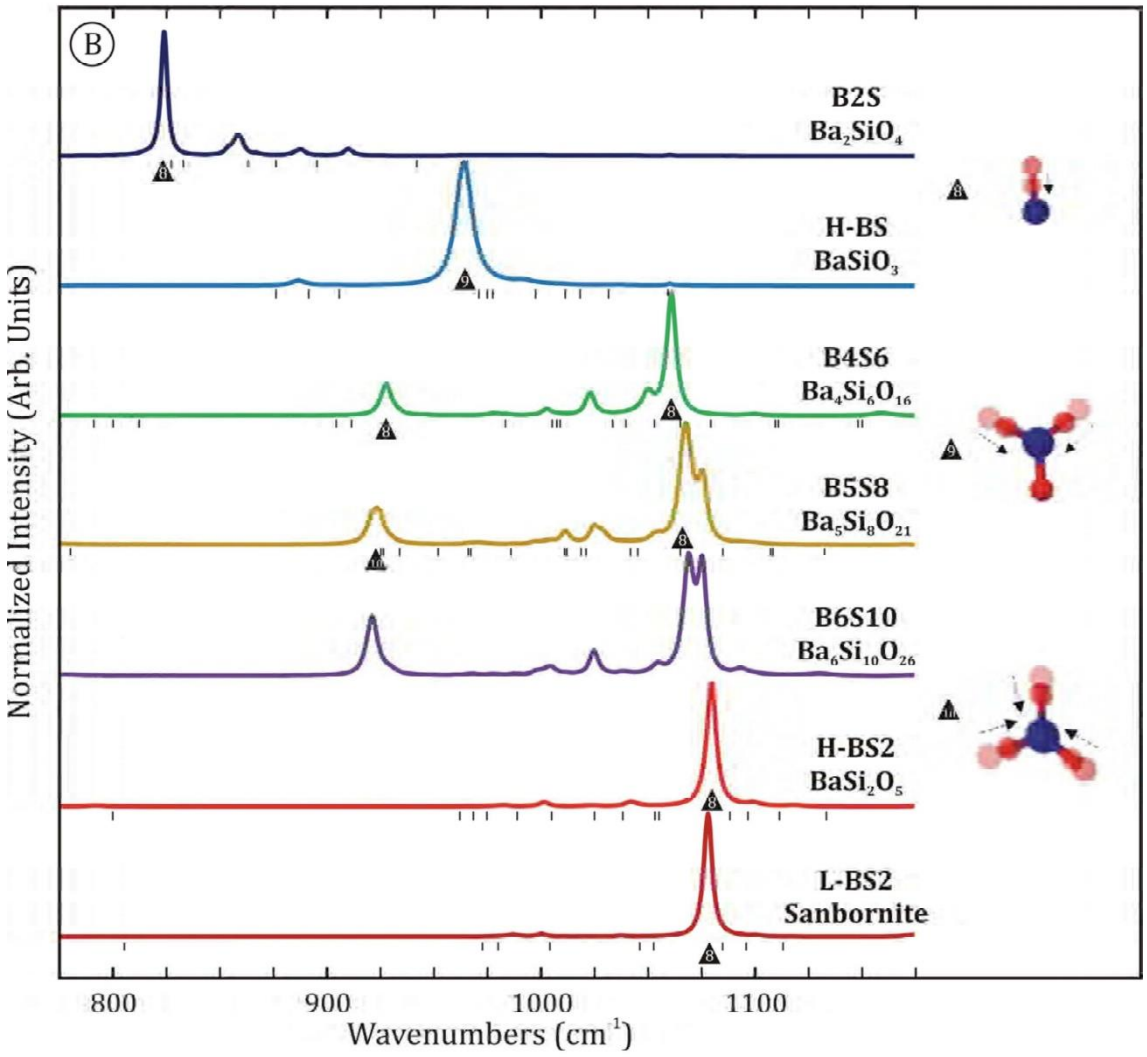

FIG 5

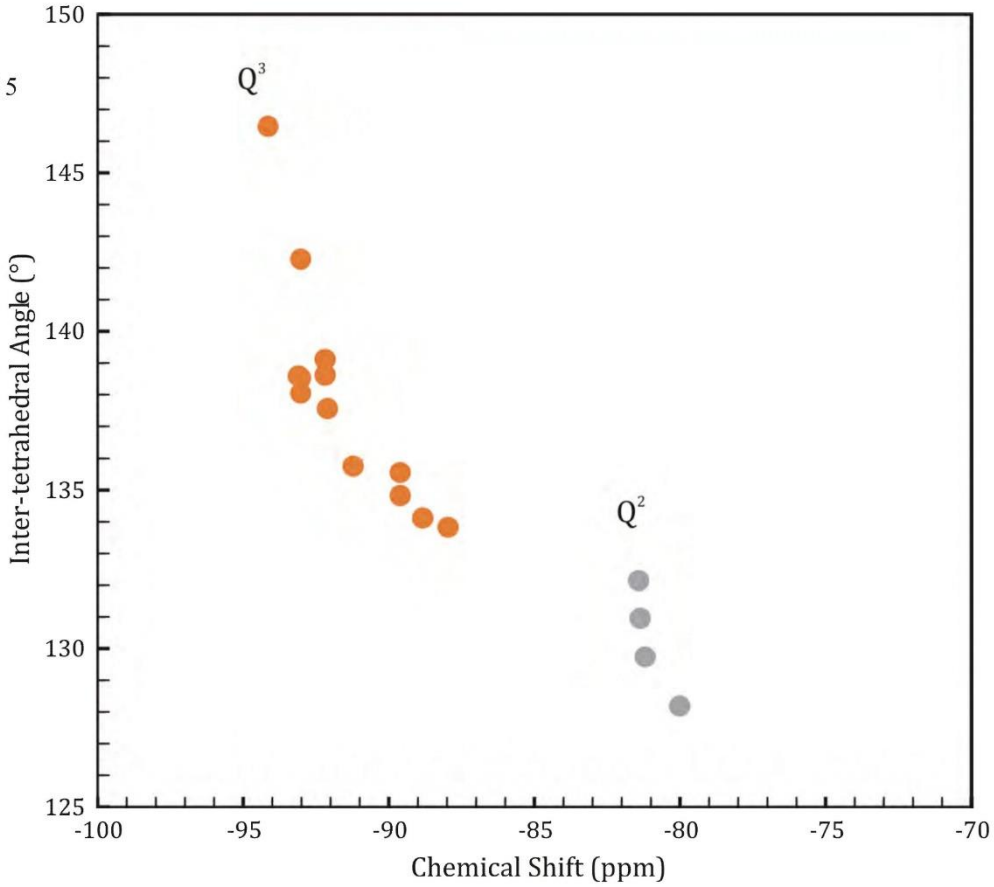

FIG 6

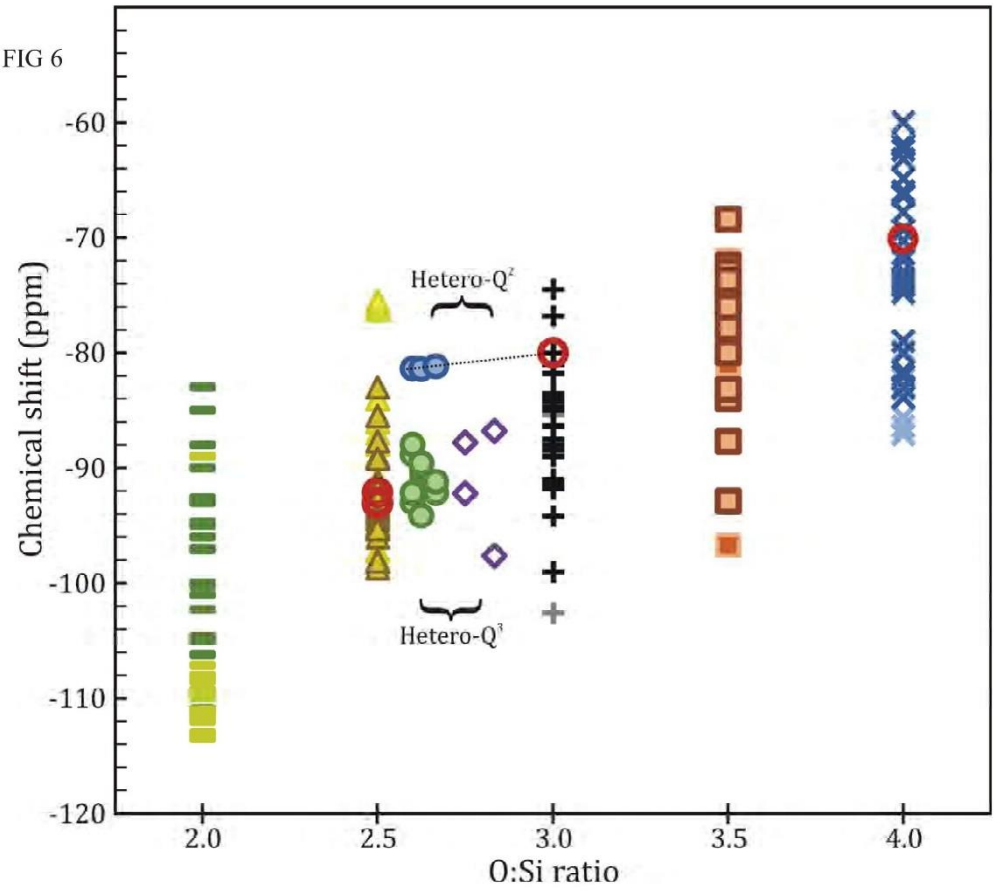

FIG 7

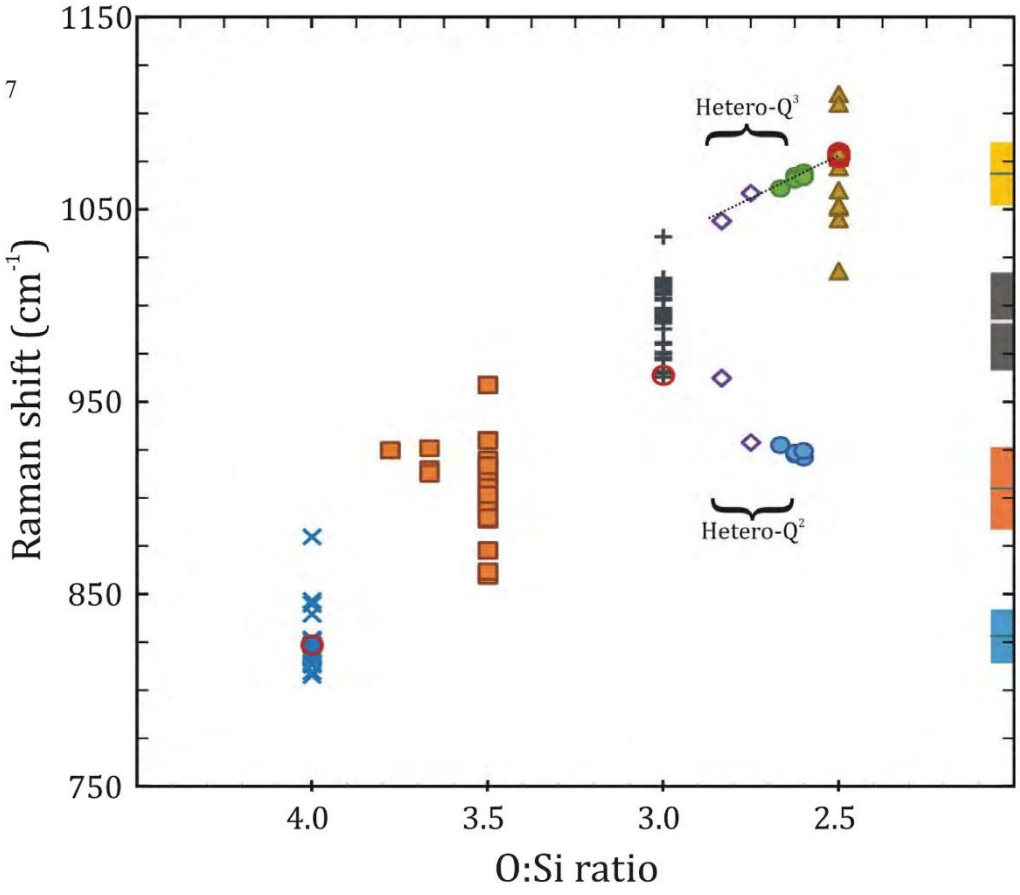

FIG 8

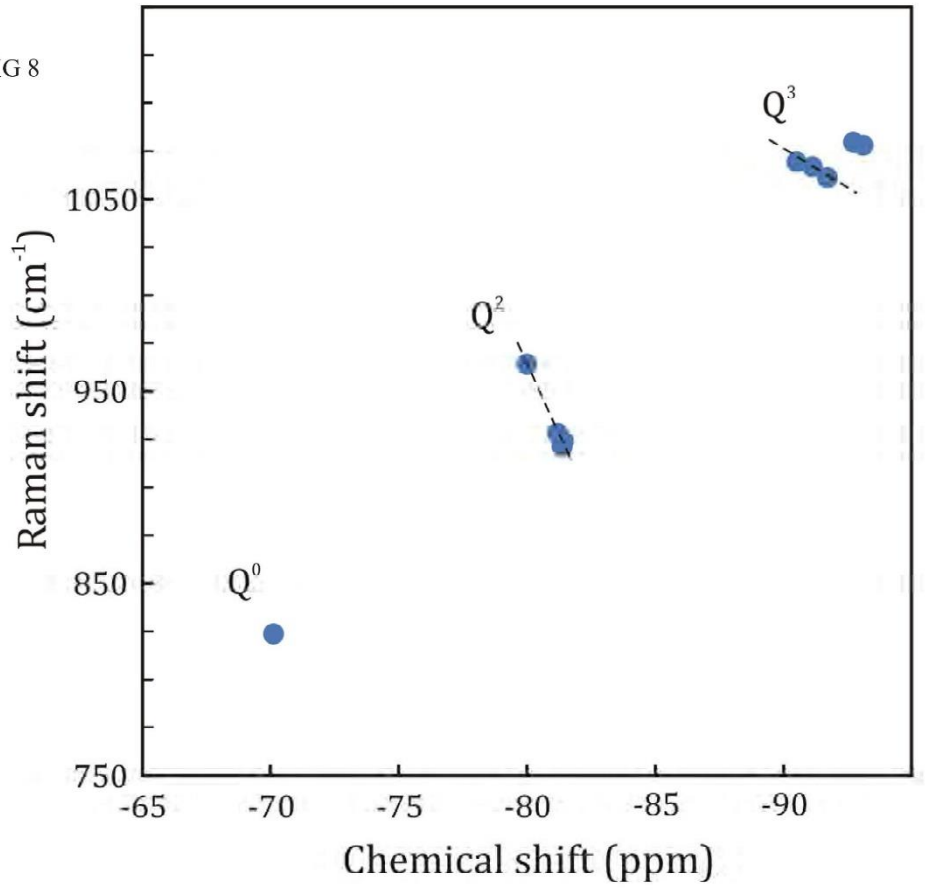

Inorganic Chemistry
Cite This: Inorg. Chem. 2019, 58, 11738−11750
Article
pubs.acs.org/IC

Joint Theoretical and Experimental Study on the La Doping Process in In_2O_3: Phase Transition and Electrocatalytic Activity

S. C. S. Lemos,[†] E. Nossol,[†] J. L. Ferrari,[†] E. O. Gomes,[‡] J. Andres,[‡] L. Gracia,[‡] I. Sorribes,[‡] and R. C. Lima*[,†]

[†]Instituto de Química, Universidade Federal de Uberlândia, 38400-902 Uberlândia, Minas Gerais, Brazil
[‡]Departament de Química Física i Analítica, Universitat Jaume I, 12071 Castellón, Spain

Supporting Information

ABSTRACT: In_2O_3 and La^{3+}-doped In_2O_3 nanostructures were synthesized through a facile and fast chemical route based on the microwave-assisted hydrothermal method combined with rapid thermal treatment in a microwave oven. The presence of the La^{3+} doping process modifies the size and morphology of the In_2O_3 nanostructures and also stabilizes the rhombohedral (rh) In_2O_3 phase with respect to the most stable cubic (bcc) polymorph. X-ray diffraction (XRD) patterns and Rietveld refinements, Raman, UV−vis, and energy dispersive X-ray (EDX) spectroscopies, transmission electron (TEM) and field-emission scanning electron (FE-SEM) microscopies, as well as PL emissions have been performed. To complement and rationalize the experimental results, first-principle calculations, based on density functional theory, are carried out to obtain the formation energies of the In_2O_3 and bcc- and rh-In_2O_3-doped phases, their geometry and electronic properties. Theoretical results are able to explain the relative stabilization of the rh-phase with respect to the bcc-phase based on the analysis geometry changes and the electronic redistribution induced by the La^{3+} doping process. In addition, Wulff construction is employed to match the theoretical and experimental morphologies of the cubic phase. The synthesized samples were applied for the O_2 evolution reaction (OER). The La^{3+}-doped In_2O_3 film presents superior electrocatalytic activity, with an onset potential lower than the undoped In_2O_3 film that can be associated with the increase in electron density caused by the La^{3+} doping process. This study provides a versatile strategy for obtaining In_2O_3 and La^{3+}-doped In_2O_3 nanostructures for practical applications.

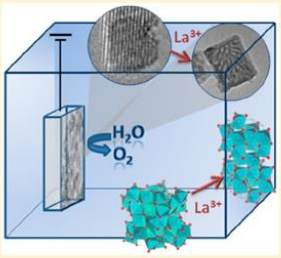

1. INTRODUCTION

Electrochemical and photochemical water splitting have been addressed as a promising and sustainable technology for energy conversion. These processes involve two half-reactions: water oxidation (or the oxygen evolution reaction (OER)) and water reduction (or the hydrogen evolution reaction (HER). The OER, requiring four proton and electron transfers per oxygen molecule, is the more complex of the two half-reactions; consequently, it limits the overall water-splitting process.[1−4] To overcome this issue, semiconductor-based catalysts meeting the band gap requirement and having a valence band below the O_2/H_2O level have been developed with the aim of improving the OER.[5,6] In this type of material, the oxidation of water is promoted by holes generated in the interface of the n-type semiconductor and the electrolyte.[6,7]

Indium oxide (In_2O_3) is a wide-band n-type semiconductor, even in the absence of intentionally added donors,[8] which satisfies the band edge position requirement for water electrolysis. In addition, the presence of defects such as oxygen vacancies or the presence of dopants allows for the possibility of decreasing the electron/hole recombination and increasing the interfacial electron transfer process.[9] Concerning the other defects generated due to reducing different aspects of the conditions that have a real and relevant impact on the catalytic activity of reduced In_2O_3, Gu et al.[10] varied the oxygen vacancies content in order to find the optimal proportion for sensing properties by varying the hydrogen annealing time. Davies et al.[11] explored the features of formation of In^+ in the In_2O_3 surface under reducing conditions by combining X-ray photoemission measurements with first-principles density functional theory (DFT) calculations.

In_2O_3 offers a wide range of applications such as transparent electronics,[12] sensors,[13,14] photovoltaic devices,[15] light-emitting diodes,[16] solar cells,[17] and gas sensors.[18,19] In this context, the study of the surface structure and defects, electron accumulation, and control of vacancies and carrier density that directly affect the material efficiency is mandatory.[20,21] In_2O_3 can crystallize in a cubic and/or rhombohedral polymorphic form.[22] The body centered cubic structure (bcc-In_2O_3) is the most stable with lattice constants $a = b = c = 10.118$ Å, in which each In^{3+} cation is situated in the center of a distorted cube with only six vertices occupied by oxygen anions, while the remaining two vertices are empty.[23] The metastable rhombohedral polymorph (rh-In_2O_3) is obtained at high temperatures and pressures, with lattice parameters of $a = b = 5.478$ Å and $c = 14.510$ Å, and in this arrangement, the In^{3+} cations are coordinated octahedrally with two layers of oxygen anions.[24] The process of phase trans-

Received: June 10, 2019
Published: August 15, 2019

DOI: 10.1021/acs.inorgchem.9b01728
Inorg. Chem. 2019, 58, 11738−11750

formation in In_2O_3 has been a focus of attention, since the different polymorphs show specific properties that directly affect the performance of the desired applications.[25] Koch et al.[26] observed from adsorption measurements that rh-In_2O_3 exhibits predominantly Lewis acidic surface sites compared to bcc-In_2O_3; thus, the cubic structure presented a superior CO_2 selectivity in methanol steam reforming. Wu et al.[27] investigated the photocatalytic activities of rh-In_2O_3 and bcc-In_2O_3 nanostructures and obtained the highest efficiency for degradation of tetracycline using rh-In_2O_3. Furthermore, In_2O_3 with coexisting cubic and rhombohedral phases showed improved performance for NO_2 sensing, with excellent selectivity and stability.[28]

The dopant processes in the oxide matrix are a useful approach to design the material properties, such as band gap engineering, morphology control, and changing the electrical carrier density.[29−32] Studies addressing the doping effect in an In_2O_3 host have been carried out, such as the work of Xu et al.,[30] who proposed a selection of suitable transition metals as dopants to achieve higher carrier density and optical transparency. In this context, Farvid et al.[33] evaluated the effect of Cr^{3+} doping on In_2O_3 host lattice, attributing the stabilization of the metastable rh-In_2O_3 phase to the inhibition of the nanoparticles growth due to the presence of dopant ions in the reaction mixture, while Li et al.[28] showed the dependence of the phase transition process and morphology transformation provoked by the dopant concentration in Zn-doped In_2O_3. Very recently, our group has successfully synthesized In_2O_3 and Er^{3+}-doped In_2O_3 nanostructures, and their PL emissions and photocatalytic activities have been investigated.[34−36] Doping processes involving rare earth elements have been proposed as a route to control the size, morphology, and even the stabilization of a specific crystallographic phase.[37−41] In particular, La^{3+} is known to perform a crucial role in advanced photocatalytic technologies. For instance, Zhang et al. reported the presence of a higher density of oxygen vacancies due to the La^{3+} doping process in TiO_2, and consequently, an improvement in photoelectric conversion efficiency was achieved. Oppong et al.[42] reported a decrease in the electron hole recombination in ZnO due to empty 4f and 5d orbitals of La^{3+}, and Wei et al.[43] achieved a higher performance for H_2S sensing due to an improved ability to adsorb the ionized oxygen species on the In_2O_3 surface throughout the La^{3+} doping process.

In the present work the microwave hydrothermal-assisted method was combined with a calcination process performed in a microwave oven.[44−48] This annealing treatment has the advantage of reducing the temperature and the calcination time,[34−36] which in this work yielded the formation of well crystallized In_2O_3 within 2 min of calcination. Adequate synthesis methods coupled with a detailed electronic and structural description of In_2O_3 promote an understanding of the fundamental knowledge to be applied for the development of the functionalities of this material. Inspired by the above-mentioned studies, herein we seek to accomplish four aims. First, we report a simple and efficient method to efficiently fabricate both In_2O_3 and La^{3+}-doped In_2O_3 by employing a microwave-assisted route. Second, the effects of the La^{3+} dopant in the phase formation (rh-In_2O_3 vs bcc-In_2O_3) have been analyzed. To support these findings, X-ray diffraction and Rietveld refinements, energy dispersive X-ray (EDX), Raman, and UV−vis spectroscopies, as well as PL emissions have been studied. The structures of the two phases have been investigated by first-principle calculation, based on DFT, to obtain their relative stabilities and structure differences at the atomistic level. In addition, from the analysis of the theoretical results, we disclose the mechanism through which the La doping process stabilizes more of the rh-In_2O_3 with respect to bcc-In_2O_3. The third objective is to explain how the theoretical and experimental morphologies from FE-SEM images of the cubic phase are rationalized based on the Wulff construction by first-principle calculations. Finally, the fourth objective is to demonstrate that the prepared In_2O_3 and La^{3+}-doped In_2O_3 films present electrocatalytic activity for water oxidation and contribute to broaden their possible applications.

2. EXPERIMENTAL AND THEORETICAL METHODS

2.1. Synthesis. The precursors were obtained from the addition of 14.40 mL of an $In(NO_3)_3$ solution (0.10 mol L^{-1}) and 2.00 mL of PEG 200 in 40 mL of distilled water under constant stirring. The pH was adjusted to 9.70 using a KOH aqueous solution (3.0 mol L^{-1}). To prepare the doped precursor, a stoichiometric amount of a $La(NO_3)_3$ solution (0.20 mol L^{-1}) was added to the mixture in order to reach a concentration of 4.0 mol % La^{3+} in relation to In^{3+} ions. The final solution was transferred into an autoclave, sealed, and placed in the microwave-hydrothermal equipment. The solutions were heated at 140 °C for 2 min, employing a heating rate of 5 °C min^{-1}. The precipitate powder was washed several times with deionized water and ethanol and dried at 60 °C for 3 h. The as-prepared $In(OH)_3$ and La^{3+}-doped $In(OH)_3$ precursors were annealed at 350 °C for 2 min in a microwave oven to obtain In_2O_3 nanostructures.

2.2. Characterization Techniques. The In_2O_3 powders were characterized by X-ray diffraction (Shimadzu XRD 6000) using Cu Kα as the radiation source. The structure was refined using the Rietveld method and the General Structure Analysis System (GSAS) package, with the EXPGUI graphical user interface.[49] The cubic and rhombohedral structures of In_2O_3 were generated using the Crystal Maker program (Version 2.2.4.445) for Windows. The morphological characterization was carried out using a field-emission scanning electron microscope (FE-SEM, Zeiss Supra35) operating at 5 kV. Transmission electron microscopy (TEM) was carried out on a FEI Tecnai G2F20, operating at 200 kV. The microanalysis by energy dispersive X-ray (EDX) spectroscopy was carried out using an Oxford Instruments system, operating at 20 kV. UV−visible spectra were obtained on a Cary 5G spectrophotometer in the region 200−900 nm. Raman spectra at room temperature were recorded on an RFS/100/S Bruker FT-Raman spectrometer, with an Nd:YAG laser providing an excitation light at 1064 nm and a spectral resolution of 4 cm^{-1}. Photoluminescence (PL) spectra were recorded at room temperature by a thermal Jarrel-Ash Monospec 27 monochromator and a Hamamatsu R446 photomultiplier (λ_{exc} = 350.7 nm).

2.3. Electrochemical Studies. To carry out the electrochemical studies, undoped and doped In_2O_3 with 4.0 mol % La^{3+} films were prepared based on the interfacial method.[50,51] For this purpose, 3.0 mg of the In_2O_3 powder were added to 20 mL of water, vigorously stirred for 30 min, and maintained in an ultrasonic bath for further 30 min. Then, the resulting dispersion was transferred to a 50 mL round-bottomed flask containing 20 mL of toluene. The two-phase system was maintained under strong magnetic stirring for 24 h. Then, the magnetic stirring was stopped, and the transparent film obtained on the interface was deposited onto the ITO surface (sheet resistance of 9−15 ohm/sq and thickness of 180 nm), and dried at 70 °C for 2h.

Cyclic voltammetry (CV) was carried out using a PGSTAT12 Autolab potentiostat equipped with a conventional one-compartment, three-electrode cell containing the nanostructured film as the working electrode, a platinum wire as the counter electrode, and Ag/AgCl (3.0 mol L^{-1} KCl) as the reference electrode. Electrocatalytic activity for water oxidation was measured in a 0.1 mol L^{-1} phosphate buffer with the addition of a 3 mol L^{-1} KOH solution for pH adjustment. CV of the electrode was obtained at a scan rate of 50 mV s^{-1}.

2.4. Computational Methods and Model Systems. First-principles calculations within the periodic DFT framework, using the hybrid B3LYP exchange−correlation functional, were performed with

DOI: 10.1021/acs.inorgchem.9b01728
Inorg. Chem. 2019, 58, 11738−11750

the CRYSTAL17 program[52] to characterize the In_2O_3 and La^{3+}-doped In_2O_3 systems. All-electron basis sets were used to describe O[53] atomic centers, a pseudopotential basis set for the In atom,[54] and an effective core potential (ECP) pseudopotential with 11 valence electrons described was used for the La^{3+}.[53] Regarding the density matrix diagonalization, the reciprocal space net was described by a shrinking factor of 4, corresponding to 36 k-points generated according to the Monkhorst–Pack scheme. The accuracy of the evaluation of the Coulomb and exchange series was controlled by five thresholds, whose adopted values were 10^{-8}, 10^{-8}, 10^{-8}, 10^{-8}, and 10^{-16}. A supercell of 80 atoms, corresponding to 2 × 2 × 1 conventional cells, was used to simulate the La^{3+}-doped In_2O_3 systems. A 12.50% substitution of In^{3+} ions by La^{3+} cations was performed in order to match the experimental value in which the rh-phase of In_2O_3 was formed.

In addition, the surface energies, E_{surf}, of the (100), (110), (111), and (211) surfaces were calculated for the cubic phase by using the Wulff construction, which minimizes the total surface free energy at a fixed volume, providing a simple correlation between the surface energy of the (hkl) plane and the distance (r_{hkl}) in the normal direction from the center of the crystallite.[55] The procedure to obtain the complete set of morphologies, based on the Wulff construction and the surface energy, has been previously presented by Andrés et al.[56] and it has been successfully used in materials science to obtain the morphology of materials, including $PbMoO_4$, $CaWO_4$, Ag_3PO_4, α-Ag_2MoO_4, $BaMoO_4$, $BaWO_4$, Ag_2CrO_4, and $LaVO_4$.[57−64] The surface energy (E_{surf}) is defined as the total energy per repeating slab cell (E_{slab}) minus the total energy of the perfect crystal per molecular unit (E_{bulk}/atom) multiplied by the number of molecular units of the surface (N) and divided by the surface area per repeating cell of the two sides of the slab: $E_{surf} = 1/2A(E_{slab} - N{\cdot}E_{bulk})$.

A schematic representation of the unit cell of bcc-In_2O_3 (a) and rh-In_2O_3 (b) structures are presented in Figure 1a,b, respectively. The In^{3+} cations in the bcc-In_2O_3 structure occupy two nonequivalent positions, 8b and 24d according to the Wyckoff notation, surrounded by oxygen anions in the octahedral and trigonal prismatic coordination, [InO_6] cluster, respectively.

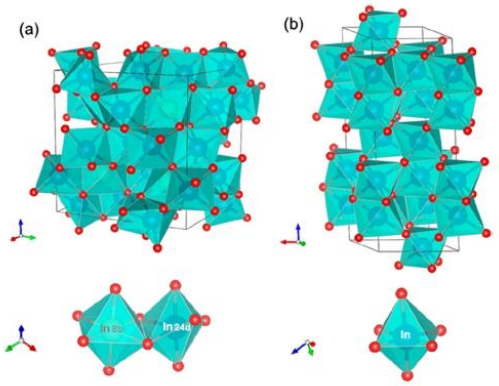

Figure 1. Schematic representation of the unit cells of (a) bcc-In_2O_3 and (b) rh-In_2O_3 structures.

3. RESULTS AND DISCUSSION

The $In(OH)_3$ and La^{3+}-doped $In(OH)_3$ precursors were obtained by a microwave synthesis at 140 °C for 2.0 min under hydrothermal conditions. The X-ray diffractograms of the precursors are shown in Figure 2a. For all samples, diffraction peaks regarding the cubic structure of indium hydroxide were indexed according to Powder Diffraction File (PDF) no. 85−1338 (Joint Committee on Powder Diffraction Standards (JCPDS), [1967]). The presence of a second phase is perceived due to the peaks at 25.9 and 33.7° for the La^{3+}-doped sample, corresponding to the orthorhombic structure of the indium oxyhydroxide (InOOH) according to PDF no. 17−0549 (JCPDS, [1964]). The short reaction time in the preparation of these materials indicates the efficiency of the microwave hydrothermal method for obtaining $In(OH)_3$ nanoparticles and the incorporation of the La^{3+} ions into the hydroxide lattice.

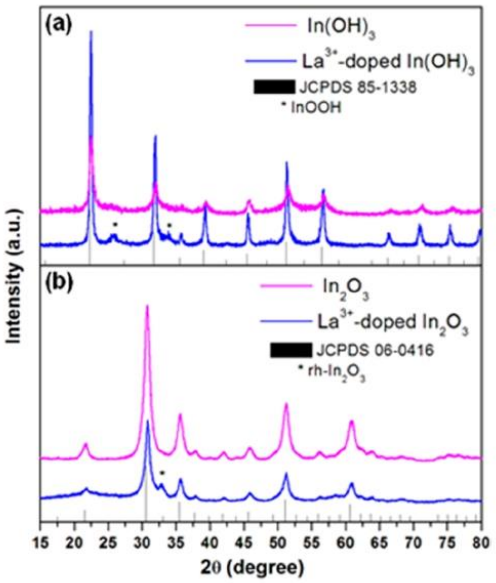

Figure 2. XRD patterns of the as-synthesized In_2O_3 and La^{3+}-doped $In(OH)_3$ (a) and of the In_2O_3 and La^{3+}-doped In_2O_3 obtained after calcination (b). PDF nos. 85−1338 and 06−0416 (JCPDS, [1967 and 1955, respectively]).

In order to obtain In_2O_3 and La^{3+}-doped In_2O_3 materials, the $In(OH)_3$ precursors were subjected to microwave oven calcination at 350 °C for 2 min. The corresponding XRD patterns are shown in Figure 2a. It was observed that a single cubic phase bcc-In_2O_3 was formed for the undoped In_2O_3 sample, in accordance with crystallographic data card PDF no. 06−0416 (JCPDS, [1955]). The diffractogram of the La^{3+}-doped In_2O_3 sample shows, in addition to the peaks of the bcc-In_2O_3 structure, a peak at 2θ = 32.63° corresponding to the plane (110) of the rhombohedral phase rh-In_2O_3, according to PDF no. 72−0683 (JCPDS, [1969]). An analysis of the results displayed in Figure 2b shows that a mixture of bcc and rh-In_2O_3 is presented; the addition of La^{3+} cations in the structure of In_2O_3 triggers the appearance of the (110) peak of the rhombohedral phase, rh-In_2O_3.

A Rietveld refinement method was performed for the In_2O_3 and La^{3+}-doped In_2O_3 samples, as shown in Figure 3. In Table 1 the values of the profile and lattice parameters obtained after the final refinement cycle are presented. The low values of χ^2 and the profile parameters (R_p, R_{wp}) indicate a high quality of refinement. The presence of the dopant influences phase formation, wherein the undoped bcc-In_2O_3 was transformed into a mixture of bcc-In_2O_3 and rh-In_2O_3. Rietveld refinement of the XRD patterns of the La^{3+}-doped In_2O_3 sample renders the

DOI: 10.1021/acs.inorgchem.9b01728
Inorg. Chem. 2019, 58, 11738−11750

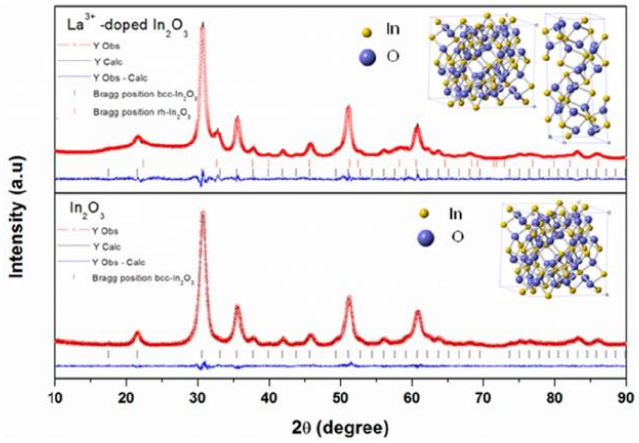

Figure 3. Rietveld refinement of XRD patterns for the In_2O_3 and La^{3+}-doped In_2O_3 samples. The respective crystal structures obtained from Rietveld refinements, comprising the cubic and rhombohedral phases, are shown in the upper right corner.

Table 1. Quality and Parameters Obtained by the Rietveld Method for the In_2O_3 Samples

	bcc-In_2O_3 cell parameters	rh-In_2O_3 cell parameters						
	$a = b = c$ (Å)	$a = b$ (Å)	c (Å)	rh phase fraction (%)	R_{wp} (%)	R_p (%)	R_{Bragg} (%)	χ^2
In_2O_3	10.1110(3)				6.23	4.65	1.09	1.191
La^{3+}-In_2O_3	10.1202(5)	5.4842(11)	14.5053(10)	19.7	6.31	4.98	1.63	1.459

presence of 80.3% bcc-In_2O_3 phase and 19.7% rh-In_2O_3. The cubic and rhombohedral structures of In_2O_3 samples were generated from the Rietveld refinement data and are represented in the inset of Figure 3.

In the present work, we observed that the La^{3+} doping process promotes the formation of the rh-In_2O_3 phase to a larger extent with respect to the Er^{3+} doping process, reported in our previous work.[36] A comparison of the results obtained from the Rietveld refinement shows that a percentage of 19.7% was achieved for the rh-In_2O_3 phase with La^{3+} doping and 12.7% with the Er^{3+} one. This result was also observed by Wang et al.,[65] in which the influence of La^{3+} doping on the crystal phase can be related to size and dipole polarizability of the substitutional dopant. The La^{3+} cation has a larger ionic radius than the Er^{3+} cation, exhibiting a greater tendency toward the distortion of the electronic cloud, thus favoring even more the formation of the rh-In_2O_3 phase.

The La^{3+} doping at both 8b and 24d sites modifies the distortion of the octahedral coordination due to mismatch in ionic radii of $La^{3+}$and In^{3+}cations. To gain further insight into the source of the relative stabilization of the rh-In_2O_3 phase with respect the bcc-In_2O_3 induced by the La^{3+} doping process, first-principles calculations were carried out to study the La^{3+}-doped In_2O_3 crystal structure at different amount of La^{3+}-doping (3.1, 9.3, and 12.5 mol %) for both phases (rh- and bcc-In_2O_3) and for the two Wyckoff positions. First, it was found that the substitution of In^{3+} by La^{3+} in the bcc-In_2O_3 structure is more energetic at the d site, 1.97×10^{-4} Hartree.

An analysis of the results presented in Table 2 shows that the undoped bcc-In_2O_3 phase is more stable than the rh-In_2O_3 one; however, as the percent of La^{3+} doping content increases, the rh-phase is stabilized with respect to the bcc-structure. Substituting In^{3+} by La^{3+} cations in both positions 8b and 24d achieves an

Table 2. Calculated Cell Parameters, a and c (Å) and the Energy Difference $E_{bcc} - E_{rh}$ (Hartree) between bcc and rh Structures of the In_2O_3 and La^{3+}-In_2O_3 Structures at Different % of La^{3+} Doping[a]

	bcc	rh		
In_2O_3	a	a	c	$E_{bcc} - E_{rh}$
undoped	10.123	5.474	14.585	−0.0071
3.1% La^{3+} (8b)	11.104	5.489	14.624	−0.0062
3.1% La^{3+} (24d)	11.078			−0.0064
9.3% La^{3+} (8b)	11.220	5.514	14.691	−0.0021
9.3% La^{3+} (24d)	11.180			−0.0022
12.5% La^{3+} (8b)	11.298	5.525	14.720	0.0010
12.5% La^{3+} (24d)	11.298			0.0393

[a]Cell parameters referred to a single unit cell. E_{bcc} = −229.73034 hartree. 8b and 24d refer to the Wyckoff positions of bcc-In_2O_3.

energy in which the rh-In_2O_3 phase is more stable than the bcc-In_2O_3 phase when the doping percentage reaches the value of 12.5% at both 8b and 24d positions.

An analysis of the values of the In−O and La−O bond distances at the [InO_6] and [LaO_6] clusters, i.e., the local coordination of both In^{3+} and La^{3+} at both undoped and doped bcc- and rh-In_2O_3 structures (see Tables S1 and S2) renders that the substitution of In^{3+} by La^{3+} provokes an expansion of the clusters due to the large ionic radius of La^{3+} with respect to In^{3+}, i.e., the La−O bonds are larger than In−O for both bcc- and rh-In_2O_3 phases. However, it is interesting to note that [LaO_6] clusters display a more remarkable structural distortion in the rh-In_2O_3 phase at 12.5% La content of the rh-In_2O_3 phase, with four different La−O distances.

Furthermore, the value O−In(8b)−O bond angle decreases from 87.5 to 80.6° in 12.5% La^{3+}-doping for the bcc-phase, while

DOI: 10.1021/acs.inorgchem.9b01728
Inorg. Chem. 2019, 58, 11738−11750

the other O−In(8b)−O bond angle increases from 93.3 to 98.8°; for the O−In(24d)−O bond angle, their values decrease from 78.5 to 76.3°, and increases from 98.3 to 104.0° on going from the bcc-phase to 12.5% amount of La^{3+} doping. The values of the O−La−O bond angles at bcc- and rh-phase for the same doping percentage are 77.0 and 103.0°, as well as 73.5 and 110.0°, respectively (see Table S3). These values indicate that the geometry of the rh phase has more flexibility than the bcc phase to carry out the La^{3+}-doping process, demonstrating that the [LaO_6] octahedra in the rh-doped structure has more liberty to expand and rotate. This fact indicates that the rh-In_2O_3 structure is more prone to accept the substitution of La^{3+} that entails larger structural distortion with a lower energy cost. These theoretical results are able to explain the experimental findings, i.e., the formation of the rh-In_2O_3 phase is promoted when In^{3+} is replaced by La^{3+} cations. Overall, the structural deformations at the lattice of the rh- and bcc-In_2O_3 arise due to two types of distortions: One is due to tilting of InO_6 octahedra, and the other results from the length asymmetry in six In−O bonds surrounding the In^{3+} cation in the [InO_6] octahedra. Considering the above observation, it is easy to realize that such structural order−disorder modifications provoked by the La^{3+} doping process is more favorable at rh than bcc phase of In_2O_3. This behavior was also found on a study based of $NaYF_4$ doped with light lanthanides, where hexagonal phase is favored compared to cubic one.[65]

The FE-SEM images of the In_2O_3 and La^{3+}-doped In_2O_3 samples are displayed in Figure 4a,b and consist of agglomerated

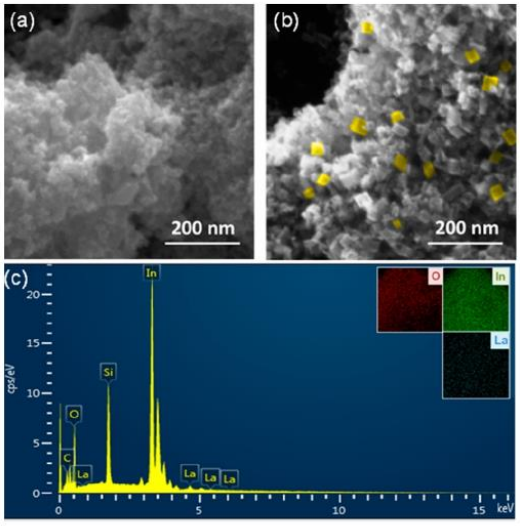

Figure 4. FE-SEM images of: In_2O_3 (a), La^{3+}-doped In_2O_3 (b), and EDX of the La^{3+}-doped In_2O_3 sample (c). The inset in (c) represents the elemental mapping of the La^{3+}-doped In_2O_3 sample.

formation and larger size cubic shaped nanoparticles, respectively. The growth process and morphology of the final nanoparticles depend on the degree of saturation of the reaction medium, the diffusion rate of the species present on the surface of the crystals and, consequently, on the interfacial energies involved in the process.[66] From the results obtained, it is clear that the presence of La^{3+} affects the morphology and size of the synthesized particles.

The presence of La^{3+} in the doped sample is confirmed by the EDX spectrum (Figure 4c). The elemental mapping of the La^{3+}-doped In_2O_3 sample is presented in the inset of Figure 4c, showing uniform distributions of the In, O, and La elements at the surface of the nanostructures.

From the thermodynamic point of view, the shape of crystals grown under a real or near equilibrium condition is dominated by the energies of the different surfaces. The (110), (100), (111), and (211) surfaces of the bcc-In_2O_3 phase were modeled using slab models with the calculated equilibrium geometries. According to the DFT calculations, the stability of the surfaces follows the order (100) < (211) < (110) < (111), with surface energies of 3.62, 2.29, 1.40, and 1.02 J m^{-2}, respectively. Since the coordination environment affects the stabilization of the surfaces, the higher stability of the (111) surface is attributed to the presence of [InO_6] clusters in the exposed surface, while for the other surfaces, the presence of oxygen vacancies in the superficial and undercoordinated In clusters increases the value of the surface energy (Figure S1). An analysis of the theoretical results reveals that the most stable morphology is an octahedron, in which only the (111) surface appears. From the energy obtained using the slab models, it is possible to modulate the surface energies to find the morphology obtained experimentally. This strategy is based on the fact that the morphology is derived from calculated surface energies using the assumption that crystal faces with the lowest surface energies control the final crystal morphology. Therefore, different possible morphologies can be obtained by increasing or decreasing the stability of the different facets. A truncated octahedron can be obtained if the surface energy of (110) is decreased to 0.80 J m^{-2}, while a truncated sphere can be produced when the surface energy of (211) is decreased to 0.50 J m^{-2} (see Figure 5).

The experimentally obtained morphology of the La^{3+}-doped In_2O_3 sample makes possible to find the path that is capable of matching the theoretical morphology. This agreement is obtained when the values of the surface energy for (100) decrease to 0.30 J m^{-2}, where the presence of La^{3+} cations in the In_2O_3 matrix lower the (100) surface energy, and thus the cubic shape is able to appear (see Figure 5). This behavior was emphasized by Cho et al.,[67] where the presence of foreign ions in the reaction environment can drive the surface energy toward the formation of a specific morphology; in particular, a well-defined cubic morphology was achieved with fluorine doping. These authors evaluated the energies of F-substitution at the surface of In_2O_3, showing that the surface binding of F atoms directs the stabilization of the (100) facets.

The analysis of the TEM images reveals a difference in the morphology of In_2O_3 and La^{3+}-doped samples. The undoped In_2O_3 sample presents smaller particles, with a size of around 8 nm and irregular shapes (Figure 6a), while the La^{3+}-doped In_2O_3 sample shows an increased size and a verified cubic morphology (Figure 6b). As can be seen in Figure 6c,d, HRTEM images of the In_2O_3 sample show the (222) lattice spacing (2.91 and 2.98 Å). For La^{3+}-doped In_2O_3, the (400) lattice spacing (2.59 Å), (211) lattice spacing (4.16 Å), and, from the rhombohedral phase, the (110) lattice spacing (2.77 Å) can also be observed (Figure 6e,f). These results indicate that the La^{3+} doping allows to access other surface facets beyond the (111), observed for the undoped In_2O_3.

The Raman spectra obtained is presented in Figure 7a. The body-centered cubic structure In_2O_3 (bcc-In_2O_3) belongs to

DOI: 10.1021/acs.inorgchem.9b01728
Inorg. Chem. 2019, 58, 11738−11750

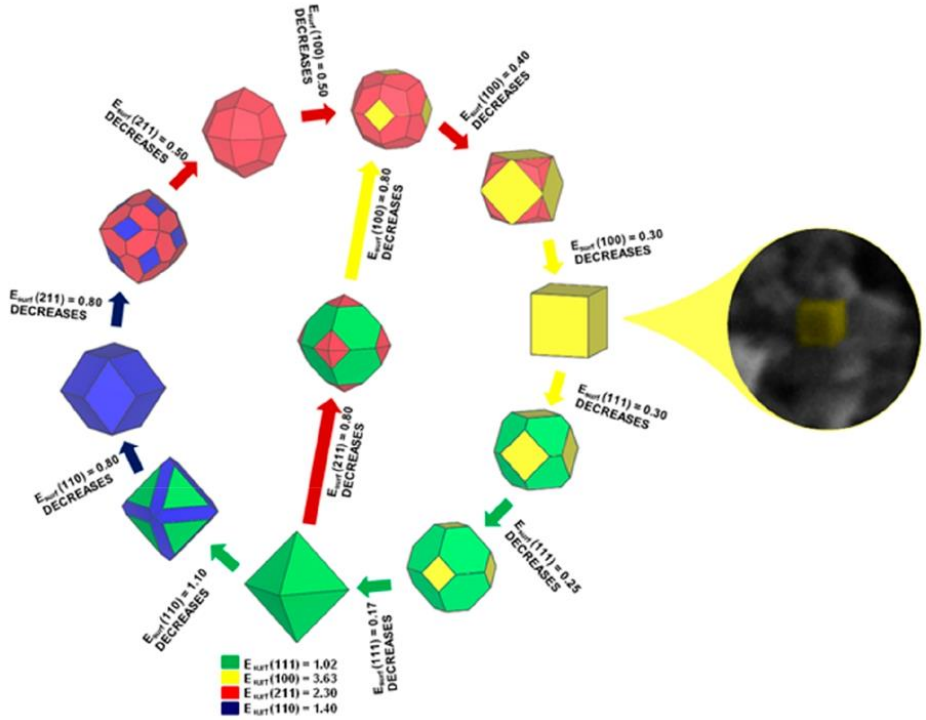

Figure 5. Map of the morphologies of bcc-In_2O_3 taking into account (100), (110), (111), and (211) surfaces (with surface energy expressed in J m^{-2}). An image of the In_2O_3 cube-form particle obtained from SEM is shown on the right.

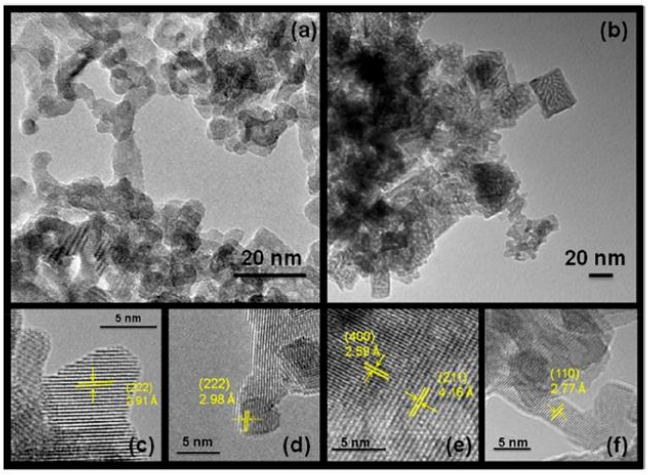

Figure 6. TEM images of In_2O_3 (a) and La^{3+}-doped In_2O_3 nanostructures (b). HR-TEM images of In_2O_3 (c, d) and La^{3+}-doped In_2O_3 nanocrystals (e, f).

space group $Ia\bar{3}$, T_h^7. For this structure, among the following predicted modes ($4A_g + 4E_g + 14F_g + 5A_u + 5E_u + 16T_u$), only A_g, E_g, and F_g are Raman active.[68] The Raman spectra of the In_2O_3 and La^{3+}-doped In_2O_3 samples display characteristic bands of the vibration modes of body-centered cubic oxide, which agree with values reported in the literature.[69,70] The main signals for the synthesized samples were observed at 131 cm^{-1} (A_g^1), which is related to In−O (vibration of InO_6 structure units) at 308 cm^{-1}, attributed to the bending vibration of the InO_6 octahedron (superposition of the F_{2g}^4 and A_g^3 modes), and

DOI: 10.1021/acs.inorgchem.9b01728
Inorg. Chem. 2019, 58, 11738−11750

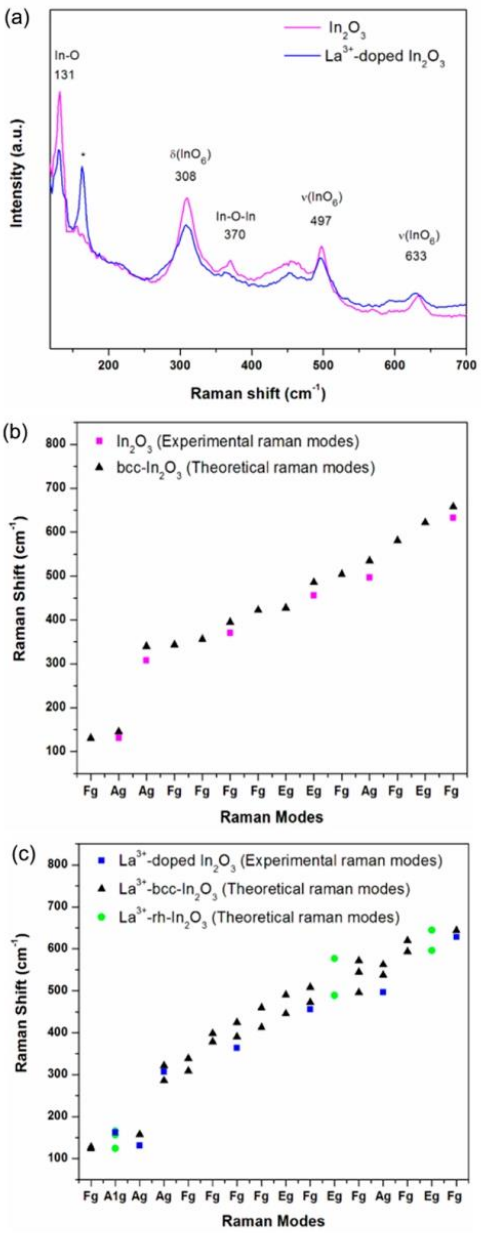

Figure 7. Raman spectra of In_2O_3 and La^{3+}-doped In_2O_3 samples (a) and comparison between the positions of theoretical and experimental Raman-active modes bcc-In_2O_3 (**b**) and rh-In_2O_3 (**c**).

a signal at 370 cm^{-1}, which is due to stretching vibrations of In−O−In (F_{2g}^5). The bands at 497 and 633 cm^{-1} are also assigned to the stretching vibrations of the InO_6 octahedrons.

The rh-In_2O_3 structure belongs to the space group $R\bar{3}c$, D_{3d}^6. The irreducible representation of the optical modes for the crystal are $2A_{1g} + 2A_{1u} + 3A_{2g} + 2A_{2u} + 5E_g + 4E_u$, of which only the vibrations with symmetry A_{1g} and E_g are active in Raman spectroscopy.[70] The Raman spectra of La^{3+}-doped In_2O_3 presents a strong band at 162 cm^{-1}, attributed to the A_{1g} symmetry of rh-In_2O_3, indicating the coexistence of cubic and rhombohedral phases of In_2O_3, which is in agreement with the X-ray diffraction characterization.

Furthermore, the vibration of the In−O−In bond is known to be affected by the presence of oxygen vacancies.[9] The relative intensity and shift of the Raman band position can reflect the density of defect states of oxygen.[71−73] The observed redshift of the In−O−In mode to 363 cm^{-1} for the La^{3+}-doped sample can be attributed to the weaker bond strength forces due to the La^{3+} insertion.

A comparison of theoretical and observed experimental positions of the Raman active modes is presented in Figure 7b,c, respectively. An analysis of the results revealed a good agreement between the Raman shifts (cm^{-1}) of the experimental modes compared to the theoretical modes for the bcc-In_2O_3 structure. The insertion of La^{3+} cations gives rise to a change in the crystal lattice with concomitant variations in the position of the Raman modes, as can be observed in Figure 7c. The bands presented in the host matrix spectrum are affected by the dopant, since the Raman bands arising from the vibrational modes that involve a significant contribution of atomic motion from the dopant atom may exhibit a shifting of the peak position (Tables S4 and S5). In addition, since the structural disorder within the undoped In_2O_3 and the La^{3+}-doped In_2O_3 compounds loses its translational symmetry, Raman spectroscopy can be used to investigate the nearest-neighbor changes in these structures. Disordering allows more phonons to contribute to the optical spectra, thus causing a general broadening of all the Raman active modes.

The values of the band gap of each sample were calculated by linear extrapolation of the curve using the method proposed by Kubelka−Munk[74] from absorption spectra in the visible region (Figure S2). The estimated band gap values are 2.9 eV for the undoped In_2O_3 sample, which presents only the bcc phase, and 3.2 eV for the sample doped with 4.0 mol % of La, presenting a mixture of bcc and rh phases.

The calculated band structures along high symmetry lines are shown in Figure 8a−d, while the total density of states (DOS) projected on atoms for the pure bcc-In_2O_3, pure rh-In_2O_3, 12.5% La^{3+} bcc-In_2O_3, and 12.5% La^{3+} rh-In_2O_3 are presented in Figure 8e−h, respectively. The analysis of the band structures indicates that pure bcc- and rh-In_2O_3 phases present similar and indirect band gap energy (3.74 and 3.76 eV, respectively). The doping of La^{3+} cations in the In_2O_3 matrix provides an increase in the indirect gap energy, which was the same behavior as that verified experimentally. This enhancement can be sensed more in rh-In_2O_3 (up to 4.11 eV) than in bcc-In_2O_3 (up to 3.82 eV) doped structures, due to the increase in electron density caused by the dopant.[75]

The DOS of pure bcc- and rh-In_2O_3 phases (Figure 8e,f, respectively) indicates that the upper part of the valence band (VB) consists mainly of 2p O orbitals, while the conduction band (CB) is mostly composed of 5p In orbitals. Doping the In_2O_3 matrix with La^{3+} resulted in a VB similar to those of both pure bcc- and rh-In_2O_3 phases. However, the CB in Figure 8h has a prevailing La 5d character, more noticeable than that in Figure 8g, showing an effective hybridization with 2p O orbitals to generate the distorted [LaO_6] clusters.

The La^{3+}-doping process for the rh-doped structure shows a strong Coulomb force between La^{3+} cations and oxygen anions

DOI: 10.1021/acs.inorgchem.9b01728
Inorg. Chem. 2019, 58, 11738−11750

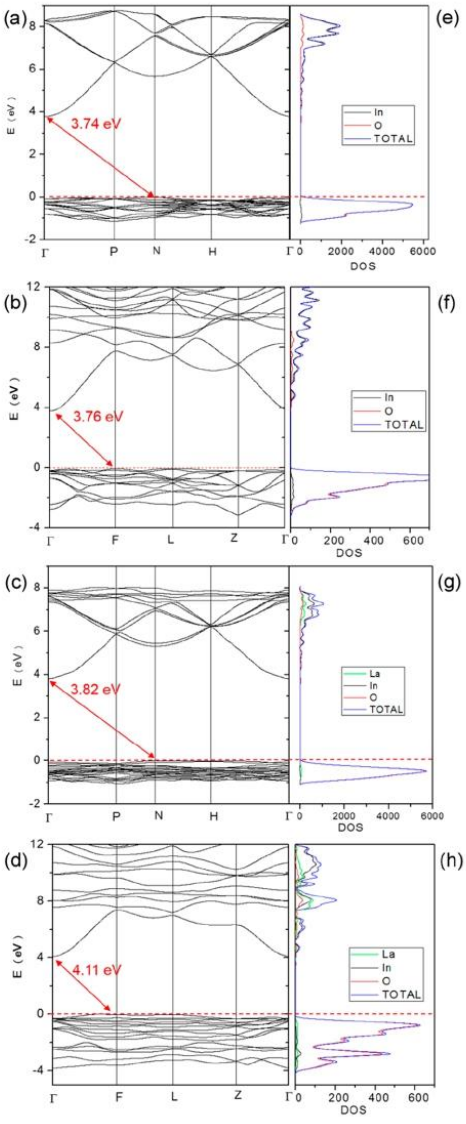

Figure 8. Band structure of bcc-In_2O_3 (a), rh-In_2O_3 (b), 12.5% La^{3+}-doped bcc-In_2O_3 (c), and 12.5% La^{3+}-doped rh-In_2O_3 (d). DOS projected on atoms for bcc-In_2O_3 (e), rh-In_2O_3 (f), 12.5% La^{3+}-doped bcc-In_2O_3 (g), and 12.5% La^{3+}-doped rh-In_2O_3 (h).

that can result in the structural rotation of the [LaO_6] octahedra. This fact can increase the La−O bond length with a concomitant increment of the rotation for the octahedra in the rh phase with respect to the bcc phase, giving rise to the appearance of long-range structural disorder. This result explains the experimental observations, in which a suitable amount of La^{3+}content (12.5%) covers states in the CB of rh-In_2O_3 structure leading to a shift in the absorption to higher energies, a result known as the Burstein−Moss effect.[76] Other authors also attributed the widening of the bandgap to this effect, reporting a blueshift in the absorption edge for the In_2O_3 doped with Fe ions,[77] and He et al.[78] noticed an increase in the band gap of ZnO with the increment of the La ions content. Oxygen vacancies also contribute to carrier density, affecting the gap energy, since they generate defects between the valence band and the conduction band.[79] The existence of these vacancies is confirmed by photoluminescence spectra.

Study of the PL emissions in materials provides valuable information about aspects involving intermediate energy levels and energy transfer mechanisms. The PL emissions obtained at room temperature with λ = 350 nm are shown in Figure 9. The

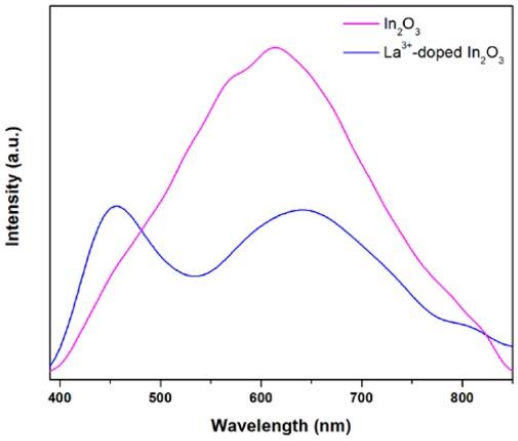

Figure 9. Photoluminescence spectra of In_2O_3 and La^{3+}-doped In_2O_3 samples.

photoluminescence of In_2O_3 nanostructures is mainly related to oxygen defects, such as oxygen vacancies and interstitial oxygen, as well as to indium vacancies. The undoped In_2O_3 sample exhibits a broad emission band centered at approximately 617 nm, while in the La^{3+}-doped In_2O_3 sample the emission band undergoes a decrease in intensity and presents an additional emission at approximately 450 nm (blue emission). Green emissions were attributed to the presence of oxygen vacancies in the bulk material, which can act as recombination centers.[80] Wu et al.[27] claimed that the blue emissions of the nanostructures of In_2O_3 can be accounted for by the radiative combination between electrons located in oxygen vacancies (V_o^x) of the donor band and holes in vacancies of indium and oxygen (V_{In}, V_o)^x. Yang et al.[81] demonstrated that the emission in the blue is the result of the recombination of electrons that occupy oxygen vacancies with photoexcited holes.

The PL behavior is strongly dependent on the structural modifications generated from intrinsic defects or dopant ions. Zhang et al.[39] observed an enhancement of PL emission for Gd^{3+}-doped rh-In_2O_3 nanoparticles, which was attributed to the deep level or trap state emissions. As it has been extensively reported in the literature, the insertion of La^{3+} ions in the In_2O_3 matrix produce a suppression of the PL intensity, thus endowing La^{3+} ions with the ability to prevent electron−hole recombination.[82] The different PL aspects observed for the undoped In_2O_3 and La^{3+}-doped In_2O_3 samples evidence the alternative

DOI: 10.1021/acs.inorgchem.9b01728
Inorg. Chem. 2019, 58, 11738−11750

recombination mechanism of each sample when defects, such as dopants, are introduced.

The electrochemical activity of undoped and doped In_2O_3 with 4.0 mol % La^{3+} films for water oxidation was investigated by cyclic voltammetry in 0.1 mol L^{-1} phosphate buffer, with the addition of KOH until pH 13. CV studies obtained for the ITO background are also included for comparison purposes. Figure 10 exhibits the electrocatalytic oxygen evolution reaction of

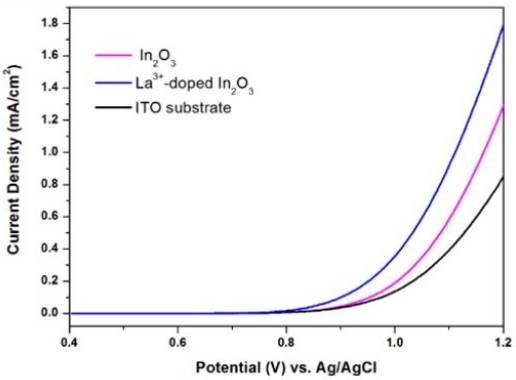

Figure 10. CVs of the ITO background, In_2O_3, and La^{3+}-doped In_2O_3 films in phosphate buffer, pH 13.

In_2O_3 films, with an onset potential of 0.80 V (vs Ag/AgCl) for In_2O_3, while for the La^{3+}-doped In_2O_3 film, this process takes place at lower potential, around 0.74 V, thus indicating a higher charge transfer kinetics.[83] In addition, the doped In_2O_3 film exhibited a higher current density when compared to the In_2O_3 film.

During the electrochemical process, the applied potential in In_2O_3 nanostructure films promotes the formation of electron−hole pairs, which are responsible for water oxidation. In this arrangement, oxygen is produced from water decomposition by holes generated in the In_2O_3 film surface, and intermediate species produced during the four-electron reaction may capture electrons from the conduction band.[6,83]

The La^{3+} doping leads to a symmetry breaking process[36,84] that can induce the formation of intermediary energy levels within the forbidden band gap and that can act as trap states reducing the electron/hole recombination rates, as observed by Liu et al.[85] and Zhou and Zhao[86] in samples containing mixed TiO_2 phases. Moreover, accordingly to Yalavarthi et al.,[87] the electron/hole recombination influences the charge transfer efficiency, and a lower recombination rate can leads to a more efficient electrochemical performance. Furthermore, an increases of the charge separation can be associated with the presence of the La empty 4f orbitals, that is able to suppress the recombination as well.[88]

The above cited factors allowed a higher electrocatalytic efficiency of O_2 evolution for La^{3+}-doped In_2O_3 films compared to the In_2O_3 sample. The Scheme 1 shows O_2 evolution bubbles on the La^{3+}-doped In_2O_3 film surface during application of 1.2 V and the respective schematic representation of electron−hole formation during this process. Oxygen vacancies are dominant defects in In_2O_3 and they are considered active sites for electrochemical processes.[89] Zhang et al.[90] provided evidence that oxygen vacancies reduce the activation energy of O−O

Scheme 1. O_2 Gas Bubbles Formed on the La^{3+}-Doped In_2O_3 Film during Application of 1.2 V and Schematic Representation of the Electron−Hole Formation

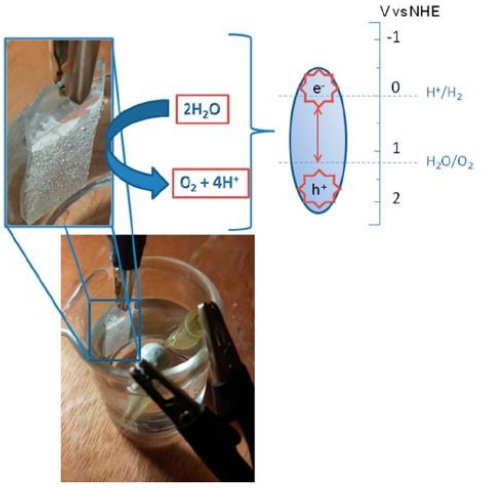

bond formation, that is, the rate-determining step for catalytic water oxidation.

The electrochemical performance in the La^{3+}-doped In_2O_3 sample is related to the bulk and surface properties resulting from the presence and the concentration of this dopant. Increasing the La amount in the In_2O_3 would not necessarily result in linear improvement of the catalytic efficiency, since aspects considered to be key factors to enhance the electrochemical activity, such as the presence of oxygen vacancies, can present a two-sided effect, being crucial to favor the electrocatalytic activation, but the excess of this oxygen defect can result in recombinative centers reducing the efficiency of the process as reported by Gan et al.[9] Therefore, the prediction of the electrochemical activity in the function of the La content constitutes a complex issue, in view of the several factors that affect the charge transfer processes in the oxide surface, being specific for each dopant amount.

These results are in accordance with the PL measurements, which exhibited a lower intensity band for the doped sample and an additional band near 450 nm, evidencing a high concentration of electron traps in La^{3+}-doped In_2O_3, assigned to oxygen vacancies. The analysis of the Raman spectra also indicated a higher number of oxygen vacancies for La^{3+}-doped In_2O_3 compared to the In_2O_3 sample. These traps are responsible for decreasing electron/hole recombination rates and, consequently, for improving the charge transfer processes in the oxide surface. Therefore, the electrochemical performance recorded from the samples indicates that the insertion of lanthanum promoted defect states that affect the charge carrier transfer process.

The influence of the pH value on the activity of In_2O_3 films for water oxidation was evaluated in order to suggest the prevailing mechanism reaction. Both undoped and doped In_2O_3 at 4.0 mol % La^{3+} samples exhibited a similar behavior in the range of pH 7.0−13.0, and the onset potential for water oxidation decreased with increasing pH values (Figure S3a,b). This pH dependence indicates a proton-coupled electron transfer (PCET) reac-

DOI: 10.1021/acs.inorgchem.9b01728
Inorg. Chem. 2019, 58, 11738−11750

tion.[4,7,91] One prevailing reaction mechanism proposed for oxides in an alkaline pH medium is the direct adsorption of OH^- molecules by the surface, forming a charged intermediate. Removing one electron and one proton from the $[(SURFACE)-OH]^-$ intermediate, the formed $[(SURFACE)-O]^-$ can interact with other H_2O molecule generating $[(SURFACE)-OOH]^-$. Another stage of deprotonation and electron transfer forms $[(SURFACE)-OO]^-$; thereafter, the loss of one electron forms $In_2O_{3(SURFACE)}-OO$ and releases the O_2 molecules with consequent recovery of the oxide surface.[4,7,92]

4. CONCLUSIONS

In_2O_3 and La^{3+}-doped In_2O_3 nanostructures were successfully synthesized by a microwave-assisted hydrothermal method followed by microwave calcination. The structures were elucidated by X-ray diffraction, which indicated the formation of the bcc-In_2O_3 structure for the undoped sample and a mixture of bcc- and rh-In_2O_3 structures for the La^{3+}-doped sample. The Rietveld refinement provided information about the effect of the doping process of La^{3+} cations in the lattice parameters of the In_2O_3 matrix and determined the proportion of bcc- and rh-In_2O_3 polymorphs obtained in La^{3+}-doped In_2O_3. The TEM images showed that the doping process of La^{3+} induces the formation of cubelike particles with a larger size when compared to the undoped In_2O_3. The Raman spectra revealed the existence of bcc- and rh-In_2O_3 for the La^{3+}-doped sample, thus corroborating the XRD results, and indicated the presence of oxygen-related defects in the materials. First-principle calculations, at the DFT level, were performed to obtain the formation energies of the undoped In_2O_3 and La^{3+}-doped In_2O_3 polymorphs, their geometry, and their electronic properties. In addition, Wulff construction was employed to match the theoretical and experimental morphologies of the cubic phase. Theoretical results indicate that for a La^{3+} substitution of 12.5%, the rh-In_2O_3 phase is more stable than the bcc-In_2O_3 phase. The structural transformation was attributed to the changes in the In−O bond lengths, O−In−O bond angles, and the electronic redistribution induced by the La^{3+}-doping process. The PL intensity decreased from undoped In_2O_3 to La^{3+}-doped In_2O_3 nanostructures, although an increase could be observed in the blue emission for the doped sample. This indicates that doping can alter the surface, generating trap states that should reduce the electron/hole recombination rates, improving the charge transfer processes, and consequently leading to a more efficient electrochemical performance.

■ ASSOCIATED CONTENT

Supporting Information

The Supporting Information is available free of charge on the ACS Publications website at DOI: 10.1021/acs.inorgchem.9b01728.

Calculated surfaces, UV−vis spectra, cyclic voltammetries, bond lengths and angles, Raman data (PDF)

■ AUTHOR INFORMATION

Corresponding Author

*E-mail: rclima@ufu.br. Tel./fax: +55-34-3239-4143.

ORCID

J. Andres: 0000-0003-0232-3957

R. C. Lima: 0000-0001-6658-7869

Present Address

L.G.: Departament de Química Física, Universitat Valencia, Burjassot, Spain.

Notes

The authors declare no competing financial interest.

■ ACKNOWLEDGMENTS

We are grateful to Coordenação de Aperfeiçoamento de Pessoal de Nível Superior (Capes), Conselho Nacional de Desenvolvimento Cientifico e Tecnologico (CNPq), Fundação de Amparo a Pesquisa do Estado de Minas Gerais (FAPEMIG) (APQ-00988-13), and Grupo de Materiais Inorgânicos do Triângulo (GMIT) - Research Group supported by FAPEMIG (APQ-00330-14) for the financial support. This work was partially supported by the Brazilian Institute of Science and Technology (INCT) in Carbon Nanomaterials. J.A. acknowledges financial support from Universitat Jaume I for project UJIB2016-25, Generalitat Valenciana (PrometeoII/2014/022, ACOMP/2014/270, and ACOMP/2015/1202), Ministerio de Economia y Competitividad, Spain (project CTQ2015-65207-P). I.S. also thanks the Spanish Ministerio de Economía, Industria y Competitividad for a postdoctoral "Juan de la Cierva-Incorporación" fellowship. We also acknowledge the Servei Informática, Universitat Jaume I, for a generous allotment of computer time.

■ REFERENCES

(1) Vineesh, T. V.; Mubarak, S.; Hahm, M. G.; Prabu, V.; Alwarappan, S.; Narayanan, T. N. Controllably Alloyed, Low Density, Free-standing Ni-Co and Ni-Graphene Sponges for Electrocatalytic Water Splitting. *Sci. Rep.* **2016**, *6*, 31202.

(2) Yang, J. H.; Wang, D. G.; Han, H. X.; Li, C. Roles of Cocatalysts in Photocatalysis and Photoelectrocatalysis. *Acc. Chem. Res.* **2013**, *46* (8), 1900−1909.

(3) Betley, T. A.; Wu, Q.; Van Voorhis, T.; Nocera, D. G. Electronic design criteria for O-O bond formation via metal-oxo complexes. *Inorg. Chem.* **2008**, *47* (6), 1849−1861.

(4) Huynh, M. H. V.; Meyer, T. J. Proton-coupled electron transfer. *Chem. Rev.* **2007**, *107* (11), 5004−5064.

(5) Mandal, H.; Shyamal, S.; Hajra, P.; Samanta, B.; Fageria, P.; Pande, S.; Bhattacharya, C. Improved photoelectrochemical water oxidation using wurtzite ZnO semiconductors synthesized through simple chemical bath reaction. *Electrochim. Acta* **2014**, *141*, 294−301.

(6) Peter, L. M.; Upul Wijayantha, K. G. Photoelectrochemical Water Splitting at Semiconductor Electrodes: Fundamental Problems and New Perspectives. *ChemPhysChem* **2014**, *15* (10), 1983−1995.

(7) Romeiro, F. C.; Rodrigues, M. A.; Silva, L. A. J.; Catto, A. C.; da Silva, L. F.; Longo, E.; Nossol, E.; Lima, R. C. rGO-ZnO nanocomposites for high electrocatalytic effect on water oxidation obtained by microwave-hydrothermal method. *Appl. Surf. Sci.* **2017**, *423*, 743−751.

(8) Bierwagen, O. Indium oxide-a transparent, wide-band gap semiconductor for (opto)electronic applications. *Semicond. Sci. Technol.* **2015**, *30* (2), 024001.

(9) Gan, J. Y.; Lu, X. H.; Wu, J. H.; Xie, S. L.; Zhai, T.; Yu, M. H.; Zhang, Z. S.; Mao, Y. C.; Wang, S. C. I.; Shen, Y.; Tong, Y. X. Oxygen vacancies promoting photoelectrochemical performance of In2O3 nanocubes. *Sci. Rep.* **2013**, *3*, 1021.

(10) Gu, F. B.; Li, C. J.; Han, D. M.; Wang, Z. H. Manipulating the Defect Structure (V-O) of In_2O_3 Nanoparticles for Enhancement of Formaldehyde Detection. *ACS Appl. Mater. Interfaces* **2018**, *10* (1), 933−942.

(11) Davies, D. W.; Walsh, A.; Mudd, J. J.; McConville, C. F.; Regoutz, A.; Kahk, J. M.; Payne, D. J.; Dhanak, V. R.; Hesp, D.; Pussi, K.; Lee, T. L.; Egdell, R. G.; Zhang, K. H. L. Identification of Lone-Pair Surface States on Indium Oxide. *J. Phys. Chem. C* **2019**, *123* (3), 1700−1709.

(12) Park, K. W.; Kang, S. B.; Jeong, J. A.; Choi, S. W.; Kim, J.; You, I. K.; Yang, Y. S.; Kim, H. K. Liquid crystal devices incorporating transparent Zn, Sn co-doped In_2O_3 electrodes prepared by direct inkjet-printing of nanosized particles. *J. Phys. D: Appl. Phys.* **2013**, *46* (14), 145301.
(13) Ibrahim, H.; Temerk, Y. Novel sensor for sensitive electrochemical determination of luteolin based on In_2O_3 nanoparticles modified glassy carbon paste electrode. *Sens. Actuators, B* **2015**, *206*, 744−752.
(14) Temerk, Y.; Ibrahim, H. Fabrication of a novel electrochemical sensor based on Zn-In_2O_3 nanorods coated glassy carbon microspheres paste electrode for square wave voltammetric determination of neuroprotective hibifolin in biological fluids and in the flowers of hibiscus vitifolius. *J. Electroanal. Chem.* **2016**, *782*, 9−18.
(15) Munoz, A. G.; Heine, C.; Hannappel, T.; Lewerenz, H. J. Solar tandem water splitting from efficient III-V photovoltaics: Implications of electrochemical surface activation. *Electrochim. Acta* **2018**, *260*, 861−871.
(16) Zhao, Y. J.; Xie, R. J.; Dierre, B.; Takeda, T.; Sekiguchi, T.; Hirosaki, N.; Wang, L. Enhanced cathodoluminescence of green beta-sialon: Eu^{2+} phosphor by In_2O_3 coating. *J. Alloys Compd.* **2017**, *727*, 1110−1114.
(17) Chen, P.; Yin, X. T.; Que, M. D.; Yang, Y. W.; Liu, X. B.; Que, W. X. Bilayer photoanode approach for efficient In_2O_3 based planar heterojunction perovskite solar cells. *J. Alloys Compd.* **2018**, *735*, 938−944.
(18) Chava, R. K.; Cho, H. Y.; Yoon, J. M.; Yu, Y. T. Fabrication of aggregated In_2O_3 nanospheres for highly sensitive acetaldehyde gas sensors. *J. Alloys Compd.* **2019**, *772*, 834−842.
(19) Yang, W.; Feng, L.; He, S. H.; Liu, L. Y.; Liu, S. T. Density Gradient Strategy for Preparation of Broken In_2O_3 Microtubes with Remarkably Selective Detection of Triethylamine Vapor. *ACS Appl. Mater. Interfaces* **2018**, *10* (32), 27131−27140.
(20) Nagata, T. Indium oxide In_2O_3. In *Single Crystals of Electronic Materials*; Elsevier: 2019.
(21) Zhang, Z. G.; Wang, X. X.; Zhang, J.; Yu, M.; Zhang, J. C.; Zhang, H. D.; Long, Y. Z. Recent advances in 1D micro- and nanoscale indium oxide structures. *J. Alloys Compd.* **2018**, *752*, 359−375.
(22) de Boer, T.; Bekheet, M. F.; Gurlo, A.; Riedel, R.; Moewes, A. Band gap and electronic structure of cubic, rhombohedral, and orthorhombic In_2O_3 polymorphs: Experiment and theory. *Phys. Rev. B: Condens. Matter Mater. Phys.* **2016**, *93* (15), 155205.
(23) Wang, C. Y.; Cimalla, V.; Romanus, H.; Kups, T.; Ecke, G.; Stauden, T.; Ali, M.; Lebedev, V.; Pezoldt, J.; Ambacher, O. Phase selective growth and properties of rhombohedral and cubic indium oxide. *Appl. Phys. Lett.* **2006**, *89* (1), 011904.
(24) Farvid, S. S.; Dave, N.; Radovanovic, P. V. Phase-Controlled Synthesis of Colloidal In_2O_3 Nanocrystals via Size-Structure Correlation. *Chem. Mater.* **2010**, *22* (1), 9−11.
(25) Yin, J. F.; Cao, H. Q. Synthesis and Photocatalytic Activity of Single-Crystalline Hollow rh-In_2O_3 Nanocrystals. *Inorg. Chem.* **2012**, *51* (12), 6529−6536.
(26) Kock, E. M.; Kogler, M.; Zhuo, C.; Schlicker, L.; Bekheet, M. F.; Doran, A.; Gurlo, A.; Penner, S. Surface chemistry and stability of metastable corundum- type In_2O_3. *Phys. Chem. Chem. Phys.* **2017**, *19* (29), 19407−19419.
(27) Wu, M. M.; Wang, C.; Zhao, Y.; Xiao, L. S.; Zhang, C.; Yu, X. Q.; Luo, B. F.; Hu, B.; Fan, W. Q.; Shi, W. D. Hydrothermal synthesis of porous rh-In_2O_3 nanostructures with visible-light-driven photocatalytic degradation of tetracycline. *CrystEngComm* **2015**, *17* (11), 2336−2345.
(28) Li, P.; Fan, H. Q.; Cai, Y.; Xu, M. M.; Long, C. B.; Li, M. M.; Lei, S. H.; Zou, X. W. Phase transformation (cubic to rhombohedral): the effect on the NO_2 sensing performance of Zn-doped flower-like In_2O_3 structures. *RSC Adv.* **2014**, *4* (29), 15161−15170.
(29) Okte, A. N. Characterization and photocatalytic activity of Ln (La, Eu, Gd, Dy and Ho) loaded ZnO nanocatalysts. *Appl. Catal., A* **2014**, *475*, 27−39.
(30) Xu, J.; Liu, J. B.; Liu, B. X.; Li, S. N.; Wei, S. H.; Huang, B. Design of n-Type Transparent Conducting Oxides: The Case of Transition Metal Doping in In_2O_3. *Adv. Electron. Mater.* **2018**, *4* (3), 1700553.
(31) Apostolov, A. T.; Apostolova, I. N.; Wesselinowa, J. M. Theoretical study of room temperature ferromagnetism and band gap energy of pure and ion doped In_2O_3 nanoparticles. *J. Magn. Magn. Mater.* **2018**, *456*, 263−268.
(32) Ouacha, H.; Kleineberg, U.; Albrithen, H. Morphology control, electronic properties and evolution of light emission in faceted indium oxide structures. *J. Phys. D: Appl. Phys.* **2017**, *50* (45), 455102.
(33) Farvid, S. S.; Hegde, M.; Radovanovic, P. V. Influence of the Host Lattice Electronic Structure on Dilute Magnetic Interactions in Polymorphic Cr(III)-Doped In_2O_3 Nanocrystals. *Chem. Mater.* **2013**, *25* (2), 233−244.
(34) Marinho, J. Z.; Montes, R. H. O.; de Moura, A. P.; Longo, E.; Varela, J. A.; Munoz, R. A. A.; Lima, R. C. Rapid preparation of alpha-FeOOH and alpha-Fe_2O_3 nanostructures by microwave heating and their application in electrochemical sensors. *Mater. Res. Bull.* **2014**, *49*, 572−576.
(35) Simoes, A. Z.; Ramirez, M. A.; Riccardi, C. S.; Longo, E.; Varela, J. A. Effect of the microwave oven on structural, morphological and electrical properties of $SrBi_4Ti_4O_{15}$ thin films grown on Pt/Ti/SiO_2/Si substrates by a soft chemical method. *Mater. Charact.* **2008**, *59* (6), 675−680.
(36) Lemos, S. C. S.; Romeiro, F. C.; de Paula, L. F.; Goncalves, R. F.; de Moura, A. P.; Ferrer, M. M.; Longo, E.; Patrocinio, A. O. T.; Lima, R. C. Effect of Er^{3+} ions on the phase formation and properties of In_2O_3 nanostructures crystallized upon microwave heating. *J. Solid State Chem.* **2017**, *249*, 58−63.
(37) Priyanka, K. P.; Revathy, V. R.; Rosmin, P.; Thrivedu, B.; Elsa, K. M.; Nimmymol, J.; Balakrishna, K. M.; Varghese, T. Influence of La doping on structural and optical properties of TiO_2 nanocrystals. *Mater. Charact.* **2016**, *113*, 144−151.
(38) Zhang, T.; Gu, F. B.; Han, D. M.; Wang, Z. H.; Guo, G. S. Synthesis, characterization and alcohol-sensing properties of rare earth doped In_2O_3 hollow spheres. *Sens. Actuators, B* **2013**, *177*, 1180−1188.
(39) Zhang, W. H.; Wang, F.; Zhang, W. D. Phase transformation of ultrathin nanowires through lanthanide doping: from InOOH to rh-In_2O_3. *Dalton Trans.* **2013**, *42* (13), 4361−4364.
(40) Keriti, Y.; Keffous, A.; Dib, K.; Djellab, S.; Trari, M. Photoluminescence and photocatalytic properties of Er^{3+}-doped In_2O_3 thin films prepared by sol-gel: application to Rhodamine B degradation under solar light. *Res. Chem. Intermed.* **2018**, *44* (3), 1537−1550.
(41) Keriti, Y.; Keffous, A.; Gabouze, N.; Trari, M. Concentration-dependent visible photoluminescence of In_2O_3:Er^{3+} under 532 nm excitation. *Optik* **2019**, *176*, 419−424.
(42) Oppong, S. O. B.; Anku, W. W.; Opoku, F.; Shukla, S. K.; Govender, P. P. Photodegradation of Eosin Yellow Dye in Water under Simulated Solar Light Irradiation Using La-Doped ZnO Nanostructure Decorated on Graphene Oxide as an Advanced Photocatalyst. *ChemistrySelect* **2018**, *3* (4), 1180−1188.
(43) Wei, D. D.; Jiang, W. H.; Gao, H. Y.; Chuai, X. H.; Liu, F. M.; Liu, F. M.; Sun, P.; Liang, X. S.; Gao, Y.; Yan, X.; Lu, G. Y. Facile synthesis of La-doped In_2O_3 hollow microspheres and enhanced hydrogen sulfide sensing characteristics. *Sens. Actuators, B* **2018**, *276*, 413−420.
(44) Romeiro, F. C.; Marinho, J. Z.; Lemos, S. C. S.; de Moura, A. P.; Freire, P. G.; da Silva, L. E.; Longo, E.; Munoz, R. A. A.; Lima, R. C. Rapid synthesis of Co, Ni co-doped ZnO nanoparticles: Optical and electrochemical properties. *J. Solid State Chem.* **2015**, *230*, 343−349.
(45) Marinho, J. Z.; Santos, L. M.; Macario, L. R.; Longo, E.; Machado, A. E. H.; Patrocinio, A. O. T.; Lima, R. C. Rapid Preparation of $(BiO)_2CO_3$ Nanosheets by Microwave-Assisted Hydrothermal Method with Promising Photocatalytic Activity Under UV-Vis Light. *J. Braz. Chem. Soc.* **2015**, *26* (3), 498−505.
(46) Kharisov, B. I. K., O, V.; Ortiz Méndez, U. Microwave hydrothermal and solvothermal processing of materials and compounds. In *The Development and Application of Microwave Heating*; Wenbin Cao, IntechOpen, 2012.

DOI: 10.1021/acs.inorgchem.9b01728
Inorg. Chem. 2019, 58, 11738−11750

(47) Kitchen, H. J.; Vallance, S. K.; Kennedy, J. L.; Tapia-Ruiz, N.; Carassiti, L.; Harrison, A.; Whittaker, A. G.; Drysdale, T. D.; Kingman, S. W.; Gregory, D. H. Modern Microwave Methods in Solid-State Inorganic Materials Chemistry: From Fundamentals to Manufacturing. *Chem. Rev.* **2014**, *114* (2), 1170−1206.
(48) Pereira, P. F. S.; Gouveia, A. F.; Assis, M.; de Oliveira, R. C.; Pinatti, I. M.; Penha, M.; Goncalves, R. F.; Gracia, L.; Andres, J.; Longo, E. $ZnWO_4$ nanocrystals: synthesis, morphology, photoluminescence and photocatalytic properties. *Phys. Chem. Chem. Phys.* **2018**, *20* (3), 1923−1937.
(49) Larson, A. C.; Von Dreele, R. B. *General Structure Analysis System (GSAS)*; Report LAUR 86−748; Los Alamos National Laboratory, 2000.
(50) Salvatierra, R. V.; Oliveira, M. M.; Zarbin, A. J. G. One-Pot Synthesis and Processing of Transparent, Conducting, and Free-standing Carbon Nanotubes/Polyaniline Composite Films. *Chem. Mater.* **2010**, *22* (18), 5222−5234.
(51) Neiva, E. G. C.; Oliveira, M. M.; Bergamini, M. F.; Marcolino, L. H.; Zarbin, A. J. G. One material, multiple functions: graphene/$Ni(OH)_2$ thin films applied in batteries, electrochromism and sensors. *Sci. Rep.* **2016**, *6*, 33806.
(52) Dovesi, R.; Saunders, V. R.; Roetti, C.; Orlando, C. M.; Zicovich-Wilson, C. M.; Pascale, F.; Civalleri, B.; Doll, K.; Harrison, N. M.; Bush, I. J.; D'Arco, P.; Llunell, M.; Causà, M., Noël, Y.; Maschio, L.; Erba, A.; Rerat, M.; Casassa, S. *CRYSTAL17*; University of Torino, 2017.
(53) Bredow, T.; Jug, K.; Evarestov, R. A. Electronic and magnetic structure of $ScMnO_3$. *Phys. Status Solidi B* **2006**, *243* (2), R10−R12.
(54) Causa, M.; Dovesi, R.; Roetti, C. Pseudopotential hartree-fock study of 17 iii-v-semiconductors and iv-iv-semiconductors. *Phys. Rev. B: Condens. Matter Mater. Phys.* **1991**, *43* (14), 11937−11943.
(55) Wulff, G. XXV. Zur Frage der Geschwindigkeit des Wachstums und der Auflſosung der Krystallflſachen. *Z. Kristallogr. - Cryst. Mater.* **1901**, *34*, 449−530.
(56) Andres, J.; Gracia, L.; Gouveia, A. F.; Ferrer, M. M.; Longo, E. Effects of surface stability on the morphological transformation of metals and metal oxides as investigated by first-principles calculations. *Nanotechnology* **2015**, *26* (40), 405703.
(57) Gouveia, A. F.; Ferrer, M. M.; Sambrano, J. R.; Andres, J.; Longo, E. Modeling the atomic-scale structure, stability, and morphological transformations in the tetragonal phase of $LaVO_4$. *Chem. Phys. Lett.* **2016**, *660*, 87−92.
(58) Oliveira, M. C.; Gracia, L.; Nogueira, I. C.; Gurgel, M. F. C.; Mercury, J. M. R.; Longo, E.; Andres, J. On the morphology of $BaMoO_4$ crystals: A theoretical and experimental approach. *Cryst. Res. Technol.* **2016**, *51* (10), 634−644.
(59) Bomio, M. R. D.; Tranquilin, R. L.; Motta, F. V.; Paskocimas, C. A.; Nascimento, R. M.; Gracia, L.; Andres, J.; Longo, E. Toward Understanding the Photocatalytic Activity of $PbMoO_4$ Powders with Predominant (111), (100), (011), and (110) Facets. A Combined Experimental and Theoretical Study. *J. Phys. Chem. C* **2013**, *117* (41), 21382−21395.
(60) Longo, V. M.; Gracia, L.; Stroppa, D. G.; Cavalcante, L. S.; Orlandi, M.; Ramirez, A. J.; Leite, E. R.; Andres, J.; Beltran, A.; Varela, J. A.; Longo, E. A Joint Experimental and Theoretical Study on the Nanomorphology of $CaWO_4$ Crystals. *J. Phys. Chem. C* **2011**, *115* (41), 20113−20119.
(61) Botelho, G.; Andres, J.; Gracia, L.; Matos, L. S.; Longo, E. Photoluminescence and Photocatalytic Properties of Ag_3PO_4 Microcrystals: An Experimental and Theoretical Investigation. *ChemPlusChem* **2016**, *81* (2), 202−212.
(62) Fabbro, M. T.; Saliby, C.; Rios, L. R.; La Porta, F. A.; Gracia, L.; Li, M. S.; Andres, J.; Santos, L. P. S.; Longo, E. Identifying and rationalizing the morphological, structural, and optical properties of beta-Ag_2MoO_4 microcrystals, and the formation process of Ag nanoparticles on their surfaces: combining experimental data and first-principles calculations. *Sci. Technol. Adv. Mater.* **2015**, *16* (6), 065002.
(63) Silva, G. S.; Gracia, L.; Fabbro, M. T.; Serejo dos Santos, L. P.; Beltran-Mir, H.; Cordoncillo, E.; Longo, E.; Andres, J. Theoretical and Experimental Insight on Ag_2CrO_4 Microcrystals: Synthesis, Characterization, and Photoluminescence Properties. *Inorg. Chem.* **2016**, *55* (17), 8961−8970.
(64) Oliveira, M. C.; Gracia, L.; Nogueira, I. C.; Carmo Gurgel, M. F. d.; Mercury, J. M. R.; Longo, E.; Andres, J. Synthesis and morphological transformation of BaWO4 crystals: Experimental and theoretical insights. *Ceram. Int.* **2016**, *42* (9), 10913−10921.
(65) Wang, F.; Han, Y.; Lim, C. S.; Lu, Y. H.; Wang, J.; Xu, J.; Chen, H. Y.; Zhang, C.; Hong, M. H.; Liu, X. G. Simultaneous phase and size control of upconversion nanocrystals through lanthanide doping. *Nature* **2010**, *463* (7284), 1061−1065.
(66) Tang, Q.; Zhou, W. J.; Zhang, W.; Ou, S. M.; Jiang, K.; Yu, W. C.; Qian, Y. T. Size-controllable growth of single crystal $In(OH)_3$ and In_2O_3 nanocubes. *Cryst. Growth Des.* **2005**, *5* (1), 147−150.
(67) Cho, S. H.; Ghosh, S.; Berkson, Z. J.; Hachtel, J. A.; Shi, J.; Zhao, X.; Reimnitz, L. C.; Dahlman, C. J.; Ho, Y.; Yang, A.; Liu, Y.; Idrobo, J. C.; Chmelka, B. F.; Milliron, D. J. Syntheses of Colloidal F:In_2O_3 Cubes: Fluorine-Induced Faceting and Infrared Plasmonic Response. *Chem. Mater.* **2019**, *31* (7), 2661−2676.
(68) White, W. B.; Keramidas, V. G. VIBRATIONAL-SPECTRA OF OXIDES WITH C-TYPE RARE-EARTH OXIDE STRUCTURE. *Spectrochim. Acta A Mol. Spectrosc.* **1972**, *28* (3), 501−509.
(69) Kranert, C.; Schmidt-Grund, R.; Grundmann, M. Raman active phonon modes of cubic In_2O_3. *Phys. Status Solidi RRL* **2014**, *8* (6), 554−559.
(70) Wang, C. Y.; Dai, Y.; Pezoldt, J.; Lu, B.; Kups, T.; Cimalla, V.; Ambacher, O. Phase stabilization and phonon properties of single crystalline rhombohedral indium oxide. *Cryst. Growth Des.* **2008**, *8* (4), 1257−1260.
(71) Cao, H. M.; Xing, P. F.; Yao, D. S.; Wu, P. Annealing temperature dependent non-monotonic d(0) ferromagnetism in pristine In_2O_3 nanoparticles. *J. Magn. Magn. Mater.* **2017**, *429*, 69−73.
(72) Khan, G. G.; Ghosh, S.; Sarkar, A.; Mandal, G.; Mukherjee, G. D.; Manju, U.; Banu, N.; Dev, B. N. Defect engineered d(0) ferromagnetism in tin-doped indium oxide nanostructures and nanocrystalline thin-films. *J. Appl. Phys.* **2015**, *118* (7), 074303.
(73) Anand, K.; Kaur, J.; Singh, R. C.; Thangaraj, R. Structural, optical and gas sensing properties of pure and Mn-doped In_2O_3 nanoparticles. *Ceram. Int.* **2016**, *42* (9), 10957−10966.
(74) Kubelka, P.; Munk, F. Ein Beitrag Zur Optik Der Farbanstriche. *Z. Technol. Phys.* **1931**, *12*, 593−601.
(75) Feneberg, M.; Nixdorf, J.; Lidig, C.; Goldhahn, R.; Galazka, Z.; Bierwagen, O.; Speck, J. S. Many-electron effects on the dielectric function of cubic In_2O_3: Effective electron mass, band nonparabolicity, band gap renormalization, and Burstein-Moss shift. *Phys. Rev. B: Condens. Matter Mater. Phys.* **2016**, *93* (4), 045203.
(76) Moss, T. S. The interpretation of the properties of indium antimonide. *Proc. Phys. Soc., London, Sect. B* **1954**, *67* (418), 775−782.
(77) Jiang, F. X.; Chen, D.; Zhou, G. W.; Wang, Y. N.; Xu, X. H. The dramatic enhancement of ferromagnetism and band gap in Fe-doped In_2O_3 nanodot arrays. *Sci. Rep.* **2018**, *8*, 2417.
(78) He, H. Y.; Huang, J. F.; Fei, J.; Lu, J. La-doping content effect on the optical and electrical properties of La-doped ZnO thin films. *J. Mater. Sci.: Mater. Electron.* **2015**, *26* (2), 1205−1211.
(79) Patel, S. K. S.; Dewangan, K.; Srivastav, S. K.; Gajbhiye, N. S. Synthesis of monodisperse In_2O_3 nanoparticles and their d(0) ferromagnetism. *Curr. Appl. Phys.* **2014**, *14* (6), 905−908.
(80) Perez-Sanchez, G. F.; Chavez, E.; Cortes-Salinas, D.; Zaca-Moran, P.; Morales-Acevedo, A.; Pena-Sierra, R.; Goiz, O.; Huerta, A. T. Synthesis of In-In_2O_3 microstructures by close-spaced vapor transport (CSVT) and their transformation to In_2O_3 nanobelts at low temperature. *Vacuum* **2014**, *107*, 236−241.
(81) Yang, J.; Lin, C. K.; Wang, Z. L.; Lin, J. $In(OH)_3$ and In_2O_3 nanorod bundles and spheres: Microemulsion-mediated hydrothermal synthesis and luminescence properties. *Inorg. Chem.* **2006**, *45* (22), 8973−8979.
(82) Tahir, M. La-modified TiO_2/carbon nanotubes assembly nanocomposite for efficient photocatalytic hydrogen evolution from

DOI: 10.1021/acs.inorgchem.9b01728
Inorg. Chem. 2019, 58, 11738−11750

glycerol-water mixture. *Int. J. Hydrogen Energy* **2019**, *44* (7), 3711−3725.
(83) Bertoluzzi, L.; Lopez-Varo, P.; Jimenez Tejada, J. A.; Bisquert, J. Charge transfer processes at the semiconductor/electrolyte interface for solar fuel production: insight from impedance spectroscopy. *J. Mater. Chem. A* **2016**, *4* (8), 2873−2879.
(84) Lima, R. C.; Macario, L. R.; Espinosa, J. W. M.; Longo, V. M.; Erlo, R.; Marana, N. L.; Sambrano, J. R.; dos Santos, M. L.; Moura, A. P.; Pizani, P. S.; Andres, J.; Longo, E.; Varela, J. A. Toward an understanding of intermediate- and short-range defects in ZnO single crystals. A combined experimental and theoretical study. *J. Phys. Chem. A* **2008**, *112* (38), 8970−8978.
(85) Liu, R. D.; Li, H.; Duan, L. B.; Shen, H.; Zhang, Q.; Zhao, X. R. Influences of annealing atmosphere on phase transition temperature, optical properties and photocatalytic activities of TiO_2 phase-junction microspheres. *J. Alloys Compd.* **2019**, *789*, 1015−1021.
(86) Zhou, Y. D.; Zhao, Z. Y. Interfacial structure and properties of TiO_2 phase junction studied by DFT calculations. *Appl. Surf. Sci.* **2019**, *485*, 8−21.
(87) Yalavarthi, R.; Naldoni, A.; Kment, S.; Mascaretti, L.; Kmentova, H.; Tomanec, O.; Schmuki, P.; Zboril, R. Radiative and Non-Radiative Recombination Pathways in Mixed-Phase TiO_2 Nanotubes for PEC Water-Splitting. *Catalysts* **2019**, *9*, 204.
(88) Ako, R. T.; Ekanayake, P.; Tan, A. L.; Young, D. J. La modified TiO_2 photoanode and its effect on DSSC performance: A comparative study of doping and surface treatment on deep and surface charge trapping. *Mater. Chem. Phys.* **2016**, *172*, 105−112.
(89) Lv, X. W.; Tao, L. M.; Cao, M. L.; Xiao, X.; Wang, M. K.; Shen, Y. Enhancing photoelectrochemical water oxidation efficiency via self-catalyzed oxygen evolution: A case study on TiO_2. *Nano Energy* **2018**, *44*, 411−418.
(90) Zhang, Y.-C.; Liu, Y.-K.; Zhang, L.; E, X.-t.-f.; Pan, L.; Zhang, X.; Fazal-e-Aleem; Zou, D.-R.; Liu, S.-H.; Zou, J.-J. DFT study on water oxidation on nitrogen-doped ceria oxide. *Appl. Surf. Sci.* **2018**, *452*, 423−428.
(91) Lei, H. T.; Han, A.; Li, F. W.; Zhang, M. N.; Han, Y. Z.; Du, P. W.; Lai, W. Z.; Cao, R. Electrochemical, spectroscopic and theoretical studies of a simple bifunctional cobalt corrole catalyst for oxygen evolution and hydrogen production. *Phys. Chem. Chem. Phys.* **2014**, *16* (5), 1883−1893.
(92) Giordano, L.; Han, B. H.; Risch, M.; Hong, W. T.; Rao, R. R.; Stoerzinger, K. A.; Shao-Horn, Y. pH dependence of OER activity of oxides: Current and future perspectives. *Catal. Today* **2016**, *262*, 2−10.

DOI: 10.1021/acs.inorgchem.9b01728
Inorg. Chem. 2019, 58, 11738−11750

PCCP

PAPER

View Article Online
View Journal | View Issue

Cite this: *Phys. Chem. Chem. Phys.*, 2020, **22**, 25876

Structure, electronic properties, morphology evolution, and photocatalytic activity in $PbMoO_4$ and $Pb_{1-2x}Ca_xSr_xMoO_4$ (x = 0.1, 0.2, 0.3, 0.4 and 0.5) solid solutions†

E. O. Gomes,[a] L. Gracia, ‡[a] A. A. G. Santiago,[b] R. L. Tranquilin,[c] F. V. Motta,[b] R. A. C. Amoresi,[ad] E. Longo,[c] M. R. D. Bomio[b] and J. Andres *[a]

Received 31st August 2020,
Accepted 19th October 2020

DOI: 10.1039/d0cp04596a

rsc.li/pccp

In this work $PbMoO_4$ and $Pb_{1-2x}Ca_xSr_xMoO_4$ (x = 0.1, 0.2, 0.3, 0.4 and 0.5) solid solutions have been successfully prepared, for the first time, by a simple co-precipitation method and the as-synthesized samples were subjected to a water-based reflux treatment. Structural characterization of these samples was performed using X-ray diffraction with Rietveld refinement analysis and Raman spectroscopy. Their optical properties were investigated by UV-Vis absorption spectroscopy and PL emissions, and the photocatalytic activity of the as-synthesized samples for the degradation process of Rhodamine B has been demonstrated. The surface structure and morphologies were characterized by field emission scanning electron microscopy. To complement and rationalize the experimental results, the geometry, electronic structures, and morphologies of as-synthesized samples were characterized by first-principles quantum-mechanical calculations at the density functional theory level. By using Wulff construction, based on the values of the surface energies for the (001), (100), (110), (111), (011) and (112) surfaces, a complete map of the available morphologies for $PbMoO_4$ was obtained and a good agreement between the experimental and theoretical predicted morphologies was found. The structural and electronic changes induced by the substitution of Pb by Ca and Sr allow us to find a relationship among morphology, the electron-transfer process at the exposed surfaces, optical properties, and photocatalytic activity. We believe that our results offer new insights regarding the local coordination of superficial Pb/Ca/Sr and Mo cations (*i.e.*, clusters) on each exposed surface of the corresponding morphology, which dictate the photocatalytic activities of the as-synthesized samples, a field that has so far remained unexplored. The present study, which combines multiple experimental methods and first-principles calculations, provides a deep understanding of the local structures, bonding, morphologies, band gaps, and electronic and optical properties, and opens the door to exploit the electrical, optical and photocatalytic activity of this very promising family of materials.

1. Introduction

Metal molybdates have aroused great interest due to their broad applications in a wide range of technological fields such as catalysis and photocatalysis, optics, magnetism, gas sensors and electrochemistry.[1–12] Among the metal molybdates, the $AMoO_4$ (A = Ca, Sr, Ba and Pb) family with a scheelite structure and spatial group $I4_1$ presents excellent photoluminescence and photocatalytic properties,[13–16] lead molybdate, $PbMoO_4$ (PMO), being one of the most promising compounds in this family.[5] It is organized structurally by two fundamental units with point of symmetry S4.[6] The larger, Pb^{2+}, and smaller, Mo^{6+}, cations are coordinated by eight and four oxygen atoms, forming a cluster with a dodecahedral arrangement, $[PbO_8]$, and a cluster of tetrahedral arrays $[MoO_4]$, respectively.[7] The valence

[a] *Department of Analytical and Physical Chemistry, Universitat Jaume I, 12071 Castelló, Spain. E-mail: andres@qfa.uji.es*
[b] *LSQM – Laboratory of Chemical Synthesis of Materials – Department of Materials Engineering, Federal University of Rio Grande do Norte – UFRN, P.O. Box 1524, Natal, RN, Brazil*
[c] *CDMF-LIEC, UFSCar, P.O. Box 676, 13565-905 São Carlos, SP, Brazil*
[d] *School of Engineering, Sao Paulo State University (UNESP), Guaratinguetá, São Paulo 12516-410, Brazil*

† Electronic supplementary information (ESI) available. See DOI: 10.1039/d0cp04596a

‡ Permanent address: Department of Physical Chemistry, University of Valencia (UV), 46100 Burjassot, Spain.

band (VB) consists of the hybridization of O 2p and Pb 6s orbitals, while the conduction band (CB) is composed mainly of Mo 4d orbitals, the band gap between CB and VB being approximately 3.2 eV.[8] PMO is employed as photocatalysts,[9] semiconductor material[10] and an antibacterial agent.[11]

Different synthetic procedures have been employed to obtain PMO, such as the solid state reaction;[12] the electrochemical method;[13] combustion synthesis;[14] polymerization of complexes;[15] reverse micro emulsion;[16] citrate complex method,[17] solvothermic synthesis,[18] conventional hydrothermal[11] and the hydrothermal microwave assisted methods.[19] Some of these methods, however, offer disadvantages, such as the generation and formation of organic residues, prolonged synthesis times, and high energy release. Other synthesis methods are therefore needed to overcome these drawbacks. The water-based reflux method is a simple, inexpensive, and easily applicable process.[20] It has already been used for the synthesis of nanoparticles,[21] nanotubes,[22] nano-shell structures and nanowires.[23] It is well known that the properties of the as-synthesized samples are highly dependent on the synthesis method and thermal treatments. The size, morphology and crystallinity of the desired nanostructures can be controlled by varying the reaction time, concentration of the precursors, and the type of solvent used.

The synthesis of solid solutions offers the advantage of the continuous change of properties with components, which is a very effective strategy to tune the properties of advanced materials with extended functionalities. Continuous series of substitutional solid solutions can provide a variation in crystal structure and changes in the band gap values and optical properties, and an opportunity to understand the structure property relationship can thus be achieved.[24,25] The design of a solid solution based on molybdate compounds is a promising strategy for developing novel materials,[26] with the aim of improving their properties, and consequently expansion wider range of applications.[27–29] In particular, Hallaoui *et al.*[30] have studied the structural and optical properties as a function of composition x for $Sr_{(1-x)}Pb_xMoO_4$ solid solutions, showing that the photocatalytic activity of PMO and $SrMoO_4$ is different despite the similarity of the structures. In this context, our research group has been engaged in a research project devoted to the study of the structural, morphological, and optical properties of different solid solutions of wolframite- and tungstate-based materials by using a combination of first principles calculations and experimental techniques.[24,31,32]

This work reports a series of new solid solutions with improved stability, which are appealing materials for several applications. Inspired by the above considerations, in this study, we seek to fulfill a four-fold objective. The first is to report, for the first time, on the synthesis of PMO and $Pb_{1-2x}Ca_xSr_xMoO_4$ (x = 0.1, 0.2, 0.3, 0.4 and 0.5 (CSMO)) solid solutions by employing the co-precipitation method, followed by a water-based reflux treatment. This synthesis method is a simple, low-cost, and easy synthesis procedure that has received special attention due to the fact that it allows the formation of oxides with a high degree of crystallinity and easy dispersion in aqueous medium, reduced reaction times, low synthesis temperatures, excellent control of reaction parameters, control of product size and morphology, and enhanced product purity or material properties. Secondly, X-ray diffraction (XRD), field emission electron microscopy (FE-SEM), Micro Raman (MR) and ultraviolet-visible (UV-Vis) spectroscopies were employed to characterize the samples and determine the effect of their chemical composition on the morphology and photoluminescence (PL) emissions. The third aim is to complement and rationalize experimental results by means of first principles calculation, at the density functional theory (DFT) level, to obtain the geometry, electronic structure, and properties of PMO and the solid solutions. The fourth aim is to apply a joint experimental and theoretical strategy that we developed in order to obtain a complete map of the morphologies. From these results, we hope to understand how the different surfaces change their energies throughout the synthesis process and propose a mechanism by which the experimental and theoretical morphologies of the solid solutions match. Finally, the insights gained through these calculations help to rationalize the mechanism and origin of the photocatalytic activity on the degradation process of Rhodamine B (RhB) dye. We discuss how knowledge of surface-specific properties can be utilized to design a number of crystal morphologies that may offer improved performance in various applications. The different activities can be associated to the presence of the number of unsaturated superficial Pb/Sr/Ca and Mo cations capable of forming the main active adsorption sites. We believe that these novel results are of significant relevance, since they may inspire the efficient synthesis of these and related molybdate solid solutions and provide critical information to expand our fundamental understanding, while also perhaps contributing to the rational design of new materials for multifunctional applications.

This paper contains three more sections. The next section describes the experimental and theoretical procedures, with the synthesis and characterization, as well as the computational methods and model systems. In section three, the results are presented and discussed. The main conclusions are summarized in the fourth and final section.

2. Experimental and theoretical procedures

2.1. Materials

Calcium nitrate hexahydrate [$Ca(NO_3)_2{\cdot}4H_2O$] (98.0% purity; Vetec), strontium nitrate [$Sr(NO_3)_2$] (99.0% purity, Vetec), molybdic acid [H_2MoO_4] (85% purity; Alfa Aesar), ammonium hydroxide (NH_4OH), and distilled water were used as reagents to prepare the Pb_{1-2x} $Ca_xSr_xMoO_4$.

2.2. Synthesis of PMO and Pb_{1-2x} $Ca_xSr_xMoO_4$ powders

Powder samples of PMO and Pb_{1-2x} $Ca_xSr_xMoO_4$. (x = 0.1, 0.2, 0.3, 0.4 and 0.5) were prepared by using the reflux method. The synthesis procedure is described as follows: molybdic acid (5.0×10^{-3} mol) was dissolved in 50 ml deionized water

(solution 1). At the same time, the respective concentrations (% mol) of lead, calcium, and strontium nitrates were dissolved in 50 ml deionized water (solution 2). Solution 2 was added dropwise to solution 1 and the pH of the solution was adjusted to 11 by adding ammonium hydroxide to it, and the formation of a white precipitate was observed. Afterward, this solution was stirred for 30 min in an ultrasound bath to accelerate the co-precipitation rate. Subsequently, this preformed mixture was transferred to a 150 ml round-bottomed flask and refluxed at 100 °C/1 h.

The resulting precipitate was washed several times with deionized water to neutralize the suspension (pH ≈ 7). Finally, the white precipitates were collected and dried at 80 °C/24 hours. The samples were named according to the concentration of Pb^{2+} cations, *i.e.*, the names of the samples are defined for each value x of the substituents (Ca^{2+}/Sr^{2+}) and the corresponding amount of Pb^{2+}: x = 0, 0.1, 0.2, 0.3, 0.4 and 0.5. Hence, they were given the denominations PMO, Pb0.8, Pb0.6, Pb0.4, Pb0.2 and CSMO, respectively.

2.3. Characterization of $Pb_{1-2x}Ca_xSr_xMoO_4$ samples

XRD patterns of the PMO and $Pb_{1-2x}Ca_xSr_xMoO_4$ samples were collected within the 10° to 120° angular range with a step speed of 0.02° min^{-1} using an XRD 7000 Shimadzu diffractometer and monochromatic Cu K_α (λ = 1.5406 Å) radiation. The powder morphology was examined using an FE-SEM (Carl Zeiss, model Supra 35-VP) operating at 6 kV. Micro Raman (MR) spectroscopy was conducted on a Horiba Jobin-Yvon (Japan) spectrometer coupled to a charge-coupled device detector and Ar-ion laser (MellesGriot, United States) operating at 514.5 nm with a maximum power of 200 mWMR, and measurements were recorded using a T-64000 spectrometer (Jobin-Yvon, France) triple monochromator coupled to a CCD detector. The UV-Vis reflectance spectrum was obtained using a UV-Vis spectrometer (Shimadzu, model UV-2600). PL spectra were measured using a Thermal Jarrell-Ash Monospec 27 monochromator and a Hamamatsu R446 photomultiplier. The excitation source used was a krypton laser with a wavelength of 325 nm (Coherent Innova) and an output of approximately 13.3 mW. The photon energies with the emitted wavelengths were calculated based on Planck-Einstein eqn (1), where E is the photon energy, in eV, and λ the photon wavelength, in nm.

$$E = \frac{1240}{\lambda} \quad (1)$$

The photocatalytic properties for the degradation of Rhodamine B (RhB) dye in an aqueous solution were tested under UV-light illumination (six UVC lamps, 15 W TUV Philips, with maximum intensity of 254 nm). About 50 mg of catalyst crystals were placed in a 150 ml beaker, and 50 ml of RhB solution (1×10^{-5} mol L^{-1}) was added. These suspensions were ultrasonicated for 10 min in an ultrasonic cleaner before illumination. During the catalytic process, one aliquot was removed 10 minutes before turning on the light and the other at zero time. Subsequently, aliquots were removed 10, 20, 30, 40, 50, and 60 min after the beginning of the photocatalysis process. The aliquots were centrifuged and analyzed using a spectrophotometer (Shimadzu, model UV-2600).

2.4. Computational methods and model systems

The structural and electronic properties of the PMO structure and $Pb_{1-2x}Ca_xSr_xMoO_4$ solid solutions were calculated using Becke's three-parameter hybrid non-local exchange functional, combined with a Lee–Yang–Parr gradient-corrected correlation functional (B3LYP), implemented in the CRYSTAL17 package.[33] The atoms were centered and described using pseudopotential databases Ca_pob_TZVP_2012, Sr_ECP28MDF_s411p411d11_Heifets_2013, Pb_ECP60MDF_doll_2011, 976-311 (d631) G and O-6-31G* (all-electron) for Ca, Sr, Pb, Mo and O, respectively. Regarding the diagonalization of the density matrix, the reciprocal space net was described by a shrinking factor of 4, generated according to the Monkhorst–Pack scheme. The accuracy of the evaluation of the Coulomb and exchange series was controlled by five thresholds, whose adopted values were 10^{-8}, 10^{-8}, 10^{-8}, 10^{-8}, and 10^{-16}.

The representation of the PMO and CSMO bulk structure is shown in Fig. 1. Mo atoms are coordinated to four O atoms, and the local coordination can be described by a tetrahedral [MoO_4] cluster. Correspondingly, the Pb, Ca and Sr are coordinated to eight O atoms, resulting in a formation of [PbO_8], [CaO_8] and [SrO_8] clusters, respectively. To simulate the substitution process and to obtain the ideal percentages presented in the experimental data, a 5 × 1 × 1 supercell, with a volume 5 times larger than the primitive cell and 60 atoms was used. The most stable distribution of Pb, Ca, and Sr atoms in the $Pb_{1-2x}Ca_xSr_xMoO_4$ solid solutions Pb0.8 (x = 0.1), Pb0.6 (x = 0.2), Pb0.4 (x = 0.3) and Pb0.2 (x = 0.4) can be seen in Fig. S1 (ESI†). We have computed the formation energy (E_f) of each system, PMO and $Pb_{1-2x}Ca_xSr_xMoO_4$ solid solutions, using the following formula:

$$\Delta E_f = \frac{E_f - (vE_{Pb} + wE_{Mo} + xE_O + yE_{Ca} + zE_{Sr})}{(v + w + x + y + z)} \quad (2)$$

where E_f is the total energy of a system, E_{Pb}, E_{Mo}, E_O, E_{Ca} and E_{Sr} denote the total energy per atom of pure elements in their

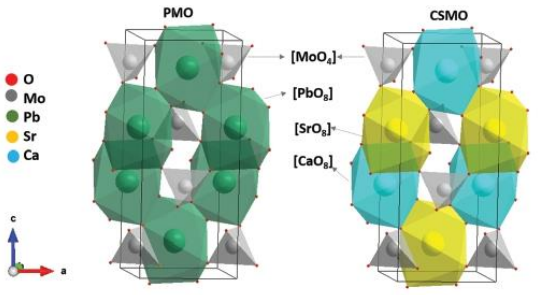

Fig. 1 Unit cell of the $PbMoO_4$ and $CaSrMoO_4$. The [MoO_4], [PbO_8], [SrO_8] and [CaO_8] clusters, *i.e.*, local coordination of Mo, Pb, Sr and Ca cations, respectively, as building blocks of the samples, are depicted for clarity purposes.

stable crystal structures indicated as subscripts, and v, w, x, y, z are the numbers of the corresponding atoms, respectively.

The values of the surface energy, E_{surf}, of the (001), (100), (110), (111) and (112) surfaces were obtained. E_{surf} is defined as the total energy of the repeating slab (E_{slab}) minus the total energy of the perfect crystal per molecular unit (E_{bulk}) multiplied by the number of molecular units of the surface (N) and divided by the surface area per repeating cell of the two sides of the slab:

$$E_{surf} = \frac{1}{2A}(E_{slab} - NE_{bulk}) \quad (3)$$

In this work, after the optimization process and convergence tests on thickness, slab models consisting of 10 molecular units containing 60 atoms were obtained. In addition, the relaxation process was performed, with the relaxed energy (E_{relax}) being calculated as the difference between the total energies for relaxed and unrelaxed slabs, as follows:

$$E_{relax} = \frac{(E_{slab}^{unrlx} - E_{slab}^{relax})}{2A} \quad (4)$$

The E_{slab}^{unrlx} and E_{slab}^{relax} correspond to the total energies for the unrelaxed and relaxed slab models, respectively.

In addition, the broken bonding density (D_b), defined as the number of broken bonds per unit cell area when a surface is created, can be calculated by using eqn (5).[34,35]

$$D_b = \frac{N_b}{A} \quad (5)$$

where N_b is the number of broken bonds per unit cell area on a specific surface and A is the unit of the surface area. From the D_b values that were calculated, it is possible to predict the order of surface stability, since it has been established that higher values are obtained when a larger number of defects are present on the surface.[36]

By using the Wulff construction, the E_{surf} at a fixed volume is minimized, thereby providing a simple correlation between the surface energy of the (hkl) plane and the distance ($rhkl$) in the normal direction from the center of the crystallite.[37] The procedure to obtain the complete set of morphologies has been presented previously by Andrés *et al.*,[38] and it has been successfully used in materials science to obtain the morphology of materials, including PMO,[39] $CaWO_4$,[40] Ag_3PO_4,[41] α-Ag_2MoO_4,[42] $BaMoO_4$,[43] $BaWO_4$,[44] Ag_2CrO_4[45] and $LaVO_4$.[46]

3. Results and discussion

3.1. X-ray diffraction

The XRD patterns of the as-synthesized samples are shown in Fig. 2. Well defined peaks are observed, indicating good crystallinity and long-range structural order without the presence of secondary phases. Being in accordance with the profile and the standards for PMO, indexed to JCPDS 44-1486, the tetragonal structure of the scheelite type and space group $I41/a$ is obtained. However, the Ca^{2+} and Sr^{2+} cation replacement processes in the PMO matrix induce an increase in peaks and

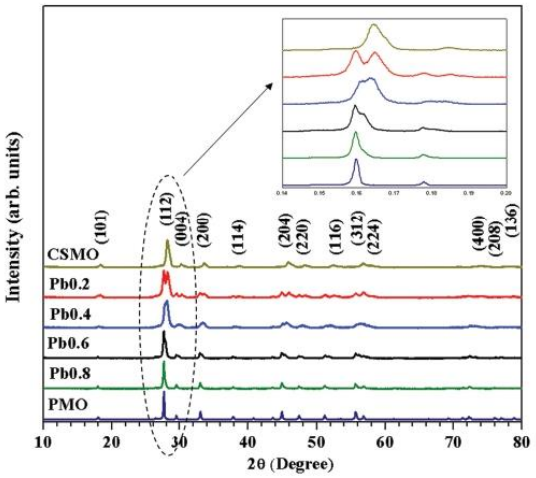

Fig. 2 XRD patterns of solid solutions $Pb_{1-2x}Ca_xSr_xMoO_4$. PMO (x = 0), Pb0.8 (x = 0.1), Pb0.6 (x = 0.2), Pb0.4 (x = 0.3), Pb0.2 (x = 0.4), CSMO (x = 0.5).

a main peak unfolding of the samples, starting with sample Pb0.6 and changing to a larger angle (see Fig. 2), which may be associated with the difference in the size of these cations. A similar result was obtained by Song *et al.* along the Cr^{3+} cation substitutions in the PMO matrix.[8]

For comparison purposes, the values of the bond lengths, the volume, and the cell parameters have been reported in Tables 1 and 2. A good agreement between experimental and theoretical values can be observed for PMO and CSMO sample, revealing a reduction in the cell volume proportional to the

Table 1 Experimental and theoretical values of lattice constants (a, b and c in Å), volume (V in Å^3), bond distances (Pb–O, Mo–O, Sr–O and Ca–O in Å), coordinates of the oxygen atom in Å and Rietveld refinement parameters of PMO and CSMO

	PMO		CSMO	
Samples	Experimental	Theoretical	Experimental	Theoretical
Cell parameters (Å)				
$a = b$	5.432	5.529	5.328	5.390
C	12.117	12.234	11.785	11.882
Volume (Å^3)	357.574	374.061	334.681	345.234
Bond distances (Å)				
Pb–O	2.602 (×4)	2.638 (×4)		
	2.781 (×4)	2.666 (×4)		
Mo–O	1.710 (×4)	1.811 (×4)	1.750 (×4)	1.807 (×4)
Sr–O			2.540 (×4)	2.572 (×4)
			2.570 (×4)	2.597 (×4)
Ca–O			2.540 (×4)	2.508 (×4)
			2.570 (×4)	2.536 (×4)
Coordinates of the oxygen atom (Å)				
X	0.2117	0.2376	0.2367	0.2426
Y	0.1247	0.1127	0.1115	0.1016
Z	0.0370	0.4408	0.0434	0.0444
Rietveld parameters				
X^2	3.365		2.075	
R (%)	20.820		16.520	
R_p (%)	15.720		12.900	

Table 2 Experimental and theoretical values of lattice constants (*a*, *b* and *c* in Å), volume (*V* in Å^3), bond distances (Pb–O, Mo–O, Sr–O and Ca–O, in Å), coordinates of the oxygen atom in Å and Rietveld refinement parameters of $Pb_{1-2x}Ca_xSr_xMoO_4$ solid solutions

PMO and Solid solutions ($Pb_{1-2x}Ca_xSr_xMoO_4$; x = 0.1, 0.2, 0.3, 0.4)									
	PMO (x = 0)	Pb0.8 (x = 0.1)		Pb0.6 (x = 0.2)		Pb0.4 (x = 0.3)		Pb0.2 (x = 0.4)	
Samples	Theoretical	Experimental	Theoretical	Experimental	Theoretical	Experimental	Theoretical	Experimental	Theoretical
$a = b$	5.529	5.425	5.499	5.429	5.467	5.428	5.439	5.429	5.409
c	12.234	12.092	12.173	12.091	12.110	12.085	12.043	12.099	11.970
Volume (Å^3)	374.061	356.001	368.427	356.385	362.740	356.086	357.010	356.720	351.152
Bond distances (Å)									
Pb–O	2.638 (×4)	2.603 (×4)	2.599–2.661*	2.680 (×4)	2.583–2.660*	2.760 (×4)	2.571–2.656*	2.622 (×4)	2.556–2.652*
	2.666 (×4)	2.708 (×4)		2.696 (×4)		2.770 (×4)		2.713 (×4)	
Mo–O	1.811 (×4)	1.723 (×4)	1.805–1.811*	1.649 (×4)	1.809–1.814*	1.530 (×4)	1.809–1.816*	1.711 (×4)	1.806–1.811*
Ca–O			2.493–2.554*		2.488–2.559*		2.491–2.541*		2.500–2.539*
Sr–O			2.598–2.637*		2.587–2.638*		2.574–2.633*		2.562–2.631*
Coordinates of the oxygen atom (Å)									
X	0.2376	0.2254	0.2380	0.2229	0.2388	0.2080	0.2397	0.2219	0.2406
Y	0.1127	0.1237	0.1120	0.1250	0.1102	0.1380	0.1075	0.1223	0.1048
Z	0.0441	0.0422	0.0441	0.0513	0.0442	0.0552	0.0442	0.0426	0.0443
Parameters Rietveld									
X^2		2.613		1.621		1.465		1.432	
R_p		15.20		11.32		10.67		9.8	
R_{wp}		19.60		15.70		14.10		13.15	

Note: * range of values for each bond distance.

molar concentration of the dopants added. This behavior, more pronounced in theoretical than in experimental data, (see Table 2) can be associated to the different values of bond distances, M–O (M = Mo, Ca, Sr), at the [MoO_4], [CaO_8], and [SrO_8] clusters due to changes in the atomic positions of the oxygen atoms.[24] Similar trend is reported by Hallaoui *et al.* for the $Sr_{(1-x)}Pb_xMoO_4$ solid solution, in which there is an increase in the Mo-O and M–O bond lengths at clusters (MoO_4) and (MO_8) (M = Sr/Pb) with increasing Pb^{2+} concentration.[30]

The negative calculated values of formation energy per unit volume for PMO and solid solution structures according to eqn (1) show that all of them are stable structures with values of −0.128, −0.217, −0.306, −0.396, −0.485 and −0.575 hartree for PMO, Pb0.8, Pb0.6, Pb0.4, Pb0.2 and CSMO, respectively. The E_f values calculated for the $Pb_{1-2x}Ca_xSr_xMoO_4$ solid solutions are found to increase monotonously with the Ca/Sr content, which is consistent with the process of continuous cation substitution from PMO to CSMO.

3.2. MR spectroscopy

Fig. 3 shows the MR spectra in the range of 50 to 1050 cm^{-1}. The PMO is a structure that presents 13 active Raman vibrational modes, which can be described by eqn (6). A and B are non-degenerate modes and E are doubly degenerate modes.[47]

$$\Gamma = 3A_g + 5B_g + 5E_g \quad (6)$$

In Fig. 3a seven Raman vibration modes are found in the PMO matrix spectrum. The peak identified at ∼860 cm^{-1} as ν1 (A_g) is associated with a characteristic symmetric stretching pattern of the molybdates. The peaks at approximately 760 and 740 cm^{-1} can be considered as corresponding to vibrational

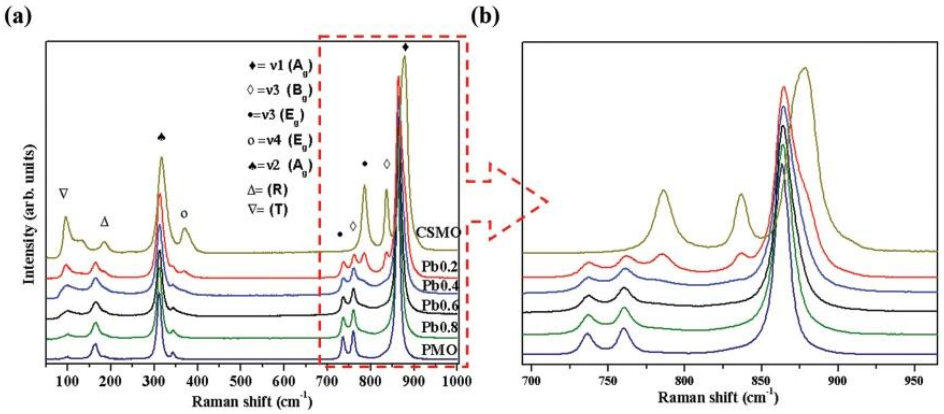

Fig. 3 Micro Raman spectra in the range from 100 to 1000 cm^{-1} of (a) $Pb_{1-2x}Ca_xSr_xMoO_4$ and (b) (zoom) range from 700 to 950 cm^{-1}.

modes of the antisymmetric stretches $\nu 3$ (B_g) and $\nu 3$ (E_g), respectively. The peaks corresponding to 345 and 310 cm^{-1} were marked as $\nu 4$ (E_g) and $\nu 2$ (B_g, A_g), which correspond to antisymmetric and symmetric stretching of the $[MO_4]^{2-}$ group. The modes at 160 and 100 cm^{-1} were identified as A_g and E_g, corresponding to the rotational and translational modes, respectively.

All the samples showed the same MR spectrum profiles, which are also in agreement with the molybdate structure, and in particular PMO.[48,49] However, a shift in the spectra to larger wavenumbers is also observed, and the appearance of two other peaks, at 785 and 840 cm^{-1}, can be observed, mainly in $Pb_{1-2x}Ca_xSr_xMoO_4$ samples with x = 0.5 (CSMO) and x = 0.4 (Pb0.2), as shown in Fig. 3b. Both peaks are also characteristic of $CaMoO_4$ and $SrMoO_4$ compounds.[50] The above results are thus a sign of the complete substitution of the Pb cations by the Ca and Sr cations in the samples.

Fig. S2a and b in the ESI† display a comparison of the theoretical and experimental Raman modes. A good agreement can be seen, although there are a large number of theoretical Raman modes in relation to the experimental data. This is explained by the fact that these modes are not easily detected by experimental techniques due to their low intensities.

3.3. FE-SEM images

Fig. 4 presents the FE-SEM images of the as-synthesized samples. Different particles sizes appear and a progressive evolution of agglomerated is observed as x = (Ca/Sr) increases. It is observed that the PMO sample presents well dispersed anisotropic microcrystals with an octahedron-type morphology. Particles with octahedron-type morphology have been found in previous work,[51] using a capping agent. In this work, without the presence of capping agents, only the synthesis method and the Ca/Sr substitution processes are responsible for the change in morphology and size. In addition, the presence of octahedra is dependent on the substitution of the Pb in the matrix, *i.e.*, with a lower concentration of Pb, the number of well-defined octahedra decreases (Fig. 4d–f). A nanometric size of particles is observed for samples Pb0.8 and the particle shape changes according to the higher proportion of substitution of Pb cations, the octahedron-type morphology becomes more isotropic (Fig. 4c and d) and there is a predominance of elongated nanoparticle morphologies (Fig. 4e and f).

A deep insight to explain the changes in morphology can be provided by applying the Wulff construction based on the values of E_{surf}. Fig. 5 shows the calculated E_{surf} values of PMO and solid solutions. The stability order of the surfaces is (001) < (011) < (112) < (110) < (100) < (111) for the PMO. For the CSMO system, there is an inversion in the order of stability between the (011) and (112) surfaces and between the (100) and (111) surfaces (Fig. S3, ESI†). In the solid solutions the change in the order stability involves the (100) and (111) surfaces, except for the system $Pb_{1-2x}Ca_xSr_xMoO_4$ with x = 0.2.

The relative stability of the exposed surfaces with the Sr cation instead of the Ca cation yields similar results in the E_{surf} values that are associated with their structural and electronic properties, *i.e.*, the arrangement of the atoms at the exposed surfaces. An analysis of the geometry of the studied surfaces suggests that all of them are O- and Pb-ended (see Fig. 6) and the atomic arrangement of the atoms on the top of each surface result in the (001) and (112) surfaces presenting exposed undercoordinated $[PbO_6]$ clusters and complete $[MoO_4]$ clusters. The use of the Kröger–Vink notation[52] allows us to analyze the number of Pb–O breaking bonds in the exposed clusters and then the superficial clusters can be written as $[PbO_6\cdots 2V_O^{\times}]$, $V_O^{\times}$ being the oxygen vacancies. However, in the (100), (110), (011) and (111) surfaces there are undercoordinated $[PbO_5]$ clusters associated with the presence of three oxygen vacancies $[PbO_5\cdots 3V_O^{\times}]$. In addition, there is a correlation between the surface stability and the N_b values, the number of Pb–O breaking bonds in the incomplete clusters at

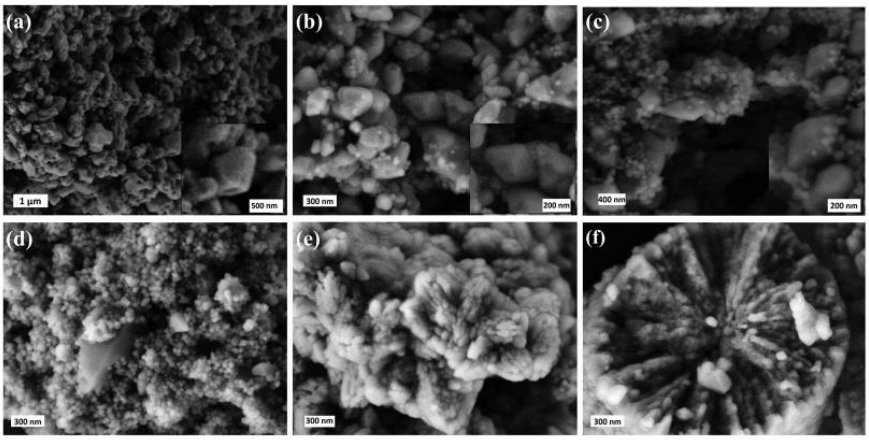

Fig. 4 FE-SEM images of the samples and magnifications of the characteristic morphology of the samples (inset). (a) PMO (b) Pb0.8, (c) Pb0.6, (d) Pb0.4, (e) Pb0.2, (f) CSMO.

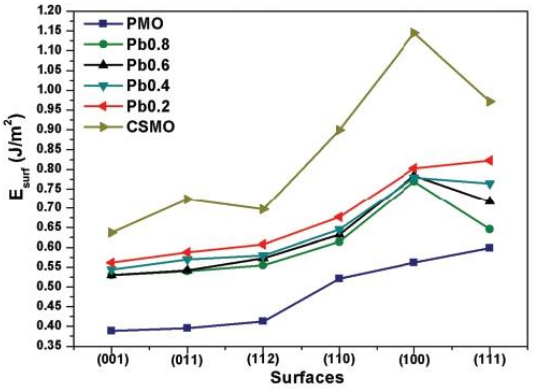

Fig. 5 Calculated values of E_{surf} for the different surfaces of PMO and $Pb_{1-2x}Ca_xSr_xMoO_4$ solid solutions.

the exposed surfaces. The D_b values are also directly linked to the order of the surface energy stability, *i.e.*, higher values of D_b represent a large number of defects on the surface and a higher surface energy value. Table S1 (ESI†) lists the surface area values and the calculated N_b and D_b values. In addition, the values of the surface bonds for PMO and $Pb_{1-2x}Ca_xSr_xMoO_4$ (Pb = 0.2, Pb0.4, Pb0.6, Pb0.8 and CSMO) solid solutions are reflected in Table S1 (ESI†). The (001), (011) and (112) surfaces have similar values of E_{surf}, *i.e.*, 0.388, 0.395 and 0.413 J m^{-2}, respectively, while low values of N_b = 2, 3 and 4, and D_b = 6.56, 8.09 and 7.05 nm^{-2}, respectively, can be sensed. The (110), (100) and (111) surfaces display the following order of stability: 0.52 < 0.56 < 0.60 J m^{-2}, respectively, with values of N_b = 4, 6, and 7, and higher values of D_b = 8.37, 8.88 and 6.97 nm^{-2}, respectively. For the (111) surface, a correlation between the surface stability and D_b values is not found due to the large surface area. For the (011) surface, different slab cuts can be performed, the most stable being the symmetric one shown in Fig. 6. In addition, some studies reported

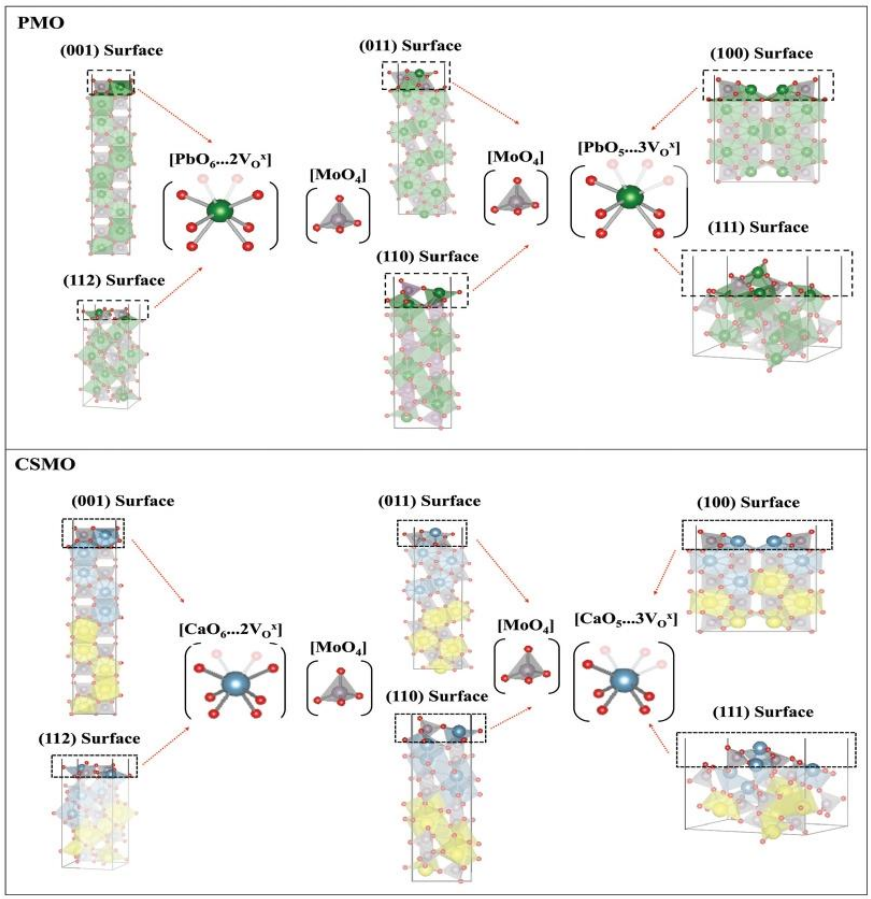

Fig. 6 Schematic representations of surfaces: (001), (011), (110), (100), (111), and (112) for PMO and CSMO systems. The clusters and oxygen vacancies are written using the Kröger–Vink notation.

another non-symmetric slab cut with exposed [MO_6] clusters, which present less stability (ΔE_{surf} = 0.25 J m^{-2}).[44,53] For the solid solutions $Pb_{1-2x}Ca_xSr_xMoO_4$, the number of Pb–O breaking bonds in the superficial clusters is maintained (as well as the D_b values), as can be seen in Fig. S4 (ESI†).

Different crystal morphologies can be achieved by tuning the E_{surf} values of the different surfaces. Based on that, it was possible to obtain the map of the available morphologies (Fig. 7), and to correlate with the experimental FE-SEM images. This map shows the available morphologies of the PMO crystals and solid solutions starting with the ideal morphology (a) (bottom of Fig. 7). As (001) E_{surf} increases to 0.65 J m^{-2}, the morphology (b) is obtained with a faceted octahedron defined mainly by the (001), (011) and (112) surfaces, similar to that found experimentally for the PMO sample. In addition, morphology (b) is in agreement with other previous works where the co-precipitation method was employed for the synthesis of PMO.[54] On the other hand, the simultaneous increase of the (001) and (112) E_{surf} values to 0.80 J m^{-2} results in the morphology (c) with the main presence of (011) surface (left side bottom in Fig. 7), similar to that found for the Pb0.8 sample. By decreasing the E_{surf} of (110) surface to 0.23 J m^{-2}, the octahedron-type morphology becomes more elongated allowing (110) surface to be exposed in the resulting morphology (d), which can match to the Pb0.6 sample, showed in Fig. 4(c).

3.4. Electronic properties

3.4.1. UV-visible spectroscopy. Diffuse reflectance spectroscopy was used to obtain the band gap energy (E_{gap}) of the

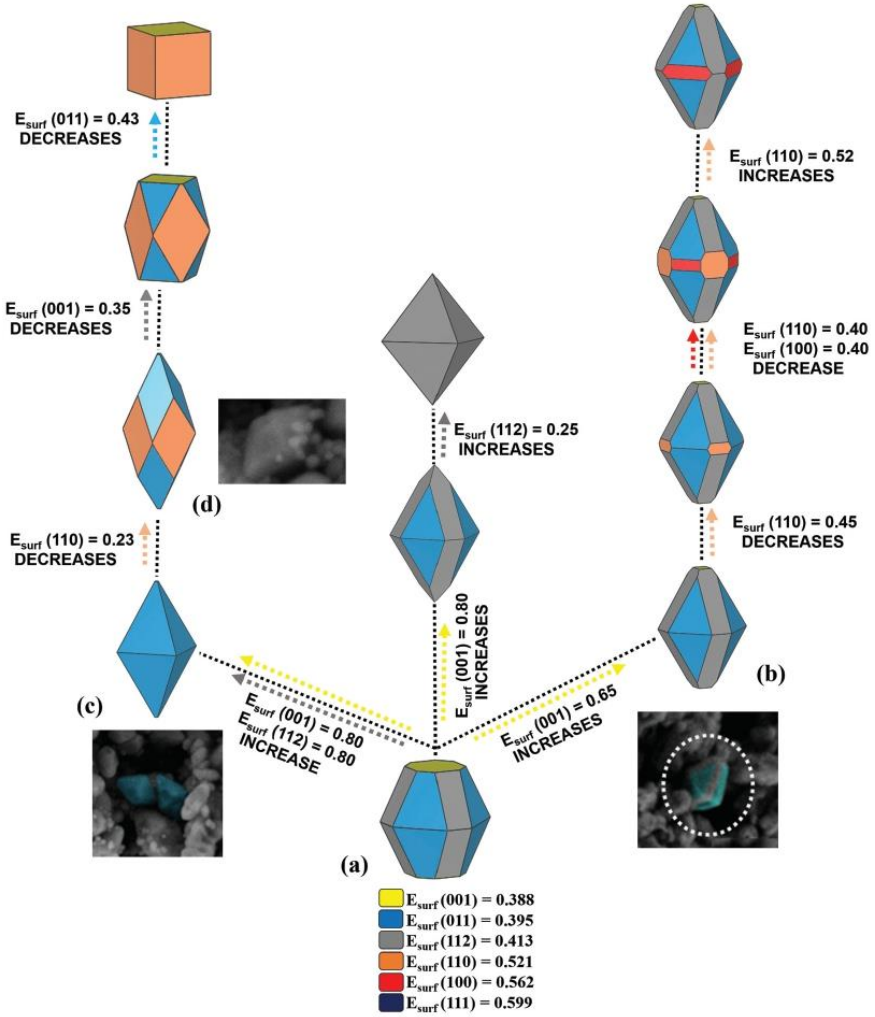

Fig. 7 The available morphology map for the PMO crystals (E_{surf} are given in J m^{-2}). The experimental FE-SEM images (inset) are included for comparison purposes.

samples and the reflectance spectra were converted to absorbance using the Kubelka–Munk function, given by eqn (7).[55]

$$F(R_\infty) = \frac{(1 - R_\infty)^2}{2R_\infty} = \frac{K}{S} \quad (7)$$

where $F(R_\infty)$ is the Kubelka–Munk function or absolute reflectance of the sample; R_∞ is the diffuse reflectance; K is the molar absorption coefficient, and S is the scattering coefficient.

E_{gap} values were estimated using the Wood and Tauc[56] method and plotted in Fig. S5 (ESI†). Although the Tauc model is appropriate for amorphous materials, we have decided its use in this work since the samples obtained by the reflux method are structurally disordered at short range. This method proposes that E_{gap} is related to the absorbance and energy of the photon, given by eqn (8):

$$\alpha h\nu = C_1(h\nu - E_{gap})^n \quad (8)$$

where α is the linear absorption coefficient; $h\nu$ is the photon energy; C_1 is a proportionality constant and n is indicated for different transitions (n = 1/2, 2, 3/2 or 3 for direct permission, indirect permission, prohibited direct, and indirect prohibition, respectively). The molybdates in general, which have a tetragonal structure of the scheelite type, allow direct electronic transitions (n = 1/2).[57,58]

The values of E_{gap} are dependent on the synthesis method, presence of defects, shape and size of the crystallite, structural and electronic modification in the lattice, and so on. In the metallic molybdates the corresponding emissions occur from charge transfer processes within $[MO_4]^{2-}$ units. In addition, the intermediate levels of energies generated from defects caused by the displacement of oxygen in the structure (vacancies) are associated with the order–disorder degree of these nanostructures.[59,60] In particular, the microwave synthesis of $PbMoO_4$ in presence of acetylacetone (acac) as chelate modifier or polyvinylpyrrolidone (PVP) as the coupling agent[39] shows morphologies of 100–200 nm and compares the values of the bandgap energy for different synthesis methods such as: reflux (3.31 eV), hydrothermal (3.21 eV), coprecipitation/thermal treatment (3.16 eV), solid-state reaction (3.1 eV), solvothermal (3.3 eV), hydrothermal/acac (3.05 eV), hydrothermal/PVP (3.17 eV).

The values of the E_{gap} of the samples are presented in Table S2 of the ESI.† Experimental and theoretical E_{gap} values obtained as a function of Pb content in $Pb_{1-2x}Ca_xSr_xMoO_4$ solid solution are displayed in Fig. 8. An analysis of the results yields a similar behavior between experimental and theoretical results. However, it can be seen that experimental values are 9–15% smaller than those determined from calculations. Such differences are due to a well-known over-estimation in the E_{gap} values obtained with the B3LYP method which can explain the discrepancy with experiments. It is observed that the sample CSMO presents a high value of E_{gap} = 4.03 eV, while the PMO has a lower value (3.35 eV), in agreement with previous reports.[7] In general, molybdates present a high E_{gap}, since few intermediate levels between VB and CB are present.[50,61]

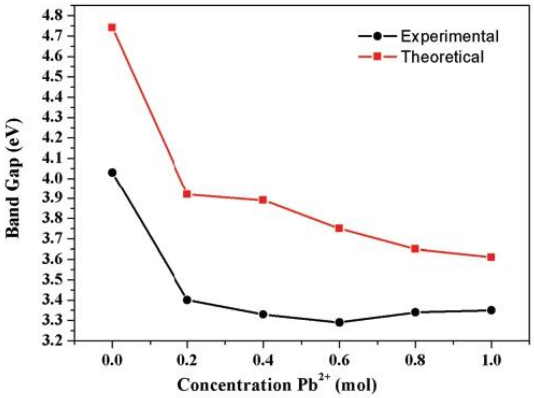

Fig. 8 Experimental and theoretical variation of the E_{gap} values as a function of Pb content.

However, in the solid solutions for values of x = 0.1, 0.2, 0.3 and 0.4, changes in the system and formation of transient structures occur, implying higher E_{gap} values as x is increased. In addition, Table S3 of the ESI† shows the E_{gap} values obtained for surfaces, where a similar behavior is obtained with bulk results. However, the E_{gap} value of the (100) surface remains almost constant.

3.4.2. Band structures, density of states and charge density maps. The valence band (VB) and conduction band (CB) of molybdates are mainly formed by the 2p O and 4d Mo states, respectively. As can be seen in Fig. 9, for PMO the upper part of VB is also composed of the 6s states of Pb hybridized with the 2p state of O, while the lower part of CB is formed mainly by the 4d states of Mo and 6p states of Pb. The band structure of the CSMO sample is similar to $SrMoO_4$ and $CaMoO_4$ structures reported in the literature,[62–64] in which the upper part of VB is composed by 2p states of the O while the 4d states for the Mo and 2p of the O are predominant in the CB, with little contribution of the 3d states of the Sr and 4d states of the Ca in the upper part of CB.

An analysis of the band structures and density of states (DOS) of the PMO and CSMO systems presented in Fig. 9 shows that their electronic structures differ. The band structure of the PMO shows an indirect band gap value of 3.61 eV, while CSMO presents a direct larger band gap value of 4.74 eV. In addition, both VB and CB of PMO are more dispersed than those of CSMO. Therefore, the 6s orbitals of Pb contribute to raising the VB resulting in a narrower band gap of PMO compared with that of CSMO.[65] This difference may be associated with a higher charge density of the Pb cation compared to Sr/Ca cations. The presence of Pb cation states in the vicinity of the band gap influences the optical and luminescence properties of $PbMoO_4$. In particular, it has been found that the hole self-trapping at $[MoO_4]^{2-}$ anion, which is typically observed in molybdates, is not possible in $PbMoO_4$ because holes can migrate along the 6s Pb states located at the top of the VB.[66,67]

The charge density maps are presented in Fig. 10 with the aim of explaining electron density differences. Fig. 10a and b show electron density maps for the PMO and CSMO, respectively,

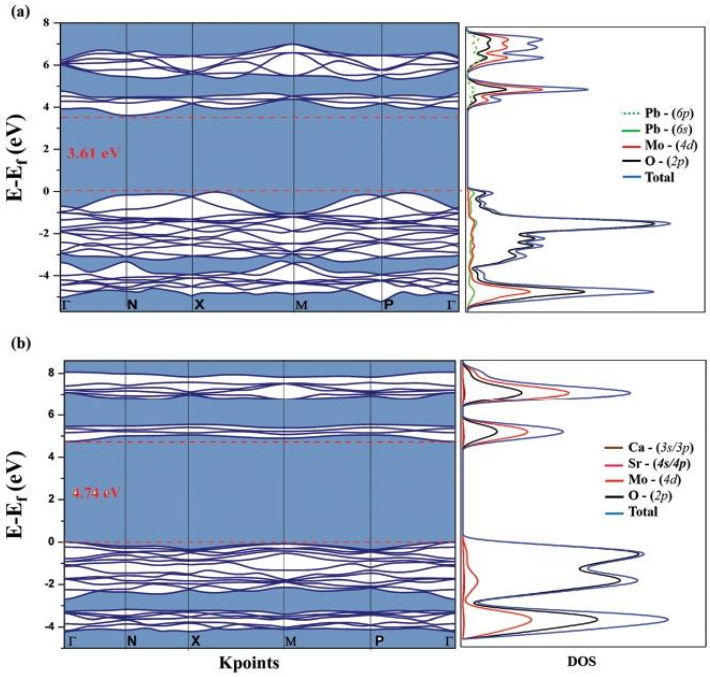

Fig. 9 Calculated band structure and DOS projected on atoms of the Pb, Ca, Mo and O atoms in (a) PMO and (b) CSMO.

with a chosen plane (100) containing the Pb/Ca/Sr, Mo and O atoms. The high and low electron density zones on each map are represented by a different color in atomic units (electron per bohr^3), the area of accumulation of electron density being depicted in red, while the depletion zones of electron density are marked in blue. Thus, as expected, there is a higher electronic density around the Pb cations in relation to the Ca and Sr cations. Therefore, the higher dispersion of electronic density around the Pb cation contributes to the higher total density of the PMO promoted by the hybridization of the 6p Pb and 2p O orbitals, which is called "split-off hybridization".[65] This fact allows PMO to have a larger charge mobility, lower recombination rate (electron–hole), and greater dispersion in its bands, resulting in lower E_{gap} values of PMO compared to CSMO.[64,68] The electron density isosurfaces (electron per bohr^3) for PMO and CSMO are shown in Fig. 10c and d, respectively.

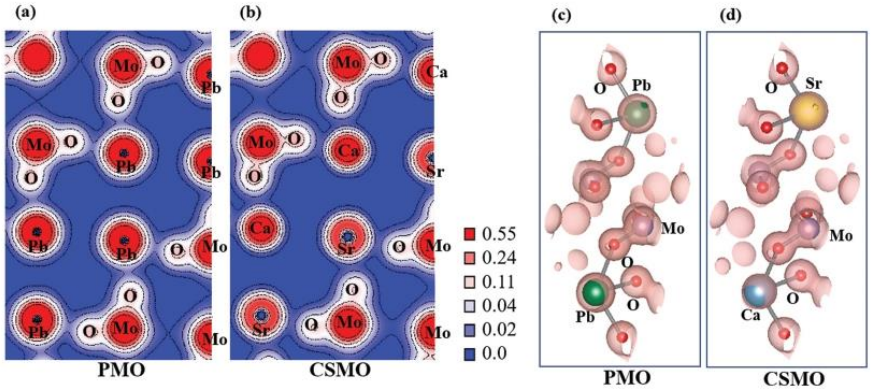

Fig. 10 Electron density difference contour maps on the (100) plane (electron per bohr^3) for (a) PMO and (b) CSMO. High and low charge density values are shown in red and blue, respectively. The blue, white and red colors are 0.00, 0.11, and 0.55 electron per bohr^3, respectively. Electron density isosurfaces (electron per bohr^3) for PMO (c) and (d) CSMO.

To verify the differences and contribution of each band, the DOS projected on atoms and orbitals for $Pb_{1-2x}Ca_xSr_xMoO_4$ structures with $x = 0.4$ (Pb0.2), $x = 0.3$ (Pb0.4), $x = 0.2$ (Pb0.6) and $x = 0.1$ (Pb0.8) are presented in Fig. 11. It can be seen that the VB in all the structures are composed of O 2p orbitals, Mo 4d, and a low contribution of the Pb/(Ca, Sr) cations.

3.5. PL measurements

Fig. 12a shows the PL spectra obtained with excitation at 325 nm at room temperature. The samples spectra displayed broadband emission behavior, with an increase in the intensity of PL emission from the PMO sample to the Pb0.4 sample followed by a decrease in the intensity for the Pb0.2 and CSMO samples, as can be seen in Fig. 12. The literature offers diverse explanations on the nature of the PL emissions in molybdates: (i) The PL emission processes are associated to the transitions that occurs within $[MoO_4]^{2-}$ moiety, among the fundamental and excited electronic states.[1,69,70] The corresponding ground state has the $^1A_1$ symmetry, and the lowest excited states present $^1T_2$, $^1T_1$, $^3T_2$, and $^3T_1$ symmetries.[64,71] The transition $^1A_1 \leftrightarrow {}^1T_2$ is a dipole-allowed transition, and lowest excited states $^3T_1$ and $^3T_2$ to the ground $^1A_1$ state are responsible for the material intrinsic luminescence, Fig. 12b. The luminescence in this case would reveal emission bands referring to sub-levels between the triplet states $^3T_1$ and $^3T_2$ (region of 400 to 600 nm) due to the Jahn–Teller effect on the symmetry of the $[MoO4]^{2-}$ moiety,[71] (ii) From a structural and electronic point of view, the high concentration of defects favors the structural disorder at short range of $[MoO_4]^{2-}$ moiety, associated to the presence of oxygen vacancies, and the formation of intermediary energy level into the band gap, enhancing the probability of non-radioactive transitions and, consequently, increasing the suppression of the PL emission.[5,39,72,73] In our work, the samples obtained by the reflux method are structurally ordered in long and disordered at short range, according to the XRD, MR spectroscopy and diffuse reflectance analyses (3.1, 3.2 and 3.4.2 sections). About the PL emission intensity was observed that the Pb0.4 and Pb0.6 samples display the highest intensity whereas samples Pb0.8, Pb0.2 and PMO have the lowest intensities. Since the intensity of PL is related to the emission of radiation with low non-radioactive states, it can be inferred that samples with higher intensities of PL have less concentration of these states. In this sense, this is strongly related to the shorter values of the Mo–O bond distances (1.649 Å and 1.530 Å for Pb0.4 and Pb0.6 samples, respectively), Table 2, due to the main clusters of surfaces exposed in these materials $[MO_6 \cdots 2V_O^{\times}]$ (M: Pb or Ca), Fig. 6. Then, PL emission and the bonding distance are related to the amount and type of defects present in the structure.[74]

Luminescent emission in oxides with high defects density occurs by several paths related to the high density of electronic states within the band gap, and this result in broad band characteristic.[58] It is commonly referred to as shallow and deep defect type in the band gap that result in different energy PL emission. The former is emissions type in few millielectron-volts close to the upper part of VB or to the lower part of CB, and monoionized defects type are predominant, which results to a more energetic PL emission (cyan-blue-violet colors). Deep type emissions are further away this maximum and minimum bands with duple-ionized defect type (lower energetic emission, green-yellow-orange-red colors).[6,57,75]

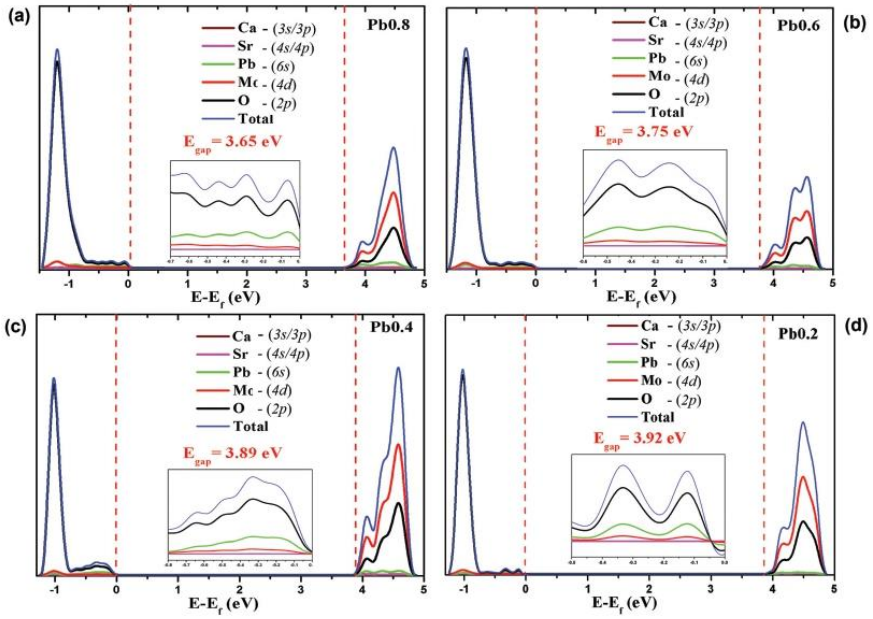

Fig. 11 Calculated total DOS projected on atoms of the samples (a) Pb0.8, (b) Pb0.6, (c) Pb0.4, and (d) Pb0.2.

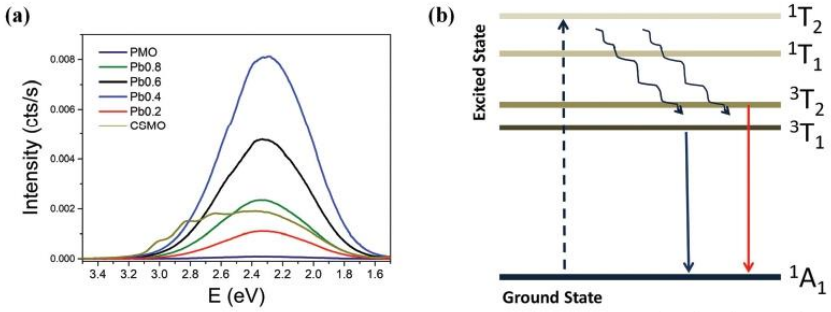

Fig. 12 (a) PL emissions, (b) schematic diagram of energetic levels of the fundamental, $^1A_1$, and excited, $^1T_2$, $^1T_1$, $^3T_2$, and $^3T_2$, electronic states for $[MoO_4]^{2-}$ anion. The intersystem crossing processes between singlet and triplet states are displayed.

The spectra deconvoluted, Fig. S6 (ESI†), show that the PMO sample and solid solution samples have mainly emissions with deep defects type (500–700 nm) the PMO sample has 76% emission in the green region, Fig. S6a (ESI†), and that by decreasing the concentration of Pb, the emission in the green region decreases, increasing the emission in the red region, Fig. S6b–e (ESI†). The CSMO sample as shown in the spectrum presents shallow and deep defects type with 40% emission in green and 40% emission in blue, Fig. S6f (ESI†). Fig. 13a–c shows the emission transition states and its relation with the band gap for the PMO, Pb0.8 and Pb0.6 samples, respectively. This relationship allows us to better consider the shallow and deep levels of each spectrum of the samples.[77,78] It would be expected that only the CSMO sample has characteristics of shallow defects, V_O type. However, considering the diagram (Fig. 13), it is possible to observe that PMO, Pb0.8 and Pb0.6 samples have defect levels below 0.8 eV characteristic of shallow defects.[75,76]

Therefore, considering the types of defects on exposed surfaces for each sample (Fig. 7 and Fig. S4, ESI†) and their corresponding gap energy (Table S3, ESI†), the emission types for each material were defined, as shown in the Fig. 13. As seen in Section 3.3, the PMO morphology presents concomitant (001), (112), and (011) surfaces, being the first and second surfaces composed by defects with two oxygen vacancies $[PbO_6\cdots 2V_O^{\times}]$, while the last one with three vacancies, $[PbO_5\cdots 3V_O^{\times}]$. Considering that the (011) and (112) surfaces have similar E_{gap} (3.62 and 3.60 eV), and the (001) surface has E_{gap} = 3.56 eV, is expected that shallow defects to be related to the chemical environment of the higher gap energy surfaces, while that deep defects to be related to the chemical environment of the lower gap energy surfaces. Thus, for PMO sample as shallow defects the chemical environment will be composed by (011) surface with Pb and Mo clusters interaction $\left([PbO_5\cdot 3V_O^{\bullet}]-2[MoO_4]'-[PbO_8]'\right)$, and for the (112) surface with the chemical environment of: $2[PbO_6\cdot 2V_O^{\bullet}]-2[MoO_4]'$. While the deep defects would be related to the (001) surface with the following chemical environment: $[PbO_6\cdot 2V_O^{\bullet\bullet}]-[MoO_4]''-[PbO_8]''$, Fig. 13a. For the Pb0.8 sample, only the (011) surface is obtained in its morphology and

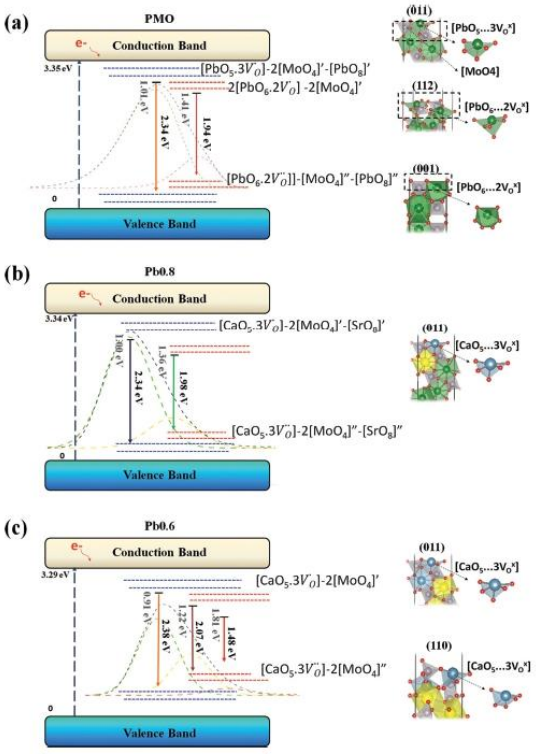

Fig. 13 A pictorial representation of the relationship between the PL emission energy and location of electronic states within the band gap for the (a) PMO, (b) Pb0.8 and (c) Pb0.6.

thus the exposed clusters of Ca and its neighborhood with Mo and Sr clusters are the chemical environment for this surface. For this sample the defects of the shallow type are due to $[CaO_5\cdot 3V_O^{\bullet}]-2[MoO_4]'-[SrO_8]'$ and similar for deep defects, $\left([CaO_5\cdot 3V_O^{\bullet\bullet}]-2[MoO_4]''-[SrO_8]''\right)$, Fig. 13b. An interesting factor is observed for the Pb0.6 sample which has the (011) and

(110) surfaces in its morphology and both have a chemical environment composed of the Ca cluster around two Mo clusters. The surface with the highest gap energy, (011), is the responsible for the emission of shallow defects $\left(\left[CaO_5 \cdot 3V_O^{\bullet}\right] - 2\left[MoO_4\right]^{'}\right)$, while the one with the lowest gap energy, (110) surface, for the emission of deep defects $\left(\left[CaO_5 \cdot 3V_O^{\bullet\bullet}\right] - 2\left[MoO_4\right]^{''}\right)$, Fig. 13c.

3.6. Degradation process of RhB dye

The photocatalytic performance was tested *via* degradation of the RhB solution under UV light. A graph of (C/C_0) *vs.* reaction time is presented in Fig. 14a, where C is the concentration of RhB solution at time t and C_0 is the initial concentration for samples. The behavior observed in the $-\ln(C/C_0)$ *vs.* reaction time diagram shown in Fig. 14b suggests a first-order kinetic reaction. Their analysis showed that with increasing concentration of the Ca/Sr cations (and consequently the decrease in the concentration of Pb cations), a reduction in the photodegradation process of the RhB can be observed. The kinetic constant is reduced from 1×10^{-2} min^{-1} to 1×10^{-3} min^{-1} in passing from PMO to CSMO, respectively. To complete the photodegradation analysis, a table was added comparing the commercial TiO_2 photocatalyst (Degussa P-25), a pure sample of literature, and the solid solution particle (Pb0.6) synthesized in this work Table S5 (ESI†). It can be observed that the solid solution obtained in this work is compared in efficiency to those reported in the literature. The improvement in the dye molecules degradation process, using a photocatalyst, is associated with the numbers of the electron–hole pair available on the surface of the photocatalyst and its low recombination rate.[49] Thus, the PMO and the samples with higher concentrations of Pb cations (Pb0.8 and Pb0.6) presented better results in the RhB degradation. The photocatalysts electronic band structure, which is one of the responsible for the photocatalytic efficiency, can be tuned changing the specific exposed surfaces,[79] as observed for calculated values of band gap energy for the PMO and $Pb_{1-2x}Ca_xSr_xMoO_4$ surfaces, Table S3 (ESI†). In addition, a comparison of DOS for PMO and CSMO surfaces is presented in Fig. S7 and S8 (ESI†), showing a similar split-off feature at the VB and the CB compared to the bulk of pure and doped systems, where the transfer of electrons is produced to generate the electron/hole pairs.

Table S4 (ESI†) shows the calculated values of the Mulliken population per atom and constitutive cluster for PMO and CSMO bulk, as well as the Mulliken population per undercoordinated cluster of surfaces. This analysis is a helpful tool that allows clarification of the nature of the electron–hole localization in the undercoordinated clusters at the exposed surfaces. An analysis of the results shows that for both PMO and CSMO bulk structures there is an accumulation of electrons at the $[Pb/Ca/SrO_8]$ clusters and there is an electron depletion (positive charge accumulation) at the $[MoO_4]$ cluster, thereby creating a difference in potential which is able to form a local electric field. In PMO the potential between $[PbO_8]$ and $[MoO_4]$ clusters are compensated, and the same occurs between the $[Ca/SrO_8]$ and $[MoO_4]$ clusters in CSMO. However, a local electric field is generated and also tends to vary on surfaces according to the number of O atom vacancies in the exposed surface clusters.[80] These differences in charge in the different clusters of the surface have an influence on the transfer of the photogenerated electron–hole.

For example, the (011), (110), (100) and (111) surfaces have higher values of D_b, compared to (001) and (112), and the presence of three oxygen vacancies $[PbO_5 \cdots 3V_O^{\times}]$, which generate higher charge differences between $[Pb/Ca/SrO_5]$ and $[MoO_4]$ clusters. Accordingly, it is observed that not only the undercoordinated cations of the exposed clusters play a decisive role in the surfaces that constitute the morphology, but they are also involved in the structural and electronic distortion of the clusters (see Table S1, ESI†). The information from the FE-SEM image reveals that the presence of nanoparticles with an octahedral morphology is controlled mainly by (001), (011) and (112) exposed surfaces. As the concentration of Pb in the samples decreases, the surface (001) becomes less predominant and the surface (110) appears in the sample Pb0.6, the most

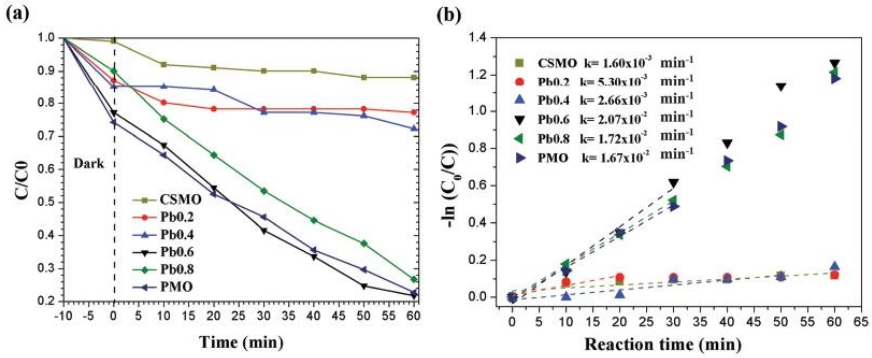

Fig. 14 Photocatalysis degradation profiles of RhB for PMO and solid solution samples: (a) Pb0.8, Pb0.6, Pb0.4, Pb0.2 and (b) CSMO photocatalytic reaction kinetics.

photoactive. It was observed that between the PMO and Pb0.6 samples the E_{gap} of the surfaces increases, Table S3 (ESI†), and the potential difference becomes greater for the $[CaO_{8-y}\cdot yV_O^{\times}]$ and $[MoO_4]$ clusters on the surface (110) as the content of Pb decreases (from −0.18 in $[PbO_5]$ for PMO to −0.41 in $[CaO_5]$ for CSMO), Table S4 (ESI†). This fact can enhance the migration of photoinduced electrons for the surface, suppressing the recombination of charge carriers, and improving the photocatalytic activity.

Moreover, the migrated electrons can be trapped by the oxygen molecules, O_2, adsorbed on the surface to generate $O_2^{\bullet-}$ radicals, while the holes on the surface react with water molecules to yield $OH^{\bullet}$ and $H^{\bullet}$ radicals. Furthermore, these photogenerated reactive oxygen species induce the degradation of RhB. Consequently, the undercoordinated and complete clusters at the surfaces, $[CaO_x]/[SrO_x]/[PbO_x]$ and distorted $[MoO_4]_d$ are the active sites capable of reacting with H_2O and O_2, respectively, and can be considered the reservoirs of holes and electrons, respectively, that constitute the active sites in the photocatalytic activity.

4. Conclusions

This study reports the successful preparation of PMO and $Pb_{1-2x}Ca_xSr_xMoO_4$ (x = 0.1, 0.2, 0.3, 0.4 and 0.5) solid solutions in the whole compositional range. Their structural, electronic, and vibrational properties, as well as the morphologies and the photocatalytic activity in the photodegradation process of RhB dye have been investigated. The samples synthesized with higher concentrations of Pb cations presented better results in RhB degradation. The photocatalysts' electronic band structure, which has an influence on photocatalysts, can be tuned using the specific exposed surfaces, and this has a significant impact on the redox abilities of photoinduced carriers. First-principles calculations were performed to obtain the energy surface values for the PMO and solid solution surfaces, based on the Wulff construction, in order to rationalize the crystal morphologies observed in the experimental FE-SEM images.

The simulations revealed that there are two important factors that must be considered when investigating the surface electronic properties of the as-synthesized samples. The first factor is that the (011) and (110) surfaces appear in the experimental FE-SEM images which show enhanced photocatalytic activity. The second involves the specific local coordination of the Pb/Ca/Sr and Mo cations in the exposed surface, *i.e.*, the Pb/Ca/Sr and Mo clusters. In particular, we found that the stability of the surfaces and their electronic properties are correlated with the presence of incomplete $[CaO_x]/[SrO_x]/[PbO_x]$ and distorted $[MoO_4]$ clusters as the reservoirs of holes and electrons, respectively, which act as the active sites in the photocatalytic activity. These subtle differences between the (011), (110) and (112) surfaces illustrate the influence of surface type on reactivity. The PL emission spectra of the samples showed predominant emission in the green-orange region, with predominantly shallow type defects for the most photoactive samples. Overall, the current study opens the door to further uses of solid solutions based on PMO with tunable properties for various applications. The reported synthetic approach is believed to have potential utility for obtaining other solid solutions, while the results described here provide new insights on the geometry, electronic structure, morphology evolution, and structure–property relationship of $AMoO_4$-type compounds. These findings show that by directing the crystal morphology it is possible to control and understand its properties, such as optical and photocatalytic properties. Exploration of semiconductor surface effects may lead to the fabrication of more efficient photocatalysts.

Conflicts of interest

There are no conflicts to declare.

Acknowledgements

The authors thank the following Spanish and Brazilian research financing institutions for financial support: E. O. G. acknowledges Generalitat Valenciana for the Santiago Grisolia program (2018/064); A. A. G. Santiago acknowledges financial support from CNPq (140231/2018-8); R. A. C. Amoresi acknowledges (FAPESP 2017/19143-7 and 2019/09296-6) to financing support to carry out a research stay at UJI. E. Longo acknowledges (FAPESP 2013/07296-2, 2013/00789-2); M. R. D. Bomio acknowledges financial support from National Council for Scientific and Technological Development – CNPq (303657/2017-0), Graduate Program in Materials Science and Engineering (PPGCEM-UFRN) and Coordination for the Improvement of Higher Education Personnel (CAPES) – Brazil (CAPES) – Finance Code 001. E. O. G., L. G, and J. A. acknowledge financial support from Universitat Jaume I (project UJI-B2019-30), and the Ministerio de Ciencia, Innovación y Universidades (Spain) (project PGC2018094417-B-I00) for financially supporting this research. We also wish to thank the Servei d'Informática, Universitat Jaume I, for their generous allocation of computer time.

References

1 V. M. Longo, L. S. Cavalcante, E. C. Paris, J. C. Sczancoski, P. S. Pizani, M. S. Li, J. Andrés, E. Longo and J. A. Varela, *J. Phys. Chem. C*, 2011, **115**, 5207–5219.
2 R. Grissa, H. Martinez, V. Pelé, S. Cotte, B. Pecquenard and F. Le Cras, *J. Power Sources*, 2017, **342**, 796–807.
3 J. Zhang, T. Zhao, L. Zou and S. Gan, *J. Photochem. Photobiol., A*, 2016, **314**, 35–41.
4 S. S. Hosseinpour-Mashkani, S. S. Hosseinpour-Mashkani and A. Sobhani-Nasab, *J. Mater. Sci.: Mater. Electron.*, 2016, **27**, 4351–4355.
5 M. R. D. Bomio, L. S. Cavalcante, M. A. P. Almeida, R. L. Tranquilin, N. C. Batista, P. S. Pizani, M. Siu Li, J. Andres and E. Longo, *Polyhedron*, 2013, **50**, 532–545.

6 T. Skibiński, S. M. Kaczmarek, G. Leniec, T. Tsuboi, Y. Nakai, M. Berkowski, Z. Kowalski and W. Huang, *J. Cryst. Growth*, 2014, **401**, 802–806.
7 G. M. Gurgel, L. X. Lovisa, L. M. Pereira, F. V. Motta, M. S. Li, E. Longo, C. A. Paskocimas and M. R. D. Bomio, *J. Alloys Compd.*, 2017, **700**, 130–137.
8 Y. I. Song and S. S. Hong, *Res. Chem. Intermed.*, 2016, **42**, 367–377.
9 S. Obregón, D. B. Hernández-Uresti, A. Vázquez and D. Sánchez-Martínez, *Appl. Surf. Sci.*, 2018, **457**, 501–507.
10 D. B. Hernández-Uresti, A. Martínez-De La Cruz and J. A. Aguilar-Garib, *Catal. Today*, 2013, **212**, 70–74.
11 J. V. B. Moura, T. S. Freitas, A. R. P. Silva, A. T. L. Santos, J. H. da Silva, R. P. Cruz, R. L. S. Pereira, P. T. C. Freire, C. Luz-Lima, G. S. Pinheiro and H. D. M. Coutinho, *Arab. J. Chem.*, 2018, **11**, 739–746.
12 C. Pupp, R. Yamdagni and R. F. Porter, *J. Inorg. Nucl. Chem.*, 1969, **31**, 2021–2029.
13 C. Cui, J. Bi, C. Wu, S. Zhang and D. Gao, *Mater. Res. Bull.*, 2008, **43**, 1160–1163.
14 C.-T. Xia, V. M. Fuenzalida and R. A. Zará, *J. Alloys Compd.*, 2001, **316**, 250–255.
15 A. P. de, A. Marques, V. M. Longo, D. M. A. de Melo, P. S. Pizani, E. R. Leite, J. A. Varela and E. Longo, *J. Solid State Chem.*, 2008, **181**, 1249–1257.
16 Y. Mi, Z. Huang, F. Hu and X. Li, *Mater. Lett.*, 2009, **63**, 742–744.
17 J. H. Ryu, J.-W. Yoon, C. S. Lim and K. B. Shim, *Mater. Res. Bull.*, 2005, **40**, 1468–1476.
18 C. Zhang, E. Shen, E. Wang, Z. Kang, L. Gao, C. Hu and L. Xu, *Mater. Chem. Phys.*, 2006, **96**, 240–243.
19 Z. Luo, H. Li, H. Shu, K. Wang, J. Xia and Y. Yan, *Mater. Chem. Phys.*, 2008, **110**, 17–20.
20 S. K. Aditha, A. D. Kurdekar, L. A. A. Chunduri, S. Patnaik and V. Kamisetti, *MethodsX*, 2016, **3**, 35–42.
21 V. Sabaghi, F. Davar and Z. Fereshteh, *Ceram. Int.*, 2018, **44**, 7545–7556.
22 P. D. Cozzoli, A. Kornowski and H. Weller, *J. Am. Chem. Soc.*, 2003, **125**, 14539–14548.
23 Y. Sun, B. Gates, B. Mayers and Y. Xia, *Nano Lett.*, 2002, **2**, 165–168.
24 M. C. Oliveira, J. Andrés, L. Gracia, M. S. M. P. de Oliveira, J. M. R. Mercury, E. Longo and I. C. Nogueira, *Appl. Surf. Sci.*, 2019, **463**, 907–917.
25 S. Vidya, S. Solomon and J. K. Thomas, *Mater. Today Proc.*, 2015, **2**, 904–908.
26 I. C. Nogueira, L. S. Cavalcante, P. F. S. Pereira, M. M. de Jesus, J. M. Rivas Mercury, N. C. Batista, M. S. Li and E. Longo, *J. Appl. Crystallogr.*, 2013, **46**, 1434–1446.
27 V. D. Zhuravlev, O. G. Reznitskikh, Y. A. Velikodnyi, T. A. Patrusheva and O. V. Sivtsova, *J. Solid State Chem.*, 2011, **184**, 2785–2789.
28 S. P. Culver, M. J. Greaney, A. Tinoco and R. L. Brutchey, *Dalton Trans.*, 2015, **44**, 15042–15048.
29 Y. Wang, C. Wu, L. Geng and S. Chen, *Phys. Chem. Chem. Phys.*, 2017, **19**, 23204–23212.
30 A. Hallaoui, A. Taoufyq, M. Arab, B. Bakiz, A. Benlhachemi, L. Bazzi, J. C. Valmalette, S. Villain, F. Guinneton and J. R. Gavarri, *Mater. Res. Bull.*, 2016, **79**, 121–132.
31 P. F. S. Pereira, C. C. Santos, A. F. Gouveia, M. M. Ferrer, I. M. Pinatti, G. Botelho, J. R. Sambrano, I. L. V. Rosa, J. Andrés and E. Longo, *Inorg. Chem.*, 2017, **56**, 7360–7372.
32 W. da, S. Pereira, M. M. Ferrer, G. Botelho, L. Gracia, I. C. Nogueira, I. M. Pinatti, I. L. V. Rosa, F. de, A. La Porta, J. Andrés and E. Longo, *Phys. Chem. Chem. Phys.*, 2016, **18**, 21966–21975.
33 R. Dovesi, A. Erba, R. Orlando, C. M. Zicovich-Wilson, B. Civalleri, L. Maschio, M. Rérat, S. Casassa, J. Baima, S. Salustro and B. Kirtman, *Wiley Interdiscip. Rev.: Comput. Mol. Sci.*, 2018, **8**, 1–36.
34 Z. Gao, W. Sun, Y. Hu and X. Liu, *Trans. Nonferrous Met. Soc. China*, 2012, **22**, 1203–1208.
35 Z. Gao, C. Li, W. Sun and Y. Hu, *Colloids Surf., A*, 2017, **520**, 53–61.
36 M. M. Ferrer, A. F. Gouveia, L. Gracia, E. Longo and J. Andrés, *Modell. Simul. Mater. Sci. Eng.*, 2016, **24**, 025007.
37 G. Wulff, *Z. Kristallogr. – Cryst. Mater.*, 1901, **34**, 449–530.
38 J. Andrés, L. Gracia, A. F. Gouveia, M. M. Ferrer and E. Longo, *Nanotechnology*, 2015, **26**, 405703.
39 M. R. D. Bomio, R. L. Tranquilin, F. V. Motta, C. A. Paskocimas, R. M. Nascimento, L. Gracia, J. Andres and E. Longo, *J. Phys. Chem. C*, 2013, **117**, 21382–21395.
40 V. M. Longo, L. S. Cavalcante, E. C. Paris, J. C. Sczancoski, P. S. Pizani, M. S. Li, J. Andrés, E. Longo and J. A. Varela, *J. Phys. Chem. C*, 2011, **115**, 5207–5219.
41 G. Botelho, I. C. Nogueira, E. Moraes and E. Longo, *Mater. Chem. Phys.*, 2016, **183**, 110–120.
42 M. T. Fabbro, C. Saliby, L. R. Rios, F. A. La Porta, L. Gracia, M. S. Li, J. Andrés, L. P. S. Santos and E. Longo, *Sci. Technol. Adv. Mater.*, 2015, **16**, 65002.
43 M. C. Oliveira, L. Gracia, I. C. Nogueira, M. F. C. Gurgel, J. M. R. Mercury, E. Longo and J. Andrés, *Cryst. Res. Technol.*, 2016, **51**, 634–644.
44 M. C. Oliveira, L. Gracia, I. C. Nogueira, M. F. Do Carmo Gurgel, J. M. R. Mercury, E. Longo and J. Andrés, *Ceram. Int.*, 2016, **42**, 10913–10921.
45 G. S. Silva, L. Gracia, M. T. Fabbro, L. P. Serejo Dos Santos, H. Beltrán-Mir, E. Cordoncillo, E. Longo and J. Andrés, *Inorg. Chem.*, 2016, **55**, 8961–8970.
46 A. F. Gouveia, M. M. Ferrer, J. R. Sambrano, J. Andrés and E. Longo, *Chem. Phys. Lett.*, 2016, **660**, 87–92.
47 T. T. Basiev, A. A. Sobol, Y. K. Voronko and P. G. Zverev, *Opt. Mater.*, 2000, **15**, 205–216.
48 K. T. Lim, G. D. Lee, S.-S. Hong, W. Y. Jung and M. S. Lee, *J. Nanosci. Nanotechnol.*, 2017, **17**, 2751–2755.
49 L. Zhang, D. Bai, M. Zhou and C. Pan, *J. Saudi Chem. Soc.*, 2017, **21**, S275–S282.
50 T. Thongtem, S. Kungwankunakorn, B. Kuntalue, A. Phuruangrat and S. Thongtem, *J. Alloys Compd.*, 2010, **506**, 475–481.
51 V. D. Araújo, R. L. Tranquilin, F. V. Motta, C. A. Paskocimas, M. I. B. Bernardi, L. S. Cavalcante, J. Andres, E. Longo and

M. R. D. Bomio, *Mater. Sci. Semicond. Process.*, 2014, **26**, 425–430.
52 F. A. Kröger and H. J. Vink, *Solid State Phys.*, 1956, **3**, 307–435.
53 F. K. F. Oliveira, M. C. Oliveira, L. Gracia, R. L. Tranquilin, C. A. Paskocimas, F. V. Motta, E. Longo, J. Andrés and M. R. D. Bomio, *J. Phys. Chem. Solids*, 2018, **114**, 141–152.
54 L. S. Cavalcante, J. C. Sczancoski, R. L. Tranquilin, J. A. Varela, E. Longo and M. O. Orlandi, *Particuology*, 2009, **7**, 353–362.
55 L. Tolvaj, K. Mitsui and D. Varga, *Wood Sci. Technol.*, 2011, **45**, 135–146.
56 D. L. Wood and J. Tauc, *Phys. Rev. B: Solid State*, 1972, **5**, 3144–3151.
57 V. S. Marques, L. S. Cavalcante, J. C. Sczancoski, A. F. P. Alcântara, M. O. Orlandi, E. Moraes, E. Longo, J. A. Varela, M. Siu Li and M. R. M. C. Santos, *Cryst. Growth Des.*, 2010, **10**, 4752–4768.
58 V. M. Longo, A. T. De Figueiredo, A. B. Campos, J. W. M. Espinosa, A. C. Hernandes, C. A. Taft, J. R. Sambrano, J. A. Varela and E. Longo, *J. Phys. Chem. A*, 2008, **112**, 8920–8928.
59 G. Botelho, I. C. Nogueira, E. Moraes and E. Longo, *Mater. Chem. Phys.*, 2016, **183**, 110–120.
60 M. F. C. Abreu, F. V. Motta, R. C. Lima, M. S. Li, E. Longo, A. P. de and A. Marques, *Ceram. Int.*, 2014, **40**, 6719–6729.
61 A. A. G. Santiago, C. R. R. Almeida, R. L. Tranquilin, R. M. Nascimento, C. A. Paskocimas, E. Longo, F. V. Motta and M. R. D. Bomio, *Ceram. Int.*, 2018, **44**, 3775–3786.
62 R. Vali, *Comput. Mater. Sci.*, 2011, **50**, 2683–2687.
63 D. A. Spassky, N. S. Kozlova, V. Nagirnyi, A. E. Savon, Y. A. Hizhnyi and S. G. Nedilko, *J. Lumin.*, 2017, **186**, 229–237.
64 Y. Zhang, N. A. W. Holzwarth and R. T. Williams, *Phys. Rev. B*, 1998, **57**, 12738–12750.
65 H. Kadowaki, N. Saito, H. Nishiyama, H. Kobayashi, Y. Shimodaira and Y. Inoue, *J. Phys. Chem. C*, 2006, **111**, 439–444.
66 A. Hofstaetter, R. Oeder, A. Scharmann and D. Sciiwabe, *Phys. Status Solidi B*, 1978, **89**, 375–380.
67 J. C. Sezancoski, M. D. R. Bomio, L. S. Cavalcante, M. R. Joya, P. S. Pizani, J. A. Varela, E. Longo, M. S. Li and J. A. Andrés, *J. Phys. Chem. C*, 2009, **113**, 5812–5822.
68 J. Bi, L. Wu, Y. Zhang, Z. Li, J. Li and X. Fu, *Appl. Catal., B*, 2009, **91**, 135–143.
69 D. A. Spassky, S. N. Ivanov, V. N. Kolobanov, V. V. Mikhailin, V. N. Zemskov, B. I. Zadneprovski and L. I. Potkin, *Radiat. Meas.*, 2004, **38**(4–6), 607–610.
70 J. W. Yoon, J. H. Ryu and K. B. Shim, *Mater. Sci. Eng., B*, 2006, **127**, 154–158.
71 W. S. Wang, L. Zhen, C. Y. Xu and W. Z. Shao, *Cryst. Growth Des.*, 2009, **9**, 1558–1568.
72 X. Pan, M. Q. Yang, X. Fu, N. Zhang and Y. J. Xu, *Nanoscale*, 2013, **5**, 3601–3614.
73 R. A. C. Amoresi, V. Teodoro, G. F. Teixeira, M. S. Li, A. Z. Simões, L. A. Perazolli, E. Longo and M. A. Zaghete, *J. Eur. Ceram. Soc.*, 2018, **38**, 1621–1631.
74 A. Arenas-hernandez, C. Zúñiga-islas and A. Torres-jacome, *Nano Express*, 2020, **1**, 010054, DOI: 10.1088/2632-959X/ab970c.
75 V. M. Longo, A. T. De Figueiredo, S. De Lázaro, M. F. Gurgel, M. G. S. Costa, C. O. Paiva-Santos, J. A. Varela, E. Longo, V. R. Mastelaro, F. S. De Vicente, A. C. Hernandes and R. W. A. Franco, *J. Appl. Phys.*, 2008, **104**, 23515.
76 E. S. Junior, F. A. La Porta, M. S. Liu, J. Andrés, J. A. Varela and E. Longo, *Dalton Trans.*, 2015, **44**(7), 3159–3175.
77 N. Zhang, C. Chen, Z. Mei, X. Liu, X. Qu, Y. Li, S. Li, W. Qi, Y. Zhang, J. Ye, V. A. L. Roy and R. Ma, *ACS Appl. Mater. Interfaces*, 2016, **8**, 10367–10374.
78 R. A. Roca, J. C. Sczancoski, I. C. Nogueira, M. T. Fabbro, H. C. Alves, L. Gracia, L. P. S. Santos, C. P. de Sousa, J. Andrés, G. E. Luz Jr., E. Longo and L. S. Cavalcante, *Catal. Sci. Technol.*, 2015, **5**(8), 4091–4107.
79 H. Chen and Y. Xu, *Appl. Surf. Sci.*, 2014, **319**(1), 319–323.
80 R. A. C. Amoresi, R. C. Oliveira, N. L. Marana, P. B. de Almeida, P. S. Prata, M. A. Zaghete, E. Longo, J. R. Sambrano and A. Z. Simões, *ACS Appl. Nano Mater.*, 2019, **2**, 6513–6526.

Materials Research Bulletin 145 (2022) 111532

Contents lists available at ScienceDirect

Materials Research Bulletin

journal homepage: www.elsevier.com/locate/matresbu

Research Papers

Integrated experimental and theoretical study on the phase transition and photoluminescent properties of ZrO_2:xTb^{3+} (x=1, 2, 4 and 8 mol %)

L.X. Lovisa [g,*], Eduardo O. Gomes [b], Lourdes Gracia [c,f], A.A.G. Santiago [a], M. Siu Li [d], Juan Andrés [b,*], E. Longo [e], M.R.D. Bomio [a], F.V. Motta [a]

[a] LSQM – Laboratory of Chemical Synthesis of Materials – Department of Materials Engineering, Federal University of Rio Grande do Norte, P.O. Box 1524, Natal, RN 59078-900, Brazil
[b] Department de Química Física i Analítica, Universitat Jaume I, Castelló de la Plana 12071, Spain
[c] Department of Physical Chemistry, University of Valencia (UV), Burjassot 46100, Spain
[d] IFSC, USP, Av. Trabalhador São Carlense, 400, CEP, São Carlos, SP 13566-590, Brazil
[e] CDMF-LIEC, UFSCar, P.O. Box 676, São Carlos, SP 13565-905, Brazil
[f] Departament de Química Física i Analítica, Universitat Jaume I, 12071, Castelló de la Plana, Spain
[g] Institute of Physics and Chemistry, Federal University of Itajubá (UNIFEI), Itajubá, MG, 37500-903, Brazil

ARTICLE INFO

Keywords:
ZrO_2: xTb^{3+} (x = 1,2,4 and 8mol%)
Energy transfer
Lighting devices
DFT calculations
Phase transition

ABSTRACT

Zirconia (ZrO_2) has been intensively studied as an important ceramic material, and numerous technological applications have been found. The present work deals with synthesizing and characterizing the phase transition (cubic *vs* tetragonal) and photoluminescence emissions of ZrO_2:xTb^{3+} (x = 1,2,4 and 8 mol%). The samples formed by the complex polymerization were thoroughly characterized for physicochemical properties such powder by X-ray diffraction (XRD), and Raman and diffuse reflectance spectroscopies. First-principle calculations at the density functional theory level were performed to complement and rationalize the experimental results. An energy transfer mechanism which promoted the f-f transitions and emitted strong characteristic emissions of Tb^{3+} is discussed in detail. A ZrO_2 lattice acts as an effective sensitizer and the green light emission and the color purity were controlled by the concentration of the Tb^{3+} cations. Moreover, this study enables us to construct a more consistent picture of the doping process of Tb^{3+} in ZrO_2 and provides a new approach for fabricating a multifunctional material and prospective application in lighting devices.

1. Introduction

Materials composed of rare earth (RE^{3+}) cations have recently garnered renewed attention for use in different technological applications [1–4]. Characteristics of RE^{3+} cations are their emission of narrow and well-defined transitions which extend from the visible-infrared range (f → f type transitions), and enable an expressive number of luminescent properties. In particular, the presence of RE^{3+} cations provide superior performance for high-tech applications in optical and communications devices [5–7].

The Eu^{3+} and Tb^{3+} cations are the most studied activators in the RE^{3+} family with intensive emissions located in the visible region due to the fact they are more resistant to the changes provoked by external structural modifications and vibrations, displaying higher luminescence purity and quantum yields [8]. The Tb^{3+} cation has been widely used for practical applications such as scintillators, phosphors, optical windows and lasers [9–11]. Their luminescent applications are mainly associated to the $^5D_3$ and $^5D_4$ levels of the $4f^8$ configuration of the Tb^{3+} cation [12–15]. These bands usually cover the range from 370 to 680 nm, while the green emissions of Tb^{3+} are mainly located around 550 nm by the $^5D_4 \rightarrow {}^7F_5$ transitions, which is close to the ideal standards required for the green tricolor component [11,16,17].

Zirconia (ZrO_2) is a classic environmentally friendly oxide, presents excellent thermal stability and tunable physicochemical properties [18–21], and its optical properties are strongly affected by the presence of defects [22,23]. ZrO_2 is used as a host matrix of RE^{3+} cations [24] guaranteeing satisfactory energy transfer processes. Crystalline ZrO_2 has a large bandgap (4–6 eV), a high refractive index (2.13–2.20), and a small absorption capacity in the visible and near-infrared spectral regions in combination with low phonon energy (470 cm^{-1}) [25], which

* Corresponding authors.
E-mail addresses: lauraengmat@hotmail.com (L.X. Lovisa), andres@qfa.uji.es (J. Andrés).

https://doi.org/10.1016/j.materresbull.2021.111532
Received 26 February 2021; Received in revised form 19 August 2021; Accepted 19 August 2021
Available online 25 August 2021

reduces the probability of the non-radiative multiphonon relaxation of excited RE^{3+} cations [26–28]. ZrO_2 also exhibits two types of electronic transitions: (i) direct at 5.22 eV; and (ii) indirect at 5.87 eV [29]; and high performance in energy conversion [30, 31]. . The band structure is highly dependent on the crystalline structure, the size of crystallites and the nature of the defects [32,33].

ZrO_2 can exist in three distinct phases at ambient pressure: monoclinic, tetragonal, and cubic. The monoclinic phase is thermodynamically stable at ambient temperatures, whereas tetragonal and cubic polymorphs can be obtained by heat treatment at high temperatures [34, 35], the inclusion of dopant metals with a lower valence into the crystal lattice, and also by increasing the surface energy of nanoparticles [36–39]. The use of dopants [23,40,41] favors stabilizing the cubic and tetragonal phases at room temperature. In addition, changes in the crystal structure and then the morphology of ZrO_2 can also lead to modifications in the excitation and emission spectra. Thus, this subtle difference makes studying phase transition very important. In this context, there is still a lot of space for studies dedicated to understanding the relationship between the luminescence properties of the ZrO_2 systems doped with RE^{3+} cations. Our research groups recently presented a combined experimental and theoretical study on the photoluminescence (PL) properties of ZrO_2:Tm^{3+}, Tb^{3+}, Eu^{3+} powders [24]. Tiwari et al [42] evaluated the change effect in Eu^{3+} concentration on structural, photo, and thermoluminescent properties. Colbea et al. [43] disclosed the relationship between the doping concentration of Eu^{3+} and phase transformation of ZrO_2. Very recently, Liu et al. [44] analyzed the PL properties of Eu^{3+} doped ZrO_2 with different morphologies and crystal structures. Vidya et al [45] investigated the color-adjustable photocatalytic activity and PL emissions, and phase transformation of ZrO_2:Tb^{3+} particles. Hui et al. [46], Marin et al. [47], Ahemen and Dejene [48] and Colbea et al. [43] have disclosed the relationship between the doping concentration of Eu^{3+} and phase transformation of ZrO_2. Furthermore, the influence of calcinating ZrO_2:Tb^{3+} powders on the PL properties was examined by Marí et al. [49]. Das et al. [50] recently studied the synthesis, and structural and PL characterization of ZrO_2:Dy^{3+}-Eu^{3+} as promising material with tunable white light [51].

It is well known that the controllable phase of crystals plays a crucial role in order to meet the optical requirements of the above applications, including the intensity, color and luminescence decay time. In this work, we systematically explore the role of Tb^{3+}as a luminescence enhancer in ZrO_2:Tb^{3+}(x = 1,2,4 and 8 mol%) material. The samples were prepared by the complex polymerization (CP) method and characterized by XRD, and Raman and diffuse reflectance spectroscopies. The relationship among the amount of Tb^{3+} in the ZrO_2 host lattice, PL emissions, and phase composition (cubic *vs* tetragonal) were analyzed in detail for the first time. Changes in the Raman vibrational frequencies associated to lattice structure and phase transition were discussed from the experimental and theoretical results. The geometries, electronic structures and properties of both ZrO_2 and ZrO_2:6% Tb^{3+} systems have been characterized and discussed in relation to their crystal structural by using density functional theory (DFT) calculations.

2. Experimental section

2.1. Materials

Zirconium nitrate (Vetec, 99%), citric acid (Vetec), terbium nitrate (Aldrich, 99.9%), ethylene glycol (Synth, 99.5%) and distilled water were used as received to prepare the ZrO_2:Tb^{3+} particles.

2.2. Experimental process

The samples were prepared by **complex polymerization (CP)** method. In the synthesis process, zirconium citrate was obtained by dissolution of zirconium nitrate (Vetec, 99%) in an aqueous citric acid solution under agitation at an approximate temperature of 80 °C. The Tb^{3+} cations were added for doping after complete dissolution of the zirconium nitrate, and the terbium nitrate was subsequently added (Aldrich, 99.9%). Ethylene glycol was employed to promote citrate polymerization through the polyesterification reaction, and the solution was constantly stirred. The molar ratio between citric acid and ethylene glycol was set to 60/40 (mass ratio). **The ratio of citric acid and metallic cation used in all syntheses was 6 mol% (CA): 1 mol% (Zr^{4+}).** Translucent resin was then formed 4 h after the water removal process. The dopant concentration was varied at 1,2,4 and 8 mol% Tb^{3+}. The polymeric resin was heat treated at 350 °C (10 °C/min) for 4 h, leading to partial decomposition of the polymeric gel and formed an expanded resin composed of partially pyrolyzed material. The particles were annealed at 500 °C for 2 h at a heating rate of 10 °C/ min.

2.3. Sample characterizations

The phases present in the ceramic powder were investigated by X-ray diffraction (XRD) using a Shimadzu XRD-7000 diffractometer with CuKα radiation. The diffraction patterns were analyzed by the general structure analysis system with an EXPGUI graphic interface [52] to perform the Rietveld refinement [53] and analyze the possible structural modifications. The following parameters were refined: scaling factor and phase fraction; background (displaced Chebyshev polynomial function); peak shape (Thomson-Cox-Hasting pseudo-Voigt); change in the network constants; fractional atomic coordinates; and isotropic thermal parameters. Micro Raman spectroscopy measurements were recorded using a *LabRAM HR Evolution spectrometer (Horiba, France)* with a triple monochromator coupled to a charge device detector. **The spectra were performed using a 633 nm wavelength of a He-Ne Laser complemented by argon ion laser,** keeping its maximum output power at 8 mW. **Raman spectroscopy measurements were performed in the range of 100 to 800 cm^{-1}.** The UV-vis reflectance spectra of the ZrO_2:Tb^{3+} particles were measured using Cary 5G equipment in the 200–800 nm range. PL spectra were obtained using a Thermal Jarrell-Ash Monospec 27 monochromator and a Hamamatsu R446 photomultiplier. The excitation source used on the samples was a laser at a wavelength of 350.7 nm with krypton ions (Coherent Innova) with an output of approximately 13.3 mW; all measurements were performed at room temperature.

2.4. Computational details

First-principle calculations at the DFT level were performed by using the Vienna *ab initio* simulation package (VASP). The Kohn-Sham equations were solved by using the Perdew, Burke, and Ernzerhof (PBE) exchange-correlation functional [54], alongside including the effect of long-range interactions using Grimme's D3 semi-classical dispersion methods [55]. The electron-ion interaction was described via the projector-augmented-wave pseudo potentials and the plane-wave expansion was truncated at a cut-off energy of 520 eV. The Brillouin zone was sampled by using 4 × 4 × 4 Monkhorst-Pack special k-point grid to ensure geometrical and energetic convergence of the ZrO_2 structures. Both cubic and tetragonal phases of ZrO_2 undoped and doped at 6% Tb substitution were tested. The valence electron density is defined by 12 ($4s^2 4p^6 5s^2 4d^2$) electrons for Zr atoms, 6 ($2s^2 2p^4$) electrons for O atoms and 19 ($5s^2 5p^6 6s^2 4f^9$) electrons for Tb atoms.

A supercell with 96 atoms was used to simulate an amount of Tb doping up to 6% for both systems, 2 × 2 × 2 and 2 × 2 × 4 for cubic and tetragonal phases, respectively. In addition, a large supercell with 192 atoms was used to simulate an amount of Tb doping up to 3% for both systems, 4 × 2 × 2 and 4 × 4 × 2 for cubic and tetragonal phases, respectively. Two Zr^{4+} were substituted by two Tb^{3+} and an oxygen vacancy was included to maintain the cell as electroneutral. The substitution process of Zr^{4+} by Tb^{3+} cations was done for both phases using structural models. The most energetically favorable arrangement can be selected to analyze theoretically the substitution

process.

The cell parameters and positions of all atoms were allowed to relax, and the conjugated gradient energy minimization method was used to obtain relaxed systems. This was achieved by setting a threshold value (i.e., 0.01 eV·Å^{-1}) for the forces experienced by each atom.

3. Results and discussion

Fig. 1 shows the XRD patterns of the ZrO_2 x mol% Tb^{3+} particles (x = 0,1,2,4 and 8%) prepared by the CP method. **For the analysis of the XRD, the standard powder diffraction cards with reference code JCPDS 81-1544 for tetragonal phase and JCPDS 89-9069 for cubic phase were used.** The Zr^{4+} cations in the tetragonal symmetry are coordinated by eight oxygen atoms, four oxygen atoms at a distance of 0.245 nm, and four other oxygen atoms at a distance of 0.206 nm. The ZrO_2 cubic shows fluorite symmetry, in which the Zr^{4+} cations are coordinated with eight oxygen atoms and the Zr−O bond length is 0.220 nm [35].

The difference between the tetragonal (metastable) and cubic phase based only on the XRD analysis becomes inaccurate because the ratio between the lattice parameters (c / $\sqrt{2}$a) for both phases is similar (≈ 1) [56]. According to Shukla et al [57], this oxygen-induced transition cannot be detected by XRD owing to the small scattering factor of the oxygen atom.

Fig. 2 represents the XRD of samples ZrO_2 and ZrO_2: 8% Tb performed in a scan of 0.02°/min. It is possible to identify changes in the characteristics of the diffraction peaks in the regions between 56 and 64° and between 71 and 76°. It is verified for sample ZrO_2 the presence of the division of the peaks represented by the planes (211) and (202) in 59.76° and 62.65° respectively in Fig. 2 (b) and (004) and (220) in 72.90° and 74.41° respectively in Fig. 2 (d) characteristic of the tetragonal phase. For the ZrO_2: 8%Tb sample, is observed the presence of peaks (311) and (400) located at 59.20° (Fig. 2(c)) and 73.40° (Fig. 2(e)) respectively, characteristic of the cubic phase. There are also peaks not well defined in (202) and (004) located at 62.5° and 72° respectively, attributed to the tetragonal phase. Comparing the peak intensities for the planes (202) and (004) for ZrO_2 and ZrO_2:8% Tb samples, there is a significant decrease in intensity for the ZrO_2:8% Tb samples. The intensity of the plane (202) for ZrO_2 is 0.060, while the intensity of the plane (202) for ZrO_2: 8%Tb decreases to 0.044. The plane intensity (004) for ZrO_2 is 0.016, in contrast the plane intensity (004) for ZrO_2: 8%Tb decreases to 0.009. It is reasonable to assume that

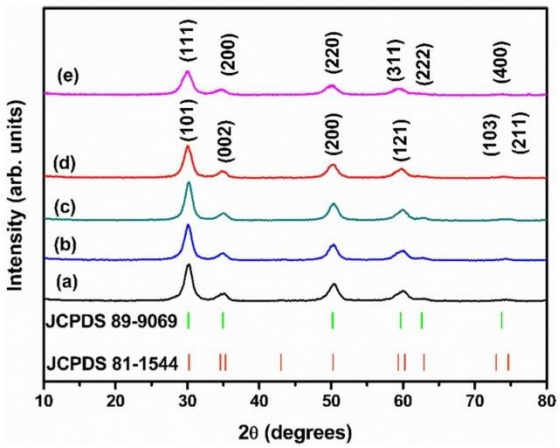

Fig. 1. XRD patterns of ZrO_2: x mol% Tb - (a) x = 0, (b) x = 1, (c) x = 2, (d) x = 4 and (e) x = 8.

at 8% Tb the phase transition from zirconia to the cubic phase is already occurring, coexisting with the tetragonal phase, the latter in smaller amounts. Vasanthavel and Kannan [58] detect the tetragonal - cubic phase transition of itrium doped ZrO_2 observing a gradual change in the peak profile.

Rietveld refinements were performed to confirm the obtained crystalline phase and the lattice parameter values and atomic positions of ZrO_2: x mol% Tb^{3+} (x = 0,1,2,4, and 8%) samples are presented in **Table S1 in the supplementary information. Fig. S1 in the Support Information** shows a schematic representation of the crystalline structures. The size of the sample crystallites was estimated from the Scherrer equation and the full-width half-maximum (FWHM) of an observed peak. The average crystallite size (D) of ZrO_2:Tb^{3+} powders was determined from the strongest peaks corresponding to the (101) tetragonal phase and (111) cubic phase.

Small changes in the lattice parameters were observed between the samples due to the substitution of $Zr^{4+} \rightarrow Tb^{3+}$ in the ZrO_2:Tb^{3+} and as a result a variation in the crystallite size and distortion in the Zr-O bond length. The cell volume increases as the amount of dopant increases due to the ionic radius of Tb^{3+} (1.04 Å) [59] being greater than the ionic radius of Zr^{4+} (0.72 Å) [60].

It is observed that the values of the lattice parameters "*a*" and "*c*" change due to the increase in the concentration of Tb^{3+} in the ZrO_2 lattice and there is no evidence of linearity between these two structural parameters as predicted by Vegard's law [61,62]. This discontinuity can be associated with structural defects and distortions within the ZrO_2 lattice. An analysis of the results renders that a decrease of the *c*/*a* ratio in the tetragonal ZrO_2 lattice can be sensed as the amount of Tb^{3+} increases. **A similar behavior can also be seen in studies [63,64]. Kumar et al. [63] states that the addition of Ce^{4+} to ZrO_2 promoted a reduction in asymmetry in the tetragonal phase. Certifying a decrease in the $c/\sqrt{2}a$ ratio by the influence of Ce^{4+} due to the introduction of oxygen vacancies in the host lattice. The emergence of vacancies is a mechanism to maintain the neutrality of material charges.**

DFT calculations were carried out to investigate the doping process at **3% and 6%** of Tb^{3+} in cubic and tetragonal ZrO_2 phases. The most stable geometries are shown in Figs. 3 and 4.

An optimized structure with Tb^{3+} cations near each other is the most stable atomic arrangement for the cubic phase. Fig. S2 in the supplementary information shows the remaining cubic arrangements studied, displaying less stability. Different Tb^{3+} arrangements show similar energy for the tetragonal phase. The difference between the formation energies of the cubic and tetragonal phases ($\Delta E_{C\text{-}T}$) of ZrO_2, $Zr_{0.97}Tb_{0.03}O_{1.97}$ and $Zr_{0.94}Tb_{0.06}O_{1.94}$ are 0.84 eV, **0.65 eV** and -0.33 eV, respectively. **These results indicate that for pure ZrO_2 and 3% doped-ZrO_2 the tetragonal structure is more stable than cubic structure.** The incorporating 6% Tb^{3+} into the ZrO_2 structure increases the stability of the cubic phase relative to the tetragonal phase, and a more favorable substitution occurs in the cubic polymorph of ZrO_2 as the amount of Tb^{+3} increases. This substitution maintains a structural symmetry in the cubic polymorph (one Tb^{3+} away from each other), as can be seen in Fig. S2, in which a less stable arrangement can be observed, and the phase transition from tetragonal to cubic is not observed.

The difference in the electron density of Zr^{4+} in relation to Tb^{3+} at 6% substitution induces distortion in the crystalline lattice of ZrO_2. In addition, the results presented in Table 1 show that the substitution process provokes a local distortion in both the cubic and tetragonal structures which are both centered on the dopant and located near the oxygen vacancy (V_o), as previously reported [24]. The introduction of Tb^{3+} to the Zr^{4+} site promotes an accumulation of negative charge, with concomitant appearance of oxygen vacancies (V_o) as a load balancing mechanism [45].

The calculated values of the cell parameters at 6% Tb^{+3} are in good agreement with the experimentally determined results **collected in**

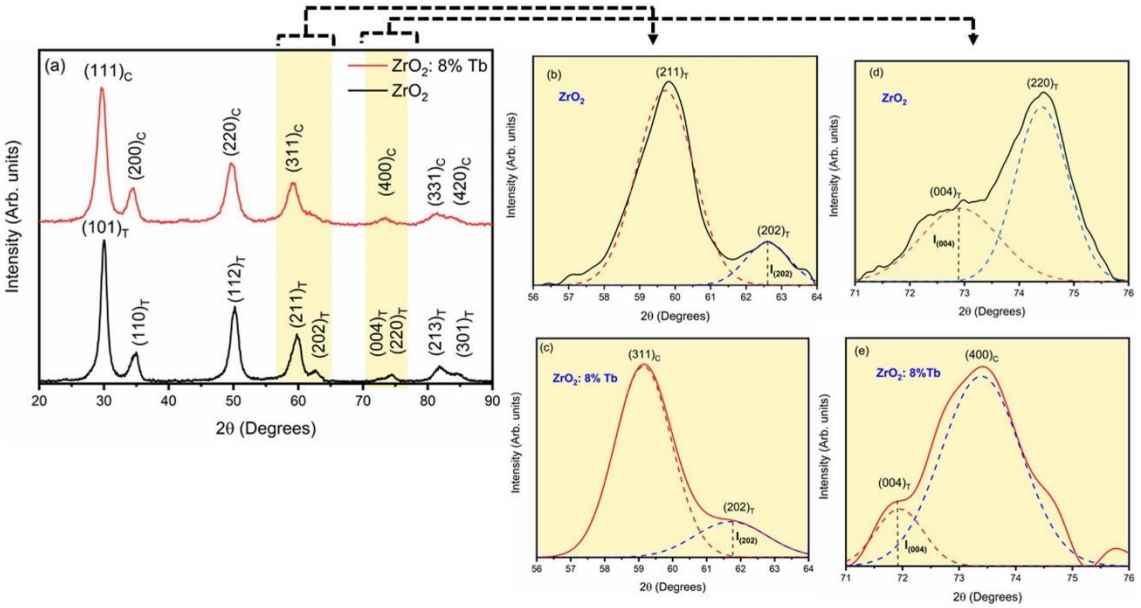

Fig. 2. XRD of ZrO_2 and ZrO_2: 8%Tb samples performed in a scan of 0.02°/min: (a) 2θ = 20–90°; (b) 2θ = 56–64° for ZrO_2; (c) 2θ = 56–64° for ZrO_2: 8%Tb; (d) 2θ = 71–76° for ZrO_2; (e) 2θ = 71–76° for ZrO_2: 8% Tb.

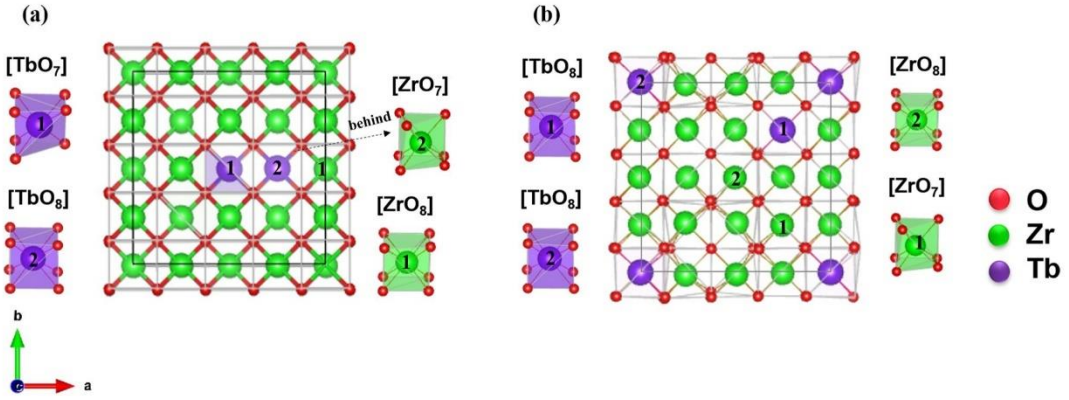

Fig. 3. Cubic structure of ZrO_2: (a) 3% and (b) 6% Tb^{3+}. The cluster coordination of the $[TbO_8]$, $[TbO_7]$, $[ZrO_8]$ and $[ZrO_7]$ are highlighted.

Table S1 (a = 5.254 Å for the cubic phase, and a = 3.651 Å and c = 5.285 Å for the tetragonal phase).

The transformation from the tetragonal phase to the cubic phase as a result of the introduction of Tb^{3+} ions into the ZrO_2 lattice can be observed by analyzing the Raman spectra of Fig. 5. The bands located in the spectra (a–d) of Fig. 5 in: **147, 266, 317, 462 and 640** cm^{-1} are characteristic bands of the tetragonal phase [43,46,50,65]. **The Raman bands associated with the ZrO_2 tetragonal phase are represented by six active modes ($A_{1g} + 2B_{1g} + 3E_g$) [66]. The bands observed at 147, 266 and 462 cm^{-1} are assigned to Eg mode. The bands located at 317 and 640 cm^{-1} refer to the B_{1g} mode. It was not possible to identify the active mode A_{1g} in the Raman spectra.** The Raman E_g (150 cm^{-1}) and B_{1g} (312 cm^{-1}) active modes are associated with the movement of the Zr sublattice. The Raman mode located at 642 cm^{-1} corresponds to the asymmetric bending vibrations of the Zr-O-Zr moiety [67]. In contrast, the cubic phase can be clearly characterized by a relatively wide band between 533 and 664 nm centered on 625 cm^{-1} [65,68]. It is observed that there is a gradual reduction in the tetragonal phase percentage with the increase in the Tb^{3+} concentration. Meanwhile, the cubic phase percentage gradually increases. **A shift of the 625 cm^{-1} band to a smaller region in the ZrO_2: 8%Tb sample is observed when compared to the ZrO_2: x% Tb (x = 0,1,2 and 4) samples which occurs at 640 cm^{-1}. This change in behavior is characteristic of the cubic phase, as evidenced by Vasanthavel et al. [69].**

Shukla et al [57] relate the $E_{g(3)}$ mode in 462 cm^{-1} to the presence of a metastable tetragonal phase of ZrO_2 (t'- ZrO_2). This band is subtly verified in the Raman spectrum of the ZrO_2: 8% Tb sample. Indicating the coexistence of the two phases: cubic (c-ZrO_2) and metastable tetragonal (t'- ZrO_2). The t'- ZrO_2 phase is

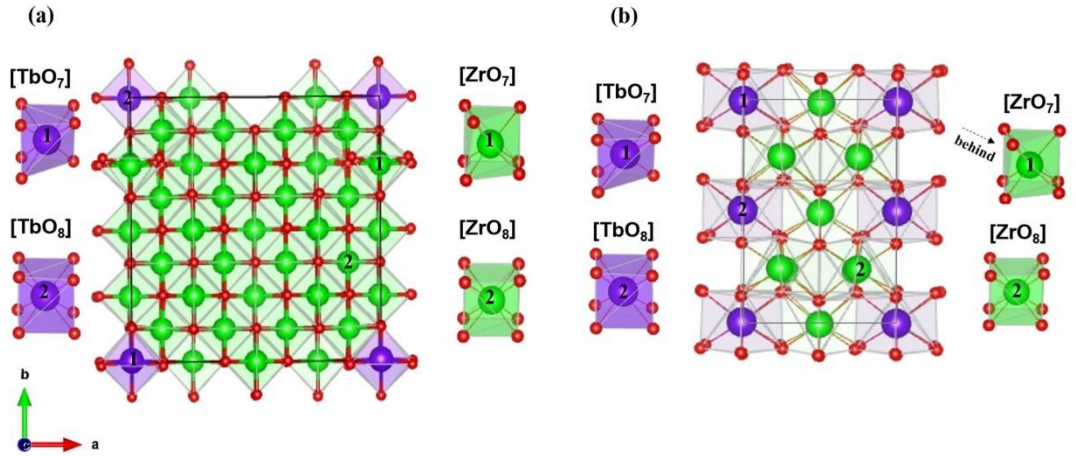

Fig. 4. Tetragonal structure of ZrO_2: (a) 3% and (b) 6% Tb^{3+}. The cluster coordination of the [TbO_8], [TbO_7], [ZrO_8] and [ZrO_7] are highlighted.

Table 1
Zr-O and Tb-O distance values at 6% Tb^{3+} substitution in the cubic and tetragonal ZrO_2 structures.

Cubic_6%			Tetragonal_6%		
Atom	Coord.	Bonds (Å)	Atom	Coord.	Bonds (Å)
Zr1	7	2.180	Zr1	7	2.334
		2.190			2.063
		2.142			2.063
		2.164			2.042
		2.176			2.400
		2.106			2.074
		2.159			2.400
Zr2	8	2.173	Zr2	8	2.155
		2.209			2.512
		2.224			2.155
		2.214			2.484
		2.179			2.345
		2.217			2.077
		2.335			2.345
		2.214			2.073
Tb1	8	2.312	Tb1	7	2.281
		2.326			2.348
		2.290			2.281
		2.289			2.245
		2.294			2.348
		2.309			2.209
		2.326			2.348
		2.312			-
Tb2	8	2.326	Tb2	8	2.351
		2.462			2.294
		2.352			2.352
		2.324			2.294
		2.298			2.326
		2.326			2.347
		2.324			2.470
		2.315			2.347

characterized by having a distorted shape of the cubic phase. Although, the relation of the lattice parameters ($c/\sqrt{2}a \rightarrow 1$) are similar in both phases; in the t'- ZrO_2 phase, the oxygen ions are shifted alternately (zigzag aspect) along the *z* axis, assuming tetragonal symmetry [57]. Fujimori et al. [70,71] describe the structural evolutions of ZrO_2 by measuring the displacements of oxygen ions on the *z* axis considering the relationship of the intensity of the bands $E_{g(3)}$ (462 cm^{-1}) and B_{1g} (640 cm^{-1}) named, respectively, by I_4 and I_5 in Fig. 6.

Fig. 6 shows the changes registered in the bands $E_{g(3)}$ (462 cm^{-1}) and B_{1g} (640 cm^{-1}) in the Raman spectra in the range of 350 to 800 cm^{-1} for the samples: ZrO_2, ZrO_2: 4% Tb and ZrO_2: 8% Tb. Spectrum adjustments were made from the Lorentzian profile ($R^2 = 0.99$). The ratio of the intensity of the I_4/I_5 bands to ZrO_2, ZrO_2: 4% Tb and ZrO_2: 8% Tb are 0.558, 0.403 and 0.130 respectively. The effect of increasing the concentration of Tb^{3+} in ZrO_2 promotes a decrease in the I_4/I_5 ratio. Considering a decrease in the displacement of the oxygen ion along the *z* axis within the unit cell, and as a consequence, a reduction in tetragonality. According to the results presented, it is reasonable to consider that the majority phase for ZrO_2: 8% Tb is cubic. The active Raman modes for the crystal structures of ZrO_2 are shown in Table 2. At this point, it is important to note that the cubic and tetragonal phases of ZrO_2 present similar XRD diffraction peaks, and therefore the relative fraction of each phase along the samples cannot obtained.

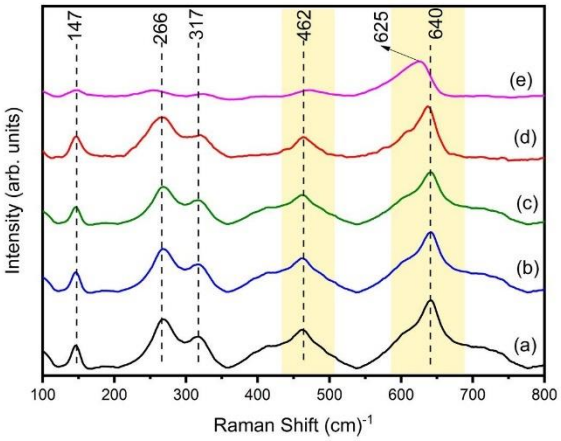

Fig. 5. Raman spectra of: (a) pure ZrO_2 (tetragonal phase); (b) ZrO_2:1 mol% Tb^{3+} (tetragonal phase), (c) ZrO_2:2 mol% Tb^{3+}, (d) ZrO_2:4 mol% Tb^{3+} (tetragonal phase), (e) ZrO_2:8 mol% Tb^{3+} (cubic phase + t'- ZrO_2).

According to Jomard et al. [72], the cubic structure is a special case of the tetragonal structure and can be obtained from it, making the ratio of the lattice constants **$c/\sqrt{2}\,a \rightarrow 1$**. This statement is in accordance with the values **($c/\sqrt{2}\,a$)** presented in **Table S1**. In the transformation of the

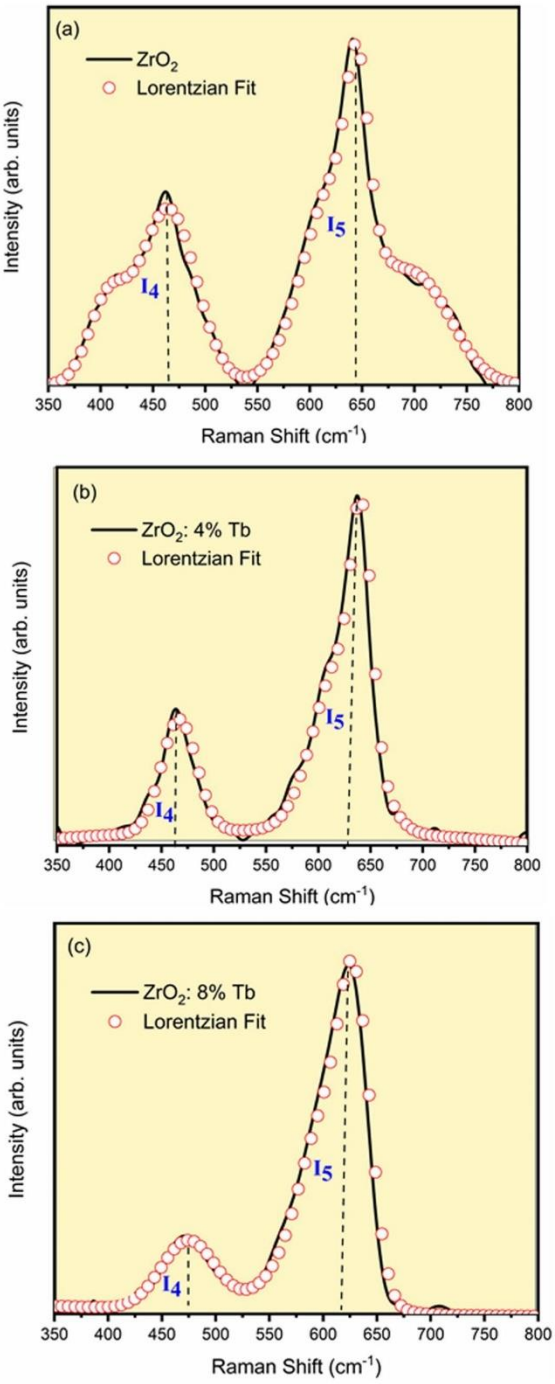

Fig. 6. Raman spectrum in the range 350 to 800 cm^{-1}. Evaluation of structural changes; ratio of I_4/I_5 intensities.

Table 2
Raman active mode, space group of the different ZrO_2 phases.

Crystalline system	Space group	Raman modes	c/a ratio
Monoclinic (*m*)	C_{2h}	$9A_g + 9B_g$	-
Tetragonal (*t*)	D_{4h}	$A_{1g} + 2B_{1g} + 3E_g$	> 1
Cubic (*c*)	O_h	T_{2g}	= 1

tetragonal → cubic phases, the pairs of oxygen atoms are displaced from the z direction to their central positions in the unit cell [72]. The fundamental difference in the zirconia phase structure is due to the displacements of oxygen atoms in the lattices. The doping effect is important to determine the stabilization of the ZrO_2 phases. According to Tiseanu et al. [67], the main structural difference between the zirconia phases refers to the displacements of oxygen atoms in the lattices, thus signaling that the importance for local atomic structure is fundamental for understanding the effect of doping process on ZrO_2.

However, Wang et al. [73] show that the location and concentration of oxygen vacancies in yttria-stabilized zirconia can be determined by measuring atomic displacements of the cationic sub-lattice. According to the DFT calculations performed by the group, the alternating presence of oxygen vacancies in the locations (1/4, 1/4, 1/4) and (1/4, 3/4, 1/4) along the direction [001] that promotes the atomic displacements of the cationic sub-lattice. The cation displacements from the ideal face-centered cubic (FCC) sites are related to the relaxation of the neighboring cations away from the vacancies. When an oxygen vacancy is created, the neighboring cations will repel each other because of Coulombic interactions, thereby resulting in larger distance between cátions [73].

Theoretical calculations of the Raman-active modes of pure tetragonal ZrO_2 yielded values of 149.4, 294.2, 301.5, 453.6, 611.5, and 650.9 cm^{-1} for the E_g, A_{1g}, B_{1g}, E_g, B_{1g}, and E_g modes, respectively. The case of pure cubic ZrO_2 (a unique mode which has T_{2g} symmetry) occurs at a wavenumber of 600.7 cm^{-1}. These values agree with previous values reported by our research group [24].

The band gap energy (E_{gap}) of the ZrO_2:x mol% Tb^{3+} sample was estimated from the Uv-visible measurements by plotting the square of the Kubelka-Munk function $[F(R)^2]$ versus (eV), extrapolating the linear part of the curve to the condition of $F(R)^2 = 0$ [74], according to Eq. (1):

$$F(R) = \frac{k}{s} = \frac{(1-R)^2}{2R} \quad (1)$$

where R is the percentage of reflected light. The incident photon energy ($h\nu$) and the gap energy (E_{gap}) are related to the transformed Kubelka-Munk function (2):

$$[F(R)h\nu]^n = A(h\nu - Egap) \quad (2)$$

where *A* is a constant which depends on the probability of the transition and *n* is the index that is related to the optical absorption process. We can then assume the following values: ½ or 2 for direct and indirect allowed transitions, respectively. The transition in the case of ZrO_2 is considered to be the direct type. It is necessary to observe the energy conservation in the crystal for a material to have direct electronic transitions. This condition is reached when the valence band (VB) maximum and the conduction band (CB) minimum are positioned in the same symmetry region of the solid. It is observed that the gap energy decreases as the Tb^{3+} concentration increases as the E_{gap} values remained between 5.11 and 4.92 eV, as shown in Fig. 7.

The effect of the band gap narrowing due to the doping process is well known in semiconductors [75]. This phenomenon happens due to the presence of defects inside the band gap which promotes the appearance of intermediate levels. **Oxygen vacancies appear to compensate for the Zr^{4+} ions replaced by Tb^{3+} ions. Due to the difference in charge of cations, oxygen waves are formed as a mechanism for charge neutrality in the material. The defect reaction equation can be described in the following Eq. 3:**

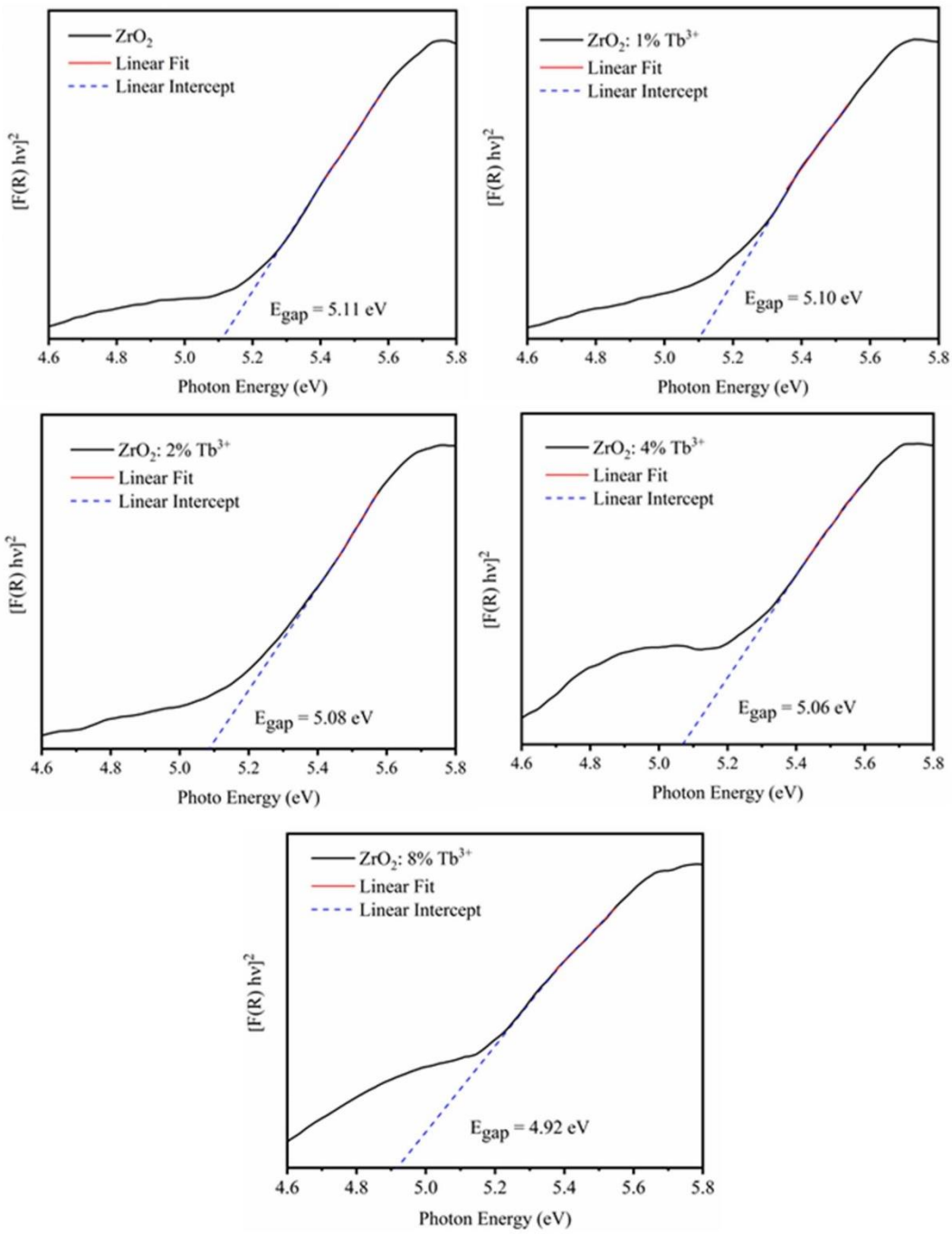

Fig. 7. Determination of the band gap for ZrO_2: x mol% Tb^{3+} (x = 0,1,2,4 and 8).

[41] F. Goumrhar, L. Bahmad, O. Mounkachi, A. Benyoussef, Ferromagnetism in Mn and Fe doped ZrO_2 by ab-initio calculations, Comput. Condens. Matter 19 (2019) 00361.
[42] N. Tiwari, R.K. Kuraria, S.R. Kuraria, Effect of variable trivalent europium concentration on photo- and thermoluminescence of zirconium dioxide nanophosphors, Mater. Sci. Semicond. Process 31 (2015) 214.
[43] C. Colbea, D. Avram, B. Cojocaru, R. Negrea, C. Ghica, V.G. Kessler, G. A. Seisenbaeva, V.I. Parvulescu, C. Tiseanu, Full tetragonal phase stabilization in ZrO_2 nanoparticles using wet impregnation: Interplay of host structure, dopant concentration and sensitivity of characterization technique, Nanomaterials 8 (2018) 988.
[44] D. Liu, M. Wang, L. Gong, J. Zhao, M. Zhu, X. Wang, Photoluminescence properties of Eu^{3+} doped ZrO_2 with different morphologies and crystal structures, J. Alloys Compd. 864 (2021), 158781.
[45] Y.S. Vidya, H.Nagabhushana K.G., S.C. Sharma, K.S. Anantharaju, C. Shivakumara, D. Suresh, H.P. Nagaswarupa, S.C. Prashantha, M.R. Anilkumar, Phase transformation of ZrO_2:Tb^{3+} nanophosphor: Color tunable photoluminescence and photocatalytic activities, J. Alloys Compd. 622 (2015) 86.
[46] Y. Hui, S. Zhao, J. Xu, L. Zhu, X. Zhou, B. Zou, Y. Wang, X. Cao, Doping concentration of Eu^{3+} as a fluorescence probe for phase transformation of zirconia, J. Rare Earths 33 (2015) 717.
[47] R. Marin, G. Sponchia, E. Zucchetta, P. Riello, F. Enrichi, G. De Portu, A. Benedetti, Monitoring the t → m martensitic phase transformation by photoluminescence emission in Eu^{3+}-doped zirconia powders, J. Am. Ceram. Soc. 96 (2013) 2628.
[48] I. Ahemen, F.B. Dejene, Effect of Eu^{3+} ion concentration on phase transition, site symmetry and quantum efficiency of ZrO_2 nanocrystal rods, J. Nanosci. Nanotechnol. 18 (2018) 2129.
[49] B. Marí, K.C. Singh, M. Sahal, S.P. Khatkar, V.B. Taxak, M. Kumar, Preparation and luminescence properties of Tb^{3+} doped ZrO_2 and $BaZrO_3$ phosphors, J. Lumin. 130 (2010) 2128.
[50] S. Das, C.Y. Yang, C.H. Lu, Structural and optical properties of tunable warm-white light-emitting ZrO_2:Dy^{3+}–Eu^{3+} nanocrystals, J. Am. Ceram. Soc. 96 (2013) 1602.
[51] S.D. Meetei, S.D. Singh, Hydrothermal synthesis and white light emission of cubic ZrO_2:Eu^{3+} nanocrystals, J. Alloys Compd. 587 (2014) 143.
[52] B. Toby, EXPGUI, a graphical user interface for GSAS, J. Appl. Crystallogr. 34 (2001) 210–213.
[53] H. Rietveld, A profile refinement method for nuclear and magnetic structures, J. Appl. Crystallogr. 2 (1969) 65–71.
[54] J.P. Perdew, M. Ernzerhof, K. Burke, Rationale for mixing exact exchange with density functional approximations, J. Chem. Phys. 105 (1996) 9982.
[55] S. Grimme, A. J., S. Ehrlich, H. Krieg, A consistent and accurate ab initio parametrization of density functional dispersion correction (DFT-D) for the 94 elements H-Pu, J. Chem. Phys. 132 (2010), 154104.
[56] S.N Basahel, T.T. Al, M. Mokhtar, K. Narasimharao, Influence of crystal structure of nanosized ZrO_2 on photocatalytic degradation of methyl orange, Nanoscale Res. Lett. 10 (2015) 73.
[57] V. Shukla, K. Balani, A. Subramaniam, S. Omar, Effect of thermal aging on the phase stability of $1Yb_2O_3$–xSc_2O_3– (99 −<x)ZrO_2 (x = 7, 8 mol %), J. Phys. Chem. C 123 (2019) 21982.
[58] S. Vasanthavel, S. Kannan, Structural investigations on the tetragonal to cubic phase transformations in zirconia induced by progressive yttrium additions, J. Phys. Chem. Solids 112 (2018) 100–105.
[59] B. Peng, K. Song, S. Zhang, S. Shen, J. Xu, J. Wu, W. Su, Color-tunable light emission of $SrLa_{4-x-y}Si_3O_{13}$:xTb^{3+}, yEu^{3+} phosphors by energy transfer process for warm white LEDs, AIP Adv. 8 (2018), 015119.
[60] N.N. Sarkar, K.G. Rewatkar, V.M. Nanoti, N.T. Tayade, D.S. Bhowmick, Structural and magnetic study of Zr^{4+} substituted magnesium ferrite nano-particles, J. Phys. Sci. 22 (2017) 107.
[61] M.J. McKelvy, R. Sharma, A.V.G. Chizmeshya, R.W. Carpenter, K. Streib, Magnesium hydroxide dehydroxylation: *in situ* nanoscale observations of lamellar nucleation and growth, Chem. Mater. 13 (2001) 921.
[62] F.V. Motta, A.P.A. Marques, M.S. Li, M.F.C. Abreu, C.A. Paskocimas, M.R.D. Bomio, R.P. Souza, J.A. Varela, E. Longo, Preparation and photoluminescence characteristics of $In(OH)_3$:xTb^{3+} obtained by Microwave-Assisted Hydrothermal method, J. Alloys Compd. 533 (2013) 338.
[63] A. Kumar, A. Jaiswal, M. Sanbui, S. Omar, Oxygen-ion conduction in scandia-stabilized zirconia-ceria solid electrolyte (xSc_2O_3–$1CeO_2$–$(99-x)ZrO_2$, $5 \leq x \leq 11$), J. Am. Ceram. Soc. 100 (2017) 659–668.
[64] A. Kumar, A. Jaiswal, M. Sanbui, S. Omar, Scandia stabilized zirconia-ceria solid electrolyte (xSc1CeSZ, $5 < x < 11$) for IT-SOFCs: structure and conductivity studies, Scr. Mater. 121 (2016) 10–13.
[65] C.G. Kontoyannis, M. Orkoula, Quantitative determination of the cubic, tetragonal and monoclinic phases in partially stabilized zirconias by Raman spectroscopy, J. Mater. Sci. 29 (1994) 5316.
[66] P. Bouvier, H.C. Gupta, G. Lucazeau, Zone center phonon frequencies in tetragonal zirconia: lattice dynamical study and new assignment proposition, J. Phys. Chem. Solids 62 (2001) 873–879.
[67] C. Tiseanu, V.I. Parvulescu, B. Cojocaru, K. Pemartin, M. Sanchez-Dominguez, M. Boutonnet, *In situ* Raman and time-resolved luminescence investigation of the local structure of ZrO_2 in the amorphous to crystalline phase transition, J. Phys. Chem. C 116 (2012) 16776.
[68] C.N. Chervin, B.J. Clapsaddle, H.W. Chiu, A.E. Gash, J.H. Satcher Jr, S. M. Kauzlarich, Aerogel synthesis of yttria-stabilized zirconia by a non-alkoxide sol-gel route, Chem. Mater. 17 (2005) 3345–3351.
[69] S. Vasanthavel, B. Derby, S. Kannan, Tetragonal to cubic transformation of SiO_2 stabilized ZrO_2 polymorph through dysprosium substitutions, Inorg. Chem. 56 (2017) 1273–1281.
[70] H. Fujimori, M. Yashima, M. Kakihana, M. Yoshimura, Structural changes of scandia-doped zirconia solid solutions: rietveld analysis and Raman scattering, J. Am. Ceram. Soc. 81 (1998) 2885.
[71] M. Yashima, K. Ohtake, M. Kakihana, H. Arashi, M. Yoshimura, Determination of tetragonal-cubic phase boundary of $Zr_{1-x}R_xO_{2-x/2}$ (R= Nd, Sm, Y, Er and Yb) By Raman scattering, J. Phys. Chem. Solids 57 (1996) 17.
[72] G. Jomard, T. Petit, A. Pasturel, L. Magaud, G. Kresse, J. Hafner, First-principles calculations to describe zirconia pseudopolymorphs, Phys. Rev. B 59 (1999) 4044.
[73] Y. Wang, C. Cai, L. Li, L. Yang, Y. Zhou, G. Zhou, Oxygen vacancy ordering induced displacements of cations in yttria-stabilized zirconia, AIP Adv. 6 (2016), 095113.
[74] P. Kubelka, K. Munk, Ein beitrag zur optik der farbanstriche, Z. Für Tech. Phys. 12 (1931) 593.
[75] V. Kumar, V.Kumar S.Som, V. Kumar, O.M. Ntwaeaborwa, E. Coetsee, H.C. Swart, Tunable and white emission from ZnO:Tb^{3+} nanophosphors for solid state lighting applications, Chem. Eng. J. 255 (2014) M541.
[76] R. Nedzinskas, B. Čechavičius, V. Karpus, J. Kavaliauskas, G. Valušis, L.H. Li, S. P. Khanna, E.H. Linfield, Photoreflectance and photoluminescence studies of epitaxial InGaAs quantum rods grown with As_2 and As_4 sources, J. Appl. Phys. 109 (2011), 123526.
[77] E. Longo, D.P. Volanti, V.M. Longo, I.C.Nogueira L.G.racia, M.A.P. Almeida, A. N. Pinheiro, M.M. Ferrer, L.S. Cavalcante, J. Andreś, Toward an understanding of the growth of Ag filaments on α-Ag_2WO_4 and their photoluminescent properties: a combined experimental and theoretical study, J. Phys. Chem. C 118 (2014) 1229.
[78] K. Hachiya, H. Oku, J. Kondoh, Photoluminescence in yttria stabilized zirconia of aging effects, Phys. Rev. B 71 (2005), 064111.
[79] V.M. Longo, L.S. Cavalcante, A.T. de Figueiredo, L.P.S. Santos, et al., Highly intense violet-blue light emission at room temperature in structurally disordered $SrZrO_3$ powders, Appl. Phys. Lett. 90 (2007), 091906.
[80] V.M. Longo, L.S. Cavalcante, R. Erlo, V.R. Mastelaro, et al., Strong violet–blue light photoluminescence emission at room temperature in $SrZrO_3$: joint experimental and theoretical study, Acta Mater. 56 (2008) 2191.
[81] K. Smits, L. Grigorjeva, D. Millers, A. Sarakovskis, J. Grabis, W. Lojkowski, Intrinsic defect related luminescence in ZrO_2, J. Lumin. 131 (2011) 2058.
[82] M. Boffelli, W. Zhu, M. Back, G. Sponchia, T. Francese, P. Riello, A. Benedetti, G. Pezzotti, Oxygen hole states in zirconia lattices: quantitative aspects of their cathodoluminescence emission, Phys. Chem. A 118 (2014) 9828.
[83] R. Martínez-Martínez, G. Juárez-López, M. García-Hipólito, J.J. Bautista Díaz, S. C. Téllez, M.A. Aguilar-Frutis, G.A. Flores, C. Falcony, Blue and bluish-white colors from the luminescent ZrO_2 and ZrO_2: Al^{3+} films prepared by the USP method, Mater. Res. Express 8 (2021), 016201.
[84] P.F.S. Pereira, C.C.S., A.F. Gouveia, M.M. Ferrer, I.M. Pinatti, G. Botelho, J. R. Sambrano, I.L.V. Rosa, J. Andres, E. Longo, α-$Ag_{2-2x}Zn_xWO_4$ ($0 \leq x \leq 0.25$) Solid solutions: structure, morphology, and optical properties, Inorg. Chem. 56 (2017) 7360.
[85] N.G. Petrik, D.P. Taylor, T.M. Orlando, Laser-stimulated luminescence of yttrias-tabilized cubic zirconia crystals, J. Appl. Phys. 85 (1999) 6770.
[86] R. Devanathan, W.J. Weber, S.C. Singhal, J.D. Gale, Computer simulation of defects and oxygen transport in yttrias-tabilized zirconia, Solid State Ion. 177 (2006) 1251.
[87] S. Lis, Factors affecting Luminescence intensity of lanthanide ions analytical apllications of lanthanide luminescence in solution, Acta Phys. Polon. A 84 (1993) 1003.
[88] J.C.G. Bunzli, G.R. Choppin, Lanthanide Probes in Life, Chemical and Earths Sciences, Elsevier, Amsterdam, 1989. Chap. 7.
[89] G. Blasse, Energy transfer between inequivalent Eu^{2+} ions, J. Solid State Chem. 62 (1986) 207.
[90] F. Kang, Y. Zhang, M. Peng, Controlling the energy transfer via multi luminescent centers to achieve white light/tunable emissions in a single-phased X2-type Y_2SiO_5: Eu^{3+},Bi^{3+} phosphor for ultraviolet converted LEDs, Inorg. Chem. 54 (2015) 1462.
[91] Y.F. Wu, Y.T. Nien, Y.J. Wang, I.G. Chen, Enhancement of photoluminescence and color purity of $CaTiO_3$:Eu phosphor by Li doping, J. Am. Ceram. Soc. 95 (2012) 1360.

Journal Pre-proof

Photoluminescence emissions of $Ca_{1-x}WO_4:xEu^{3+}$: Bridging between experiment and DFT calculations*

Amanda Fernandes Gouveia, Marcelo Assis, Lara Kelly Ribeiro, Aline Estefany Brandão Lima, Eduardo de Oliveira Gomes, Daniele Souza, Yara Gobato Galvão, Ieda Lucia Viana Rosa, Geraldo Eduardo da Luz, Jr., Eva Guillamón, Elson Longo, Juan Andrés, Miguel Angel San-Miguel

PII: S1002-0721(21)00240-4

DOI: https://doi.org/10.1016/j.jre.2021.08.023

Reference: JRE 1095

To appear in: *Journal of Rare Earths*

Received Date: 28 May 2021

Revised Date: 9 August 2021

Accepted Date: 30 August 2021

Please cite this article as: Gouveia AF, Assis M, Ribeiro LK, Brandão Lima AE, de Oliveira Gomes E, Souza D, Galvão YG, Viana Rosa IL, da Luz GE Jr, Guillamón E, Longo E, Andrés J, San-Miguel MA, Photoluminescence emissions of $Ca_{1-x}WO_4:xEu^{3+}$: Bridging between experiment and DFT calculations*, *Journal of Rare Earths*, https://doi.org/10.1016/j.jre.2021.08.023.

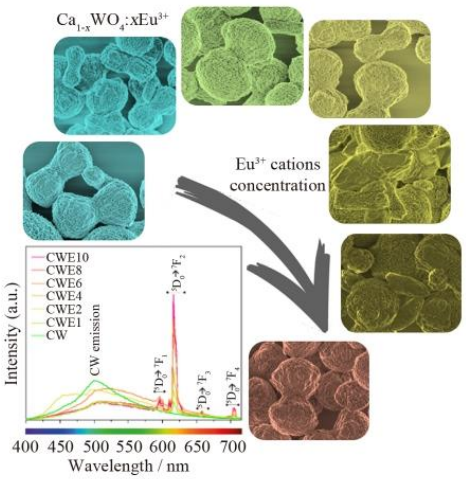

Photoluminescence emissions of $Ca_{1-x}WO_4:xEu^{3+}$: Bridging between experiment and DFT calculations*

Amanda Fernandes Gouveia[a,b,*], Marcelo Assis[a,c], Lara Kelly Ribeiro[c], Aline Estefany Brandão Lima[d], Eduardo de Oliveira Gomes[b], Daniele Souza[e], Yara Gobato Galvão[e], Ieda Lucia Viana Rosa[c], Geraldo Eduardo da Luz Jr[d], Eva Guillamón[a], Elson Longo[c], Juan Andrés[a,*], Miguel Angel San-Miguel[b]

[a]Department of Physical and Analytical Chemistry, University Jaume I (UJI), 12071Castelló, Spain.
[b]Institute of Chemistry, State University of Campinas (Unicamp), 13083-970 Campinas, SP, Brazil.
[c]CDMF, Federal University of São Carlos (UFSCar), P.O. Box 676, 13565-905, São Carlos, São Paulo, Brazil.
[d]Departamento de Química, State University of Piauí (UFPI), 64049-550 Teresina, Piauí, Brazil.
[e]Physics Department, Federal University of São Carlos (UFSCar), P.O. Box 676, 13565-905, São Carlos, São Paulo, Brazil.

ABSTRACT

In this work, the impact of the doping process on the photoluminescence emission of $CaWO_4$ as a function of the concentration of Eu^{3+} cation (0.01 mol%, 0.02 mol%, 0.04 mol%, 0.06 mol%, 0.08 mol%, and 0.10 mol%) is discussed in detail. $Ca_{1-x}WO_4:xEu^{3+}$ samples were successfully synthesized by a simple co-precipitation method followed by microwave irradiation. The blue shift in the absorption edge confirmed the quantum confinement effect and the band gap energy cover the range from 3.91 to 4.18 eV, as the amount of Eu^{3+} cations increases. The experimental results are sustained by first-principles calculations, at the density functional theory level, to decipher the geometry and electronic properties, thereby enabling a more accurate and direct comparison between theory and experiment for the $Ca_{1-x}WO_4:xEu^{3+}$ structure.

* Corresponding author. gouveiad@uji.es

Foundation item: Project supported in part by Fundação de Amparo à Pesquisa do Estado de São Paulo - FAPESP (2013/07296-2; 2016/23891-6; 2017/26105-4; 2019/01732-1), Financiadora de Estudos e Projetos - FINEP, Conselho Nacional de Desenvolvimento Científico e Tecnológico – CNPQ (166281/2017-4, 305792/2020-2), and CAPES.

Keywords: $Ca_{1-x}WO_4:xEu^{3+}$; DFT calculations; photoluminescence emissions; rare earths.

1. Introduction

The high chemical stability of $CaWO_4$ (CW)-based phosphors and the excellent photoluminescence (PL) emissions have attracted a lot of attention due to the ability to serve as a luminescence host with low phonon threshold energy and wide visible emission spectra [1-6].

Lanthanide luminescence has become essential in the lighting industry [7], and the Eu^{3+} cations are the most studied activators in the rare-earth cations (RE^{3+}) family with intense emissions located in the visible region, displaying higher luminescence purity and quantum yields [8-13]. The substitution of Ca^{2+} by Eu^{3+} cations leads to the formation of [EuO_8] clusters. $Ca_{1-x}WO_4$:xEu^{3+} (CWE) doped materials have been obtained through different synthesis methods. Zhang et al. analyzed the effect of synthesis conditions, such as pH, temperature, and doping concentrations, in the morphology and sizes of CWE [14]. Xiong et al. prepared CWE nanoparticles with excellent load-carrying capacity, and friction-reducing properties in a water-soluble [15]. Very recently, the precipitation route to obtain CW nanoparticles containing Eu^{3+} and Dy^{3+} cations were used by Kaur et al. [16].

The changes induced by the addition of Eu^{3+} cations in different concentrations in the CW host matrix increase their performance, due that this material has numerous scientific and technological applications, such as light-emitting diodes converted into phosphors, sensors, capacitors, catalysts and others [15,17-19]. In particular, the CWE samples were previously obtained with different concentration of Eu^{3+} cation and the PL properties as well as the chromaticity coordinates and lifetimes of the samples were investigated [20].

This paper reports a combined experimental and theoretical work to investigate the events that occur in the PL activity and their relationship with the excited electronic states of Eu-doped CW crystals. The main novelty of this study is the use of first-principles quantum-mechanical calculations, at the density functional theory (DFT) level, to study and predict the structure and PL emissions, which would promote the development of CWE based phosphors. The samples were prepared by a simple co-precipitation (CP) method followed by microwave irradiation (MI) without any surfactant. This enabled to be promising materials in inorganic single-emitting component regions for optical applications.

2. Experimental and theoretical procedure

2.1. Synthesis and Characterizations

The synthesis of CW sample was performed using the CP method followed by MI. 1×10^{-3} mol of $Ca(CH_3CO_2)_2\cdot H_2O$ (Aldrich, 99%) and 1×10^{-3} mol of $Na_2WO_4\cdot 2H_2O$ (Aldrich, 99%) were added in two separate beakers containing 50.0 mL of distilled water each. The $Ca(CH_3CO_2)_2\cdot H_2O$ solution was then added to the $Na_2WO_4\cdot 2H_2O$ solution, and the suspension were transferred to a Teflon autoclave, sealed, and placed in the microwave

assisted hydrothermal system (2.45 GHz, maximum power of 800 W). The reaction mixture was heated to 160 °C for 32 min. The products were washed with deionized water several times and dried at 60 °C for 12 h.

For the CWE samples, the same procedure describe above was done with the addition of 0.01 mol%, 0.02 mol%, 0.04 mol%, 0.06 mol%, 0.08 mol%, and 0.10 mol% of Eu^{3+} and the removed of the corresponding Ca^{2+} mass. The reagent used was Eu_2O_3 (Aldrich, 99.9%) dissolved in water from the addition of HNO_3. The doped samples were called by: CWE1, CWE2, CWE4, CWE6, CWE8, and CWE10 for 0.01 mol%, 0.02 mol%, 0.04 mol%, 0.06 mol%, 0.08 mol%, and 0.10 mol% Eu^{3+}, respectively.

The CW and CWE samples were structurally characterized by different techniques such as: X-ray diffraction (XRD) with Rietveld refinement analysis, field emission scanning microscopy (FE-SEM), and spectroscopies of micro-Raman (MR) and Fourier Transform Infrared (FT-IR), ultraviolet-visible (UV-Vis) absorption, energy dispersive (EDS), X-ray photoelectron (XPS), and X-ray fluorescence (XRF).

The XRD using a D/Max-2500PC diffractometer (Rigaku, Japan) with CuK α radiation (λ = 0.15406 nm) in the 2θ range of 10°–110° with a scanning speed of 1 (°)/min. FE-SEM and EDS were performed using an equipment Inspect F50 (FEI Company, Hillsboro, OR), operated at 15 kV. UV-vis diffuse reflectance measurements were obtained using a Cary 5G spectrophotometer (Varian, USA) in diffuse reflection mode. The MR spectra were obtained by the Micro Raman spectrometer (HORIABA Jobin Yvon T64000) with a radiation of 514 nm in the 50–3500 cm^{-1} range. The FT-IR was performed using a Jasco FT/IR-6200 (Japan) spectrophotometer operated in turn mode at room temperature and the spectra were carried out in the range of 470–4000 cm^{-1}. A Kimmon He-Cd laser (325 nm laser; 40 mW maximum power) was used as the excitation source for PL measurements. XPS analyses were performed on a Scientia Omicron ESCA spectrometer (Germany) using a monochromatic X-ray source of Al Kα (1486.7 eV). Peak deconvolution was performed using a 70%:30% Gaussian-Lorentzian line shape and a Shirley nonlinear sigmoid-type baseline. The binding energies of all elements were calibrated with reference to the C 1s peak at 284.8 eV. Element analysis of the samples was performed an XRF 720 (Shimadzu Corp, Kyoto, Japan) operating at 4 kV and 80 mA. The luminescence lifetime measurements were carried out as well using a 1940D model spectrophotometer coupled to the spectrofluorometer.

2.2. Computational Methods

First-principles calculations were performed to study the effect of Eu-doped in the $CaWO_4$ structure. In this way, two models were constructed, the pure CW and CWE. All calculations were performed with the CRYSTAL17 software package [21, 22]. The CRYSTAL package performs *ab initio* calculations of the ground state energy, energy gradient, electronic wave function and properties of periodic systems. Hartree-Fock or KohnSham Hamiltonians (that adopt an Exchange-Correlation potential following the postulates of Density-Functional Theory) can be used. Systems periodic in 0 (molecules, 0D), 1 (polymers, 1D), 2 (slabs, 2D), and 3 dimensions (crystals, 3D) are treated on an equal footing. In each

case the fundamental approximation made is the expansion of the single particle wave functions ('Crystalline Orbital', CO) as a linear combination of Bloch functions (BF) defined in terms of local functions (hereafter indicated as 'Atomic Orbitals', AOs).

The computational method is based on the DFT associated with B3LYP hybrid functional [23,24]. Ca, W, O, and Eu atomic centers were described by the Ag_HAYWSC-311d31G_apra_1991, W_cora_1996, and O_6-31d1_corno_2006 basis sets, respectively, which were obtained from the Crystal website [25,26]. The diagonalization of the Fock matrix was performed using a 6×6×6 grid with 44*k*-point grids in the reciprocal space. The thresholds controlling the accuracy of the calculation of the Coulomb and exchange integrals were set to 10^{-8}, 10^{-8}, 10^{-8}, 10^{-8}, and 10^{-16}, and the percentage of Fock/Kohn–Sham matrix mixing was set to 30.

A full optimization process of the lattice parameters (*a* and *c*) and the internal atomic coordinates (*x*, *y,* and *z*) for the bulk was carried out until all force components were less than 10^{-5} eV/nm^2. From this optimized bulk structure, two periodic models, were built by selecting a 2×2×2 supercell: (1) the pure CW model of 192 atoms in the structure, composed by 32 Ca atoms, 32 W atoms and 128 O atoms and (2) the CWE model, in which two Ca^{2+} cations were replaced by two Eu^{3+} cations. To keep the electroneutrality of the system, a Ca^{2+} cation ghost was considered. This model contains 6.90% molar Eu in the structure. The band structure and density of states (DOS) of de CW and CWE models were obtained for 200 $\vec{k}$ points along the appropriate high-symmetry directions of the corresponding irreducible Brillouin zone.

3. Results and discussion

An analysis of the XRD patterns of the CW and CWE samples in **Fig. 1** renders that all materials exhibit well defined diffraction peaks, corresponding to the scheelite phase with tetragonal structure and space group $I4_1a$; this was in accordance with card No. 5510 [27] in the Inorganic Crystal Structure Database (ICSD). There was no secondary phase formation, indicating that the Eu^{3+} cation substitution process takes places successfully.

Figure 1. XRD patterns of the CW and CWE samples.

From the structural point of view, the lattice of the CW is composed by distorted octahedra [CaO_8] and tetrahedra [WO_4] clusters, in which the Ca atoms are coordinated with eight O atoms in an octahedral symmetry, while the W atoms are surrounded by four O atoms (see **Fig. 2**); each [CaO_8] cluster shares corners with eight [WO_4] tetrahedron to form chains parallel to [110] direction.

Figure 2. CW structure and the distorted octahedra [CaO_8] and tetrahedra [WO_4] clusters. The substitution of the Ca^{2+} by Eu^{3+} cation leads to the formation of [EuO_8] clusters.

Assuming that the samples present a spherical morphology, the average crystallite size (D) and the lattice strain (LS) of the as-synthetized samples were calculated and the values are presented in **Table 1**. The D value was obtained through the Scherrer's equation (**Eqs. (1)-(2)**), using the full width half maximum (FWHM) of the most intense peak [112].

$$D = {0.89\lambda}/{(\beta \cos\theta)} \quad (1)$$

$$\beta = \sqrt{\beta_e^2 - \beta_s^2} \quad (2)$$

where D is the average crystallite size, λ the X-ray wavelength (0.15406 nm), θ the Bragg angle, β_e the experimental full width at half maximum (FWHM) of the sample and β_s the FWHM of LaB_6 standard [28]. The LS parameter[29] can be obtained by Eq. (3):

$$\text{LS} = {\beta}/{(4 \tan\theta)} \quad (3)$$

Table 1. FWHM (°) values, crystallite size (D, nm) and lattice strain (LS, $\varepsilon \times 10^{-3}$) calculated from XRD data.

An elemental analysis of the CWE samples were performed by XRF spectrometry to obtain effective amount of Eu^{3+} cations along the doping process at the CW lattice and the results are in **Table 2**. The X-ray energy (spectral line Lα) for the Eu element it was observed in 5.849 keV. The amount of Eu^{3+} cations obtained by XRF compared to the nominal concentration of each sample is very close, confirming the substitution of Ca^{2+} by Eu^{3+} cations in the CW lattice.

Table 2. Amount of Eu^{3+} cations obtained by XRF spectrometry and the nominal value.

The distribution of Ca, W, O and Eu atoms in the CWE10 sample was analyzed by EDS mapping and it was observed a homogeneous distribution for all elements in the observed micro-dumbbells morphology, as can be seen in **Fig. SI-1** (see the Supporting Information, SI).

The XPS technique was used as a powerful tool to qualitatively determine the surface composition of the materials. According to the results (see **Fig. SI-2**), the characteristic peaks of Ca, W and O display that the samples are of high purity and the doping process of Eu^{3+} cations take place at the sites occupied by the Ca^{2+} cations. This analysis also demonstrated that the Eu content in the region close to the surface is much lower than that of the bulk. More details can be found in the XPS section in the SI.

Fig. 3(a) shows the MR spectrum in the range of 50–3500 cm^{-1}. Two different regions can be sensed, one related to $CaWO_4$ (**Fig. 3(b)**) and the other related to Eu substitution (**Fig. 3(c)**) since such modes are observed only with substitution. Both parts of the spectrum presented well defined modes, showing a high degree of order of the samples at short-range. **Fig. 3(b)** shows the spectrum of 50–1000 cm^{-1} in which is related to CW and a full discussion of these modes can be found in the SI. In the spectrum of **Fig. 3(c)**, the bands at 2536.3, 2957.1, 3112.0, and 3195.7 cm^{-1} can be sensed. These bands become even more intense as

the amount of Eu^{3+} cations increases and, according Tiseanu et al., these bands correspond to a fingerprint of substitution by Eu^{3+} cations in a tetragonal structure [30]. The analyses of the FT-IR spectra it was also performed, and the discussion can be found in the SI.

Figure 3. (a) Micro Raman spectra of CW and CWE samples; (b) zoom of the region between 50 and 1000 cm^{-1}; (c) Zoom of the region between 2500 and 3500 cm^{-1}.

For the study of the optical behavior of CWE samples, it was performed by calculating the band gap energy (E_{gap}) using the method proposed by Kubelka and Munk (more details in SI). **Fig. SI-4** shows that the band gap structures of the CW and CWE samples are characteristic of well-defined direct transitions, which is of the nature of crystalline semiconductors. The CW sample presented an E_{gap} of 4.12 eV, the CWE samples presented an E_{gap} of 3.91, 4.01, 4.11, 4.09, 4.10, and 4.18 eV, respectively in ascending order of doping Eu^{+3} cations. The decreasing in the E_{gap} can be attributed to the existence of structural defects localized in the forbidden band gap region.

By using the results of the DFT calculations an analysis of the energy levels in the valence band (VB) and the conduction band (CB) has been performed (see **Fig. 4(a, b)**). As can be seen, a direct electronic transition at the Γ-point in the Brillouin zone can be sensed. The CWE model has a lower band gap value (3.90 eV) when compared with the CW model (5.71 eV). This decrease of the band gap is due to the structural defect caused by the substitution of Ca^{2+} by Eu^{3+} cations, which involves the creation of new energy levels between the VB and CB.

Figure 4. Band structure for (a) CW and (b) CWE models and DOS for **(c)** CW and **(d)** CWE models.

In **Fig. 4(c, d)**, the DOS for the CW and CWE models are displayed, respectively. An analysis of the results renders that despite of the small contribution to CB from the Eu orbitals, the presence of Eu^{3+} cations in the CW structure caused a perturbation in the electronic states into the two bands (VB and CB). The position of Fermi level changed, from −4.40 eV in the CW model to −3.36 eV in the CWE model, while the first empty level in CB, goes from 1.31 to 0.44 eV. In both theoretical models, VB is formed mainly by the 2p orbitals of the O atoms, while CB is composed mainly by the hybridization of the 5d and 2p orbitals, between W and O atoms, respectively.

In order to analyze the morphology of the samples in function of the Eu^{3+} cations concentration, the FE-SEM was performed and images of CW and CWE samples is shown in **Fig. 5**. For the CW sample, the formation of microspheres and micro-dumbbells is observed, with an average size of 4.05 ± 0.49 μm (**Fig. 5(a)**). The microspheres have already been obtained by conventional hydrothermal [31, 32], sonochemical [33] and reverse micelle methods [34]; while the micro-dumbbells morphology was obtained by the microwave hydrothermal method [35]. For the CWE samples (**Fig. 5(b-g)**), the formation of microspheres was not observed, obtaining only micro-dumbbells with sizes of 4.22 ± 0.45, 4.27 ± 0.57,

4.24 ± 0.42, 4.29 ± 0.43, 4.91 ± 0.88, 4.95 ± 0.57 μm for samples CWE1, CWE2, CWE4, CWE6, CWE8, and CWE10, respectively.

Figure 5. FE-SEM images for the samples. (a) CW; (b) CWE1; (c) CWE2; (d) CWE4; (e) CWE6; (f) CWE8; (g) CWE10.

The PL emissions of the samples with different amount of Eu^{3+} cations are displayed in **Fig. 6(a)**. The pure CW has a broadband emission profile, characteristic of a multiphonic process, involving several intermediate energy states. The maximum emission of the CW sample is found in approximately 500 nm, in the cyan-green region, which are the result of internal charge transfers from the $[WO_4]$ clusters and oxygen vacancy (V_O) in the $[WO_4]$ and $[CaO_8]$ clusters [4, 36]. With the replacement of Ca^{2+} by Eu^{3+} cations, the appearance of specific transitions of Eu^{3+} is observed ($^5D_0 \rightarrow {}^7F_j$, j = 1, 2, 3, and 4), with maximum emission located at 596, 616, 659, and 704 nm, and these become more intense with the increased concentration of Eu^{3+} cations (**Fig. 6(a)**) [37]. The intensities of the observed transitions are dependent on the coordination of the Eu^{3+} cations [38].

Figure 6. (a) PL spectra for CW and CWE samples (λ = 350 nm); (b) Ratio of relative area for transitions $^5D_0 \rightarrow {}^7F_2$ / $^5D_0 \rightarrow {}^7F_1$; (c) Schematic luminescence model of CWE samples; (d) Coordinates of the Commission Internationale de l'Eclairage (CIE) by Spectralux software.

The peak located at 596 nm comes from a magnetic dipole transition $^5D_0 \rightarrow {}^7F_1$, that were almost independent of the local environment. The peak of greatest intensity, located at 616 nm, is called a hypersensitive red emission, and it comes from the transition of electric dipole $^5D_0 \rightarrow {}^7F_2$, that was strongly dependent of the environment. The appearance of this transition suggests that the Eu^{3+} cation is located in a symmetrical site where there is no inversion of symmetry [39], while the absence of the transition $^5D_0 \rightarrow {}^7F_0$ implies that the Eu^{3+} cations are not occupying sites with C_s, C_n or C_{nv} symmetry [40]. The ratio of relative area of the $^5D_0 \rightarrow {}^7F_2$ to $^5D_0 \rightarrow {}^7F_1$ transitions provides information about the local distortions in the clusters which the Eu^{3+} cations were inserted into the structure [41]. As presented in **Fig. 6(b)**, when increasing the concentration of Eu^{3+} in the CWE samples, there is an increase in local distortions related to the $[EuO_8]$ clusters of the crystalline lattice.

Fig. 6(c) shows the schematic luminescence model of CWE samples. When the sample is excited, electrons are promoted from the VB, made up of the O 2p levels, to the CW CB, made up of the W 5d levels. The emission of these samples occurs when the excited electrons decay radiative from the CB to the VB, or when the transfer of electrons from the CB to the excited levels of the Eu^{3+} cations. When populated, 4f states decay non-radiative to the level of emission characteristic of the Eu^{3+} cations ($^5D_0$) and then radiative to the fundamental states (^7F_j, j = 1, 2, 3, and 4), emitting in the observed characteristic lengths.

The change in the color emission perceptible by the human eye of the CW and CWE samples were evaluated by the coordinates of the Commission Internationale de l'Eclairage

(CIE) by Spectralux software [42] from the emission spectra obtained at under laser excitation at 350 nm (**Fig. 6(d)**). As expected, the CW has an emission in the cyan-green region, with a shift to orange with an increase in the substitution of Ca^{2+} by Eu^{3+} cations. This change occurs due to the sum of the characteristic emissions of Eu^{3+} cations in the red region ($^5D_0 \rightarrow {}^7F_j$, j = 1, 2, 3, and 4) with the emissions of the CW matrix. Therefore, the ions substitution in a semiconductor matrix by Eu^{3+} cations can lead to modulation of the final characteristic emission, resulting in potential materials for application in optical devices.

The lifetimes of the CWE samples were calculated for the luminescence decay of $^5D_0 \rightarrow {}^7F_2$ transition, with emission and excitation fixed at 616 and 394 nm, respectively. **Fig. SI-5** shows the mono exponential decay of the samples fitted with an exponential function as the **Eq. (4)**:

$$y = y_0 + A_1 \exp(t/\tau) \quad (4)$$

Where, y is the intensity, y_0 the intensity at the 0 ms, A_1 the amplitude, and τ the lifetime of the transition $^5D_0 \rightarrow {}^7F_2$.

The τ values obtained for the CWE samples were close, being 0.70 ± 0.04, 0.70 ± 0.04, 0.72 ± 0.03, 0.72 ± 0.02, 0.70 ± 0.01, and 0.67 ± 0.01 ms for samples CWE1, CWE2, CWE4, CWE6, CWE8, and CWE10, respectively. The CWE samples were fitted to a linear fit of lg$y$ versus t, indicating the samples have only one time of decay (see **Fig. SI-5**). These results indicate that Eu^{3+} cations occupy only one place of symmetry in the CW matrix and that there is only one process for the luminescence of the CWE samples.

4. Conclusions

In summary, the present work combines the experimental and theoretical results for better understanding of the PL emissions of the CW and CWE samples with different Eu^{3+} cations concentration. First-principles calculations, within the framework of DFT, were performed to achieve a deeper understanding of the effects caused by the Eu^{3+} cations in the CW electronic structure in order to correlate with the PL emissions experimentally observed. These findings allow to find a luminescent material in which by varying the Eu^{3+} cations concentration, the color emissions can be modulated. This work also paves the way for the further design of CWE-based materials for various applications as red-blue phosphors in different kinds of display devices.

Declaration of competing interest

The authors declare that they have no known competing financial interests or personal relationships that could have appeared to influence the work reported in this paper.

Acknowledgements

This work was funded in part by Fundação de Amparo à Pesquisa do Estado de São Paulo - FAPESP (2013/07296-2; 2016/23891-6; 2017/26105-4; 2019/01732-1), Financiadora de Estudos e Projetos - FINEP, Conselho Nacional de Desenvolvimento Científico e Tecnológico – CNPQ (166281/2017-4, 305792/2020-2), and CAPES. This work used computational resources of the "Centro Nacional de Processamento de Alto Desempenho em São Paulo" (CENAPAD-SP), "Centro de Computação John David Rogers" (CCJDR-UNICAMP), and the CENAPAD-RJ (SDumont). J.A. acknowledges Universitat Jaume I (project UJI-B2019-30), and the Ministerio de Ciencia, Innovación y Universidades (Spain) (project PGC2018094417-B-I00) for financially supporting this research.

Appendix A. Supplementary data

Supplementary data to this article can be found online.

References

1. Yu MQ, Xu HY, Li YZ, Dai QL, Wang GF, Qin WP. Morphology luminescence and photovoltaic performance of lanthanide doped $CaWO_4$ nanocrystals. J Colloid Interface Sci. 2020; 559:162.
2. Chai RT, Liu YT, Zhang G, Feng JJ, Kang QW. In situ preparation and luminescence properties of $CaWO_4$ and $CaWO_4$:Ln (Ln=Eu^{3+}, Tb^{3+}) nanoparticles and transparent $CaWO_4$:Ln/PMMA nanocomposites. J Lumin. 2018; 202:65.
3. Bae Y-J, Lee KH, Byeon S-H. Synthesis and Eu^{3+} concentration-dependent photoluminescence of $Gd_{2-x}Eu_xO_3$ nanowires. J Lumin. 2009; 129:81.
4. Gracia L, Longo VM, Cavalcante LS, Beltran A, Avansi W, Li MS, et al. Presence of excited electronic state in $CaWO_4$ crystals provoked by a tetrahedral distortion: An experimental and theoretical investigation. J Appl Phys. 2011; 110:043501.
5. Longo VM, Cavalcante LS, Paris EC, Sczancoski JC, Pizani PS, Li MS, et al. Hierarchical Assembly of $CaMoO_4$ Nano-Octahedrons and Their Photoluminescence Properties. J Phys Chem C. 2011; 115:5207.
6. Luo XF, Xie RJ. Recent progress on discovery of novel phosphors for solid state lighting. J. Rare Earths. 2020; 38:464.
7. Bunzli JCG, Wang XJ, Chen XY. Preface to the Special Issue of Rare Earth Luminescent Materials. J Rare Earths. 2020; 38:I.
8. Bunzli JCG. On the design of highly luminescent lanthanide complexes. Coord Chem Rev. 2015; 293:19.
9. Zhu HM, Lin CC, Luo WQ, Shu ST, Liu ZG, Liu YS, et al. Highly efficient non-rare-earth red emitting phosphor for warm white light-emitting diodes. Nat Commun. 2014; 5:4312.
10. Carlos LD, Ferreira RAS, Bermudez VD, Ribeiro SJL. Lanthanide-Containing Light-Emitting Organic-Inorganic Hybrids: A Bet on the Future. Adv Mater 2009; 21:509.

11. Richards BS. Luminescent layers for enhanced silicon solar cell performance: Down-conversion. Sol Energy Mater Sol Cells. 2006; 90:1189.
12. Kang FW, Li LJ, Han J, Lei DY, Peng MY. Emission color tuning through manipulating the energy transfer from VO_4^{3-} to Eu^{3+} in single-phased $LuVO_4:Eu^{3+}$ phosphors. J Mater Chem C. 2017; 5:390.
13. Xie W, Mo YW, Zou CW, Kang FW, Sun GH. Broad color tuning and Eu^{3+}-related photo-emission enhancement via controllable energy transfer in the $La_2MgGeO_6:Eu^{3+},Bi^{3+}$ phosphor. Inorg Chem Front. 2018; 5:1076.
14. Zhang Y, Abraha A, Zhang R, Shahbazyan T, Fadavi M, Heydari E, et al. Luminescence properties of $CaWO_4$ and $CaWO_4:Eu^{3+}$ nanostructures prepared at low temperature. Opt Mater. 2018; 84:115.
15. Xiong S, Liang D, Wu H, Lin W, Chen JS, Zhang BS. Preparation, characterization, tribological and lubrication performances of Eu doped $CaWO_4$ nanoparticle as anti-wear additive in water-soluble fluid for steel strip during hot rolling. Appl Surf Sci. 2021; 539:148090.
16. Kaur P, Khanna A, Fabian M. Effects of annealing temperature on structural and photoluminescence properties of Eu, Dy and Sm doped $CaWO_4$ nanoparticles. Ceram Int. 2020; 46:27262.
17. Kaur P, Khanna A, Kaur J, Kumar R, Chandra R. Rare earth doped $CaWO_4$ and $CaMoO_4$ thin films for white light emission. J Vac Sci Technol B. 2021; 39:012205.
18. Singh M, Ul Haq W, Bishnoi S, Singh BP, Arya S, Khosla A, et al. Investigating photoluminescence properties of Eu^{3+} doped $CaWO_4$ nanoparticles via Bi^{3+} amalgamation for w-LEDs application. Mater Technol. DOI: 10.1080/10667857.2021.1918866
19. Oliveira MC, Ribeiro RAP, Gracia L, Lazaro SR, Assis M, Oliva M, et al. Experimental and theoretical study of the energetic, morphological, and photoluminescence properties of $CaZrO_3:Eu^{3+}$. Crystengcomm. 2018; 20:5519.
20. Goncalves RF, Cavalcante LS, Nogueira IC, Longo E, Godinho MJ, Sczancoski JC, et al. Rietveld refinement, cluster modelling, growth mechanism and photoluminescence properties of $CaWO_4:Eu^{3+}$ microcrystals. CrystEngComm. 2015; 17:1654.
21. Dovesi R, Erba A, Orlando R, Zicovich-Wilson CM, Civalleri B, Maschio L, et al. Quantum-mechanical condensed matter simulations with CRYSTAL. Wiley Interdisciplinary Reviews-Computational Molecular Science. 2018; 8:1.
22. Dovesi R, Saunders VR, Roetti C, Orlando R, Zicovich-Wilson CM, Pascale F, et al., CRYSTAL17 User's Manual. University of Torino. 2017, Torino.
23. Becke AD. Density-Functional Thermochemistry .3. The Role of Exact Exchange. J Chem Phys. 1993; 98:5648.
24. Lee CT, Yang WT, Parr RG. Development of the Colle-Salvetti Correlation-Energy Formula into a Functional of the Electron-Density. Phys Rev B: Condens Matter Mater Phys. 1988; 37:785.
25. Dovesi R, Orlando R, Civalleri B, Roetti C, Saunders VR, Zicovich-Wilson CM. *Crystal Basis Sets Library*. <http://www.crystal.unito.it/basis-sets.php>.

26. Crystal. Basis Sets Library. http://www.crystal.unito.it/Basis_Sets/Ptable.html.
27. Gomez GE, Lopez CA, Ayscue RL, Knope KE, Deluigi MDT, Narda GE. Strong photoluminescence and sensing performance of nanosized $Ca_{(0.8)}Ln_{(0.1)}Na_{(0.1)}WO_{(4)}$ (Ln = Sm,Eu) compounds obtained by the dry "top-down" grinding method. Dalton Trans. 2019; 48:12080.
28. Klug HP, Alexander LE. X-Ray Diffraction Procedures: For Polycrystalline and Amorphous Materials. 2nd Edition ed. 1974: Wiley-VCH.
29. Jayachandraiah C, Kumar KS, Krishnaiah G, Rao NM. Influence of Dy dopant on structural and photoluminescence of Dy-doped ZnO nanoparticles. J Alloys Compd. 2015; 623:248.
30. Tiseanu C, Cojocaru B, Parvulescu VI, Sanchez-Dominguez M, Primus PA, Boutonnet M. Order and disorder effects in nano-ZrO_2 investigated by micro-Raman and spectrally and temporarily resolved photoluminescence. Phys Chem Chem Phys. 2012; 14:12970.
31. Ningombam GS, Nongmaithem RS. Morphology and photoluminescence of self-assembled $CaWO_4:Sm^{3+}$ microspheres: effect of pH and surfactant concentration. Int Nano Lett. 2017; 7:133.
32. Chen GQ, Wang FL, Ji WC, Liu YX, Zhang X. Improved luminescence of $CaWO_4:Eu^{3+}$ microspheres by codoping Gd^{3+}. Superlattice Microst. 2016; 90:30.
33. Janbua J, Mayamae J, Wirunchit S, Baitahe R, Vittayakorn N. Directed synthesis, growth process and optical properties of monodispersed $CaWO_4$ microspheres via a sonochemical route. RSC Adv. 2015; 5:19893.
34. Ningombam GS, Singh NR, Ningthoujam RS. Controlled synthesis of $CaWO_4:Sm^{3+}$ microsphere particles by a reverse-micelle method and their energy transfer rate in luminescence. Colloids Surfaces A: Physicochem Eng Aspects. 2017; 518:249.
35. Goncalves RF, Godinho MJ, Marques APA, Santos MRC, Rosa ILV, Longo E, et al. Structure, Morphology, and Optical Properties of $(Ca_{(1-3x)}Eu_{(2x)})WO_4$ Microcrystals. Electron Mater Lett. 2015; 11:193.
36. Cavalcante LS, Longo VM, Sczancoski JC, Almeida MAP, Batista AA, Varela JA, et al. Electronic structure, growth mechanism and photoluminescence of $CaWO_4$ crystals. CrystEngComm. 2012; 14:853.
37. Mazzo TM, Pinatti IM, Macario LR, Avansi W, Moreira ML, Rosa ILV, et al. Europium-doped calcium titanate: Optical and structural evaluations. J Alloys Compd. 2014; 585:154.
38. Wang WX, Yang PP, Gai SL, Niu N, He F, Lin J. Fabrication and luminescent properties of $CaWO_4:Ln(^{3+})$ (Ln = Eu, Sm, Dy) nanocrystals. J Nanopart Res. 2010; 12:2295.
39. Pinatti IM, Nogueira IC, Pereira WS, Pereira PFS, Gonçalves RF, Varela JA, et al. Structural and Photoluminescence Properties of Eu^{3+} Doped α-Ag_2WO_4 Synthesized by the Green Coprecipitation Methodology. Dalton Trans. 2015; 44:17673.
40. Su YG, Li LP, Li GS. Synthesis and Optimum Luminescence of $CaWO_4$-Based Red Phosphors with Codoping of Eu^{3+} and Na^+. Chem Mater. 2008; 20:6060.
41. Volanti DP, Rosa ILV, Paris EC, Paskocimas CA, Pizani PS, Varela JA, et al. The role of the Eu^{3+} ions in structure and photoluminescence properties of $SrBi_2Nb_2O_9$ powders. Opt Mater. 2009; 31:995.

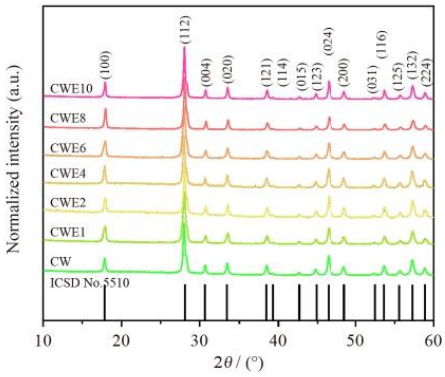

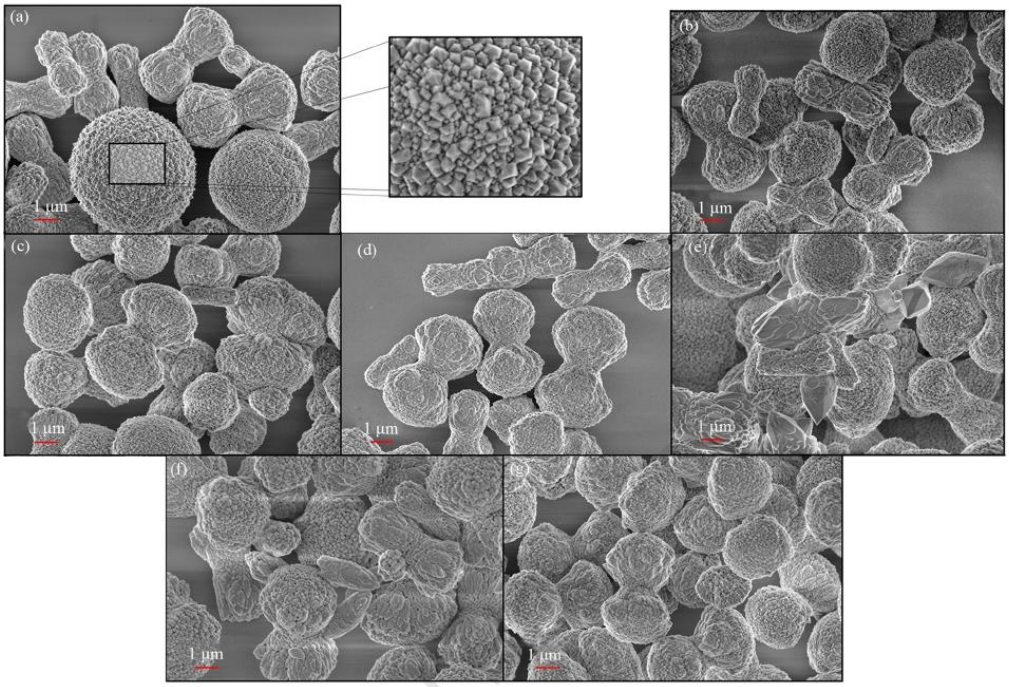

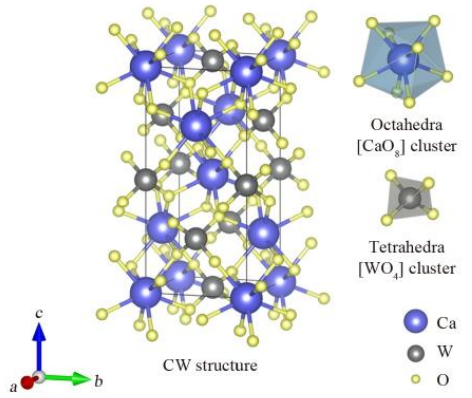

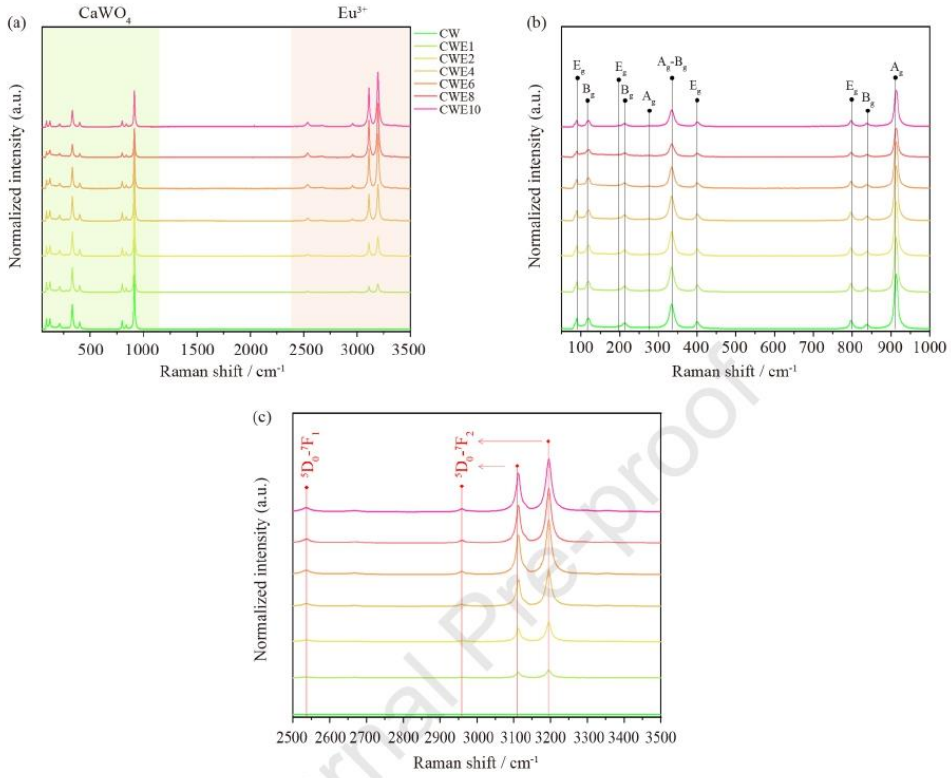

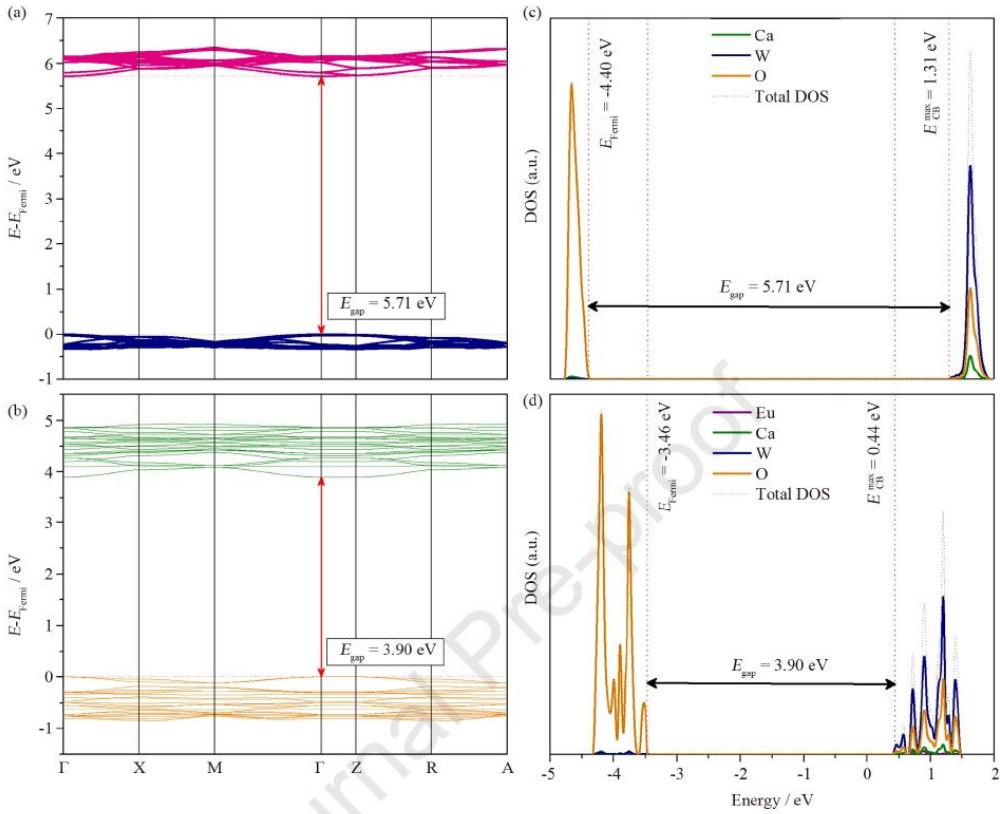

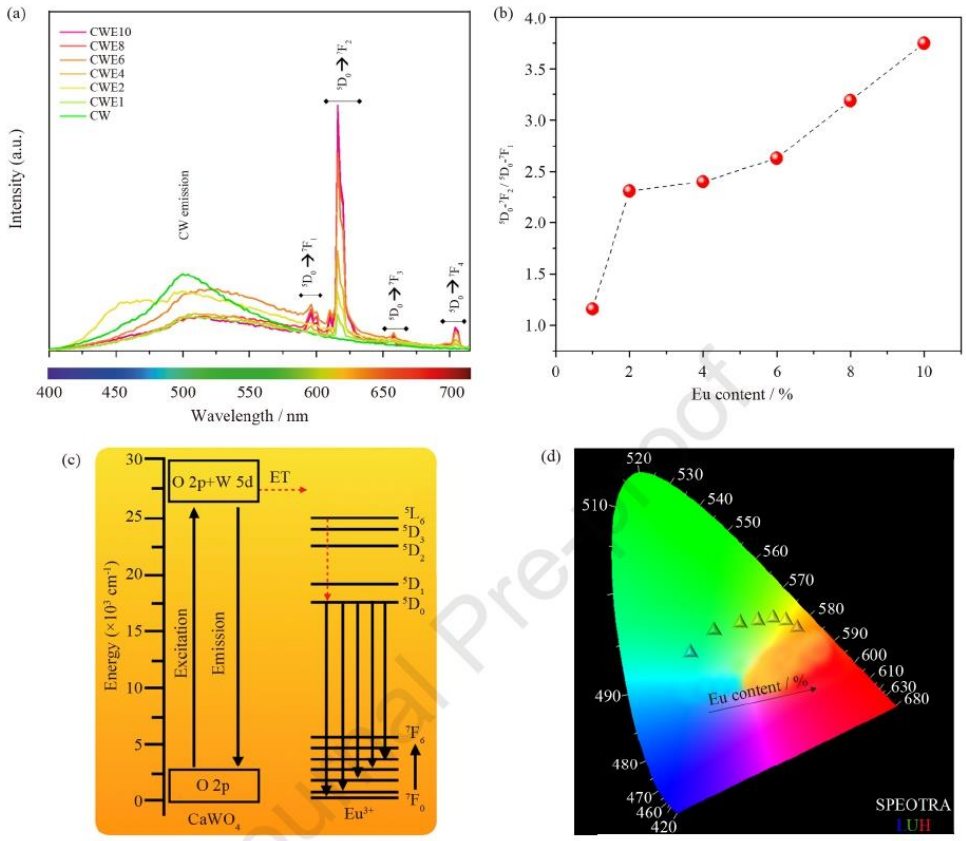

Photoluminescence emissions of $Ca_{1-x}WO_4:xEu^{3+}$: Bridging between experiment and DFT calculations

Amanda Fernandes Gouveia[a,b,*], Marcelo Assis[a,c], Lara Kelly Ribeiro[c], Aline Estefany Brandão Lima[d], Eduardo de Oliveira Gomes[b], Daniele Souza[e], Yara Gobato Galvão[e], Ieda Lucia Viana Rosa[c], Geraldo Eduardo da Luz Jr[d], Eva Guillamón[a], Elson Longo[c], Juan Andrés[a,*], Miguel Angel San-Miguel[b]

[a]Department of Physical and Analytical Chemistry, University Jaume I (UJI), 12071Castelló, Spain.
[b]Institute of Chemistry, State University of Campinas (Unicamp), 13083-970 Campinas, SP, Brazil.
[c]CDMF, Federal University of São Carlos (UFSCar), P.O. Box 676, 13565-905, São Carlos, São Paulo, Brazil.
[d]Departamento de Química, Federal University of Piauí (UFPI), 64049-550 Teresina, Piauí, Brazil.
[e]Physics Department, Federal University of São Carlos (UFSCar), P.O. Box 676, 13565-905, São Carlos, São Paulo, Brazil.

Supporting Information

EDS mapping

To analyze the distribution of Ca, W, O, and Eu atoms in the CWE samples, an EDS mapping was performed. **Figure SI-1** illustrated the mapping for the CWE10 sample and in this analysis, it was possible to observe a homogeneous distribution for all elements in the observed micro-dumbbells morphology. This distribution indicates a delocalized substitution of Eu^{3+} cations throughout the sample, corroborating with the XRD analyzes, where it is not observed the formation of secondary phases from the replacement of Ca^{2+} by Eu^{3+} cations.

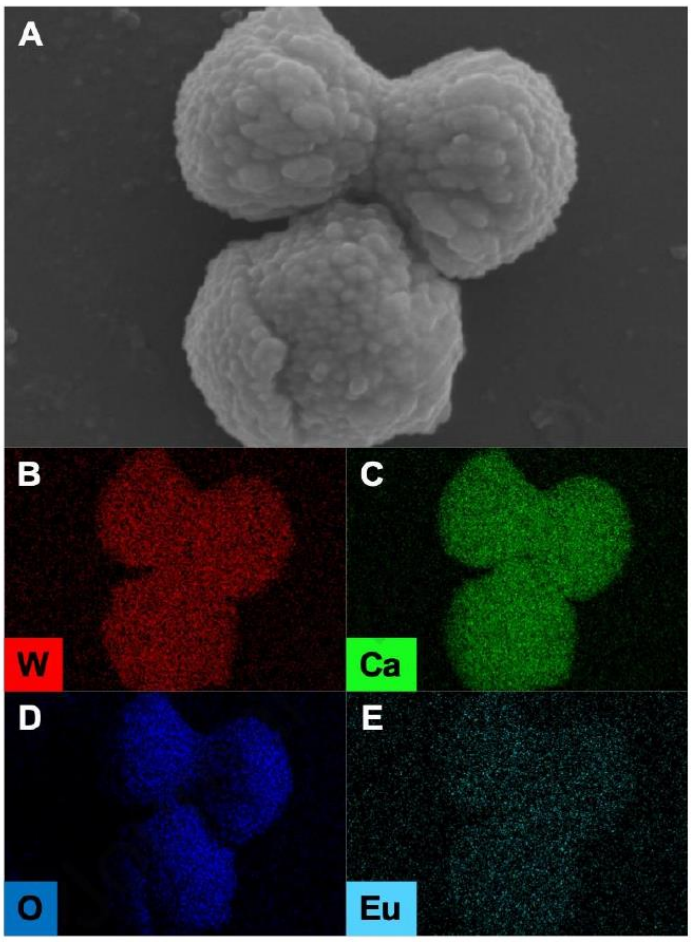

Figure SI-1. EDS mapping for the CWE10 sample.

X-ray photoelectron

In **Figure SI-2A**, the XPS spectrum of the survey of CW and CWE samples show the presence of a large amount of C (derived from the sample holder) and the characteristic peaks of Ca, W and O atoms, indicating that the samples are of high purity. The binding energy (calibrated using C (1*s*, 284.7 eV) as a reference) is shown for the Ca (2*p*, ~346.7 eV), W (4*f*, ~34.8 eV) and O (1*s*, ~530.25 eV) atoms.

The scan of the binding energy survey of the Ca, W and O core of the CW and CWE samples, in the range 0–1200 eV, are shown in **Figure SI-2B-H**. The XPS spectra of Ca (2*p*) were obtained in the range of 339 to 358 eV. In **Figure SI-2B(a)**, for the CW samples, the peak corresponding to Ca (2*p*) has a core binding energy of 346.2 eV ($2p_{3/2}$) and 349.6 eV ($2p_{1/2}$) with full width the half maximum (FWHM) of 1.7 and 2.09 eV, respectively. These results confirm the +2 oxidation state of Ca present in the structure [1, 2]. For CWE samples, in **Figure SI-2C(a)-H(a)**, the peaks corresponding to Ca (2*p*) have a core binding energy that varies from 346 to 348 eV for the $2p_{3/2}$ state and from 349 to 351 eV for the state of $2p_{1/2}$. These shifts in the binding energies of the Ca nucleus for the CWE samples indicate that the presence of Eu generates changes in the effective charge felt by the internal electrons, thus occurring an increase in the binding energies [3, 4].

The XPS spectra of W atoms (4*f*) were observed in the range 30–46 eV. In **Figure SI-2B(b)**, for the CW samples, the peak corresponding to W (4*f*) has a core binding energy of 34.4 eV ($4f_{7/2}$) and 36.4 eV ($4f_{5/2}$) with FWHM of 1.9 and 1.4 eV, respectively. For CWE samples, in **Figure SI-2C(b)-H(b)**, the peaks corresponding to W (4*f*) have a core binding energy that varies from 34 to 35 eV for the $4f_{7/2}$ state and from 36 to 37 eV for the state of $4f_{5/2}$. These results indicate that the oxidation state of W in the structure corresponds to +6 [4].

The XPS spectra of O atoms (1*s*) were observed in the range 525–535 eV. In **Figure SI-2B(c)**, for the CW samples, the peak corresponding to O (1*s*), these materials calcium-based oxygen carriers by possess were three types of oxygen species: surface adsorbed oxygen (O_{ads}), surface lattice oxygen ($O_{surf\text{-}lat}$), and bulk lattice oxygen ($O_{lattice\text{-}bulk}$) [5-8]. In **Figure SI-2C(c)-H(c)** it is possible to verify that these three species were also identified in the CWE samples, being able to attribute the peak of the photoelectron with binding energy located at approximately 529 eV to oxygen in the network ($O_{lattice\text{-}bulk}$), the second peak of the

photoelectron with binding energy located around 530-531 eV surface oxygen of the network ($O_{surf\text{-}lat}$), while the third photoelectron in 531-533 eV was attributed to the oxygen adsorbed on the surface (O_{ads}). In the CWE samples, the peak intensity of (O_{ads}) increased with the increase of Eu^{3+} doping. This increase in peak intensity (O_{ads}) may be due to the fact that oxygen vacancies caused by the insertion of Eu^{3+} cations can capture more species in the environment, such as carbonates and hydroxides [7, 9]. Although it is not possible to observe the presence of Eu 3*d*/4*d* in the survey spectrum, a high-resolution spectrum was applied in the region of 120-180 eV (Eu 4*d*) [10]. In the XPS technique the penetration layer is ~ 3 nm and if the sample has low concentration and few atoms in the surface in relation to the bulk, the signal will be of low intensity.

It can be observed in **Figure SI-2C(d)-H(d)** that the peak signal of the photoelectron with binding energy located around 120-180 eV referring to Eu 4*d* appears with the increase in doping performed on the $CaWO_4$ structure. The replacement of Eu atoms at the Ca^{2+} sites take place in the +3 oxidation state. That the doping occurred with the replacement of Eu^{3+} ions in the Ca^{2+} sites and that the Eu content in the region close to the surface is much lower than that of the bulk.

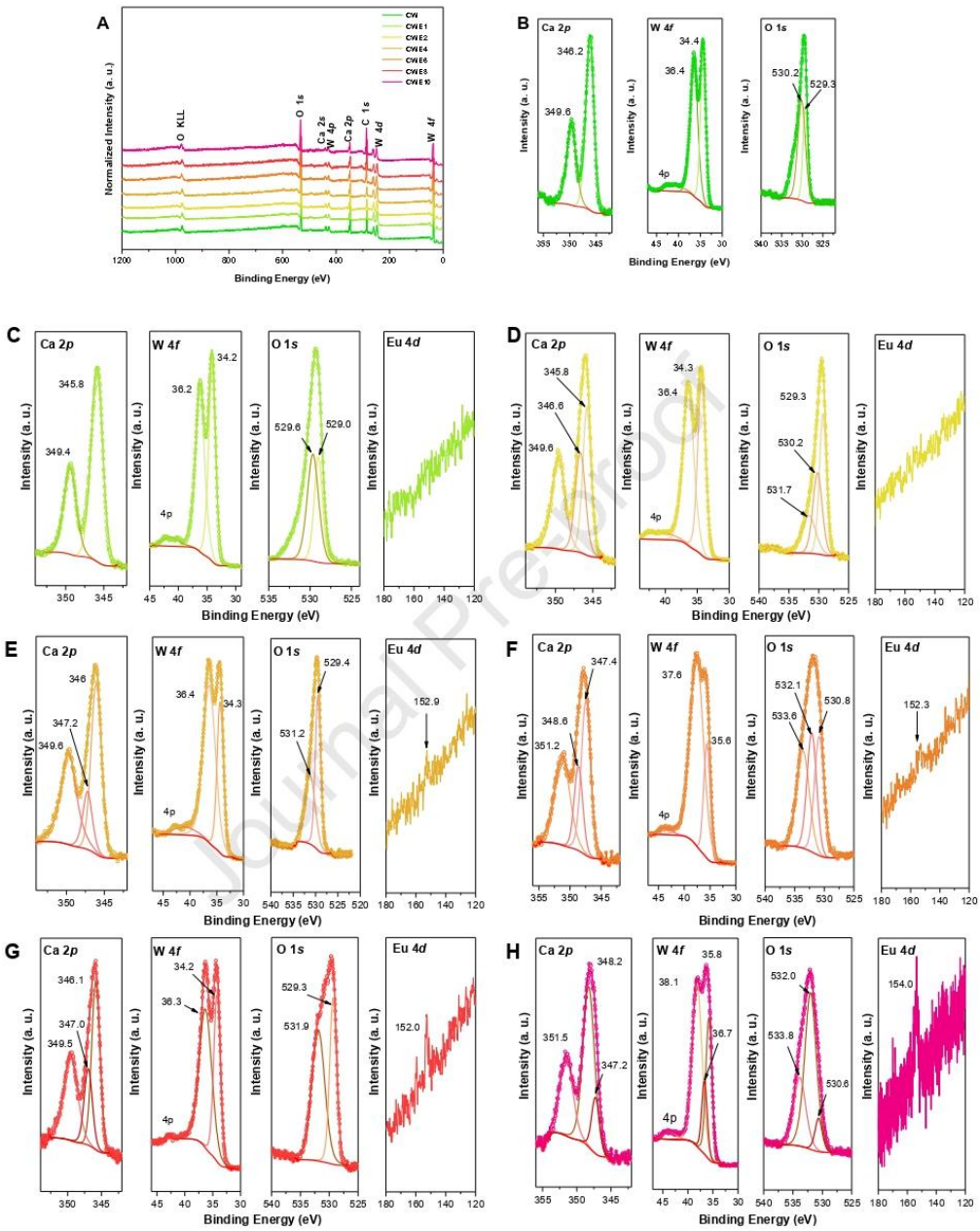

Figure SI-2. A) Survey XPS spectra for CW and CWE samples. **B**-**H**) High XPS spectra of Ca, W and O for CW samples and Ca, W, O and Eu for CWE samples. The figures are followed by **B)** CW, **C)** CWE1, **D)** CWE2, **E)** CWE4, **F)** CWE6, **G)** CWE8, and **H)** CWE10 samples.

Micro-Raman

According to group theory analysis, the allowed representation for each of the corresponding Wyckoff positions of the tetragonal $CaWO_4$ structure indicates 13 active Raman modes corresponding to the decomposition at the point $\Gamma = (3A_g + 5Bg + 5E_g)$ [11, 12]. A total of 11 active Raman modes are observed, related to $3A_g$ vibrations (275.3, 333.9 and 914.0 cm^{-1}), $4B_g$ vibrations (121.5, 213.1, 333.9, and 838.0 cm^{-1}) and $4E_g$ vibrations (88.6, 193.6, 400.0, and 797.3 cm^{-1}). The bands observed at 88.6 and 213.1 cm^{-1} are related to symmetric bending and stretching of the $[CaO_8]$ clusters [13]. The $[WO_4]$ clusters has T_d symmetry, which can be decomposed into 4 internal modes (ν_1, ν_2, ν_3, ν_4), a rotational mode ($\nu_{f.r}$) and a translational mode [11, 14]. The bands observed in 121.5, 193.6 and 275.3 cm^{-1} are related to translational and free rotation modes of the $[WO_4]$ clusters [15, 16]. The bands located at 333.9 and 400.0 cm^{-1} are related to symmetrical (ν_2) and asymmetrical bending (ν_4) of the O–W–O bond angles [11, 15]. The bands located at 729.3 and 838.00 cm^{-1} are related to asymmetric stretching (ν_3) of the O–W–O bonds [11]. Finally, the most intense band located in 914.0 cm^{-1} is related to the symmetric stretching (ν_3) of the W–O bonds [15].

Fourier Transform Infrared

Figure SI-3 illustrates the FT-IR spectra with the corresponding positions of IR-active modes of CWE samples. The scheelite-type structure has eight stretching and/or bending IR-active vibrational modes [13], presented by $\Gamma = (4A_u + 4E_u)$. Only three modes were identified for the CW and CWE samples in the range from 400 to 3500 cm^{-1}. Firstly, the CW and CWE samples exhibited a 443 cm^{-1} band that are assigned to the υ_4 $A_u + E_u$ mode that arise from symmetric bending vibrations with in the $[WO_4]$ clusters. The modes located at 802 and 849 cm^{-1} are attributed to an overlapping of two intense bands referring to υ_4 A_u and E_u,

respectively, which were ascribed to the O–W–O anti-symmetric stretching vibrations with in the [WO_4] clusters. The band located at 3153 cm^{-1} refer to OH stretching.

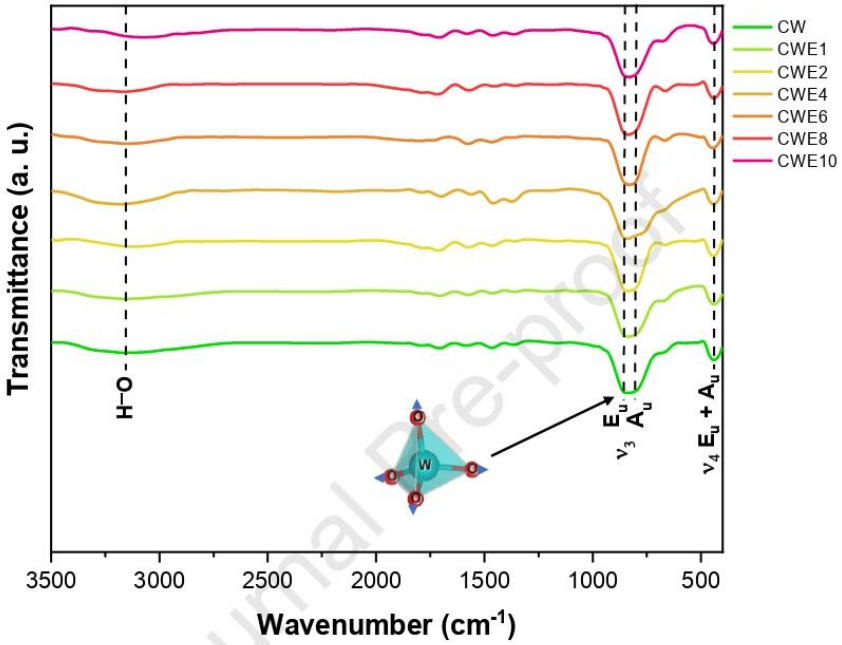

Figure SI-3. FT-IR spectra of the CW and CWE samples.

Ultraviolet-visible

The optical band gap is related to the absorbance and the photon energy by the following the equation (1).

$$h\nu\alpha \propto (h\nu - E_{gap})^{1/2} \quad (1)$$

where h is the Planck constant, ν is the frequency, α is the absorbance, and E_{gap} is the optical band gap. The CW exhibit an optical absorption spectrum governed by direct electronic

transitions characterized as n = 0.5 (n is a constant associated to the different kinds of electronic transitions).

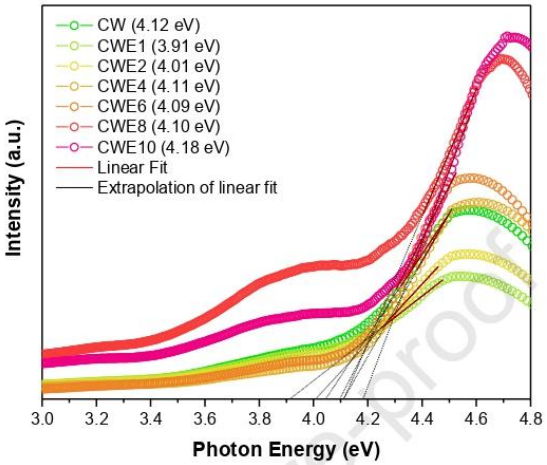

Figure SI-4. E_{gap} values obtained from the Kubelka-Munk method for CW and CWE samples.

Lifetimes

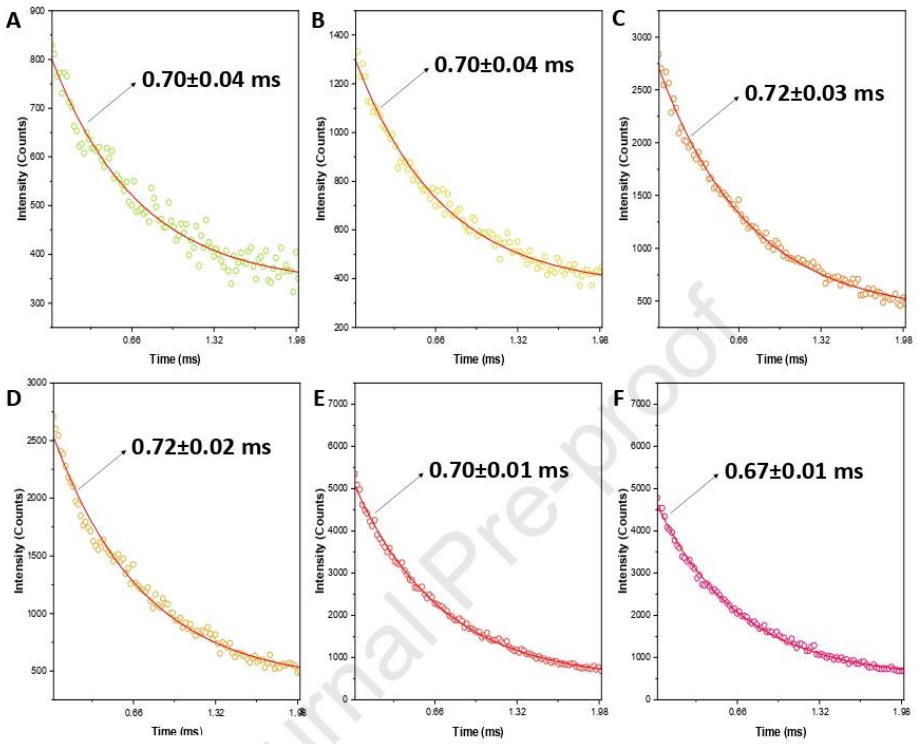

Figure SI-5. Lifetime decay curves of the $^5D_0 \rightarrow {}^7F_2$ transition for Eu^{3+} ion for **(a)** CWE1, **(b)** CWE2, **(c)** CWE4, **(d)** CWE6, **(e)** CWE8 and **(f)** CWE10.

References

1. Kumar D, Singh BP, Srivastava M, Srivastava A, Singh P, Srivastava A, et al. Structural and photoluminescence properties of thermally stable Eu^{3+} activated $CaWO_4$ nanophosphor via Li+ incorporation. J Lumin. 2018; 203:507.
2. Yu MQ, Xu HY, Li YZ, Dai QL, Wang GF, and Qin WP. Morphology luminescence and photovoltaic performance of lanthanide doped $CaWO_4$ nanocrystals. J Colloid Interface Sci. 2020; 559:162.
3. Chen LP, Gao YH, Yuan JX, Zhang QH, Yin YH, and Wang CX, *Fabrication of $CaWO_4:Eu^{3+}$ Thin Films Via Electrochemical Methods Assisted by a Novel Post Treatment*, in *Advanced Engineering Materials, Pts 1-3*, J.M. Zeng, T.S. Li, S.J. Ma, Z.Y. Jiang, and D.G. Yang, Editors. 2011. p. 2458.
4. Chen Y, Lee JH, Park SW, Moon BK, Choi BC, Jeong JH, et al., *A Novel Synthesis of $CaWO_4:Eu^{3+}$ Flower Like Microcrystals in Ethanol/water Mixed System and Characterization*, in *Materials Science and Nanotechnology I*, C.L. Zhang and L.C. Zhang, Editors. 2013. p. 512.
5. Chen DK, He DD, Lu JC, Zhong LP, Liu F, Liu JP, et al. Investigation of the role of surface lattice oxygen and bulk lattice oxygen migration of cerium-based oxygen carriers: XPS and designed H-2-TPR characterization. Appl Catal B:Environ. 2017; 218:249.
6. Ahmad MI and Bhattacharya ss. Size effect on the lattice parameters of nanocrystalline anatase. Appl Phys Lett. 2009; 95:
7. Wu HJ, Wang LD, Guo SL, Wang YM, and Shen ZY. Electromagnetic and microwave-absorbing properties of highly ordered mesoporous carbon supported by gold nanoparticles. Mater. Chem. Phys. 2012; 133:965.
8. Shpak AP, Korduban AM, Medvedskij MM, and Kandyba VO. XPS studies of active elements surface of gas sensors based on WO_{3-x} nanoparticles. J Electron Spectros Relat Phenomena. 2007; 156:172.
9. Palmqvist AEC, Wirde M, Gelius U, and Muhammed M. Surfaces of doped nanophase cerium oxide catalysts. Nanostruct Mater. 1999; 11:995.
10. Kumar S, Prakash R, Choudhary RJ, and Phase DM. Resonant photoemission spectroscopic studies of Eu2O3 thin film. J Appl Phys. 2016; 120:
11. Janbua J, Mayamae J, Wirunchit S, Baitahe R, and Vittayakorn N. Directed synthesis, growth process and optical properties of monodispersed $CaWO_4$ microspheres via a sonochemical route. RSC Adv. 2015; 5:19893.
12. Goncalves RF, Godinho MJ, Marques APA, Santos MRC, Rosa ILV, Longo E, et al. Structure, Morphology, and Optical Properties of $(Cal_{(1-3x)}Eu_{(2x)})WO_4$ Microcrystals. Electron Mater Lett. 2015; 11:193.
13. Cavalcante LS, Longo VM, Sczancoski JC, Almeida MAP, Batista AA, Varela JA, et al. Electronic structure, growth mechanism and photoluminescence of $CaWO_4$ crystals. CrystEngComm. 2012; 14:853.
14. Cavalcante LS, Sczancoski JC, Espinosa JWM, Varela JA, Pizani PS, and Longo E. Photoluminescent behavior of BaWO4 powders processed in microwave-hydrothermal. J Alloys Compd. 2009; 474:195.
15. Singh MBP and Singh RA. Color tuning in thermally stable Sm^{3+}-activated $CaWO_4$ nanophosphors. New J Chem. 2015; 39:4494.

16. Porto SPS and Scott JF. Raman Spectra of $CaWO_4$ $SrWO_4$ $CaMoO_4$ and $SrMoO_4$. Phys. Rev. 1967; 157:716.

Advances in Material Research and Technology
Series Ed.: Ikhmayies, Shadia Jamil
ISSN: 2662-4761

ACCEPTANCE LETTER

29 September, 2021

Dear Prof. Dr. Amanda Fernandes Gouveia, Luis Henrique da Silveira Lacerda, Eduardo de Oliveira Gomes, Lourdes Gracia, Marcelo Assis, Camila Cristina de Foggi, Elson Longo, Juan Andrés, Miguel Angel San-Miguel

I am glad to inform you that your chapter entitled **"Morphology-Dependent Properties in Inorganic Semiconductors: An Experimental and Theoretical Approach"** is accepted for publication in the e-book series on materials entitled "**Advances in Materials Research and Technology**"

in the Volume: **Advanced Semiconductors**,

edited by: Shadia Jamil Ikhmayies,

which will be published by Springer Publisher

I would like to thank you for your interest in this ebook series.

Yours sincerely,

Shadia Jamil Ikhmayies

Morphology-Dependent Properties in Inorganic Semiconductors: An Experimental and Theoretical Approach

Amanda Fernandes Gouveia[a,b], Luis Henrique da Silveira Lacerda[b], Eduardo de Oliveira Gomes[a], Lourdes Gracia[a,†], Marcelo Assis[a,c], Camila Cristina de Foggi[a,c], Elson Longo[c], Juan Andrés[a,*], Miguel Angel San-Miguel[b]

[a]Department of Physical and Analytical Chemistry, University Jaume I (UJI), 12071Castelló, Spain.
[b]Institute of Chemistry, State University of Campinas (Unicamp), 13083-970 Campinas, São Paulo, Brazil.
[c]CDMF, Federal University of São Carlos (UFSCar), P.O. Box 676, 13565-905 São Carlos, São Paulo, Brazil.
[†]Permanent address: Department of Physical Chemistry, University of Valencia (UV), 46100Burjassot, Spain.

Abstract

Inorganic semiconductors figure prominently in many current technologies, and they will play an important role in enabling a host of future applications. Since many of the beneficial properties of these materials arise from their morphology, achieving morphology control is important yet still elusive in many instances. Progress with experimental techniques, particularly those based on field emission-scanning electron microscopy, and similarly, theoretical developments provide deep insight on the mechanisms for achieving a selected morphology. The confluence of theory, experiment, and applications increases our capacity to describe the exposed surfaces at the morphology and provides new views into restructuring and morphology transformation mechanisms. In particular, the morphology of metal oxide semiconductors could lead to significant progress in advancing new applications along numerous fronts. First-principles calculations, based on the joint use of the density functional theory calculations and Wulff construction, were performed to investigate the surface structures, electronic and magnetic properties of Ag-based semiconductors (Ag_2MoO_4, Ag_2CrO_4, Ag_2WO_4, and Ag_2O). An equilibrium Wulff construction using absolute surface energies for various orientations is conducted to elucidate the morphological evolution. The calculated results manifest that our approach is capable of matching the experimental and theoretical morphologies, and a relationship among morphology and photocatalytic and biocide activity is achieved through a careful analysis of the coordination environment surrounding the surface metals at the morphology. We hope that our calculations can provide valuable hints for improving the performance of metal oxides semiconductors.

Keywords: Inorganic semiconductors, electronic properties, magnetic properties, morphology.

1 How does an inorganic semiconductor work?

Over the past few years, great effort has been dedicated to studying inorganic metal oxides as semiconductors. The preparation of these novel semiconductors has always been the goal of chemistry and material scientists because almost all contemporary electronic technologies involve the use of semiconductors [1-3]. The study of these materials constitutes an active research topic due to their excellent performance. They are often encountered in science and engineering disciplines, and figure prominently in many current technologies, and they will play an important role in enabling a host of future applications, ranging from the degradation of pollutants (such as various organic dyes, poisonous molecules/ions, etc.), energy conversion, and biocidal activity, among others. The long-lasting popularity of this field has led to the discovery or creation of numerous semiconductors, the heterojunction with other semiconductors, and the combination with metals displaying surface plasmon resonance effect, with impressive functionalities in three areas: renewable energy, health, and environmental sustainability [4].

The semiconductor photocatalysts are used for several decades in the past, called green technology, having received great attention, and shows an excellent ability for degrading contaminant by utilizing sunlight without causing any pollution. They also offer high versatility since it is possible to tune the band gap by modifying the geometrical and electronic structure. The achievable rapid fabrication of these materials with tunable physical and chemical properties facilitates tailoring the macroscopic properties of particle assemblies through contacts at the nanoscale.

An ideal semiconductor needs to fulfill the following: it should be chemically and biologically inert, stable, photochemically active, and cheap. Nowadays, semiconductors play a central role in acing new global environment- and energy-related issues [5]. In fact, this research field is broad, not only for promoting the solar into chemical energy conversion through thermodynamically up-hill reactions producing fuels, such as H_2 evolution from H_2O [6-9], but also the obtention of CH_4 and CH_3OH from CO_2 [10-12].

The typical mechanism of a semiconductor involves three key processes, namely harvesting light to generate charges, charge separation and transfer to active surface sites, and specific interfacial catalytic reactions [13-15]. In other words, the activity of a semiconductor begins with the generation of charge carriers. Following rapid hot carrier thermalization, the energy of the charge carriers is determined by the band alignment and occupancy in the semiconductor. In the excited state (conduction band, CB), there exists a competition between recombination and spatial charge separation, and this kinetics are strongly influenced by the presence of surface defects and mid-gap states in the material. If the carriers avoid recombination long enough, the possibility for interfacial charge injection provides a pathway for chemical rearrangement (redox) taking place at the surface. The competition between charge generation, separation, recombination, and injection determines the efficiency of the material. Many of these processes occur on the ultrafast time scale. Additionally, they are strongly influenced by complex surface chemistry due to various structural defects and associated electronic/magnetic states. In addition to the catalytic property of surface atomic activity, how to separate electron/hole (e^-/h^+) pairs efficiently is thus crucial for increasing the activity of semiconductors.

In order to verify if the inorganic semiconductor is capable of splitting the H_2O molecule to generate the hydroxyl radicals (•OH) and/or reduce the O_2 to superoxide radical ($•O_2^-$), it is possible to compare the position of the valence band (VB) and the CB with the potential of H_2O/•OH and O_2/$•O_2^-$ at different pH, such as 0 and 7. The VB and CB positions of the inorganic semiconductors can be determined using the empirical **equations**:

$$E_{CB} = \chi - E_e - 0.5E_{gap} \quad (1)$$
$$E_{VB} = E_{CB} + E_{gap} \quad (2)$$

where χ is the absolute electronegativity of the semiconductor, E_e is the energy of free electrons on the hydrogen scale (4.5 eV), E_{gap} is the band gap energy of the semiconductor, and E_{VB} and E_{CB} refer to the VB and CB potentials, respectively. **Figure 1** illustrates the calculated VB and CB values of some Ag-based semiconductors [16].

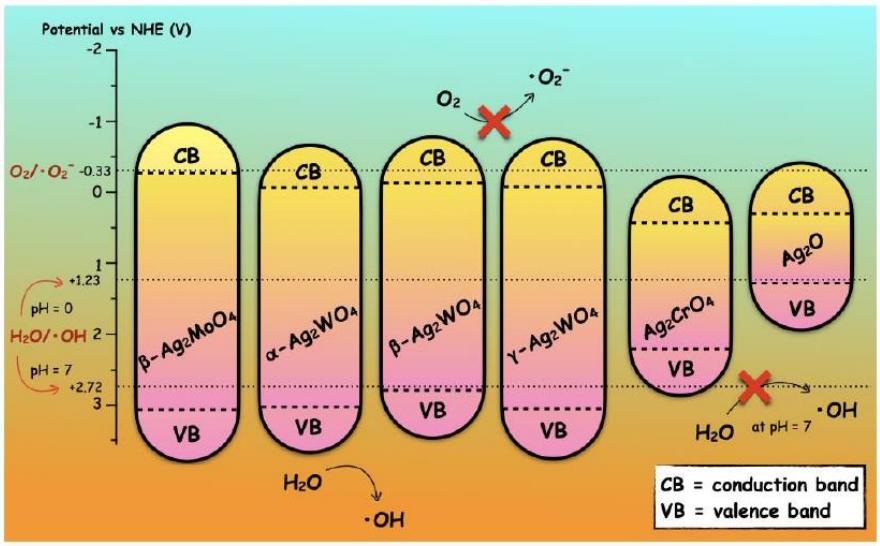

Figure 1. Scheme for the band structure of some Ag-based semiconductors and the potentials of radical generation in pH = 0 and 7.

A particular substrate can undergo chemical reactions on the semiconductor photocatalysts depending on the relative positions between its redox potentials and the band edges of semiconductor photocatalysts. There are four possibilities, as follows: (1) If the redox potential of the substrate is lower than the CB edge of the semiconductor photocatalyst, then the substrate can undergo reductive reactions; (2) If the redox potential of the substrate is higher than the VB edge of the semiconductor photocatalyst, then, the substrate can undergo oxidative reactions; (3) If the redox potential of the substrate is higher than the CB edge or lower than the VB of the semiconductor photocatalyst, then the substrate can undergo neither reductive nor oxidative reactions; and, (4) If the redox potential of the substrate is lower than the CB edge and higher than the VB of the semiconductor photocatalyst, then the substrate can undergo either reductive or oxidative reactions.

According to **Figure 1**, the position of VB of β-Ag_2MoO_4, α-Ag_2WO_4, β-Ag_2WO_4, and γ-Ag_2WO_4 renders that they can be used as photocatalysts due to the strong oxidation ability. The activations of both molecular oxygen, O_2, and water, H_2O, are the fundamental steps in almost all photocatalytic oxidation/reduction reactions. In terms of thermodynamic conditions, the estimated VB positions of β-Ag_2MoO_4, α-Ag_2WO_4, β-Ag_2WO_4, and γ-Ag_2WO_4 are more positive than the redox potential +2.72 V for $\bullet OH/H_2O^-$ versus NHE [17], leading to the oxidation of H_2O to form •OH, as a strong oxidant species for dye degradation. However, these Ag-based semiconductors are energetically unfavorable to carry out the reduction reactions, i.e., because they do not fit the redox potentials -0.33 V to carry out the reduction reaction to transform O_2 to $\bullet O_2^-$.

A deep understanding of the structural, electronic, magnetic properties indicates that the driving force for charge separation and the spatial distribution of active reaction sites is still lacking. From a chemical reactivity point of view, photocatalytic activity is a rather complex process that usually involves multiple e^-/h^+ transfers and significantly affects the fundamental reaction mechanisms, and largely determines reaction products [18-21]. Characterization techniques of surfaces and/or bulk are used to find a correlation among the semiconductor surface properties and the resultant activity performance of semiconductor materials [2, 22]. This research field is very active, and different procedures have been reported for the modification, tailoring, and engineering of structure and electronic/magnetic properties at the morphology to modulate the bulk diffusion, surface trapping, and interfacial transfer of the electrons and holes photoproduced on the semiconductor surface [23-34].

1.1 Semiconductor as a generator of highly reactive species

The energy absorbed by a photocatalyst comprises the range of ultraviolet and/or visible light, even natural sunlight. When a semiconductor absorbs light, if the energy of the photons is enough to excite the electrons in the valence band (VB), they migrate to a higher energy level in the CB of the material. This phenomenon generates the charge carriers known as e^-/h^+ pairs.

Activation of molecular oxygen (O_2) and water (H_2O) is one of the most important chemical processes of enormous interest and practical importance. In a semiconductor, the photogenerated h^+ at the VB can migrate to the surface of the material and react with H_2O molecules to produce •OH and proton (H^+), while the photoexcited e^- in the CB can react with the adsorbed molecular O_2 to produce $•O_2^-$. Besides, through further reactions, $•O_2^-$ and •OH species can transform into other highly oxidative species: singlet oxygen ($^1O_2$), perhydroxyl radical ($•O_2H$), or hydrogen peroxide (H_2O_2), as illustrated in **Figure 2**. These photogenerated species are called reactive oxygen species (ROS) [35]. The ROS are the key signaling molecules in both photocatalytic and physiological processes and play an important role in the development and function of photocatalytic and biocide materials. Density functional theory (DFT) calculations revealed that p-type and n-type conductivity in inorganic semiconductors can be ascribed to shallow acceptors (metal vacancies) and shallow donors (oxygen vacancies), respectively. The different clusters in the semiconductor structure form the e^-/h^+ pair: the $[MO_x \cdot xV_O^{\bullet}]$ clusters (hole species) located on the top of the surface of the nanocrystals interact with the H_2O forming the •OH and H^+ reactive species. In contrast, the $[MO_x]$ clusters (electron species) can interact with O_2 to form the $•O_2^-$, thereby the unstable radical $•O_2H$ can be formed by means of the reaction between $•O_2^-$ and H^+.

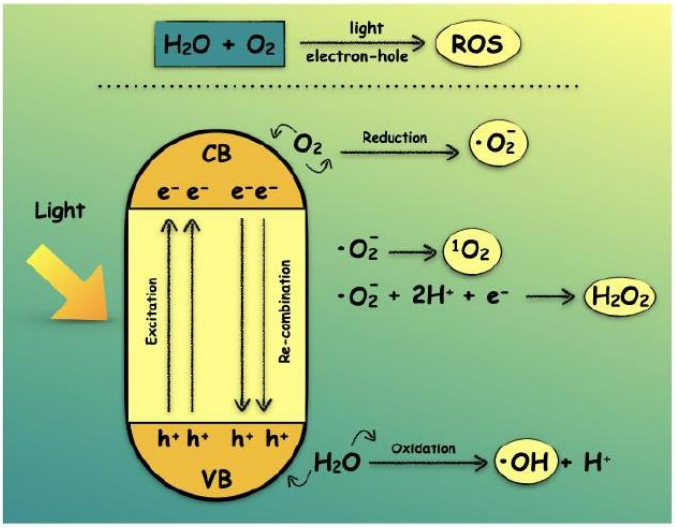

Figure 2. Illustrated scheme of ROS generation.

Therefore, the generation of ROS due to e^-/h^+ pairs is based on the following reactions [36-43]:

$$O_2 + e^- \rightarrow \bullet O_2^- \quad \textbf{(3)}$$
$$\bullet O_2^- + H^+ \rightarrow \bullet O_2H \quad \textbf{(4)}$$
$$\bullet O_2H + H^+ \rightarrow H_2O_2 \quad \textbf{(5)}$$
$$H_2O_2 + e^- \rightarrow \bullet OH + OH^- \quad \textbf{(6)}$$
$$H_2O + h^+ \rightarrow \bullet OH + H^+ \quad \textbf{(7)}$$
$$OH^- + h^+ \rightarrow \bullet OH \quad \textbf{(8)}$$

Furthermore, some electronic states can appear in the forbidden gap to undergo an ionization process to form electronic defects, i.e., quasi-free e^- and h^+ [44, 45]. In addition, it was demonstrated that the recombination of e^-/h^+ pairs is probable at bulk sites while surface defects improve the reactivity by promoting the adsorption of O_2 and H_2O. Then, exposed surfaces with a difference in charge density (due to the dipole moment) bind the adsorbates strongly and drive the photocatalytic reactions [46, 47]. The ability to control these properties at the nanoscale has allowed correlations to be made between nanocrystal structure and their optical, magnetic, and electronic properties, which has implicated these materials in various applications ranging from biomarkers to photocatalysts [48-51].

2 Theoretical methods, computing procedures, and model systems

The atomic and molecular world, unlike the macroscopic world, can only be accurately described by quantum mechanics. The natural properties and behavior of molecules and materials are difficult to imagine, and they are impossible to predict without resorting to approximations.

The goal of many computational physicists and chemists is to bridge the gap between atomistic lengths scales of about a few multiples of an Ångström (Å), i. e., 10^{-10} m, and meso- or macroscopic length scales by simulations.

The theoretical studies reported here are based on periodic models, and the first-principles calculations are performed mainly by using the DFT associated to an exchange-correlation functional, such as the PBE and the B3LYP. Several computational programs can be used, and, in our research, we mainly use the VASP and/or CRYSTAL software packages. The atoms are described using all-electron or pseudo-potential basis sets. The initial atomic positions and lattice parameters are set according to experimental and/or theoretical studies.

The first step of the theoretical study is the structural optimization of the bulk model, followed by calculating the numerical second derivatives of the total energy with respect to the ionic displacements. After that, it is possible to define slab models for the Wulff's construction to obtain the available set of morphologies and perform the magnetism investigation. Therefore, the structural analysis and the electronic properties can be performed to correlate with the experimental results.

2.1 Calculations of surface structure and Wulff's construction

Although controlling the morphology taken by a material may initially seem like a scientific curiosity, its implication goes far beyond aesthetic appeal. The morphology not only controls its physicochemical properties but also determines its relevance and merit for the applications. Therefore, understanding the physical and chemical properties of semiconductor surfaces is important for improving the performance of related applications while determining the surface structures and broken chemical bonds on the exposed surfaces that contribute to material properties is generally the prerequisite. For example, photocatalytic processes are initiated by the excitation of a semiconductor photocatalyst by photons of energy higher than the semiconductor band gap resulting in the formation of e^{-}/h^{+} pairs. Then, a great variety of environmentally friendly redox transformations may occur involving chemical species with suitable redox potentials adsorbed on the photocatalyst surface [52].

Different surface and/or bulk characterization techniques [2, 22] can be employed to get better insight into the potential specific correlation existing between the semiconductor surface properties and the resultant photoactivity performance of photoactive semiconductor materials, to be considered in the design of efficient and easily applicable photocatalysts [53].

Traditional surface science has established that the surfaces of large crystals can lower their energy by moving surface atoms away from lattice sites in the process of surface reconstruction, dangling bonds can introduce new electronic states, and foreign molecules (surfactants or adsorbates) can alter the energy and reactivity of a crystal surface. However, many fundamental properties of the semiconductor surfaces are still poorly understood due to their inherent complexity. The main reason behind such poor knowledge lies in the fact that the properties of metal oxides depend on the interplay between the geometric structure, the band structure, the local stoichiometry of the surface, and the oxidation states of the components. In this context, a significant challenge is the elaboration of an atomic-scale surface theory for metal oxides. Such a theory would undoubtedly be the groundwork for the rational design of metal oxides as semiconductors.

A crystalline system can present several surfaces, being the main direction observed as the most prominent peaks on X-ray diffraction (XRD) analysis [54, 55]. The main feature of a surface is the broken crystalline symmetry resulting in a new structural arrangement with novel chemical and physical properties. In the computational context, a surface model is obtained from cuts along a specific direction, and the surface model is defined as a bi-dimensional model with a finite thickness (z-axis). Similar to that observed for experimental XRD analysis, the surface models are also represented in terms of [hkl] Miller index [56].

Thus, the surface models can be seen as atomic layers (slab) stacking along with a specific Miller index, keeping the translational symmetry observed in bulk. The construction of the

surface model takes into account two factors: thickness and vertical symmetry, which are strongly connected to surface chemical nature and stability [54, 57]. The first refers to the number of layers represented by the model and should be large enough to make the interaction between the up and down slab terminations negligible. Meanwhile, a particular vertical symmetry is observed for each crystalline direction; thus, the symmetry features may or may not result in the existence of a macroscopic dipole moment perpendicular to the surface [54, 57].

A macroscopic dipole moment affects the surface stability and can be responsible for a reconstruction mechanism resulting in a novel arrangement for atoms. In computational approaches, the surface is fully optimized (relaxed) rising new chemical bonds, as expected in a reconstruction process. An extremely efficient method to surface model interpretation was developed by Tasker [58]. This model is based on ionic crystals since it can be understood as an agglomerate of slabs composed of cations and anions leading to surfaces with different charge distributions. **Figure 3** presents the three different types of Tasker's surfaces. Type 1 consists of stoichiometric atomic planes with zero total charge. Type 2 is characterized by formally charged planes distributed so that the macroscopic dipole moment (μ_z) obtained from the sum of the charges in the repetition unit is zero. The charge of such planes is related to the non-stoichiometric distribution of cations and anions along the planes; however, the macroscopic dipole for the model repetition unit is null. The last Tasker surface (type 3) presents an allocation of formally charged slabs, resulting in a repetition unit with a non-zero macroscopic dipole moment [58].

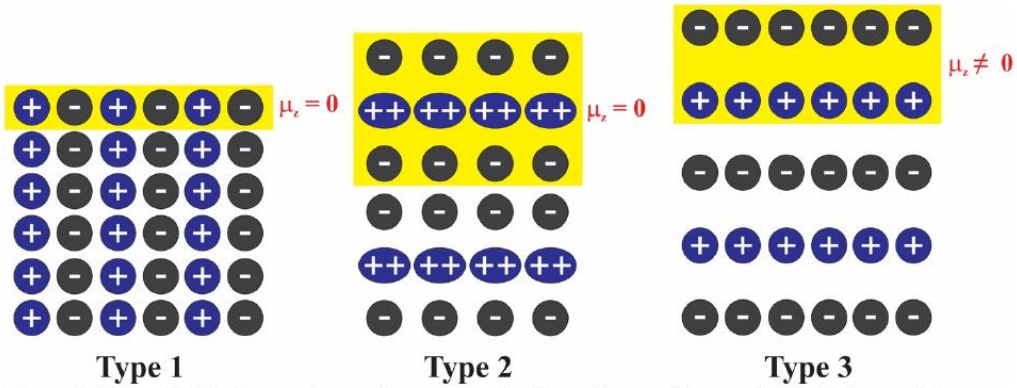

Figure 3. Charge distribution on atomic planes composing the surface models according to Tasker models.

According to the Tasker classification, the type 1 and type 2 surfaces are potentially stable since they do not present macroscopic dipole moment perpendicular to the slab. Otherwise, the type 3 surfaces characteristically possess electrostatic surface energy arising from the macroscopic dipole [58]. It is noteworthy that several oxides and complex oxides present surfaces with non-zero macroscopic dipole (a.k.a. polar surfaces), which are routinely obtained from different synthesis routes [55, 59, 60]. Therefore, the investigation of this kind of surface is mandatory.

The atom distribution, stability, magnetic and electronic properties can be studied by using first-principles calculations. In particular, the investigation of polar surfaces by computational approaches represents a challenging task since the macroscopic dipole moment can drastically increase the computational cost and hamper the model convergence [54]. Thus, some alternatives were developed to minimize macroscopic dipole influence, such as molecule adsorption on the surface, reconstruction process, or theoretical corrections that cancel the dipole moment, included in some simulation packages [57]. In addition to these, a recent

methodology represents a simple and efficient method that does not require chemical adsorption or surface reconstruction to cancel/minimize macroscopic dipole influence. In such an approach, the surface models consist of two-dimensional periodic models composed of atomic layers parallel to specific [hkl] crystalline planes "cut out" from the fully optimized bulk structure. The surface directions are usually chosen from the XRD analysis, being the most prominent peaks the most important to surface investigation. To each selected crystalline direction, there are several possibilities of stoichiometric and non-stoichiometric surfaces with different properties. All possible stoichiometric models should be evaluated compared to each other in terms of total energy, being the minor energy model the most stable surface composition. For this surface model, a slab growth is performed until energy and properties convergence is reached. To adequately reproduce the features of a surface, it is mandatory to create a model large enough to represent the termination on the top of the model, an internal region (mimicking the bulk), and the lower termination [54, 57]. In general, a model with three bulk units is the minimum model size to reproduce a surface correctly. Furthermore, the growth is mandatory for polar surfaces since it minimizes the macroscopic dipole influence on the surface calculation.

Once the surface model for each direction is constructed, the first step consists of evaluating non-relaxed cleavage energy ($\gamma^{unrelax}$) for up and down terminations (T_U and T_D, respectively). The $\gamma^{unrelax}$ value represents the energy required to cut out a crystal into two non-relaxed terminations. The **equation (9)** represents mathematically this step, where being $E_{slab}^{unrelax}$ refers to the energy of the non-relaxed model, E_{bulk} is the total energy of a bulk containing one unit cell, n is the number of bulk units, and A represents the surface area.

$$\gamma^{unrelax} = \frac{(E_{slab}^{unrelax} - nE_{bulk})}{2A} \quad \textbf{(9)}$$

The next step consists of the relaxation of the complementary terminations (T_U and T_D). The energy for relaxed surfaces (γ) is computed by **equation 10**. The scientific explanation that justifies surface relaxation is the need for structural modifications to increase surface stability.

$$\gamma = \frac{(E_{slab}^{relax} - nE_{bulk})}{2A} \quad \textbf{(10)}$$

The methodology described above is very representative and has successfully predicted the surface properties of several materials, such as $FeCrO_3$, $LiNbO_3$, $PbNiO_3$, $MnTiO_3$, and others [61-66].

The γ of a single-element solid is dependent on temperature, vapor pressure, and surface relaxations or reconstructions. But measuring γ is generally a difficult task even for simple cases [67-69]. Wulff's construction is a reliable tool to understand and predict (nano)particle morphology based on minimizing the energy associated with all surrounding surfaces of an independent particle [70-74]. According to the theory, the structure and morphology of crystals are determined by the γ of planes on thermodynamic equilibrium conditions [75]. These γ values, obtained from first-principles calculations in association with the Wulff's construction model, provide a strong correlation between structure–function, highlighting the importance of theoretical chemistry in materials science and nanotechnology.

Andres *et al.* [76] reported a careful revision of the use of this methodology for solid-state materials. This type of analysis is helpful for understanding how to achieve morphological control of complex three-dimensional crystals by tuning the γ values of the different surfaces. As reported in several works in the literature [63, 77-87], theoretical surface calculations

associated with Wulff's construction are a powerful tool to obtain the available morphologies of (nano/micro) materials, as shown in **Figure 4**.

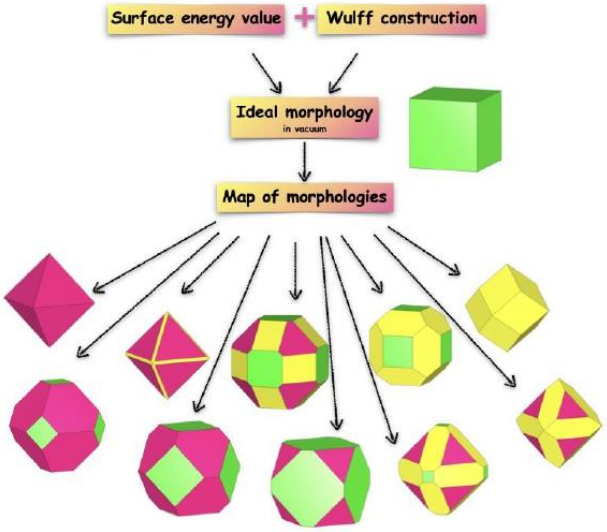

Figure 4. A schematic representation of the flow diagram to obtain the available morphologies.

2.2 Calculations of electronic properties

The theoretical analysis of the electronic properties starts from the optimized structure, i.e., from the geometry relaxation. A Mulliken population analysis can be performed, providing total atomic charges, atomic orbital, and shell populations and the overlap populations. The ground-state electron charge density, unlike the previous features, is a quantum mechanical observable of primary importance. It may be expected that both HF and DFT hamiltonians reproduce the essential features of the electron density. Thus, helpful information can be extracted from single-particle hamiltonian (HF/DFT) eigenvalues such as the band structure. In 2D systems, the occurrence of surface states in the band gaps can be detected and their dependence on surface relaxation or reconstruction processes. To obtain the band structure, some information must be specified, such as the path in the Brillouin zone of the reciprocal space (which depends on the reciprocal lattice) and the range of energy/bands to be visualized. Finally, the calculation of density of states requires the Fock/KS eigenvectors in the k-points defined by the Pack-Monkhorst mesh.

2.3 Calculations of magnetic properties

The study of magnetic materials through computational methodologies reproducing their electronic structure and other properties correctly is critical. Several works have successfully applied DFT simulations to study the bulk and surfaces of complex magnetic semiconductors [61, 88-90]. Such studies employ a simple and powerful theoretical tool to predict magnetic features of materials: the Ising Model. This model enables the determination of the magnetic coupling constant (J) and magnetic states energy difference (ΔE_T). **Equations 11 and 12** represent the Ising Model mathematically, being N the number of magnetic cations in the unit cell, Z is the coordination number of magnetic species, and S_x represents the spin-charge of each magnetic site. The usage of the Ising model is mandatory to adequately measure electronic

interactions since the Slater determinant is not an eigenvalue of Heisenberg hamiltonian, commonly used to describe unpaired electrons [91].

$$\Delta E_T = E_{T_{AFM}} - E_{T_{FM}} \quad \textbf{(11)}$$

$$\Delta E_T = -N.Z.S_x.S_x.J \quad \textbf{(12)}$$

Generally, a computational investigation of a magnetic system uses the following steps: i) the system structure is fully relaxed considering an FM order; ii) the AFM order is calculated from the fully-relaxed structure and compared using the Ising equation set. Positive values for ΔE_T and J indicate an FM ordering as the most stable, while negative values indicate that the AFM or FeM ordering is the most stable (magnetic ground state); iii) for systems with more than two possible magnetic order, a final model representing the ground state should be calculated to reproduce the electronic structure of the material correctly. The ordering of unpaired electrons is based on all the results obtained from the Ising equation aiming to reproduce the minor energy magnetic interactions existing in the crystalline structure.

As observed in **equation 12**, the Ising Model considers the coordination number of magnetic cations. Therefore, this method is only suitable for the system with a reasonable symmetry degree, predicting all magnetic features of crystalline space groups in bulk form. It is noteworthy that the Ising model is not entirely suitable for surface evaluation since each magnetic site possesses a particular coordination number. Consequently, only **equation 11** can be employed for the analysis of magnetic surfaces. Thus, Ising Model determines the magnetic ground state of the surface without estimating the J values. As performed for solid-state materials bulks, all possible magnetic orderings for surfaces should be evaluated to determine the magnetic ground state.

The efficiency of Ising calculations to study magnetic semiconductors is evidenced by several manuscripts being successfully employed to bulk [88-90, 92-94] or surfaces [61, 64, 95, 96].

In the following, we discuss theoretical and experimental progress in understanding the surface properties and morphologies of different silver-based metal oxides, such as Ag_2MoO_4, Ag_2CrO_4, Ag_2WO_4, and Ag_2O.

3 Morphology-dependent properties

Considering that the chemical reaction proceeds on the surface of semiconductors, the surface physicochemical properties are important for improving their activity. Since many of the beneficial properties of inorganic metal oxides arise from their morphology, and it is becoming increasingly apparent that control over the morphology of a semiconductor is imperative for many applications, being one of the critical issues for the design, engineering, and utilization of their desired properties [97]. Surface control begins with seed crystals nanometer- or sub-nanometer sized particles that grow post nucleation, and that may fluctuate through several shapes prior to achieving a set of morphologies that act as templates for growth of the final crystals.

The surface structure is composed of defective sites generated by the improper termination of the crystal lattice. In metal oxides, the terminating species can be lattice oxygen or lattice metal cation, acting as donor and acceptor of electrons, respectively. These surface states are located within the band gap and may induce band bending themselves, depending on their position with respect to both band gap and Fermi level. Therefore, the Fermi level of the bulk may be different from the Fermi level of the exposed surfaces, and the transitions within the band gap, which are forbidden in bulk, can now be allowed through the introduction of states

by surface terminated species [98-100]. The catalytic and biocidal performances are determined by the number and the intrinsic activity of these active sites.

In this context, crystal facet engineering allows the obtention of functionalized semiconductor-based materials with different morphologies and compositions and has been successfully applied for numerous applications [101, 102]. Plausible mechanisms were proposed to explain how different morphologies modulate the electronic structure of semiconductors by a synergistic effect between the active component promoted by oxygen vacancies, undercoordinated metal clusters at the exposed surface, thereby altering the catalytic and biocidal activities. These findings provide a new way to enhance the properties of a semiconductor by structure-activity relationship.

As a clear-cut example, we can select the work of Huang et al. [103] in which the authors have shown that the electronic, photocatalytic, and optical properties of semiconductor materials are highly facet-dependent. According to Huang et al. [103], the photocatalysts' efficiency of Cu_2O crystals is related to the exposed surface in the crystal morphology and its band bending value. Cu_2O presents three morphologies: cube, octahedra, and rhombic dodecahedra with different photocatalytic responses, as it is displayed in **Figure 5**. Therefore, the ability to generate h^+ and e^- in the VB and CB, respectively, is linked to the band gap interval of each surface present in the morphology. The morphology and, in particular, the structure and electronic properties at the exposed surfaces, control the formation and recombination of e^- and h^+ pairs and then the activity of the material.

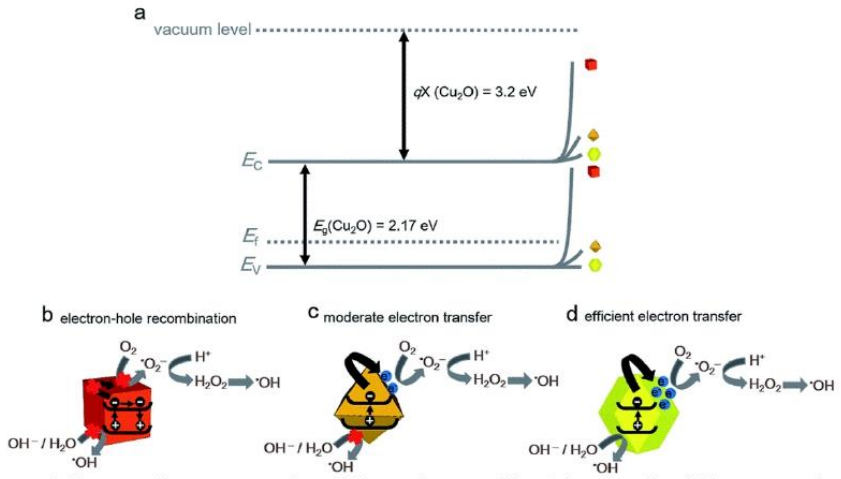

Figure 5. Band diagram of Cu_2O presenting different degrees of band bending for different crystal surfaces to account for their photocatalytic behaviors. The drawings show different photocatalytic responses of Cu_2O with different morphologies: cubes, octahedra, and rhombic dodecahedra. Printed with permission from Ref. [104] copyright(2021) Royal Society of Chemistry.

With the confluence of promising new applications, rapidly developing capabilities in experimental techniques, and new theoretical developments in quantum and statistical mechanics, there has been a renewed effort in this area, and significant advances seem imminent. Recent experimental and theoretical studies have tracked a variety of phenomena associated with shape evolution, and there are many exciting prospects for advancing this field [48, 49, 76, 105, 106]. Below, we delineate a few areas ripe for progress and review recent advances in the field and discuss challenges for the future.

3.1 Electronic properties

The inorganic semiconductors are the subjects of much research because of their multifunctionality, resulting in an outstanding application due to their electronic properties. From the theoretical point of view, the electronic properties of given materials can be analyzed from calculated band structure and Density of States (DOS), featuring the band gap energy (E_{gap}) region in both cases. From band structure analysis, it is possible to classify the E_{gap} as direct or indirect according to high symmetry points of the Brillouin zone. Meanwhile, the DOS evaluation provides the contribution of each atomic species to the formation of VB and CB energy levels. The electronic properties of semiconductors can also be discussed in terms of charge distribution from Mulliken populations, charge density maps, or Bader charges obtained from topological analysis in the framework of the QTAIM.

The analysis of the electronic properties is fundamental not only for the bulk model but also for the surface models. Once the properties of the inorganic semiconductor materials are morphology-dependent, the analysis of the surfaces that compose the crystal shape is crucial for a good interpretation of materials properties. Hence, we can analyze the electronic transitions in each surface and calculate the E_{gap} of the morphology (polyhedron) using the E_{gap} values from the surfaces [107].

3.2 Magnetic properties

In recent years, semiconductor materials with magnetic properties have attracted the interest of scientists worldwide due to their potential for the development of the next generation of devices, such as spintronic-based [108-110]. Magnetism was firstly studied in ancient Greece, where the naturalists and philosophers had observed the magnetic behavior of Fe_3O minerals at the Magnesia region [91]. The name of this region comes from magnetism, and their name means “place of magic stones” since the minerals attract each other. Moreover, some Chinese historical reports point out that the Chinese scientists had investigated a ferrous meteorite in 3000 b.C. – 2500 b.C and, posteriorly, in the middle of 900 b.C., the magnetic compass was discovered. Over the years, the magnetic behavior has been broadly investigated and, among the scientists dedicated to this topic, stands out William Gilbert, also known as the “father of magnetism” [91]. In the current days, magnetism is still investigated, and semiconductors have emerged as potential magnetic alternatives.

Since the knowledge about magnetic materials has drastically increased, the Classic theory cannot describe this kind of feature, being replaced by interpretations based on quantum theory [111]. In short, the Classic theory describes magnetism from the existence of small magnets within the structure. Also, it proposes that all substances possess such magnets oriented along with different directions according to the local chemical environment [111]. Still, within the scope of classical theory, the description of magnetism is based on magnetic domains separated by well-defined borders [111]. In turn, the modern theories are based on quantum mechanics and in the concept of electron angular momentum (spin). Thus, the magnetism of atoms or molecules is raised from unpaired electrons (open-shells) and is strongly dependent on their interaction with other electrons in the system [112].

In particular, the magnetism in solid-state materials is determined by the magnetic resultant observed in the unit cell, which can be oriented at a specific crystalline direction for distorted structures, presenting a behavior known as magnetocrystalline anisotropy [91]. In the case of semiconductors, the magnetic behaviors arise from the existence of unpaired electrons in d or f orbitals of transition metals.

The ordering of all unpaired electrons determines the magnetic resultant in solid-state material within the unit cell, and, according to such arrangement, a semiconductor can be

classified as ferromagnetic (FM), antiferromagnetic (AFM), or ferrimagnetic (FeM). An FM material presents all unpaired electrons oriented along a preferential spin direction. An AFM material possesses unpaired electrons equally oriented in two opposite spin directions, resulting in a null magnetic resultant. This kind of magnetic ground state can be observed in three different types according to the ordering of magnetic neighbors. The G-type AFM includes the materials where the nearest magnetic neighbor is always oriented in the opposite spin direction; meanwhile, the A- and C-types consist of crystalline planes oriented along different spin directions. In turn, the FeM behavior occurs when the unpaired electrons are non-equally distributed along two opposite directions, resulting in a residual magnetic resultant [113, 114]. As observed for AFM ordering, the FEM materials can also be classified as G-, C- or A-types. **Figure 6** presents the possible magnetic ordering for semiconductor materials.

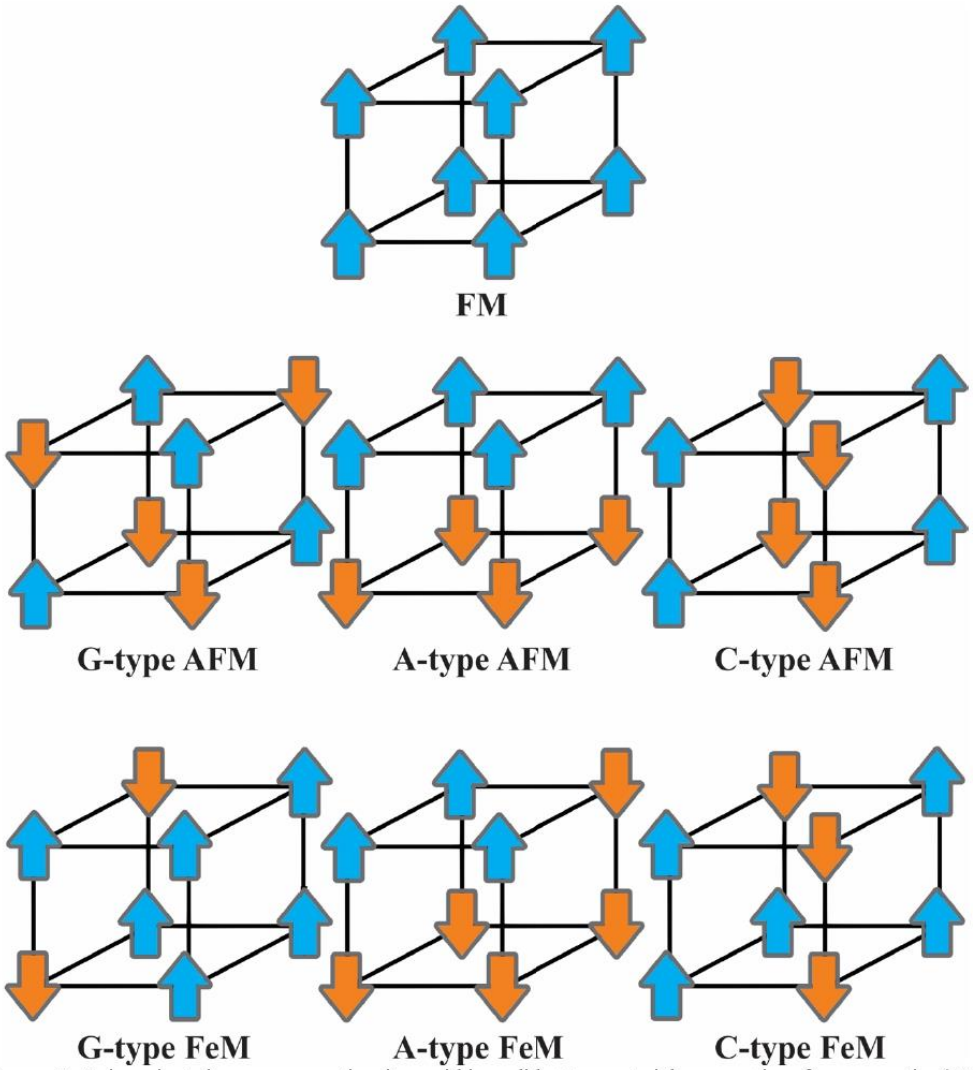

Figure 6. Spin orientation on magnetic sites within solid-state materials presenting ferromagnetic (FM), antiferromagnetic (AFM), and ferrimagnetic (FeM) ordering. The alpha and beta spin directions are represented by blue and orange arrows, respectively.

For semiconductor materials, the AFM ordering is the most observed in nature as found in NiO, Cr_2O_3, CoO, $BiFeO_3$, MnF_2 [114]. Some relevant examples of FeM semiconductors are complex oxides such as $FeCrO_3$ [90] and $PbFeO_3$ [89]. In turn, $PbNiO_3$ [95], $SnNiO_3$ [94], $HfNiO_3$ [94], $NiGeO_3$ [93], $FeGeO_3$ [89], and $FeSnO_3$ [89] are important examples of semiconductor materials with FM magnetic ordering.

At current days, the investigation of semiconductor materials with magnetic properties emerges as a trending topic in science due to its high suitability for promising technologies as spintronics and other devices as magnetic sensors, magnetic readers, actuators, tunneling devices, data storage devices, and others [115, 116].

3.3 Photocatalytic and biocide activities

Applications of photocatalysis include H_2O splitting for hydrogen production [117], breaking of N_2 [118], CO oxidation [119, 120], commodity production catalysts [120], and water treatment [121]. In all these processes, the action's mechanism from the semiconductor is conducted by the ROS.

On the other hand, ROS can be considered a powerful weapon to destroy microorganisms, mainly due to its selectivity for microbial cells over mammalian cells. Although exogenous ROS, present in the environment, are capable of disrupting microorganism's cells, leading to death, ROS are also byproducts from normal microbial cell metabolism [122]. Intracellular ROS are continuously eliminated by microbial cells, but the semiconductors can produce many of these species, overcoming the mechanisms that regulate cellular oxidative stress.

Although some bacteria can develop resistance to $\bullet O_2^-$ and H_2O_2, they are unable to defend themselves against other types of ROS, such as $^1O_2$ and •OH. This is because there are two regulatory antioxidants systems in bacteria: SoxRS and OxyR, responsible for the adaptive responses to stresses caused by $\bullet O_2^-$ and H_2O_2, respectively [123]. Since the specific targets in the desired application are known, there is the possibility of developing semiconductors with functions directed specifically to them.

4 Results and applications

Silver-based metal oxides are an important family of inorganic materials and have both technological and theoretical importance. Silver molybdate, chromate, and tungstate, as also the silver oxide, exhibit a wide range of electrical and optical properties that can find widespread applications in various fields such as photocatalysis, solar energy conversion, energy storage, as well as antimicrobial agents [48, 49, 105, 107, 124, 125:Fabbro, 2016 #2416, 126-128].

4.1 Ag_2MoO_4

Silver molybdate (Ag_2MoO_4) exists at ambient pressure in two allotropic forms: a metastable α-tetragonal form (obtained at pH 5–6), which is irreversibly transformed to a β-Ag_2MoO_4 (above 280 °C, with a cubic spinel structure). The conventional cubic unit cell of β-Ag_2MoO_4 contains eight formula units. The Mo atoms occupy 8a tetrahedral sites, the Ag atoms reside at the octahedral 16d position, and the O atoms remain at 32e positions. This crystal structure provides some features suitable for catalyst, sensors, photoluminescence, and antibacterial and antifungal agents [85, 129-132].

In 2015, Fabbro et al. modeled the (001), (011) and (111) surfaces of β-Ag_2MoO_4 by an unreconstructed slab model using a calculated equilibrium geometry (a = 9.454 Å, and u(O) =

0.2351) [133]. Through Wulff's construction it was obtained some available morphologies for this semiconductor and the results suggests that the (011) surface is the dominating face in the ideal morphology.

In other reports, the β-Ag_2MoO_4 crystals were prepared by a coprecipitation method using water, ethanol, and ammonia as solvents [49, 85]. The experimental images reveal that a morphological change in the shape of the β-Ag_2MoO_4 crystals occurs according to the used solvent. From the ideal morphology obtained using the Wulff's construction and the γ calculated values, it was possible to reach the experimental morphologies. The morphology obtained in water is achieved by decreasing the value of γ for the (111) surface. In turn, the ethanol and ammonia affect simultaneously the values of γ for the (001) and (111) surfaces, where the (001) is more stabilized in ethanol. Therefore, it is possible to affirm that the predominant morphologies obtained experimentally by using different solvents (water, ammonia, and ethanol) display the exposed (001), (011), and (111) surfaces, which support the hypothesis that these surfaces are stabilized by interacting with the solvent molecules. This observation suggests that the Wulff's shape of β-Ag_2MoO_4 is closely related to the chemical environment: when water was used as the solvent [49].

β-Ag_2MoO_4 synthesized in different solvents has distinct morphologies, as well as differences in biocidal effectiveness. It is recognized that β-Ag_2MoO_4 microcrystals have fungicidal and bactericidal properties against *Candida albicans* (*C. albicans*), and methicillin-resistant *Staphylococcus aureus* (MRSA) and *Escherichia coli* (*E. coli*), respectively [49, 85].

Antibacterial and antifungal efficiency of the β-Ag_2MoO_4 microcrystals increased in the following order: water < ammonia < ethanol. According to the predicted theoretical morphologies, the appearance of the (001) surface increased the antibacterial efficiency, and also the inactivation of the MRSA and *E. coli* was mainly caused by the presence of the [$AgO_5.V_O^x$] complex clusters. Then, the faces with low surface energy are more easily polarized and able to generate •OH, •O_2, and •O_2H radicals, which are responsible for cell death.

4.2 Ag_2CrO_4

Under ambient temperature and pressure conditions, silver chromate (Ag_2CrO_4) has an orthorhombic structure belonging to the *Pnma* space group. An induced structural polymorphism can occur at high pressures, passing it to a cubic structure of $Fd\bar{3}m$ space group [134]. Its stable orthorhombic structure has four molecules per cell unit (Z = 4). The Cr atoms occupy tetrahedral sites 4c, the Ag atoms occupy octahedral sites in positions 4 and 4c, and the O atoms are in positions 4c and 8d [135].

The methods of synthesis of Ag_2CrO_4 can be changed to obtain morphological changes in the particles, with the coprecipitation method in aqueous media being used more frequently [136-139]. However, several other methods are reported in the literature, such as the cation exchange method of the solid-state reaction [140], sonochemical [86, 141], conventional hydrothermal [142], microwave-assisted hydrothermal [143], and wet-chemical reaction [144]. Physical methods for modifying Ag_2CrO_4, such as femtosecond laser irradiation [145, 146] and pressure [142] can also result in significant surface changes, which are reflected in their properties.

Through the Wulff's construction model and first-principles calculations, it is possible to obtain the morphological evolution of Ag_2CrO_4. All the observed surfaces are asymmetrical, with the external atomic arrangement being the main stability factor. The (111) surface is the most energy-efficient (lowest γ), in contrast to the (001), (011), and (110) surfaces (largest γ), as they have a high number of surface broken bonds. As expected, the most stable theoretical morphology has the most exposed (111) surface, whereas changes in γ can abruptly alter the obtained morphology. Experimentally, the alteration of γ in the formation of Ag_2CrO_4 particles

can be done by changing the synthesis method, using surfactants [147], chelating agents [48], doping with other ions [148], and the use of organic solvents [149]. Thus, the final Ag_2CrO_4 morphology is directly related to its chemical environment and pressure and temperature conditions.

Ag_2CrO_4 is widely used due to its photodegradation activity of organic pollutants and its biocidal activity against fungi (*C. albicans*) and bacteria (MRSA) [48, 141, 147, 148]. These effects are reported due to the increased exposure of the (011) surface in the stabilized morphologies. In this way, different activities can be associated with different surface compositions, and the presence of the $[AgO_3.3V_o^x]$ and $[AgO_4.2V_o^x]$ clusters at the top of the (011) surface is crucial to increase photocatalytic and biocidal efficiency [48, 148].

4.3 Ag_2WO_4

Silver tungstate (Ag_2WO_4) shows structural polymorphism with different phases, and the most studied are the α-Ag_2WO_4 (orthorhombic), β-Ag_2WO_4 (hexagonal), and the γ-Ag_2WO_4 (cubic), in which the first one is the most stable thermodynamically and the others are metastable phases. Ag_2WO_4 is very studied due to its many applications, such as photocatalysis, catalysis, biocide, gas sensor [127, 150-152]. Their structures are formed by different kinds of clusters, i.e., different metal coordination numbers. The α-Ag_2WO_4 structure is formed by Ag clusters with 2, 4, 6, and 7 atoms of O and by one W cluster with coordination 6 [153]. The β-Ag_2WO_4 is constituted by Ag clusters with 5 and 6 O atoms and by W clusters with 4 and 5 O atoms [154], while the γ-Ag_2WO_4 structure is built by only Ag clusters with coordination 6 and W clusters with coordination 4 [87].

The map of morphologies for the α-Ag_2WO_4, β-Ag_2WO_4, and the γ-Ag_2WO_4 was obtained and reported in the literature [77, 81, 87]. A morphological change was observed by Macedo et al. in the α-Ag_2WO_4 crystals synthetized by a simple controlled precipitation method with and without surfactant (SDS) [155]. In this paper, a theoretical and experimental approach demonstrated that the (101) surface controls the photocatalytic activity of the α-Ag_2WO_4 in the rod-like morphology. In another study, the morphological change of the α-Ag_2WO_4 samples was investigated using the coprecipitation method followed by microwave irradiation for different times [156]. It was observed that microwave irradiation affects the α-Ag_2WO_4 morphology in which is directed related to the antibacterial and photocatalytic activities.

The β-Ag_2WO_4 and γ-Ag_2WO_4 samples were obtained using a precipitation method in aqueous media without any surfactants at low temperature, and the structural characterization was performed by an experimental and theoretical approach [87, 154, 157]. The coprecipitation method of synthesis at room temperature to obtain the γ-Ag_2WO_4 metastable pure phase was reported by Neto et al [158]. In this methodology, the authors used the polyvinylpyrrolidone (PVP) as a surfactant and observed that the stabilization of the γ-Ag_2WO_4 phase is efficient at 0.3 g of PVP, wherein larger or smaller amounts favored the formation of α-Ag_2WO_4 and β-Ag_2WO_4 as secondary phases. The γ-Ag_2WO_4 microcrystals obtained with PVP demonstrated better photocatalytic activity than the α-Ag_2WO_4 and β-Ag_2WO_4 against the methylene blue dye [158].

Recently, we reported a selective and successful synthesis method through a simple precipitated route at temperature to obtain the three polymorphisms. This method consists of controlling the volumetric ratios of the silver nitrate/tungstate sodium dehydrate precursors in solution [107].

The ability to fight bacteria and fungi by Ag_2WO_4 happens due to the production of ROS by the semiconductor [127, 159, 160], which is increased when the microcrystal has metallic nanoparticles on its surface [128, 161, 162]. When α-Ag_2WO_4 is irradiated with electrons, its antibacterial capacity against MRSA increases 4-fold [128]. When it is irradiated with laser in

femtoseconds, its effectiveness increases 32-fold in comparison with non-irradiated material [161]. This phenomenon occurs because metallic Ag was reduced and emerged from the α-Ag_2WO_4. This fact creates a disorder in the semiconductor and the formation of e^-/h^+ pairs. Both Ag^0 metallic and α-Ag_2WO_4 surface interact with O_2 and H_2O generating a large amount of ROS that attack microbial cells.

Different α-Ag_2WO_4 morphologies are observed when the solvents of the precursors used in the coprecipitation synthesis are varied [127]. The greater antifungal (*C. albicans*) and antibacterial (MRSA and *E. coli*) activities were attributed to microcrystals synthesized in alcoholic solution because both [WO_6] and [AgO_x] distorted clusters act together to produce a large amount of ROS. In the α-Ag_2WO_4 synthesized using the ammoniacal solution and water, only distorted [AgO_x] clusters are present, producing a small amount of •OH and •O_2H.

Among the polymorphs α-, β- and γ-Ag_2WO_4, the antibacterial activity against MRSA is more accentuated in the material in β- phase because the exposed (110) surface represents 81% of its morphology and e^-/h^+ separation taking place from the distorted $[WO_4]_d$ cluster to the undercoordinated [$AgO_3 \cdot 2V_x^o$], [$AgO_2 \cdot 3V_x^o$], and [$WO_3 \cdot V_x^o$] clusters [107]. The antibacterial and photocatalytic activity improvement occurs due to the exposed surfaces enhancing the migration of photoinduced e^-, suppressing the recombination of charge carriers.

4.4 Ag_2O

The silver oxide (Ag_2O) is a versatile material with proven efficiency in several technological applications, including photocatalysis, antibacterial, dyes, electrodes, and electronic devices [163-166]. The properties of Ag_2O are strongly facet-dependent; for instance, the highest photocatalytic activity was obtained from (110), (100), and (111) surfaces. The nanocrystals majorly composed of such surfaces present cubic, octahedral, rhombic dodecahedral, and rhombicuboctahedral morphologies [163, 167-170]. It is well-known in the literature that oxygen vacancies are intrinsically related to control the electronic properties of simple and complex oxides aiming for photocatalytic purposes [61, 171, 172]. In the case of Ag_2O, the electronic properties are mainly tuned by the existence of oxygen vacancies (responsible for the electronic and structural disorder), Ag coordination number, and atomic diffusion processes [173-175].

The electronic properties of Ag_2O bulks and surfaces were extensively evaluated over the years [176-179]. However, the relation between photocatalytic potential, electronic structure, and crystalline morphology was not depicted. In front of this scenario, Ribeiro et al. [63] performed a broad investigation on surfaces, morphology, and properties of the pristine cubic ($Pn\bar{3}m$) Ag_2O through a comprehensive and systematical DFT approach. In this work, the analysis of the energetic, structural, and electronic properties rationalizes the nature of photoinduced charge carriers and shape-dependent photocatalytic mechanisms.

The calculated structure of Ag_2O indicates that the Ag cations are in a linear arrangement with two O atoms; otherwise, each O site is neighbored by four Ag atoms forming a tetrahedral (O_{4c}). The structural investigation also predicts the influence of different kinds of vacancies on Ag_2O properties, considering neutral and charged Ag and O vacancies. The results suggest that neutral Ag vacancies (V_{Ag}^x) reduce the Ag–O bond lengths. Similarly, the bulk structure containing charged Ag vacancies (V_{Ag}') presents a more accentuated decrease of bond lengths, resulting in trigonal planar O sites instead of the tetrahedral O sites found in the non-defective bulk structure.

In the case of neutral O vacancies (V_O^x), a higher distortion is observed since the Ag–O bonds become longer while the Ag–Ag distance shortens. Further, V_O^x reduces the Ag cations and the reminiscent electrons behave as coupled electron pair, enabling a metallic Ag–Ag bond. In the case of monocharged (V_O') and bicharged (V_O'') O vacancies, it is observed a decrease of

Ag–O bond distance and an increase of Ag–Ag bond lengths regarding the non-defective bulk Ag_2O. The increase of the Ag–Ag bonds comes from high electrostatic repulsion observed between Ag atoms and Ag cations which are unfavorable to the metallic bond suggested by V_O^x.

The creation of vacancies also presents a major influence on the electronic structure. The non-defective Ag_2O bulk presents a typically semiconductor direct band gap of 2.07 eV (Γ-Γ) and the creation of V_{Ag}^x creates intermediary levels (in the form of flat bands) in the band gap region due to electron uncoupled from vacancies between O atoms. The dangling bonds observed in this model cause imperfect doublet states occupied by three electrons in an energy level closer to the top of VB, which plays the role of acceptor levels. Also, this system presents an indirect band gap of 0.40 eV. In particular, the existence of V_{Ag}^x is responsible for forming h^+ and a doublet ground state with metallic features since the h^+ are allocated at the top of the VB. For Ag_2O bulk structure with V_{Ag}', a diamagnetic character arises, and a semiconductor behavior characterized by a direct band gap of 2.15 eV is observed.

In turn, the insertion of V_O^x causes the shift of the energy levels on the top of VB and the bottom of CB, resulting in the increase of the band gap to 2.49 eV. This behavior was also experimentally reported by Yin et al. [180]. In summary, neutral O vacancies create four dangling bonds. The defect center occupies the lower energies in the VB, whereas the unoccupied levels compose the levels above the bottom of CB. Thus, V_O^x sites act as a deep donor site. In the case of V_O', the electronic structure evidence that this kind of vacancies can be raised from V_O^x trapping a hole while the remaining electron is trapped on empty states of surrounding metal sites, creating paramagnetic species. The existence of V_O' creates intermediary levels (flat bands) responsible for the indirect band gap of 0.25 eV. Similarly, V_O' can be ionized into V_O'' rising a diamagnetic character - null magnetic moment (μ_Z) - from coupled electrons. As a matter of fact, the electronic structure of Ag_2O containing this defect exhibits a non-magnetic behavior with a metallic character.

A critical comment on Ag_2O features lies in residual magnetism, while the other Ag-based semiconductors discussed in this chapter are non-magnetic. The magnetic behavior of silver oxide comes from neutral Ag vacancies or monovalent O vacancies in the surface. From theoretical approaches previously depicted in this chapter, it is denoted that Ag vacancies induce the redistribution of the remaining electrons, resulting in reduced Ag cations with unpaired electron occupation (μ_z = 0.343). Otherwise, oxygen vacancies are responsible for localizing unpaired electrons within metallic Ag clusters creating magnetic centers (μ_z = 0.214). Hence, these results pave the way to state that creating this kind of vacancy is an accessible tool to generate magnetic features in non-magnetic Ag_2O. This behavior was also experimentally reported [181-185].

The electronic properties of Ag_2O were also evaluated in terms of charge carrier stability. The results show that neutral and charged Ag vacancies favor the photocatalytic behavior of Ag_2O once the recombination rate between electrons and holes decreased. Meanwhile, the creation of O vacancies reduces the photocatalytic activity of Ag_2O since the recombination rate of charge carriers increases, making the photocatalytic process inefficient.

Moreover, the low index (100), (110), and (111) surfaces of Ag_2O were investigated, and the following surface stability order is observed (111) > (110) > (100), reflecting the defects density on the surfaces agreeing with previous theoretical results [165]. The calculated electronic structure of these surfaces suggests a metallic band gap for (110) and (110) surfaces and a semiconductor band gap for (111) surfaces. Moreover, the charge carriers' investigation indicates that photogenerated e^- and h^+ possess distinct mobility paths along each crystallographic direction. In particular, (100) and (110) planes present the highest photocatalytic efficiency due to high charge carrier stability.

From all surface results obtained from the DFT approach, several morphologies were predicted using the Wulff's theory [186] and reported by Ribeiro et al. [63]. The results indicate

that the two low-energy (100) and (010) surfaces are predominant in the morphologies. In addition, Ag_2O nanocrystals, majorly composed of (100) and (110) surfaces, have enhanced photocatalysis properties, enabling the photogenerated carriers to generate radical species effectively.

Finally, the theoretical results provide valuable insights into the origin of the electronic, magnetic, and photocatalytic properties of Ag_2O and demonstrate the potential for developing electronic devices and photocatalytic-based materials.

5 Conclusions and outlook

The design of new materials with tailored properties is the heart of materials research and nanotechnology and making them accessible for different applications. In this context, metal oxide semiconductors are an important area of research because almost all contemporary electronic technologies involve the use of these materials. Much research effort has focused on the synthesis of these inorganic semiconductors with controlled chemistry, size, shape, and composition driven by their intriguing, quantized behavior. They present themselves with marvelous morphology-dependent physical and chemical properties. They have attracted huge attention due to their unique material properties and their consequent theoretical and practical applications in chemistry, physics, materials science, biology, and medicine. This enormous progress has boosted new research due to their unanticipated novel properties, and consequently, a plethora of applications have stimulated further research efforts in this large field. To make possible the development of these technological applications, a complete understanding and rationalization, at the atomic level, of the physical and chemical, and thus the functions are of equal importance.

This chapter addresses these questions by presenting recent investigations performed by our research on different semiconductors. In particular, the metal oxides composed of Ag have been investigated by combining experimental studies and simulations based on first-principles calculations. The morphological modulations could be achieved by carefully analyzing the coordination environment surrounding the metals on the exposed surfaces at the morphology (defined here as the active sites where the electron transfer process involving O_2 and the bond making/-breaking processes associated to H_2O take place). From this analysis, an understanding of the mechanisms is obtained to explain the photocatalytic and biocide activity of semiconductors in advancing industrial and biomedical applications. Therefore, this strategy provided a gain of deep insight to modulate their geometric, electronic, and magnetic properties.

Acknowledgments

The authors are grateful to Fundação de Amparo à Pesquisa do Estado de São Paulo (FAPESP) for grants 2013/07296-2 (related to Centro de Desenvolvimento de Materiais Funcionais), 2016/23891-6, 2017/26105-4, 2019/01732-1, and 2020/03780-0. J.A. acknowledges Universitat Jaume I for project, UJI-B2019-30, and Ministerio de Ciencia, Innovación y Universidades (Spain) project PGC2018-094417-B-I00 for supporting this research financially. MASM thanks Brazilian Council for Scientific and Technological Development (CNPq) for research grant #305792/2020-2. This work used computational resources of the "Centro de Computação John David Rogers" (CCJDR-UNICAMP), CENAPAD-RJ (SDumont) and CENAPAD-SP. We also wish to thank the Servei d'Informática, Universitat Jaume I, for their generous allocation of computer time.

References

1. Y.B. Wang, T.H. Wu, J. Barbaud, W.Y. Kong, D.Y. Cui, H. Chen, X.D. Yang, and L.Y. Han, Science **365**, 687 (2019).
2. L.P. Zhang, J.R. Ran, S.Z. Qiao, and M. Jaroniec, Chem. Soc. Rev. **48**, 5184 (2019).
3. C. Kranz and M. Wachtler, Chem. Soc. Rev. **50**, 1407 (2021).
4. M.R. Lukatskaya, B. Dunn, and Y. Gogotsi, Nat. Commun. **7**, (2016).
5. F.E. Osterloh, ACS Energy Lett. **2**, 445 (2017).
6. J.S. Cai, J.L. Shen, X.N. Zhang, Y.H. Ng, J.Y. Huang, W.X. Guo, C.J. Lin, and Y.K. Lai, Small Methods **3**, (2019).
7. F. Pellegrino, F. Sordello, M. Minella, C. Minero, and V. Maurino, Catalysts **9**, (2019).
8. Y.O. Wang, H. Suzuki, J.J. Xie, O. Tomita, D.J. Martin, M. Higashi, D. Kong, R. Abe, and J.W. Tang, Chem. Rev. **118**, 5201 (2018).
9. Z. Wang, C. Li, and K. Domen, Chem. Soc. Rev. **48**, 2109 (2019).
10. X.X. Chang, T. Wang, and J.L. Gong, Energy Environ. Sci. **9**, 2177 (2016).
11. P. Prabhu, V. Jose, and J.M. Lee, Adv. Funct. Mater. **30**, (2020).
12. S.Z. Xu and E.A. Carter, Chem. Rev. **119**, 6631 (2019).
13. Y.C. Wu, X. Zhang, Y.T. Xing, Z.C. Hu, H.R. Tang, W. Luo, F. Huang, and Y. Cao, ACS Mater. Lett. **1**, 620 (2019).
14. S.B. Wang, Y. Wang, S.L. Zhang, S.Q. Zang, and X.W. Lou, Adv. Mater. **31**, (2019).
15. Y.Y. Zhou, L. Zhang, and W.Z. Wang, Nat. Commun. **10**, (2019).
16. M. Mousavi, A. Habibi-Yangjeh, and M. Abitorabi, J. Colloid Interface Sci. **480**, 218 (2016).
17. H.A. Schwarz and R.W. Dodson, J. Phys. Chem. **88**, 3643 (1984).
18. Y.Y. Gao, W. Nie, X.L. Wang, F.T. Fan, and C. Li, Chem. Commun. **56**, 1007 (2020).
19. Y. Ma, X.L. Wang, Y.S. Jia, X.B. Chen, H.X. Han, and C. Li, Chem. Rev. **114**, 9987 (2014).
20. S. Corby, L. Francas, S. Selim, M. Sachs, C. Blackman, A. Kafizas, and J.R. Durrant, J. Amer. Chem. Soc. **140**, 16168 (2018).
21. A. Kudo and Y. Miseki, Chem. Soc. Rev. **38**, 253 (2009).
22. C.Z. Luo, X.H. Ren, Z.G. Dai, Y.P. Zhang, X. Qi, and C.X. Pan, ACS Appl. Mater. Interfaces **9**, 23265 (2017).
23. S. Bai, L.L. Wang, Z.Q. Li, and Y.J. Xiong, Adv. Sci. **4**, (2017).
24. K.L. Wang, M. Janczarek, Z.S. Wei, T. Raja-Mogan, M. Endo-Kimura, T.M. Khedr, B. Ohtani, and E. Kowalska, Catalysts **9**, (2019).
25. S.J.A. Moniz, S.A. Shevlin, D.J. Martin, Z.X. Guo, and J.W. Tang, Energy Environ. Sci. **8**, 731 (2015).
26. K. Afroz, M. Moniruddin, N. Bakranov, S. Kudaibergenov, and N. Nuraje, J. Mater. Chem. A **6**, 21696 (2018).
27. L.P. Zhang and M. Jaroniec, Appl. Surf. Sci. **430**, 2 (2018).
28. L.F. Wei, C.L. Yu, Q.H. Zhang, H. Liu, and Y. Wang, J. Mater. Chem. A **6**, 22411 (2018).
29. S. Bera, D.I. Won, S.B. Rawal, H.J. Kang, and W.I. Lee, Catal. Today **335**, 3 (2019).
30. N. Guijarro, M.S. Prevot, and K. Sivula, Phys. Chem. Chem. Phys. **17**, 15655 (2015).
31. S.G. Kumar and K. Rao, Appl. Surf. Sci. **391**, 124 (2017).
32. W. Yang, R.R. Prabhakar, J. Tan, S.D. Tilley, and J. Moon, Chem. Soc. Rev. **48**, 4979 (2019).
33. C.R. Jiang, S.J.A. Moniz, A.Q. Wang, T. Zhang, and J.W. Tang, Chem. Soc. Rev. **46**, 4645 (2017).

34. M. Xiao, B. Luo, Z.L. Wang, S.C. Wang, and L.Z. Wang, Solar Rrl **4**, (2020).
35. Y. Nosaka and A.Y. Nosaka, Chem. Rev. **117**, 11302 (2017).
36. Y. Li, W. Zhang, J.F. Niu, and Y.S. Chen, ACS Nano **6**, 5164 (2012).
37. G. Applerot, A. Lipovsky, R. Dror, N. Perkas, Y. Nitzan, R. Lubart, and A. Gedanken, Adv. Funct. Mater. **19**, 842 (2009).
38. A. Lipovsky, Y. Nitzan, A. Gedanken, and R. Lubart, Nanotechnology **22**, (2011).
39. Y. Li, J.F. Niu, W. Zhang, L.L. Zhang, and E.X. Shang, Langmuir **30**, 2852 (2014).
40. V.L. Prasanna and R. Vijayaraghavan, Langmuir **31**, 9155 (2015).
41. D.M. Chen, Z.H. Wang, T.Z. Ren, H. Ding, W.Q. Yao, R.L. Zong, and Y.F. Zhu, J. Phys. Chem. C **118**, 15300 (2014).
42. W.W. He, H.K. Kim, W.G. Warner, D. Melka, J.H. Callahan, and J.J. Yin, J. Amer. Chem. Soc. **136**, 750 (2014).
43. C.E. Tsai, S.M. Yeh, C.H. Chen, and H.N. Lin, Nanoscale Res. Lett. **14**, (2019).
44. J. Xiong, J. Di, J.X. Xia, W.S. Zhu, and H.M. Li, Adv. Funct. Mater. **28**, (2018).
45. J. Nowotny, M.A. Alim, T. Bak, M.A. Idris, M. Ionescu, K. Prince, M.Z. Sahdan, K. Sopian, M.A.M. Teridi, and W. Sigmund, Chem. Soc. Rev. **44**, 8424 (2015).
46. T. Hisatomi and K. Domen, Nat. Catal. **2**, 387 (2019).
47. B. Mei, K. Han, and G.D. Mul, ACS Catal. **8**, 9154 (2018).
48. M. Assis, C.C. de Foggi, V. Teodoro, J.P.D. da Costa, C.E. Silva, T. Robeldo, P.F. Caperucci, C.E. Vergani, R.C. Borra, I. Sorribes, A.F. Gouveia, M.A. San-Miguel, J. Andres, and E. Longo, Appl. Surf. Sci. **545**, (2021).
49. C.C. De Foggi, R.C. De Oliveira, M. Assis, M.T. Fabbro, V.R. Mastelaro, C.E. Vergani, L. Gracia, J. Andrés, E. Longo, and A.L. Machado, Mater. Sci. Eng.: C, 110765 (2020).
50. M. Assis, M.A. Ponce, A.F. Gouveia, D. Souza, J. da Costa, V. Teodoro, Y.G. Gobato, J. Andres, C. Macchi, A. Somoza, and E. Longo, Cryst. Growth Des. **21**, 1093 (2021).
51. M. Assis, R.A.P. Ribeiro, M.H.C. Costa, M.M. Teixeira, Y.G. Gobato, G.A. Prando, C.R. Mendonca, L. de Boni, A.J.A. de Oliveira, J. Bettini, J. Andres, and E. Longo, ACS Omega **5**, 10052 (2020).
52. X.G. Yang and D.W. Wang, ACS Appl. Energy Mater. **1**, 6657 (2018).
53. Q. Guo, C.Y. Zhou, Z.B. Ma, and X.M. Yang, Adv. Mater. **31**, (2019).
54. F. Giustino, *Materials modelling using density functional theory : properties and predictions*. Vol. 1st ed. 2014, Oxford University press: Oxford University press.
55. J.Q. Dai, J.W. Xu, and J.H. Zhu, ACS Appl. Mater. Interfaces **9**, 3168 (2017).
56. Q.X. Cai, J.G. Wang, Y. Wang, and D.H. Mei, J. Phys. Chem. C **120**, 19087 (2016).
57. J.G. Lee, *Computational Materials Science: An introduction*. 2016, Boca Raton: CRC Press
58. P.W. Tasker, J. Phys. C: Solid State Phys. **12**, 4977 (1979).
59. C. Yue, X.M. Lu, J.T. Zhang, F.Z. Huang, and J.S. Zhu, Phys. Rev. B **100**, (2019).
60. X.X. Tian, T. Wang, L.F. Fan, Y.K. Wang, H.G. Lu, and Y.W. Mu, Appl. Surf. Sci. **427**, 357 (2018).
61. L.H.d.S. Lacerda and S.R. de Lazaro, Surfaces and Interfaces **22**, 100837 (2021).
62. L.H.D. Lacerda and S.R. de Lazaro, J. Am. Ceram. Soc. **103**, 5688 (2020).
63. R.A.P. Ribeiro, M.C. Oliveira, M.R.D. Bomio, S.R. de Lazaro, J. Andres, and E. Longo, Appl. Surf. Sci. **509**, (2020).
64. R.A.P. Ribeiro, L.H.S. Lacerda, E. Longo, J. Andres, and S.R. de Lazaro, J. Magn. Magn. Mater. **475**, 544 (2019).
65. R.A.P. Ribeiro, E. Longo, J. Andres, and S.R. de Lazaro, Phys. Chem. Chem. Phys. **20**, 28382 (2018).

66. R.A.P. Ribeiro, S.R. de Lazaro, L. Gracia, E. Longo, and J. Andres, J. Magn. Magn. Mater. **453**, 262 (2018).
67. J.J. Metois and P. Muller, Surf. Sci. **548**, 13 (2004).
68. D.J. Eaglesham, A.E. White, L.C. Feldman, N. Moriya, and D.C. Jacobson, Phys. Rev. Lett. **70**, 1643 (1993).
69. C. Bombis, A. Emundts, M. Nowicki, and H.P. Bonzel, Surf. Sci. **511**, 83 (2002).
70. G. Wulff, Z. Kristallogr. **34**, 449 (1901).
71. H. Guo and A.S. Barnard, J. Mater. Chem. **21**, 11566 (2011).
72. L.D. Marks and L. Peng, J. Phys.: Condens. Matter **28**, 053001 (2016).
73. M.M. Ferrer, A.F. Gouveia, L. Gracia, E. Longo, and J. Andres, Modell. Simul. Mater. Sci. Eng. **24**, 025007 (2016).
74. F.Z. Jiang, L. Yang, D.L. Zhou, G. He, J.B. Zhou, F.H. Wang, and Z.G. Chen, Appl. Surf. Sci. **436**, 989 (2018).
75. J.J. Gilman, J. Appl. Phys. **31**, 2208 (1960).
76. A.F. Gouveia, L. Gracia, E. Longo, M.A. San-Miguel, and J. Andres, Comput. Mater. Sci. **188**, (2021).
77. J. Andrés, L. Gracia, A.F. Gouveia, M.M. Ferrer, and E. Longo, Nanotechnology **26**, 405703 (2015).
78. P.F.S. Pereira, A.F. Gouveia, M. Assis, R.C. de Oliveira, I.M. Pinatti, M. Penha, R.F. Goncalves, L. Gracia, J. Andres, and E. Longo, Phys. Chem. Chem. Phys. **20**, 1923 (2018).
79. W.d.S. Pereira, J. Andres, L. Gracia, M.A. San-Miguel, E.Z. da Silva, E. Longo, and V.M. Longo, Phys. Chem. Chem. Phys. **17**, 5352 (2015).
80. R.C. de Oliveira, L. Gracia, M. Assis, M.S. Li, J. Andres, E. Longo, and L.S. Cavalcante, CrystEngComm **18**, 6483 (2016).
81. R.A. Roca, A.F. Gouveia, P.S. Lemos, L. Gracia, J. Andres, and E. Longo, Inorg. Chem. **55**, 8661 (2016).
82. R.C. de Oliveira, C.C. de Foggi, M.M. Teixeira, M.D.P. da Silva, M. Assis, E.M. Francisco, B. Pimentel, P.F.D. Pereira, C.E. Vergani, A.L. Machado, J. Andres, L. Gracia, and E. Longo, ACS Appl. Mater. Interfaces **9**, 11472 (2017).
83. A.C.M. Tello, M. Assis, R. Menasce, A.F. Gouveia, V. Teodoro, N. Jacomaci, M.A. Zaghete, J. Andres, G.E. Marques, M.D. Teodoro, A.B.F. da Silva, J. Bettini, and E. Longo, Inorg. Chem. **59**, 7453 (2020).
84. A.C. Catto, M.M. Ferrer, O.F. Lopes, V.R. Mastelaro, J. Andres, L.F. da Silva, E. Longo, and W. Avansi, Appl. Surf. Sci. **529**, (2020).
85. M.T. Fabbro, C.C. Foggi, L.P.S. Santos, L. Gracia, A. Perrin, C. Perrin, C.E. Vergani, A.L. Machado, J. Andres, E. Cordoncillo, and E. Longo, Dalton Trans. **45**, 10736 (2016).
86. G.S. Silva, L. Gracia, M.T. Fabbro, L.P.S. dos Santos, H. Beltran-Mir, E. Cordoncillo, E. Longo, and J. Andres, Inorg. Chem. **55**, 8961 (2016).
87. R.A. Roca, P.S. Lemos, L. Gracia, J. Andres, and E. Longo, RSC Adv. **7**, 5610 (2017).
88. L.H.D. Lacerda and S.R. de Lazaro, J. Magn. Magn. Mater. **500**, (2020).
89. L.H.D. Lacerda, R.A.P. Ribeiro, and S.R. de Lazaro, J. Magn. Magn. Mater. **480**, 199 (2019).
90. L.H.D. Lacerda and S.R. de Lazaro, New J. Chem. **43**, 10610 (2019).
91. D.C. Mattis, *The Theory of Magnetism Made Simple*. 2006: World Scientific.
92. R.A.P. Ribeiro, S.R. de Lazaro, and S.A. Pianaro, J. Magn. Magn. Mater. **391**, 166 (2015).
93. L.H.D. Lacerda and S.R. de Lazaro, J. Magn. Magn. Mater. **465**, 412 (2018).
94. L.H.D. Lacerda and S.R. de Lazaro, Comput. Mater. Sci. **153**, 228 (2018).

95. L.H.D. Lacerda and S.R. de Lazaro, J. Mater. Sci. **55**, 6875 (2020).
96. R.A.P. Ribeiro, J. Andres, E. Longo, and S.R. Lazaro, Appl. Surf. Sci. **452**, 463 (2018).
97. Y.N. Xia, Y.J. Xiong, B. Lim, and S.E. Skrabalak, Angew. Chem. Int. Ed. **48**, 60 (2009).
98. P.Y. Yu and M. Cardona, *Fundamentals of Semiconductors: Physics and Materials Properties, Fourth Edition*, in *Fundamentals of Semiconductors: Physics and Materials Properties, Fourth Edition*. 2010. p. 1.
99. Z. Zhang and J.T. Yates, Chem. Rev. **112**, 5520 (2012).
100. A. Zangwill, *Physics at Surfaces*. 1988, Cambridge: Cambridge University Press.
101. K.Z. Qi, X.H. Xing, A. Zada, M.Y. Li, Q. Wang, S.Y. Liu, H.X. Lin, and G.Z. Wang, Ceram. Int. **46**, 1494 (2020).
102. S. Wang, P.Y. Kuang, B. Cheng, J.G. Yu, and C.J. Jiang, J. Alloys Compd. **741**, 622 (2018).
103. M.H. Huang and M. Madasu, Nano Today **28**, (2019).
104. C.Y. Chu and M.H. Huang, J. Mater. Chem. A **5**, 15116 (2017).
105. G. Botelho, J. Andres, L. Gracia, L.S. Matos, and E. Longo, ChemPlusChem **81**, 202 (2016).
106. E.Z. da Silva, G.M. Faccin, T.R. Machado, N.G. Macedo, M. de Assis, S. Maya-Johnson, J.C. Sczancoski, J. Andrés, E. Longo, and M.A. San-Miguel, J. Phys. Chem. C **123**, 11310 (2019).
107. R. Alvarez-Roca, A.F. Gouveia, C.C. de Foggi, P.S. Lemos, L. Gracia, L.F. da Silva, C.E. Vergani, M. San-Miguel, E. Longo, and J. Andrés, Inorg. Chem. **60**, 1062 (2021).
108. Y.X. Wei, C.Q. Jin, and Y.M. Zeng, J. Inorg. Mater. **32**, 1009 (2017).
109. W. Kleemann, J. Phys. D: Appl. Phys. **50**, (2017).
110. X. Yang, Z. Zhou, T. Nan, Y. Gao, G.M. Yang, M. Liu, and N.X. Sun, J. Mater. Chem. C **4**, 234 (2016).
111. M. Getzlaff, *Fundamentals of Magnetism*. Berlim: Springer.
112. R. Singh, J. Magn. Magn. Mater. **346**, 58 (2013).
113. J.B. Goodenough, *Magnetism and the Chemical Bond*. 1963, New York: Interscience Publisher.
114. V. Baltz, A. Manchon, M. Tsoi, T. Moriyama, T. Ono, and Y. Tserkovnyak, Rev. Mod. Phys. **90**, (2018).
115. D.D. Awschalom and M.E. Flatte, Nat. Phys. **3**, 153 (2007).
116. R. Lebrun, A. Ross, S.A. Bender, A. Qaiumzadeh, L. Baldrati, J. Cramer, A. Brataas, R.A. Duine, and M. Klaui, Nature **561**, 222 (2018).
117. S.C. Warren and E. Thimsen, Energy Environ. Sci. **5**, 5133 (2012).
118. S.C. Wang, L.Z. Wang, and W. Huang, J. Mater. Chem. A **8**, 24307 (2020).
119. P. Christopher, H.L. Xin, and S. Linic, Nat. Chem. **3**, 467 (2011).
120. L. Zhou, C. Zhang, M.J. McClain, A. Manavacas, C.M. Krauter, S. Tian, F. Berg, H.O. Everitt, E.A. Carter, P. Nordlander, and N.J. Halas, Nano Lett. **16**, 1478 (2016).
121. S. Navalon, M. de Miguel, R. Martin, M. Alvaro, and H. Garcia, J. Amer. Chem. Soc. **133**, 2218 (2011).
122. F. Vatansever, W. de Melo, P. Avci, D. Vecchio, M. Sadasivam, A. Gupta, R. Chandran, M. Karimi, N.A. Parizotto, R. Yin, G.P. Tegos, and M.R. Hamblin, FEMS Microbiol. Rev. **37**, 955 (2013).
123. V.I. Lushchak, Comp. Biochem. Physiol. C Toxicol. Pharmacol. **153**, 175 (2011).
124. A.B. Trench, T.R. Machado, A.F. Gouveia, M. Assis, L.G. da Trindade, C. Santos, A. Perrin, C. Perrin, M. Oliva, J. Andres, and E. Longo, Appl. Catal., B **238**, 198 (2018).

125. A.B. Trench, T.R. Machado, A.F. Gouveia, C.C. Foggi, V. Teodoro, I. Sanchez-Montes, M.M. Teixeira, L.G. Trindade, N. Jacomaci, A. Perrin, C. Perrin, J.M. Aquino, J. Andres, and E. Longo, ACS Omega **5**, 23808 (2020).
126. C.A. Oliveira, D.P. Volanti, A.E. Nogueira, C.A. Zamperini, C.E. Vergani, and E. Longo, Mater. Des. **115**, 73 (2017).
127. C.C. de Foggi, R.C. de Oliveira, M.T. Fabbro, C.E. Vergani, J. Andres, E. Longo, and A.L. Machado, Cryst. Growth Des. **17**, 6239 (2017).
128. V.M. Longo, C.C. De Foggi, M.M. Ferrer, A.F. Gouveia, R.S. Andre, W. Avansi, C.E. Vergani, A.L. Machado, J. Andres, L.S. Cavalcante, A.C. Hernandes, and E. Longo, J. Phys. Chem. A **118**, 5769 (2014).
129. T. Kokulnathan, T.W. Chen, S.M. Chen, J.V. Kumar, S. Sakthinathan, and E.R. Nagarajan, Compos. B: Eng. **169**, 249 (2019).
130. J.L. Zhang and Z. Ma, RSC Adv. **7**, 2163 (2017).
131. Y.Y. Bai, Y. Lu, and J.K. Liu, J. Hazard. Mater. **307**, 26 (2016).
132. A. Beltran, L. Gracia, E. Longo, and J. Andres, J. Phys. Chem. C **118**, 3724 (2014).
133. M.T. Fabbro, C. Saliby, L.R. Rios, F.A. La Porta, L. Gracia, M.S. Li, J. Andres, L.P.S. Santos, and E. Longo, Sci. Technol. Adv. Mater. **16**, (2015).
134. D. Santamaria-Perez, E. Bandiello, D. Errandonea, J. Ruiz-Fuertes, O. Gomis, J.A. Sans, F.J. Manjon, P. Rodriguez-Hernandez, and A. Munoz, J. Phys. Chem. C **117**, 12239 (2013).
135. M.T. Fabbro, L. Gracia, G.S. Silva, L.P.S. Santos, J. Andrés, E. Cordoncillo, and E. Longo, J. Solid State Chem. **239**, 220 (2016).
136. J. Luo, X.S. Zhou, L. Ma, X.M. Ning, L. Zhan, X.Y. Xu, L.M. Xu, L.L. Zhang, H.T. Ruan, and Z.B. Zhang, Adv. Powder Technol. **28**, 1018 (2017).
137. S.Y. Yao, J.M. Wu, W. Li, R.F. Zheng, R. Li, Y.Q. Chen, J. Luo, and X.S. Zhou, Sep. Purif. Technol. **227**, (2019).
138. J. Luo, X.S. Zhou, L. Ma, X.Y. Xu, J.X. Wu, and H.P. Liang, Mater. Res. Bull. **77**, 291 (2016).
139. M. Pirhashemi and A. Habibi-Yangjeh, Ceram. Int. **41**, 14383 (2015).
140. S.X. Ouyang, Z.S. Li, Z. Ouyang, T. Yu, J.H. Ye, and Z.G. Zou, J. Phys. Chem. C **112**, 3134 (2008).
141. M. Azami, M. Haghighi, and S. Allahyari, Ultrason. Sonochem. **40**, 505 (2018).
142. M. Miclau, S. Kumar, D. Ursu, C. Orha, N. Miclau, J.M. Rueff, S. Malo, and C. Martin, Mater. Charact. **158**, (2019).
143. Y. Liu, H.B. Yu, M. Cai, and J.W. Sun, Catal. Commun. **26**, 63 (2012).
144. L.F. Zhu, D.Q. Huang, H.F. Ma, D.R. Wu, M.R. Yang, and S. Komarneni, Ceram. Int. **41**, 12509 (2015).
145. R.O. Torres-Mendieta, M.M. Teixeira, G. Minguez-Vega, D. de Souza, Y.G. Gobato, M. Assis, H. Beltran-Mir, E. Cordoncillo, J. Andres, M. Cernik, and E. Longo, J. Phys. Chem. C **124**, 26404 (2020).
146. P.S. Lemos, G.S. Silva, R.A. Roca, M. Assis, R. Torres-Mendieta, H. Beltran-Mir, G. Minguez-Vega, E. Cordoncillo, J. Andres, and E. Longo, Phys. Chem. Chem. Phys. **21**, 6101 (2019).
147. X.J. Zou, Y.Y. Dong, S.J. Li, J. Ke, and Y.B. Cui, Solar Energy **169**, 392 (2018).
148. I.M. Pinatti, A.C.M. Tello, A.B. Trench, C.C. de Foggi, P.F.S. Pereira, M.M. Teixeira, N. Jacomaci, J. Andres, and E. Longo, J. Alloys Compd. **835**, (2020).
149. D.F. Xu, S.W. Cao, J.F. Zhang, B. Cheng, and J.G. Yu, Beilstein J. Nanotechnol. **5**, 658 (2014).

150. E. Longo, D.P. Volanti, V.M. Longo, L. Gracia, I.C. Nogueira, M.A.P. Almeida, A.N. Pinheiro, M.M. Ferrer, L.S. Cavalcante, and J. Andres, J. Phys. Chem. C **118**, 1229 (2014).
151. Z. Lin, J. Li, Z. Zheng, J. Yan, P. Liu, C. Wang, and G. Yang, ACS Nano **9**, 7256 (2015).
152. L.F. da Silva, A.C. Catto, W. Avansi, L.S. Cavalcante, V.R. Mastelaro, J. Andres, K. Aguir, and E. Longo, J. Alloys Compd. **683**, 186 (2016).
153. L.S. Cavalcante, M.A. Almeida, W. Avansi, Jr., R.L. Tranquilin, E. Longo, N.C. Batista, V.R. Mastelaro, and M.S. Li, Inorg. Chem. **51**, 10675 (2012).
154. P.S. Lemos, A. Altomare, A.F. Gouveia, I.C. Nogueira, L. Gracia, R. Llusar, J. Andrés, E. Longo, and L.S. Cavalcante, Dalton Trans. **45**, 1185 (2016).
155. N.G. Macedo, A.F. Gouveia, R.A. Roca, M. Assis, L. Gracia, J. Andrés, E.R. Leite, and E. Longo, J. Phys. Chem. C **122**, 8667 (2018).
156. L.O. Laier, M. Assis, C.C. Foggi, A.F. Gouveia, C.E. Vergani, L.C.L. Santana, L.S. Cavalcante, J. Andres, and E. Longo, Theor. Chem. Acc. **139**, (2020).
157. R.A. Roca, P.S. Lemos, J. Andres, and E. Longo, Chem. Phys. Lett. **644**, 68 (2016).
158. N.F.A. Neto, J.M.P. Silva, R.L. Tranquilin, E. Longo, M.R.D. Bomio, and F.V. Motta, Ceram. Int. **46**, 14864 (2020).
159. C.C. Foggi, M.T. Fabbro, L.P.S. Santos, Y.V.B. de Santana, C.E. Vergani, A.L. Machado, E. Cordoncillo, J. Andres, and E. Longo, Chem. Phys. Lett. **674**, 125 (2017).
160. F.X. Nobre, I.S. Bastos, R.O. dos Santos Fontenelle, E.A.A. Júnior, M.L. Takeno, L. Manzato, J.M.E. de Matos, P.P. Orlandi, J. de Fátima Souza Mendes, W.R. Brito, and P.R. da Costa Couceiro, Ultrason. Sonochem. **58**, 104620 (2019).
161. M. Assis, E. Cordoncillo, R. Torres-Mendieta, H. Beltran-Mir, G. Minguez-Vega, R. Oliveira, E.R. Leite, C.C. Foggi, C.E. Vergani, E. Longo, and J. Andres, Sci. Rep. **8**, (2018).
162. M. Assis, T. Robeldo, C.C. Foggi, A.M. Kubo, G. Mínguez-Vega, E. Condoncillo, H. Beltran-Mir, R. Torres-Mendieta, J. Andrés, M. Oliva, C.E. Vergani, P.A. Barbugli, E.R. Camargo, R.C. Borra, and E. Longo, Sci. Rep. **9**, 9927 (2019).
163. H. Wang, L. Qiao, H. Xu, Y. Lin, Y. Shen, and C. Nan, Soft Nanosci. Lett. **6**, 11 (2016).
164. Y. Ida, S. Watase, T. Shinagawa, M. Watanabe, M. Chigane, M. Inaba, A. Tasaka, and M. Izaki, Chem. Mater. **20**, 1254 (2008).
165. G. Wang, X. Ma, B. Huang, H. Cheng, Z. Wang, J. Zhan, X. Qin, X. Zhang, and Y. Dai, J. Mater. Chem. **22**, 21189 (2012).
166. Y.-W. Harn, T.-H. Yang, T.-Y. Tang, M.-C. Chen, and J.-M. Wu, ChemCatChem **7**, 80 (2015).
167. Y. Peng and S. Tsang, Nano Today **18**, 15 (2018).
168. Y.-J. Chen, Y.-W. Chiang, and M.H. Huang, ACS Appl. Mater. Interfaces **8**, 19672 (2016).
169. C.-S. Tan, Y.-J. Chen, C.-F. Hsia, and M.H. Huang, Chem. Asian J. **12**, 293 (2017).
170. M.-J. Kim, Y.-S. Cho, S.-H. Park, and Y.-D. Huh, Cryst. Growth Des. **12**, 4180 (2012).
171. D. Yan, Y. Li, J. Huo, R. Chen, L. Dai, and S. Wang, Adv. Mater. **29**, 1606459 (2017).
172. G. Wang, Y. Yang, D. Han, and Y. Li, Nano Today **13**, 23 (2017).
173. Q. Wu, M. Si, B. Zhang, K. Zhang, H. Li, L. Mi, Y. Jiang, Y. Rong, J. Chen, and Y. Fang, Nanotechnology **29**, 295702 (2018).
174. X. Wang, S. Li, H. Yu, J. Yu, and S. Liu, Chem. Eur. J. **17**, 7777 (2011).